STUDY OF FLUCTUATIONS AND INTRINSIC FLOWS IN A SIMPLE TOROIDAL PLASMA

By

T Shekar Goud

Institute for Plasma Research, Bhat, Gandhinagar,
Gujarat, India.

A thesis submitted to the
Board of Studies in Physical Sciences

In partial fulfillment of the requirements
For the Degree of

DOCTOR OF PHILOSOPHY

of

HOMI BHABHA NATIONAL INSTITUTE

May 2012

Homi Bhabha National Institute

Recommendations of the Viva Voce Board

As members of the Viva Voce Board, we recommend that the dissertation prepared by **T Shekar Goud** entitled "Study of fluctuations and intrinsic flows in a simple toroidal plasma" may be accepted as fulfilling the dissertation requirement for the Degree of Doctor of Philosophy.

\- **Date :**
Chairman : Y C Saxena

\- **Date :**
Convener : Rajaraman Ganesh

\- **Date :**
Member : Daniel Raju

\- **Date :**
Member : Joydeep Ghosh

\- **Date :**
Member : P Chattopadhyay

Final approval and acceptance of this dissertation is contingent upon the candidate's submission of the final copies of the dissertation to HBNI.

I hereby certify that I have read this dissertation prepared under my direction and recommend that it may be accepted as fulfilling the dissertation requirement.

\- **Date :**
Guide : Rajaraman Ganesh

DECLARATION

I, hereby declare that the investigation presented in the thesis has been carried out by me. The work is original and the work has not been submitted earlier as a whole or in part for a degree/diploma at this or any other Institution or University.

T Shekar Goud

To my family

ACKNOWLEDGEMENTS

It gives me an immense pleasure to be a part of Institute for Plasma Research, during my Ph.D. work. I would like to thank each and everyone, who have been involved directly or indirectly in the research activities carried as a part of my thesis. First of all I would like to thank my thesis supervisor, Dr. Rajaraman Ganesh, with a deep sense of gratitude, for his guidance and continuous support during this thesis work. I could not have imagined the completion of such an important piece of work, without his instructions and enormous attention he has paid.

I would like to thank all the Doctoral Committee members for following up the step by step progress made during my thesis work. Especially, I convey deep gratitude to Prof. Y.C. Saxena for his scrutiny of the all the experimental activities, starting from the techniques used to reporting the observations. I appreciate the crucial role played by other Doctoral Committee members, Dr. Raju, Dr. Joydeep and Dr. P. Chattopadhyay, by reviewing my work and their encouragement to learn additional techniques. I am pleased to acknowledge the critical support in the initial phase, from other members of BETA team, K. Sathyanarayana, Chhaya Chavda and K.K. Mohandas, in starting up the machine, experiments and measurements. I am grateful to other faculty members, Prof. Amita Das, Prof. R. Jha, Prof. Bora, Dr. S. Chaturvedi, Dr. P.Vasu, Dr. S.K. Pathak, Dr. R. Srinivasan, Dr. Manoj Warrier, Dr. S. Mukherjee, Dr. S. Sengupta, Dr. Ahalpara, Dr. S. Pradhan, Dr. Chenna Reddy and others, who have taught me basic plasma physics, experimental, computational techniques or other disciplines of physics during the course work.

There were several instances during the experimental and other activities, when I was in need of information or equipments. I have always secured an unflinching support from my colleagues in the lab, Sambaran, Awasthi, Pankaj, Amulya, Ravi Kumar, Lavkesh, Manu, Karan, Priyavandana, Anitha, Renu, Ganguli, Jayesh, Ashish, Ramasubramanian, and I convey my sincere thanks to all. There were many helping hands in bringing up the experimental system to a working stage in the beginning; I appreciate the support by Ziauddin, D.C. Raval, Pratibha Semwal, Prashant, and S.B. Bhatt in restoring the vacuum system. It is hard for me to forget the assistance provided, very often, by the Electronics section of IPR. Especially, I am very much thankful to Praveen, R. Rajpal, Jignesh, Abhijeet, Pramila and Praveena. I am grateful to Y.S.S. Srinivas for his support in procurement of power supplies. The Workshop and Drafting sections have a significant contribution in fabrication of several accessories for the experimental system and diagnostic probes; my special thanks to Vijay, Gautam, Acharya, Sadhrakiya, Vishnubhai, S. Patnaik. I would like to thank all the staff of Purchase, A/C, Stores, Electrical, Computer Center, Library, and Administrative sections for their support in procurement, maintenance and development activities during the experimental progress related to this thesis work.

I express my sincere thanks to the seniors and friends in the hostel for their company and unconditional support ever. Best wishes to Pintu Banerjee, Niraj Jain, Jyotirmoy Pramanik, Shyama Mukherjee, Ritu Dey, Manash Paul, Suraj Sinha, Rajneesh Yadav, Anand Srivastav, Santosh Dhanpath, Bhaskar Choudhury, Vijay Srivastav, Vikrant, Kishor, Maya, Subhash, Anurag Mishra, Surendra Prasad, Sharad, Satya, Jugal, Sunita, Puraram, Kshitish, Deepak, Ujjwal, Gurudatt, Vikram, Prabal, Ashwin, Sita, Tayyab, Linthish, Rameswar, Sushil, Sanat, Pravesh, Partha, Sayak, Manjit, Aditya, Soumen, Illiyas, Vikram Dharodi, Veda Prakash, and Rana Pratap.

It is undoubtedly true that this work would not have been possible, without the consistent support and encouragement from my family. My hearty gratitude to my parents, my wife and my other family members.

T Shekar Goud

Synopsis

Magnetically confined plasmas in toroidal devices have gained significance decades ago, for their potential to achieve controlled fusion [5]. In spite of the remarkable advance in this field, transport of particles and energy have been found to be anomalous and pose challenges in improving the plasma confinement further. Some of the mechanisms which lead to the above mentioned anomalous transport are the density and temperature gradient driven instabilities in curved magnetic fields [6, 7, 8]. A clear understanding of these processes, therefore, is of the paramount importance. The presence of complex magnetic field geometry in fusion devices, sets constraints in carrying out individual studies on instabilities mentioned above. A simple magnetized torus with a pure toroidal field provides an excellent alternate facility to carry out the above mentioned studies in much simplified conditions. Though mean plasma parameters are much limited in their range compared to tokamak edge plasma, the plasma behavior observed is relatively similar. For instance, the results of turbulence simulation codes which are applicable to the fusion edge plasmas, agree well with the experimental results for simple toroidal devices, when used with suitable normalized parameters as applicable to them [9]. Hence much useful studies on instabilities and transport can be conducted in such simple toroidal devices.

Plasmas produced in confinement devices, in general possess intrinsic gradients in typical plasma parameters such as density, electron or ion temperature and plasma potential. In presence of magnetic field, the density gradient commonly leads to density gradient driven instabilities. When the ratio of temperature gradient and density gradient scale-lengths exceeds a threshold, the temperature gradient driven instabilities can dominate the fluctuations [6, 7, 8]. Furthermore a gradient in the plasma potential indicates a finite electric field in the plasma, which can drive $\mathbf{E} \times \mathbf{B}$ flow. Presence of a velocity shear can lead to Kelvin-Helmholtz instability [10]. The above mentioned waves and velocity shear driven instabilities can exist in typical confinement devices with linear or curved magnetic fields. In toroidal devices, the curved magnetic field can lead to additional class of instabilities due to inherent gradient and curvature in the magnetic field. The radius of curvature in a curved magnetic field is analogous to the gravity; when the density gradient is opposite to the radius of curvature, Rayleigh-Taylor instabilities can become unstable [11]. In fusion devices such as tokamaks, simultaneous fluctuations in density and potential lead to finite fluctuation induced radial transport, degrading the confinement [12]. The poloidal rotation by self-consistent electric field or external electric field has been seen to lead to reduced turbulence and high confinement mode in tokamak[13]. An understanding of the origin of the poloidal rotation is crucial to achieve high confinement mode. It is also known that due to nonuniform B-field, plasma confined in toroidal fusion devices can be compressible. This compressibility is believed to play a crucial role. The above mentioned instability studies in simple toroidal plasmas are highly desirable not only due to their relevance to tokamaks, but also because these physical processes are of fundamental importance.

Plasma produced in a pure toroidal configuration suffers from the particle loss due to magnetic field gradient and curvature drifts, which further lead to a vertical electric field $\mathbf{E_z}$ and hence radial $\mathbf{E_z} \times \mathbf{B}$ drift. It is well known theoretically, that there is no rotational transform in a current less toroidal device (CTD) and hence stationary equilibrium does not exist [14]. The measured confinement time observed in experiments [16], is however, found to be nearly one order higher than that is predicted theoretically from single particle and $E \times B$ drifts. This paradox has not been fully resolved. Several devices such as ACT-I [17], BETA [18], BLAAMANN [19], THORELLO [20] and more recently TORPEX [21] and LATE [22] have been constructed leading to several interesting and fundamental findings. For example, in ACT-I at PPPL, USA, different kinds of plasma production such as using hot filament, electron cyclotron waves and lower hybrid waves were demonstrated; experiments demonstrating wave propagation, heating and current generation in plasma were conducted [17]. Another such device is BETA [18] at IPR, India, in which large fluctuations in plasma parameters, either in coherent or turbulent condition were observed [23]. Similarities have been drawn with plasma in equatorial spread F region of ionosphere [24, 11]; wave propagation, role of finite parallel wave number and existence of coherent structures were also studied in this device [25, 26, 27, 28]. In the context of understanding existence of an average equilibrium in BETA, a theoretical model of fluctuation-flow cycle in the plasma has been suggested wherein an initial "seed" equilibrium achieved by a conducting limiter is believed to be further reinforced by the fluctuation driven flow [29]. It was further suggested that the fluctuations in turn may get modified by the flow it generates. Direct experimental demonstration of such a flow-fluctuation cycle has not been reported. Experiments on yet another current less toroidal device BLAAMANN at University of Tromso, Norway, where plasma is produced using a hot filament, have shown that classical transport is insufficient to explain the observed cross-field diffusion of charge injected by the filament [19]. The anomalous transport is found to be due to a large, coherent flute-mode type vortex, driven by fluctuating cross-field radial current observed in simulations as well as in BLAAMANN experiments [30, 31, 32, 33]. The simulations further suggest that the radial cross-field current, which determines essential features of the fluctuating plasma equilibrium, is due to a fluctuating ion polarization drift [34]. Similar turbulence characterizing measurements have been conducted on THORELLO [20] at Milano, Italy. Recently, intermittent cross-field particle transport in the form of blobs was observed on TORPEX experiments [21] at CRPP, Switzerland. The generation of blobs from radially elongated interchange modes and detailed mechanism was studied extensively on this device [35, 36, 37, 38, 39]. In relevance to the experimental observations on TORPEX, recent 3-D fluid simulations seem to suggest that depending on parallel wave number or collisionality, an ideal interchange mode or resistive interchange mode or drift mode may become unstable leading to the turbulence [40]. These authors, however, themselves comment that boundary conditions used in this work are debatable, especially in the presence of shear flow. In a recent experiment on LATE, another CTD at Kyoto University, Japan, the explicit measurements were conducted for current through the device, compensating for the vertical charge separation [22].

Generation of flow and its effects on confinement are of general physics interest. In general, in the plasmas occurring in nature, magnetic or electrostatic fluctuations are believed to drive plasma flows or vice versa. In the objects such as stars, the inter-dependency of flows and magnetic fluctuations is believed to be significant. In the laboratory plasmas either magnetic or electrostatic fluctuations can be interrelated with the plasma flows. For example, the poloidal flows are found to be strongly connected to the formation of magnetic islands due to external magnetic field perturbations which degrade confinement in stellarators and tokamaks [1, 2].

The investigation of plasma flow has gained further significance in recent times, due to its dynamo action in stars and other astronomical objects. To investigate plasma dynamo in the laboratory, a new experimental facility with the name of 'Madison Dynamo'has been constructed at University of Wisconsin, Madison, US [3]. Thus addressing these flows and fluctuations would throw light on all the above said phenomena and hence is of fundamental importance.

In spite of the experimental and theoretical work described above, to our knowledge, the role of fluctuations and flows in the formation of an average equilibrium have not yet been completely resolved. An experimental study of self-consistent generation of fluctuations and flows, their role in sustaining mean profiles is not reported so far. In this thesis work, a detailed experimental investigation of the role of fluctuations and self-consistently generated poloidal flows in sustaining mean profiles is demonstrated, for the first time in a currentless toroidal device. The co-existence of fluctuations and flows is demonstrated experimentally; the onset of fluctuations and flows is found to be accompanied by enhanced plasma filling on the high field side, which otherwise has lower densities. The fluctuation induced particle flux is found to contribute significantly to the total poloidal flow. The measured toroidal plasma flows are found to be small, and within the measurement resolution of the flow probe. Though the fluctuations are large, the relative phase and coherence between density and potential are found to play important role in generating finite flux. Furthermore, to see the effect of fluctuations on the poloidal transport and mean plasma profiles, experimental investigation with varying toroidal magnetic field strength and ion mass are undertaken. On changing the toroidal magnetic field, a transition occurs in the nature of fluctuations, from highly coherent at low magnetic field to turbulent at high magnetic field. With the change in the nature of fluctuations, the associated poloidal flows and mean plasma profiles are determined experimentally. To see the role of ion mass in the fluctuation-flow generation, plasma is produced using other inert gases such as Krypton and Xenon, keeping all other operating conditions similar. The nature of fluctuations change from coherent to turbulent with increase in ion mass; the associated poloidal flows and mean plasma profiles are determined experimentally. The results presented in this thesis, indicate that the poloidal flow velocities change systematically with the change in the nature of turbulence; nevertheless, the fluctuations and flows play a crucial role in sustaining the mean profiles. In the following, a summary of each chapter, with a comprehensive understanding of major physical observations is described.

In **Chapter 1**, a detailed literature survey and current status of the research work in simple toroidal devices is presented. The important advances in this field are highlighted and open problems in the area of fluctuations and intrinsic flow generation are indicated.

In **Chapter 2**, the Experimental apparatus-BETA [18] is described in detail. Various diagnostic techniques used for measurements on this device, including construction of probes, method of operation and estimation of parameters from the measurements are discussed.

In **Chapter 3**, the role of fluctuations and poloidal flows in sustaining the mean profiles is investigated. Significant poloidal flows are found to be driven by mean and fluctuating radial electric fields. The charge injected by the filament form a vertically extended source region, toroidally spread in the neighborhood of the magnetic field lines intercepting the filament. This region is found to coincide with the bottom of the observed potential well in the plasma. The experimental determination of the radial spread of primary energetic electrons is important for two reasons. First, it indicates the typical radial width upto which the excess negative charge injected by the filament is confined; the excess negative charge plays an important role in the formation of a potential well and mean electric field driven poloidal flow. Second, it indicates the region in which a significant population of non-thermal electrons is present, potentially affecting the Langmuir probe measurements. The experimental detection of the fast electrons is carried using a Retarding Field Energy Analyzer (RFEA) [48, 49]. Using RFEA, a suitable sequence of potential barriers is applied to collect the fast electrons; typical fast electron densities are estimated. The limitations and important issues in using RFEA [50, 51], have been discussed. The observed radial spread of fast electrons is used to identify the possibility of erroneous estimation of electron temperature due to non-thermal electrons, in the subsequent experimental investigations. The major findings of this work have been published in **(T. S. Goud et al) J. of**

Phys.: Conf. Ser. 208, 012029 (2010). In continuation to the above work, the radial profiles of mean plasma parameters are obtained. From simultaneous probe measurements at different locations, the co-existence of fluctuations and radial filling of plasma on high field side is observed. Significant poloidal flows and well-spread radial profiles are found to sustain when large fluctuations are present. To understand the role of fluctuations in poloidal flow more quantitatively, poloidal flow measurements are carried out [52, 53]. The fluctuation induced poloidal flow [54, 55, 56] is found to account for the significant portion of the total poloidal flow, in addition to the mean electric field driven flow. The present experimental findings are in partial support of the theoretical model suggesting the fluctuation-flow cycle as an "effective rotational transform", in a current less toroidal device [29, 47, 11]. The major experimental findings in this chapter have been published in **(T. S. Goud et al) Phys. Plasmas 18, 042310 (2011)**.

The above experimental studies demonstrate that fluctuation induced flux plays an important role in generating flows and sustaining radially well spread plasma profiles. Nature of fluctuations is therefore, important in deciding the mean plasma profiles. Magnetic field is found to be an important control parameter to obtain transitions in fluctuation regimes in a CTD [20]. In continuation to the above experimental studies, varying the strength of the magnetic field, a change in the nature of fluctuations, poloidal flow generation and attaining mean profiles are investigated. The results are presented in **Chapter 4**. A transition occurs in the nature of fluctuations from highly coherent at low magnetic field to turbulent at high magnetic field. The transition from coherence to turbulence is found to be accompanied by enhanced flow and density on high field side. The dispersion relation [57] and nonlinear coupling of the fluctuations [58, 59] in each case are estimated. The dominant mechanisms of instabilities are identified [20, 56, 60, 10, 61]. Through this work, it is demonstrated for the first time that in a toroidal compressible plasma, an intimate relationship exists between the fluctuations, self-consistently generated flows and enhanced confinement. The major findings presented in this chapter are published in **(T. S. Goud et al) Phys. Plasmas 19, 032307 (2012)**.

Through the above experimental studies, it is understood that change in the nature of fluctuations with increasing magnetic field is associated with enhanced flow and confinement. Plasma flow is intrinsically associated with ion mass, thus making it another important parameter through which the mean plasma profiles and transport in plasma in a CTD can vary [62]. In general, the experimental investigation of confinement with mass scaling in tokamak have indicated that the confinement increases with increase in ion mass, which is opposite of the theoretical prediction [63]. In continuation to study the change in the nature of fluctuations, consequent flows and attaining mean profiles plasmas are investigated for different gases, viz. Argon, Krypton and Xenon. The results are presented in **Chapter 5**. The net poloidal flow and the fundamental frequency of fluctuations, which is seen to be approximately the rotation frequency of the plasma itself [64], are found to increase with decrease in ion mass. Highly coherent fluctuations which occur in the case of Argon, become turbulent at higher ion mass. The dominant fluctuations are, however, found to be flute-like for all ion masses. The major findings presented in this chapter are published in **(T. S. Goud et al) Phys. Plasmas 19, 072306 (2012)**. In the experimental findings described till now, the estimated fluctuation induced flux is used to calculate an average fluctuation driven flow. A better understanding of the nature of the fluctuation induced flux is possible with statistical analysis [12, 65]. From the time series of fluctuation induced flux, probability distribution function (PDF) can be calculated which will be useful in quantifying the sporadic, large transport bursts. The local PDF can reveal non-Gaussian nature of fluctuations [66], indicating a definite correlation between the density and electric field fluctuations, therefore fluctuations inducing transport. It has been observed in other similar devices that the coherent structures do not contribute to the anomalous transport; rather transport occurs around the vortical coherent structures where dissipative processes takes place [60]. Consequently, the fluctuation induced flux can be sporadic or bursty in nature, which can be established from statistical analysis mentioned above. A manuscript with the results of this statistical analysis is **under preparation**.

In summary, fluctuations and intrinsic poloidal flow generation and their role in sustaining mean profiles in a currentless toroidal plasma is investigated for the first time in a currentless toroidal device under various fluctuation regimes. The variation in fluctuation regime is achieved by two control parameters namely magnetic field strength and mass of the species. Firstly, the nature of fluctuations is found to vary with increase in magnetic field; the consequent mean plasma profiles and poloidal flows are obtained. Enhanced poloidal flows and improved densities are seen with increasing magnetic field. In the second part, the nature of the fluctuations is also found to vary with increase in ion mass, the corresponding mean plasma profiles and poloidal flows are estimated. Reduced poloidal flows are observed with increase in ion mass. The underlying mechanism of the instabilities under various fluctuation regimes is identified. This thesis work provides the first clear experimental evidence for generation of intrinsic poloidal flow from fluctuations and hence may be regarded as partial support to the model of flow-fluctuation cycle as a mechanism of producing an "effective rotational transform", in a currentless toroidal device.

List of Publications

1. *"Experimental determination of radial spread of residual fast electrons in a hot filament toroidal magnetized plasma"*, T. S. Goud, R. Ganesh, K. Sathyanarayana, D. Raju, K. K. Mohandas, C. Chavda, A. M. Thakar and N. C. Patel, J. of Phys.: Conf. Ser. **208**, 012029 (2010).

2. *"Role of fluctuations and flows in sustaining mean profiles in a current less toroidal plasma"*, T. S. Goud, R. Ganesh, Y. C. Saxena, D. Raju, K. Sathyanarayana, K. K. Mohandas and C. Chavda, Phys. Plasmas **18**, 042310 (2011).

3. *"Coherent to turbulence transition, enhanced flow and confinement in a simple toroidal plasma"*, T. S. Goud, R. Ganesh, Y. C. Saxena, D. Raju, K. Sathyanarayana, K. K. Mohandas and C. Chavda, Phys. Plasmas **19**, 032307 (2012).

4. *"Role of ion mass in fluctuations and poloidal flows in a simple toroidal plasma"*, T. S. Goud, R. Ganesh, Y. C. Saxena and D. Raju, Phys. Plasmas 19, 072306 (2012).

5. *"Statistical properties of fluctuation induced poloidal flux and flow in a current less toroidal plasma"*, T. S. Goud, R. Ganesh, D. Raju and Y. C. Saxena, manuscript under preparation

Contents

List of Figures

List of Tables

1

Introduction

1.1 Fluctuations and flows in confined plasmas

1.1.1 Significance of plasma flows

Generation of plasma flow and its effects on plasma confinement are of general physics interest. In the plasmas occurring in nature, magnetic or electrostatic fluctuations are believed to drive plasma flows and/or vice versa [1, 2, 3]. In the objects such as stars, the inter-dependency of flows and magnetic fluctuations is believed to be significant [3]. In the laboratory plasmas, either magnetic or electrostatic fluctuations can be interrelated with the plasma flows. For example, the poloidal flows are found to be strongly connected to the formation of magnetic islands formed due to external magnetic field perturbations, which degrade confinement in stellarators and tokamaks [1, 2]. Further, the improved plasma confinement in tokamaks is found to be associated with increased toroidal rotation [4]. The investigation of plasma flow has gained further significance in recent times, due to its dynamo action in stars and other astronomical objects. To investigate plasma dynamo in the laboratory, a new experimental facility with the name of 'Madison Dynamo' has been constructed at University of Wisconsin, Madison, US [3]. Thus addressing these flows and fluctuations would throw light on all the above mentioned phenomena and hence is of fundamental importance.

1.1.2 Magnetically confined laboratory plasmas

Magnetically confined plasmas in toroidal devices have gained significance decades ago, for their potential to achieve controlled fusion [4, 5]. In spite of the remarkable advance in this field, transport of particles and energy have been found to be anomalous and pose challenges in further improving the plasma confinement. Some of the mechanisms which lead to the above mentioned anomalous transport are the density and temperature gradient driven instabilities in curved magnetic fields [6, 7, 8]. A clear understanding of these processes, therefore, is of the paramount importance. The presence of complex magnetic field geometry in fusion devices, sets constraints in carrying out individual studies on instabilities mentioned above. A simple magnetized torus with a pure toroidal field provides an excellent alternate facility to carry out the above mentioned studies in much simplified conditions. Though mean plasma parameters are much limited in their range compared to tokamak edge plasma, the plasma behavior observed is relatively similar. For instance, the results of turbulence simulation codes which are applicable to the fusion edge plasmas, agree well with the experimental results for simple toroidal devices, when used with suitable normalized parameters as applicable to them [9]. Hence much useful studies on instabilities and transport can be conducted in such simple toroidal devices.

Plasmas produced in confinement devices, in general, possess intrinsic gradients in typical plasma parameters such as density, electron or ion temperature and plasma potential. In presence of magnetic field, these gradients commonly lead to gradient-driven instabilities. When the density gradient scale-length exceeds the temperature gradient scale-length above a threshold, then the temperature gradient driven instabilities can have dominant contributions to the fluctuations [6, 7, 8]. Furthermore a gradient in the plasma potential indicates a finite electric field in the plasma, which can drive $\mathbf{E} \times \mathbf{B}$ flow. Presence of a velocity shear can lead to Kelvin-Helmholtz instability [10]. The above mentioned instabilities and waves can co-exist in typical confinement devices with linear or curved magnetic fields. In toroidal devices, the curved magnetic field can lead to additional class of instabilities due to inherent gradient and curvature in the magnetic field. The radius of curvature in a curved magnetic field is analogous to the gravity; when the density gradient is opposite to the radius of curvature, Rayleigh-Taylor instabilities can become unstable [11]. In fusion devices such as tokamaks, simultaneous fluctuations in density and potential lead to finite fluctuation induced radial transport, degrading the plasma confinement [12]. The poloidal rotation, by self-consistent electric field or external electric field, has been seen to lead to reduced turbulence and high confinement mode in tokamak [13]. An understanding of the origin of the poloidal rotation is crucial to achieve high confinement mode. Moreover, the low and high confinement modes in tokamaks were found to be associated with opposite directions of intrinsic toroidal flow generation; an inter-machine comparison of tokamaks have shown that the intrinsic toroidal rotation velocity increases with plasma stored energy or pressure [4]. Experimental observations on COMPASS-C tokamak have predicted that a rotating plasma will resist externally induced magnetic tearing until the applied resonant magnetic perturbations exceed a critical threshold [2]. Above this threshold, stationary magnetic islands are induced in the background rotating plasma, degrading the confinement. It is also known that due to nonuniform B-field, plasma confined in toroidal fusion devices can be compressible. This compressibility is believed to play a crucial role. Possibility of experimentally studying the above discussed instabilities in a simple toroidal plasmas is highly desirable not only due to its relevance to tokamaks, but also because these physical processes are of fundamental importance. In the following, the fundamental issues concerning the lack of equilibrium in a simple toroidal plasma are described.

1.2 Simple toroidal plasma

Plasma produced in a pure toroidal magnetic field is subject to single particle drifts given by

$$\mathbf{v_R} + \mathbf{v_{\nabla B}} = \frac{m}{q}\frac{\mathbf{R_c} \times \mathbf{B}}{R_c^2 B^2}\left(v_\parallel^2 + \frac{1}{2}v_\perp^2\right), \qquad (1.1)$$

where $v_\parallel$ and $v_\perp$ are the parallel and perpendicular components of the velocity with respect to the magnetic field, of the particle with charge q and mass m. The first and second terms in Eq.(1.1) correspond to curvature and gradient drifts respectively. Both the drifts add up for each charge particle; the combined drift is opposite for oppositely charged species, leading to vertical charge separation building-up a vertical electric field ($\mathbf{E_z}$). The enhanced vertical electric field leads to increased $\mathbf{E_z} \times \mathbf{B}$ drift directed radially outward; hence stationary equilibrium does not exist in a simple toroidal plasma [14].

The non-existence of plasma equilibrium in a pure toroidal plasma can also be understood from the magneto-hydro dynamic (MHD) equations. The two essential conditions for the existence of plasma in equilibrium are

$$\mathbf{J} \times \mathbf{B} = \nabla p, \tag{1.2}$$

$$\nabla \cdot \mathbf{J} = 0, \tag{1.3}$$

where $\mathbf{J}$ is the current density in the plasma, $\mathbf{B}$ is the magnetic field and p is the plasma pressure. For a simple toroidal plasma, the validity of the Eq.(1.2) and (1.3) is verified as follows. Taking cross product with $\mathbf{B}$ on both sides of Eq.(1.2), one arrives at

$$B^2\mathbf{J} - (\mathbf{B} \cdot \mathbf{J})\mathbf{B} = \mathbf{B} \times \nabla p. \tag{1.4}$$

Since there is no toroidal plasma current, $\mathbf{B} \cdot \mathbf{J} = 0$. Now taking divergence on both sides of Eq.(1.4), and on further simplifying

$$\nabla \cdot \mathbf{J} = \frac{\partial p}{\partial z} B \frac{\partial}{\partial R} \left(\frac{1}{B^2} \right). \tag{1.5}$$

Hence Eq.(1.3) is not satisfied whenever $\partial p / \partial z \neq 0$, which is usually the case. This suggests that charge separation would occur.

The restoration of plasma equilibrium in a simple toroidal plasma, using a conducting limiter was suggested by Yoshikawa *et al* [14]. In this equilibrium, the plasma pressure is constant at the core of the plasma and a sharp pressure gradient exists in the boundary. The vertical charge-separation current flows along the magnetic field lines into the limiter, and the short circuit effect inhibits the $\mathbf{E_z} \times \mathbf{B}$ drift. There still remains a certain potential difference between the top and bottom because of the potential drop along the path of the short-circuit current and finite resistivity of the conducting limiter. Physically, the current to the limiter is limited by the ion saturation current. If the charge separation current exceeds this limit, stationary equilibrium without any time dependence can no longer be maintained. The vertical potential difference can be calculated assuming a finite width boundary for the plasma. The thickness of the plasma boundary is determined by the rate of diffusion of the plasma across the magnetic field. The confinement time τ_c in this equilibrium model, can be calculated from the distance between the inner to the outer edge of the limiter ($\sim 2a$) divided by the average velocity $kT_e u_0/(eaB_0)$, obtained by averaging E_z/B from $R-a$ to $R+a$. Thus τ_c is given by

$$\tau_c \approx 2ea^2 B_0/kT_e u_0, \tag{1.6}$$

where a is the minor radius, R is the major radius, B_0 is the toroidal magnetic field at the minor axis, T_e is the electron temperature, and u_0 is a numerical factor; usually $u_0 \ll 1$ which indicates the existence of a finite potential difference between the top and bottom of the limiter. Using this model, the plasma confinement time estimated for a real limiter will be less than that estimated for an ideal conducting limiter. The restoration of plasma equilibrium, using conducting limiter is schematically shown in Fig. 1.1.

Another model is suggested by Nieuwenhove to explain the restoration of plasma equilibrium in a pure toroidal field which is based on fast poloidal rotation [15]. The vertical charge separation is weakened by charge neutralization due to fast poloidal rotation. This is schematically shown in Fig. 1.2. A stationary solution can be found in which the charge density can be kept sufficiently small by imposing a fast poloidal rotation such that

$$\left|\frac{n_i - n_e}{n}\right| \ll 1, \tag{1.7}$$

where n is the average plasma density, n_i and n_e are the corresponding densities of ions and electrons respectively. Equation (1.7) imposes a condition on the poloidal rotation velocity v_θ, given by Eq.(1.8)

$$|v_\theta| \gg \left|\frac{r}{\Lambda} v_D\right|, \tag{1.8}$$

where r is the radius of rotating plasma, $\Lambda = |nkT/d(nkT)/dr|$, in which $T = T_i + T_e$, and $v_D \equiv |\mathbf{v_R} + \mathbf{v_{\nabla B}}|$, given by Eq.(1.1). For a Maxwellian distribution,

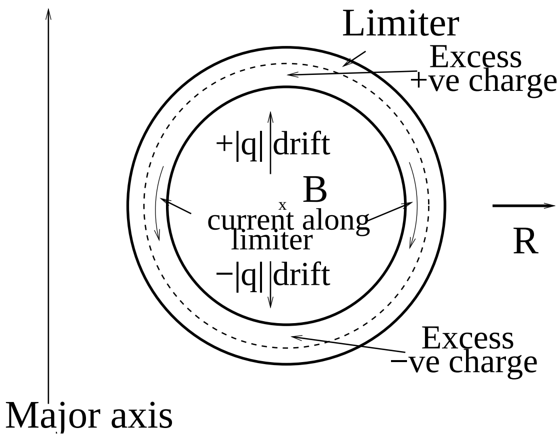

Figure 1.1: A schematic figure showing the restoration of "equilibrium" using the limiter. Vertical charge separation occurs throughout the torus. The excess positive charge flows into the top of the limiter; the excess negative charge flows into the bottom of the limiter, and the current flows poloidally along the limiter.

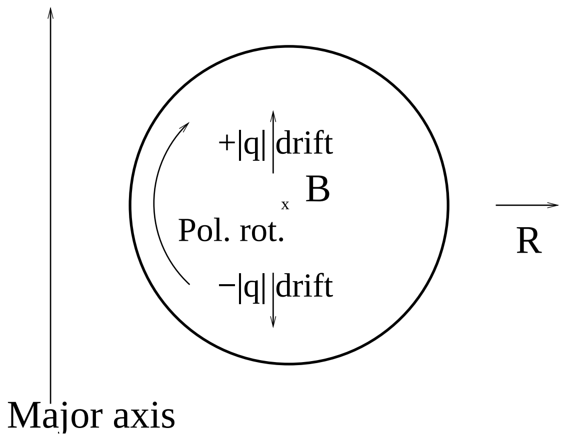

Figure 1.2: A schematic figure showing the restoration of the "equilibrium" by fast poloidal rotation. Vertical charge separation occurs throughout the torus. Fast poloidal rotation reduces the vertical charge separation.

$v_D \simeq r_L v_{th}/R$, where r_L is the Larmor radius, v_{th} is the thermal velocity, and R is the radius of curvature. Since $v_{th} = c_s\sqrt{m_i/m_e}$, v_D in Eq.(1.8) can be replaced by $r_L c_s\sqrt{m_i/m_e}/R$. This model, therefore, suggests that even in the absence of magnetic rotational transform, a stationary equilibrium can exist in a simple toroidal plasma if a fast poloidal plasma rotation exists. Whether or not the Eq.(1.8) is satisfied in the present experimental conditions, will be discussed in Chapter 3. A suggested application of this model is that in a tokamak plasma, produced initially with low density and low plasma current, is switched to a rapidly spinning state using neutral beam injection (NBI) power; finally the plasma current can be ramp down to zero, while maintaining the simple toroidal magnetic field, NBI power and gas feed to see whether the plasma can assume a new currentless magneto-electric equilibrium. Following the above necessary theoretical understanding of the simple toroidal plasma and issues in attaining equilibrium, a brief review of the previous experimental and theoretical investigation of simple toroidal plasmas is given below.

1.3 Review of previous works

In the experimental observations in simple toroidal plasmas, neither uniform plasma pressure profiles are seen in the core plasma as predicted by Yoshikawa's model, nor a fast poloidal rotation of magnitude predicted by Nieuwenhove's model. As suggested by the above two models, the plasma equilibrium in a simple toroidal plasma, therefore, need not exist. The measured confinement time observed in experiments [16], is however, found to be nearly one order higher than that is predicted theoretically from single particle and $E \times B$ drifts described in Sec.1.2; mean profiles accompanied by large fluctuations are seen in such plasmas. This paradox has not been fully resolved. Several devices such as ACT-I [17], BETA [18], BLAAMANN [19], THORELLO [20], TORPEX [21] and more recently LATE [22] have been constructed leading to several interesting and fundamental findings. For example, in ACT-I at PPPL, USA, different kinds of plasma production such as using hot filament, electron cyclotron waves and lower hybrid waves were demonstrated [17]. The plasmas produced in ACT-I using hot filament and electron cyclotron waves was found to possess poloidal asymmetry. An approximately poloidally symmetric plasma could be produced with lower hybrid waves launched from a poloidally symmetric slow wave structure. In the above mentioned work, experiments demonstrating wave propagation, heating and current generation in plasma were also conducted. Another such device is BETA [18] at Institute for Plasma Research, India, in which large fluctuations in plasma parameters, either in coherent or turbulent condition were observed [23]. The plasma behavior was found to be similar to the plasma in equatorial spread F region of ionosphere [24, 11], where the fluctuations due to R-T instability, generated in the favorable region below the density peak, are also found in the unfavorable region above the density peak. Further in BETA, wave propagation, role of finite parallel wave number and existence of coherent structures were also studied [25, 26, 28]. In another set of experiments in BETA, applying a finite vertical magnetic field in either directions, suppression in the fluctuation levels has been observed [27]. In the context of understanding existence of an average equilibrium in BETA, a theoretical model of flow-fluctuation cycle in the plasma has been suggested wherein an initial "seed" equilibrium achieved by a conducting limiter is believed to be further reinforced by the fluctuation driven flow [29]. It was further suggested that the fluctuations in turn may get modified by the flow it generates. This model is described in detail in the next section. Experiments on yet another simple toroidal device BLAAMANN at University of Tromso, Norway, where plasma is produced using a hot filament, have shown that classical transport is insufficient to explain the observed cross-field diffusion of charge injected by the filament [19]. The anomalous transport is found to be due to a large, coherent flute-mode type vortex, driven by fluctuating cross-field radial current observed in simulations as well as in BLAAMANN experiments [30, 31]. The coherent structures have been found to possess no inherent propagation velocity, rather they were found to propagate with $\mathbf{E} \times \mathbf{B}$ drift velocity; the lifetimes of the structures were found to be the time of one full azimuthal rotation of the plasma column [32]. In another set of experiments in BLAAMANN, the threshold nature for the excitation of fluctuations is demonstrated, where the plasma is found to be quiescent at low magnetic field and transport occurs along the equipotential surfaces; on increasing the field at the threshold monochromatic drift modes are excited which act as a seed for the flute mode instabilities above the threshold [33]. In the coherent flute type vortex, the simulations further suggest that the radial cross-field current, which determines essential features of the fluctuating plasma equilibrium, is due to a fluctuating ion polarization drift [34]. Similar turbulence characterizing measurements have been conducted on THORELLO [20] at Milano, Italy. Recently, intermittent cross-field particle transport in the form of blobs was observed on TORPEX experiments [21] at CRPP, Switzerland. The generation of blobs from radially elongated interchange modes increasing in amplitude, sheared off by $\mathbf{E} \times \mathbf{B}$ flow has been investigated [35, 36, 38]. Later it was found that, blobs which are 3-D structures, exist in drift-interchange regime too; further it is seen that the existence of $\mathbf{E} \times \mathbf{B}$ flow is not essential for generation of blobs [37]. Varying the blob size by changing the ion mass, the analytical expression for the cross-field velocity of the blob including ion polarization currents, parallel currents to sheath, and ion-neutral collisions is derived and found to be in agreement with the experimental results [39]. In relevance to the experimental observations on TORPEX, recent 3-D fluid simulations seem to suggest that depending on parallel wave number or collisionality, an ideal interchange mode or resistive interchange mode or drift mode may become unstable leading to the turbulence [40]. These authors, however, themselves comment that boundary conditions used in this work are debatable, especially in the presence of shear flow. In a recent experiment on LATE, another simple toroidal device at Kyoto University, Japan, the explicit measurements were conducted for current through the device, compensating for the vertical charge separation [22]. Through the above mentioned experimental and theoretical investigations in various devices, several mechanisms of cross-field anomalous transport seem to exist, for effective poloidal transport in a simple toroidal plasma. Understanding the poloidal transport mechanism in a simple toroidal plasma, therefore, is of fundamental importance.

In tokamaks, poloidal $\mathbf{E} \times \mathbf{B}$ rotation by self-consistent $\mathbf{E}$ or external $\mathbf{E}$ field has been seen to lead to reduced turbulence and improved confinement [13]. Hence it is understood that turbulence, flow generation and improved confinement are interrelated and need to be understood well for a successful fusion device. As it is well known, sheared flows in tokamak plasmas are believed to be triggered by an external radial electric field or self-consistent turbulent Reynolds stress [41]. In such devices compressibility plays a vital role. However, a clear identification of instability in tokamak plasma, which contributes to Reynolds stress is a difficult experimental problem. Simple toroidal devices could play an important role in improving our understanding of such complex phenomena. For example, in a set of interesting experiments in cylindrical plasma columns, the existence of intrinsically generated azimuthal flow has been observed [42, 43, 44, 45]. It has been also shown in this work that a transfer of energy occurs from collisional drift turbulence fluctuations with high frequency into a linearly stable low frequency azimuthally symmetric radially sheared $\mathbf{E} \times \mathbf{B}$ flow. The observed shear flow has been found to be nonlinearly driven by the turbulent Reynolds stress. The coherent drift waves at low magnetic field are observed to turn into a broadband spectrum with increasing magnetic field close to the shear layer, with reduced coherence. In some of the other observations on linear devices, transition from flute modes to drift mode fluctuations is seen with increase in magnetic field [46]. However, due to the cylindrical geometry, the flow is incompressible through out, i.e. $\nabla \cdot \mathbf{v}_{\mathbf{E}\times\mathbf{B}} \simeq 0$.

In spite of the above crucial findings, a clear understanding of what plays the role of a "effective rotational transform", is still lacking. In the present experimental studies, the role of fluctuations in the transport and hence a possible "effective rotational transform" is investigated. A theoretical model of flow-fluctuation cycle suggested by R. Singh *et al.* [29], relevant to the present experimental work is briefly described as follows.

1.4 Flow-fluctuation cycle in a simple toroidal plasma

In the context of understanding the existence of equilibrium in BETA, a flow-fluctuation model has been suggested [29, 47], as mentioned in Sec.1.3. According to this model, initially, the limiter provides the "seed" equilibrium. In this equilibrium, fluctuations which are generally due to Rayleigh-Taylor instability, grow to a significant level. These fluctuations provide an "effective rotational transform" in two ways. First, fluctuations directly drive a radial current and hence a poloidal rotation which improves the limiter equilibrium. Second, the flow back reacts on fluctuations to modify the rms level profile. The mean ponderomotive force due to these fluctuations then opposes the free fall of the plasma and further fortifies the limiter equilibrium. The theoretical arguments of this model are briefly described below.

The first of the two ways of providing an "effective rotational transform", is that fluctuations drive a poloidal flow. In a simple toroidal plasma this can occur as follows. Simultaneous radial electric field and density fluctuations can result in a $\tilde{\mathbf{E}} \times \mathbf{B}$ drift; depending up on the cross-phase between the $\tilde{\mathbf{E}}$ and $\tilde{n}$, a finite fluctuation induced flux can occur in a particular poloidal direction. The fluctuation induced flux is a time varying quantity, therefore, is calculated as a time average, on sampling large number of cycles. Such estimation is represented by the following expression:

$$\Gamma_{fluct} = \frac{1}{B}\langle \tilde{n}\tilde{E} \rangle. \tag{1.9}$$

The second way of providing an "effective rotational transform" can be realized as follows. The basic equations describing the equilibrium are the continuity and momentum equations for electron and ion [47]:

$$\frac{\partial n_j}{\partial t} + \nabla \cdot (n_j \mathbf{V}_j) = 0, \tag{1.10}$$

$$m_j n_j \frac{d\mathbf{V}_j}{dt} = -\nabla p_j + q_j n_j \left(\mathbf{E} + \frac{\mathbf{V}_j \times \mathbf{B}}{c}\right) - m_j n_j \nu_{jn} \mathbf{V}_j, \tag{1.11}$$

where $j = e, i$ stands for the electron and ion, respectively; $n, p, m, \mathbf{B}, \mathbf{E}$, and $\mathbf{V}_j$ are the density, pressure, mass, toroidal magnetic field, electric field and velocity respectively; ν_{jn} corresponds to charge-neutral collision frequency. In the limit $\nu_{en}/\Omega_e \ll 1$, $\nu_{in}/\Omega_i < 1$, $T_i/T_e \ll 1$, and with negligible flow along the magnetic field (i.e. $V_{i\|} = V_{e\|} \approx 0$), the above continuity and momentum equations are used to derive an equation in partial time derivative of $(n_i - n_e)$ [47]. The Poisson equation, with the dominant electric field in the vertical direction, is given by

$$\nabla \cdot \mathbf{E} = \frac{dE_z}{dz} = 4\pi e(n_i - n_e). \tag{1.12}$$

Substituting Eq.(1.12) in the above mentioned equation in partial time derivative of $(n_i - n_e)$, simplifying further and solving, a steady state plasma fall velocity V_R along the major radius can be expressed as [47]

$$V_R = \frac{1}{\nu_{in}} \left[2\frac{c_s^2}{R} - \frac{1}{2}\frac{\partial}{\partial R}|\tilde{v}_R|^2 \right], \tag{1.13}$$

where $c_s = \sqrt{kT_e/m_i}$. The radial component of mean ponderomotive force due to low frequency fluctuations $m_i n_i \langle (\mathbf{V_i} \cdot \nabla)\mathbf{V_i} \rangle$ can be approximated as $\sim (1/2) m_i n_i \partial |\tilde{v}_R|^2 / \partial R \, \hat{R}$, where $|\tilde{v}_R|$ is the amplitude of velocity oscillations of the fluid in the radial direction. Clearly if $\partial |\tilde{v}_R|^2 / \partial R > 0$, then the fluctuation driven ponderomotive force (radial component) opposes the free fall due to the effective gravity. The plasma confinement time ($\tau_c = a/V_R$), therefore, is increased. In this way, the flow-fluctuation cycle results in an "effective rotational transform". In the present work we examine the role of fluctuation driven poloidal flow in a simple toroidal plasma, i.e. estimating $\langle \tilde{v}_\theta \rangle$ and calculating other poloidal flows. The role of $\tilde{v}_R$ in creating an effective ponderomotive force experimentally is not being investigated.

1.5 Present work

In spite of the experimental and theoretical work described till now, to our knowledge, the role of fluctuations and flows in the formation of an average equilibrium has not yet been completely resolved. In this thesis, a detailed experimental investigation on the role of fluctuations and self-consistently generated poloidal flows in sustaining mean profiles has been carried out, for the first time, in a simple toroidal device. The co-existence of fluctuations and flows is demonstrated experimentally; the onset of fluctuations and flows is found to be accompanied by enhanced plasma filling on the high field side, which otherwise has lower densities. The fluctuation induced particle flux is found to contribute significantly to the total poloidal flow. The measured toroidal plasma flows are found to be small, and within the measurement resolution of the flow probe. Though the fluctuations are large, the relative phase and coherence between density and potential are found to play important role in generating finite flux. Furthermore, to see the effect of fluctuations on the poloidal transport and mean plasma profiles, experimental investigation with varying toroidal magnetic field strength and ion mass are undertaken. On changing the toroidal magnetic field, a transition occurs in the nature of fluctuations, from highly coherent at low magnetic field to turbulent at high magnetic field. With the change in the nature of fluctuations, the associated poloidal flows and mean plasma profiles are determined experimentally. To see the role of ion mass in the fluctuation-flow generation, plasma is produced using other inert gases such as krypton and xenon, keeping all other operating conditions similar. The nature of fluctuations change from coherent to turbulent with increase in ion mass; the associated poloidal flows and mean plasma profiles are determined experimentally. The results presented in this thesis, indicate that the poloidal flow velocities change systematically with the change in the nature of turbulence; moreover, the fluctuations and flows play a crucial role in sustaining the mean profiles in all the cases. In the following, the lay-out of the thesis is presented; the major topics are organized in chapters, each chapter elucidating a comprehensive summary of motivation behind the measurements, major findings followed by appropriate discussions.

1.6 Thesis outline

Rest of the thesis is organized as follows. In **Chapter 2**, the Experimental apparatus-BETA, a simple toroidal device in which all the present experimental investigations are carried out, is described in detail. Various diagnostic techniques developed for measurements on this device are described, which are based on measuring charge flux incident on electrodes. Appropriate theoretical models for the interpretation of the measurements are explained. The details of diagnostic probes, including construction of probes, method of operation and estimation of parameters from the measurements are discussed.

The role of fluctuations and poloidal flows in sustaining the mean profiles is investigated, and the results are presented in **Chapter 3**. Significant poloidal flows are found to be driven by mean and fluctuating radial electric fields. The charge injected by the filament form a vertically extended source region, toroidally spread in the neighborhood of the magnetic field lines intercepting the filament. This region is found to coincide with the bottom of the observed potential well in the plasma. The experimental determination of the radial spread of primary energetic electrons is important for two reasons. First, it indicates the typical radial width upto which the excess negative charge injected by the filament is confined; the excess negative charge plays an important role in the formation of a potential well and mean electric field driven poloidal flow. Second, it indicates the region in which a significant population of non-thermal electrons is present, potentially affecting the Langmuir probe measurements. The experimental detection of the fast electrons is carried out using a Retarding Field Energy Analyzer (RFEA) [48, 49]. Using RFEA, a suitable sequence of potential barriers is applied to collect the fast electrons; typical fast electron densities are estimated. These measurements using RFEA are described in the Appendix A. The limitations and important in issues using RFEA [50, 51], are also discussed. The observed radial spread of fast electrons is used to identify the possible regions for erroneous estimation of electron temperature due to non-thermal electrons, in the subsequent experimental investigations. In continuation to the above work, the radial profiles of mean plasma parameters are obtained. From simultaneous probe measurements at different locations, the co-existence of fluctuations and enhanced filling of plasma on high field side is observed. Significant poloidal flows and well-spread radial profiles are found to sustain when large fluctuations are present. To understand the role of fluctuations in poloidal flow more quantitatively, poloidal flow measurements are carried out [52, 53]. The fluctuation induced poloidal flow [54, 55, 56] is found to account for the significant portion of the total poloidal flow, in addition to the mean electric field driven flow. The present experimental findings are in partial support of the theoretical model suggesting the fluctuation-flow cycle as an “effective rotational transform”, in a current less toroidal device [29, 47, 11].

The experimental studies described in Chapter 3 demonstrate that fluctuation induced flux plays an important role in generating flows and sustaining radially well spread plasma profiles. Nature of fluctuations is, therefore, important in determining the mean plasma profiles. Magnetic field is found to be an important control parameter to obtain transitions in fluctuation regimes in a simple toroidal device [20]. In continuation to the above experimental studies, varying the strength of the magnetic field, a change in the nature of fluctuations, poloidal flow generation and attaining mean profiles are investigated. The results are presented in **Chapter 4**. A transition occurs in the nature of fluctuations from highly coherent at low magnetic field to turbulent at high magnetic field. The transition from coherence to turbulence is found to be accompanied by enhanced flow and density on high field side. The dispersion relation [57] and nonlinear coupling of the fluctuations [58, 59] in each case are estimated. The dominant mechanisms of instabilities are identified [20, 56, 60, 10, 61].

Through the above experimental studies, it is understood that change in the nature of fluctuations with increasing magnetic field is associated with enhanced flow and confinement. Plasma flow is intrinsically associated with ion mass, thus making it another important parameter through which the mean plasma profiles and transport in plasma in a simple toroidal device can vary [62]. In general, the experimental investigation of confinement with mass scaling in tokamak have indicated that the confinement increases with increase in ion mass, which is opposite of the theoretical prediction [63]. In the next set of experiments, fluctuations and flows in plasmas are investigated with different gases, viz. argon, krypton and xenon. The results are presented in **Chapter 5**. The net poloidal flow and the fundamental frequency of fluctuations, which is seen to be approximately the rotation frequency of the plasma [64], are found to increase with decrease in ion mass. Highly coherent fluctuations which occur in the case of argon, become turbulent at higher ion mass. The dominant fluctuations are, however, found to be flute-like for all ion masses. In the experimental findings described till now, the estimated fluctuation induced flux is used to calculate an average fluctuation driven flow. A better understanding of the nature of the fluctuation induced flux is possible with statistical analysis [12, 65]. From the time series of fluctuation induced flux, probability distribution function (PDF) can be calculated which will be useful in quantifying the sporadic, large transport bursts. The results of this analysis are presented in **Chapter 6**. The local PDF can reveal non-Gaussian nature of fluctuations [66]; the non-Gaussian nature of the fluctuations indicate a coupling between the density and electric field fluctuations which can result in finite fluctuation inducing flux. It has been observed in other similar devices that the coherent structures do not contribute to the anomalous transport; rather transport occurs around the vortical coherent structures where dissipative processes takes place [60]. Consequently, the fluctuation induced flux can be sporadic or bursty in nature, which can be established from statistical analysis mentioned above.

In **Chapter 7**, the conclusions of the experimental investigations and results of various analysis techniques are presented. This thesis work provides the first clear experimental evidence for generation of intrinsic poloidal flow from fluctuations and hence may be regarded as partial support to the model of flow-fluctuation cycle as a mechanism of producing an "effective rotational transform", in a simple toroidal device.

In the next chapter, the experimental setup and diagnostic methods are described. The construction of the probes, method of operation and interpreting parameters from measurements are discussed.

2

Experimental device and diagnostics

2.1 Device description

2.1.1 Experimental chamber

The experimental chamber in BETA apparatus is a toroidal vacuum vessel with a major radius of 45 cm and a minor radius of 15 cm. The vacuum vessel consists of four separate quadrants made up of stainless steel-304 elbows with circular cross section and wall thickness of 6 mm. The vessel has a toroidal electric-break through proper insulation at one of the four joints of the quadrants. In total, the vessel has 40 ports to have access to the interior of the vacuum vessel and other purposes such as vacuum pumping, mounting components and diagnostics. There are 12 radial ports on the outer wall, each with 15 cm inner diameter and 20 ports of 10 cm inner diameter at the top and bottom of the vessel. Eight ports of 5 cm inner diameter are also located on the top side of the vacuum vessel with 2 ports at the centre of the each quadrant. All the ports on the vessel are provided with grooves for viton 'O' rings for vacuum tight contact with flanges.

The vacuum vessel is pumped out to the base vacuum by two diffusion pumps through radial ports, diametrically opposite to each other. Each diffusion pump is a Diffstak Model-250 of Edwards make, with a pumping speed of 2000 L/s. Each Diffstak has a pneumatically operated baffle valve at the inlet, and is backed by a rotary pump at the outlet, with a pumping speed of 40 $m^3/hour$. Base vacuum with 3×10^{-6} $torr$ pressure is achieved and the typical working pressure during the experiments is $1 \times 10^{-4}\,torr$.

2.1.2 Toroidal Magnetic field coils

The vacuum vessel is enclosed in a toroidal structure made up of 16 square frame coils (referred as TF coils), on a toroidal radius of 50 cm. Hence, the minor axis of the vacuum vessel has a radial inward shift of 5 cm from the minor axis of the toroid. Each square frame coil has a side of 50 cm, with 3 windings made up of 5 cm wide and 1 cm thick copper bars. The copper bars are dressed in insulation to isolate the windings from each other. A large DC current (maximum of 5 kA) is passed through the copper bars to produce toroidal magnetic field, with a maximum of 0.1 T, for a typical duration of 5 s. The toroidal field coils heated due to large current, are cooled by a continuous chilled water circulation through the copper tubes brazed at the inner edge of the copper bars. A maximum of 2% ripple in the toroidal field is observed at the outer wall of the toroidal vessel.

2.1.3 Vertical Magnetic field coils

A pair of circular coils (referred as VF coils) is placed symmetrically, 60 cm above and below the equatorial mid-plane, coaxially with the major axis. Each coil having 230 cm inner diameter is made up of 10 windings of copper sheet, with dimensions of 2.5 cm width and 0.3 cm thickness. A vertical field of order of $10^{-3}\,T$, can be applied externally by passing a current of 100 A through these coils. These coils are not energized during present set of experiments. Due to inherent misalignment of the TF coils, however, a finite B_z can still exist as an offset in the present experimental conditions. Experimental determination of this offset is a subject of future work.

2.1.4 Supporting structure

The entire toroidal structure of BETA, including the experimental vessel and magnetic field coils, is supported by a set of aluminium stands and a buckling cylinder at the centre. The supporting structure is designed in such a way that it facilitates to assemble or disassemble the quadrants and also to withstand the mechanical forces generated while passing large currents in the toroidal field coils. For convenience, each quadrant is supported by a separate aluminium stand. One of the quadrants is fixed in position with its stand bolted on to the floor and the other three quadrants can be moved apart, through wheels attached to their stands, with reference to the fixed quadrant. Each quadrant of the vessel is supported at three locations; one at the central radial port, other two at the quadrant joints.

The buckling cylinder is placed on a table at the centre of the toroidal system, supported by a separate aluminium stand. The toroidal field coils are supported by stainless steel channels at the top and bottom legs and the buckling cylinder at the inner leg. Stainless steel wedges are placed between the inner legs of the coils along the length of the buckling cylinder, also at the top and bottom at the outer legs of the coils leaving open space to access the radial ports. The experimental chamber is isolated electrically from the entire supporting structure and vacuum pumping system.

2.2 Plasma production

A hot biased filament is used to produce plasma in the present set of experiments. Use of other techniques such as electron cyclotron resonance (ECR) source and radio frequency (RF) source to produce plasma is also feasible. The filament source is known to produce large gradients in the plasma parameters, which can offer relatively, a better control of the fluctuations. Hence, the filament source is preferred in the present experiments. The filament, made up of a pure tungsten wire with 0.2 cm diameter and a length of $\sim 20\ cm$, is mounted vertically on the minor axis at one toroidal location. The filament is clamped through flexible supports made of SS-304, suspended from the flanges at top and bottom ports of 10 cm diameter. Current feed through rods are welded at the centre of the flanges, to which the filament supports are connected inside the vacuum vessel and to electric cables of filament heating power supply outside the vessel. The filament is heated by passing a continuous current from a DC power supply with a maximum rating of 200 A, to a sufficient high temperature for thermionic emission. The filament flanges are electrically isolated from the ports of the vacuum vessel using vacuum tight insulation between them. A conducting limiter with an open circular aperture of 18 cm diameter, made up of SS-304, is placed coaxially with the minor axis, approximately 180^0 toroidally away from the filament. The limiter and vacuum vessel are maintained at the ground potential.

In order to produce a pulsed discharge of the toroidal plasma and carryout the measurements, a sequence of TTL trigger pulses with preset delays is generated using a multiple pulse generator circuit. Using this multiple trigger generator, toroidal field power supply is triggered first. The toroidal field, initially with few large oscillations, reaches a steady value after 500 ms. While toroidal field is steady, a negative bias pulse of 1 s duration is applied to the hot filament with respect to the vacuum vessel leading to the breakdown of the filled gas. The diagnostic circuits and data acquisition system are triggered with an approximate delay of 100 ms with respect to the bias pulse to the filament. The details of the diagnostic techniques and measurement methods are described in the next section. A photograph of the the experimental set-up is shown in Fig. 2.1. The schematic view of the cross-section of BETA, diagnostics and the bias to the electrodes are shown in Fig. 2.2. The top view of the vacuum vessel, top ports, radial ports and pumping lines, along with location of filament, limiter, and probe shafts are shown schematically in Fig. 2.3.

2.3 Diagnostics

Measurement of mean and fluctuating plasma parameters is performed using particle flux probes. In principle, the particle flux probes collect the charge flux incident on their surface, where the current drawn depends on one or several plasma parameters. Though collecting probes have the advantage in obtaining local measurements, the potential disadvantage is perturbation in the plasma and hence a possible modification in the parameters being measured. It is necessary to confirm, therefore, that the above probes being used may cause minimum perturbations in the plasma. The particle flux probes used in this thesis work constitute cold collecting probes and emissive probe. The cold collecting probes used are single and triple Langmuir probes, array of probes and directional probes.

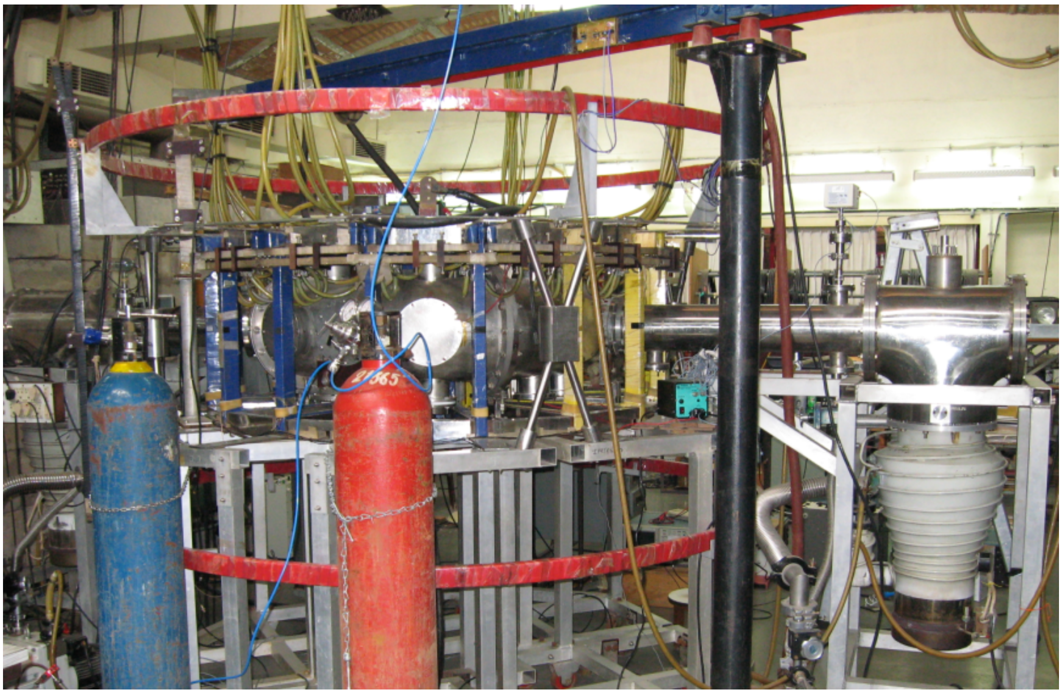

Figure 2.1: A photograph of the simple toroidal device BETA. The blue and yellow vertical bars in the middle of the photograph are the outer legs of TF coils. The experimental chamber is placed inside the toroid.

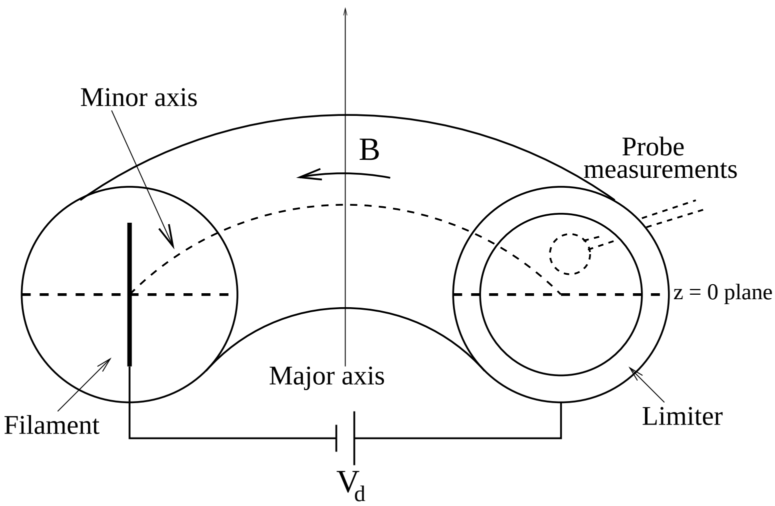

Figure 2.2: A schematic view of the cross-section of BETA and diagnostics. Schematic electrical connection for discharge is also shown. All the probe measurements are done close to the plane of the limiter. The filament heating circuit is not shown here.

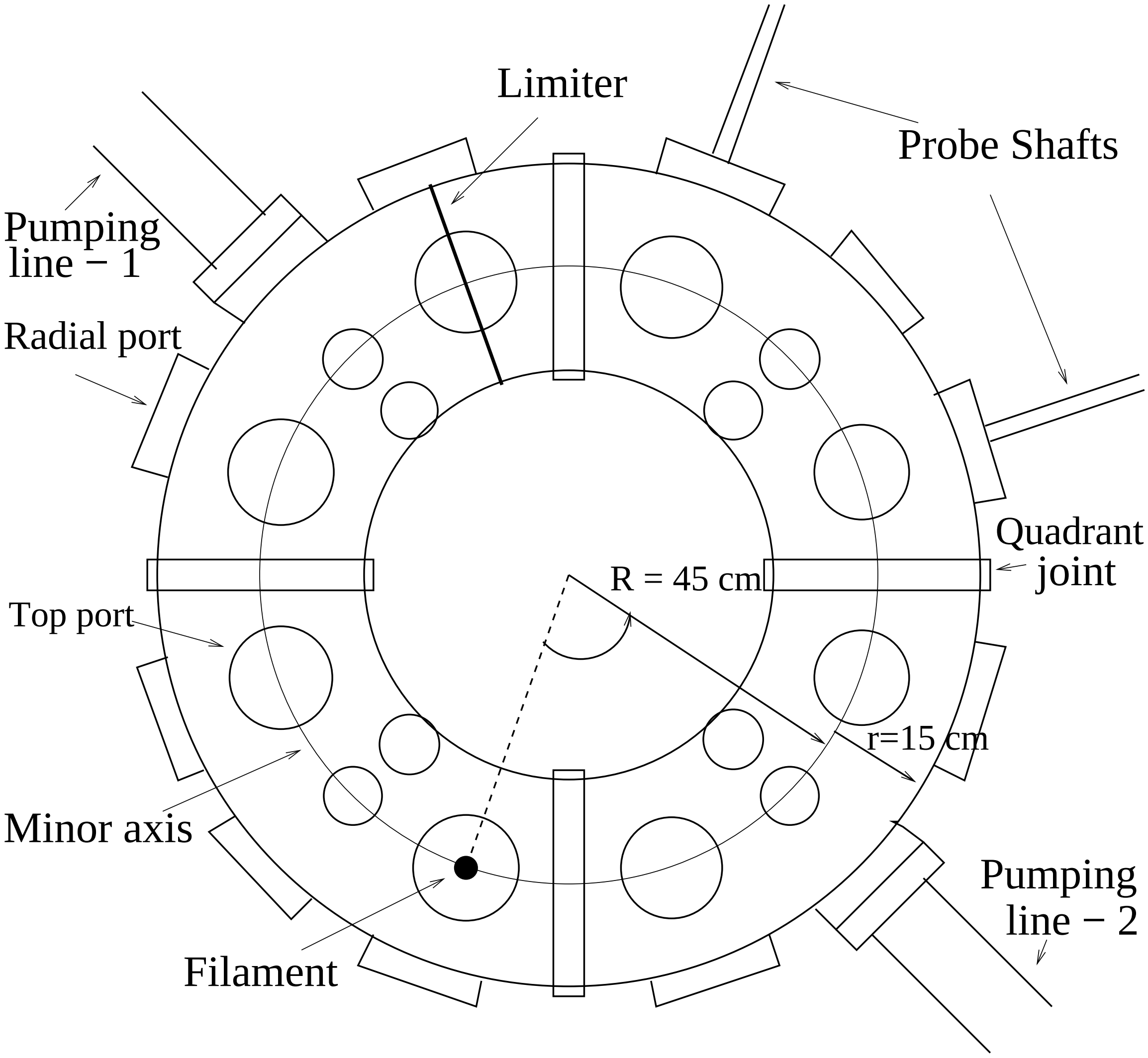

Figure 2.3: A schematic top view of BETA vacuum vessel and other parts. The toroidal and vertical magnetic field coils are not shown here. The cylindrical coordinates (R, θ, z) are defined such that R is along the major radius, θ is the azimuthal angle with reference to the filament location, and z is the vertical coordinate. The plane $z = 0$ indicates the equatorial mid-plane.

2.3.1 Single Langmuir probe

Probe construction and theory

The single Langmuir probes (SLPs) are made up of tungsten wire of 1 mm diameter, either 3 or 4 mm length and hence cylindrical in shape. The probe inserted in the plasma is such that the cylindrical axis of the probe is perpendicular to the toroidal magnetic field. The probe is mounted through ceramic holders with thin ceramic sleeves shielding upto certain length, to reduce shadowing effect of bulk insulating material close to the collecting surface of the probe. In general, arrays of SLPs with a specific probe separation are used to facilitate the measurement of several quantities simultaneously. The entire probe structure along with the ceramic holder is mounted on a stainless steel shaft, which can slide through a vacuum tight Wilson feed-through on a radial port. The probes can be accessed for electrical connections, using suitable connectors at the other end of the shaft outside the vacuum system. The probes are kept either floating or biased with reference to the chamber for diagnosis of the plasma; usually probe voltage and probe current are measured.

Langmuir probes are easy to make but the measurements are difficult to interpret, especially in the presence of magnetic field. The accuracy of the estimation of the physical quantities from the measurements using Langmuir probes, is subject to the use of an appropriate theoretical model for the charge collection by the probe surface. Since the reporting of the first detailed theory for charge collection on conducting surfaces in plasma by Mott-Smith and Langmuir [67], several probe designs with either fully or partially understood theoretical models have been developed, depending on the ambient conditions in the plasma. For example, charge collection of probes in unmagnetized plasma is understood to a significant extent [68]. A brief summary of the charge collection by the probe with collisionless thin sheath, and its relevance to the plasma parameters in an unmagnetized plasma is described below.

For a Maxwellian velocity distribution of particles with an average thermal velocity $\bar{v}_{th}$ and density n, the thermal particle flux (Γ_{th}) in any direction due to random motion is given by

$$\Gamma_{th} = \frac{1}{4} n \bar{v}_{th}. \tag{2.1}$$

Because of the lighter mass of the electrons, usually $v_{th,e} \gg v_{th,i}$, i.e. electron thermal velocities are higher than that of ions, therefore, electron thermal flux dominates usually over the ion thermal flux in the plasma. Consequently, a metal surface inserted in the plasma tend to acquire a negative potential with respect to the ambient plasma; the potential on the metal surface measured with respect to chamber or ground is referred as floating potential (ϕ_f), at which the net current to the probe is zero. For a Maxwellian velocity distribution of electrons with temperature T_e, the electron density at a point with potential V with respect to the far unperturbed location, arbitrarily chosen as zero, is given by

$$n_e = n_\infty exp(eV/kT_e), \tag{2.2}$$

where n_∞, is the electron density at a far, unperturbed location. Nevertheless, this potential at far, unperturbed location can be finite with respect to the wall or chamber potential which is referred as plasma potential (ϕ_p).

On biasing a probe inserted in the plasma, sufficiently negative with respect to ϕ_p, all the electrons are repelled and thus an ion sheath is formed. Under these conditions the current drawn by the probe is called as ion saturation current (I_{is}). The ion saturation current is given by

$$I_{is} = exp\left(-\frac{1}{2}\right) n_\infty q A c_s, \tag{2.3}$$

where n_∞ is the ion or electron density at unperturbed location far from the probe, q is the charge of ion, A is the surface area of sheath and c_s is the ion acoustic velocity with ion mass m_i, given by $c_s = (kT_e/m_i)^{1/2}$, with T_i, the ion temperature assumed to be much smaller compared to T_e. For a given arbitrary voltage V applied across the probe, the current drawn by the probe is determined by the net charge flux incident on the probe. When $T_i \ll T_e$, the probe biased negatively with respect to ϕ_p will collect ion current equal to I_{is} and an electron current I_e

given by

$$I_e = I_{es}\, exp(e(V-\phi_p)/kT_e) = \frac{1}{4}n_\infty eA\bar{v}_{th,e}\, exp(e(V-\phi_p)/kT_e). \tag{2.4}$$

Thus the characteristic $I_e - V$ curve obtained on sweeping voltage across the probe, when plotted on logarithmic scale for current, the slope gives an estimate of T_e. At $V = \phi_p$, there is no electric field in the vicinity of the probe and the probe current is the resultant of ion and electron thermal fluxes. Using these arguments and Eq.(2.4), a relation can be found between the floating potential and the plasma potential. For unmagnetized plasma, the floating potential and plasma potential are related by

$$\phi_p = \phi_f + \mu\frac{kT_e}{e} \tag{2.5}$$

where $\mu = (1/2)(ln(m_i/2\pi m_e)+1)$. Hence knowing μ, ϕ_p can be calculated from ϕ_f and T_e obtained experimentally.

Though well established theoretical models exist for charge collection in an unmagnetized plasma as described above, in the presence of magnetic field, it is understood only to an extent despite the concrete efforts [69, 70]. This is due to the complex structure of sheath surrounding the conducting surface in the presence of magnetic field, which can alter the charge collection scheme significantly. Using suitable cross-field diffusion models, appropriate modifications for electron and ion collection in presence of magnetic field have been suggested [71]. The ratio of I_{es}/I_{is} is found to deviate substantially from $(m_i/m_e)^{1/2}$ which pertains to the field free case [72]. Though the electron collection can be modified significantly, it has been shown that the electron current given by Eq.(2.4) for probe voltage $V < \phi_f$ is only weakly modified. Therefore, this region of the characteristics can be used for the density and T_e calculations. Use of a significant portion of the characteristic curve with probe voltage $V > \phi_f$ has been found to result in spuriously high values of T_e, in measurements on JET Tokamak by Tagle et al [73]. In strongly magnetized plasma, probe-size effects have been observed to affect Langmuir probe measurements. For example, in the measurements in DITE tokamak when larmour radius becomes comparable to the probe-size, density has been seen to be overestimated [74].

For the typical magnetic fields used in the present experimental work, the ion larmour radius is found to be larger than the probe dimensions. The ion collection by the probe, therefore, pertains to a weakly magnetized case. The typical plasma parameters are estimated as follows. The density is interpreted from I_{is} as

$$n_\infty = \frac{I_{is}}{\frac{1}{2}qAc_s}. \tag{2.6}$$

From the characteristic current-voltage curve obtained on sweeping voltage across the probe, comparison is made with Eq.(2.4), for $V < \phi_f$ to estimate T_e. Though Eq.(2.5) do not hold strictly with theoretically calculated value for μ for a magnetized plasma, this equation can still be used to calculate ϕ_p with experimentally determined value for μ [75]. A direct measurement of ϕ_p is, however, obtained using emissive probe as described in Sec.2.3.6.

Signal electronics for SLP measurements

Sweeping voltage across a SLP with respect to the chamber, using a sawtooth wave generator, current to voltage (I-V) characteristic curve is obtained. The diagram of the circuit used for the generation of sawtooth wave, to sweep across the Langmuir probe is shown in Fig. 2.4. Using this circuit, sawtooth wave form of voltage in a typical range of $-60\,V$ to $+20\,V$, with $10\,ms$ period is repeatedly swept across the probe for 40 cycles typically, and the probe current thus obtained is averaged for a single sawtooth period. With this circuit, a sawtooth waveform of low amplitude ($< 5\,V$) is amplified to a large amplitude using a high common mode voltage op-amp (PA-85), the output of which is applied across the probe, with a shunt resistance of $100\,\Omega$ to measure the probe current. To improve the measurement resolution for the voltage drop across the shunt at high common mode voltage, an instrumentation amplifier is used. Typical I-V characteristics from theoretical description are shown in Fig. 2.5, with sweep voltage (V) and probe current (I_p). For comparison, the I-V characteristic curve obtained experimentally is shown in Fig. 2.6. Three different regions are observed in the typical I-V characteristics, viz. a saturation region for relatively large negative bias (where $I_p = I_{is}$), a transition region with increasing voltage, and another saturation region (where $I_p = I_{es}$) for

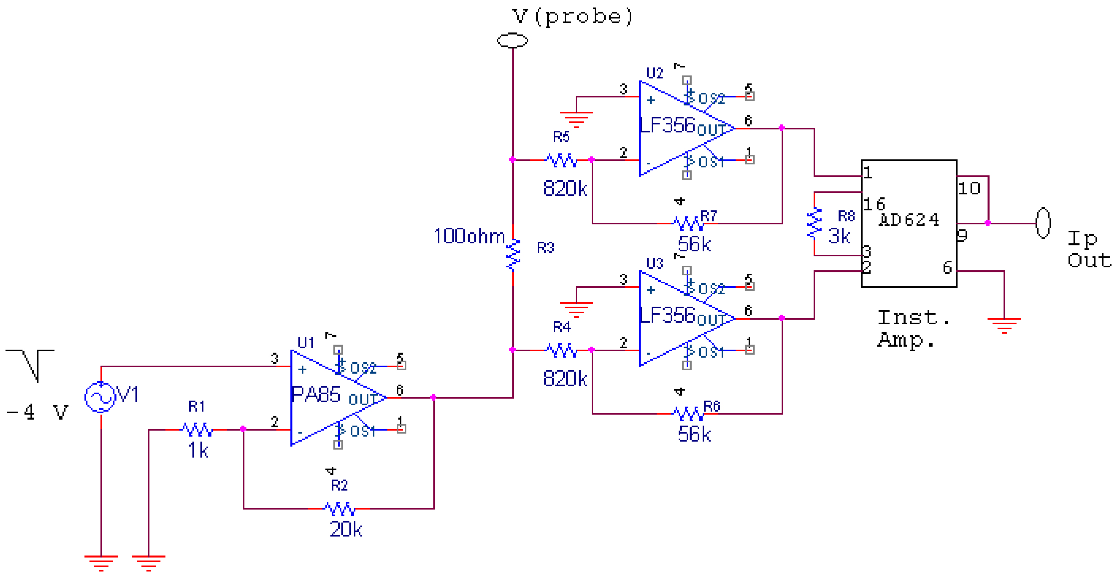

Figure 2.4: Diagram of the circuit used to sweep voltage across the single Langmuir probe, for obtaining full I-V characteristics.

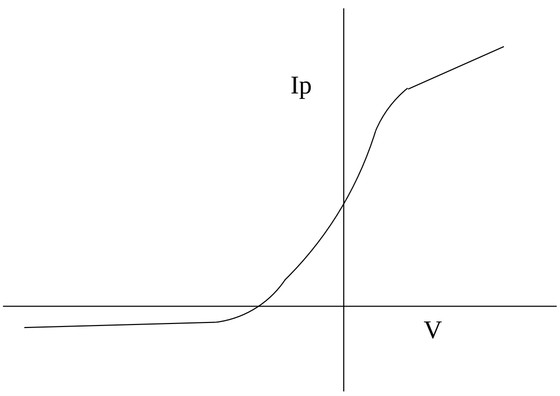

Figure 2.5: Typical schematic of I-V characteristics for a single Langmuir probe, assuming a single Maxwellian temperature for electrons and ions.

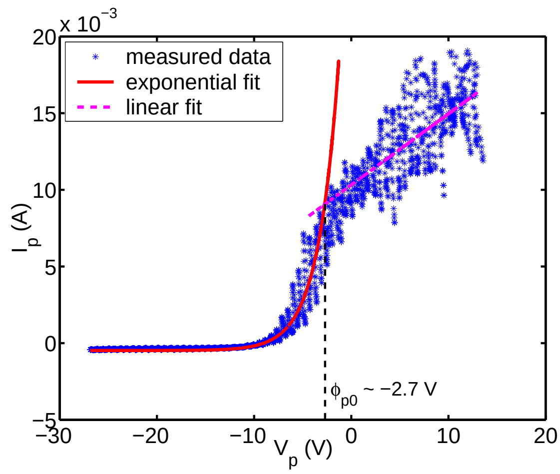

Figure 2.6: The I-V characteristics obtained experimentally, on averaging the characteristics from repeated voltage sweeping. The method of acquiring this curve will be described in Sec.3.3.2.

relatively large positive bias. At $V = \phi_f$, the electron current collected is equal to I_{is} in magnitude, hence the probe draws no net current. A knee observed between the transition region and the electron saturation region gives an approximate estimate of the ϕ_p. Obtaining full I-V characteristics, therefore, gives an average estimate of n_∞, T_e and an approximate ϕ_p. In order to obtain the above said parameters as a function of time the following measurement techniques are used.

To measure I_{is} as a function of time directly, without sweeping voltage across the probe, a sufficient fixed negative bias is applied across the probe, on which the probe draws a current equal to I_{is}. The fixed bias V must be such that $V < \phi_f - 3kT_e/e$, on which almost all the electrons are repelled. A bias of typically $V \sim -40$ to $-50\,V$, is applied using a current to voltage (I-V) converter circuit, which also gives the measure of the probe current. A circuit diagram of the I-V converter made using opamp OPA454 for I_{is} measurement is shown in Fig. 2.7. These op-amps have a maximum common mode voltage rating of 100 V.

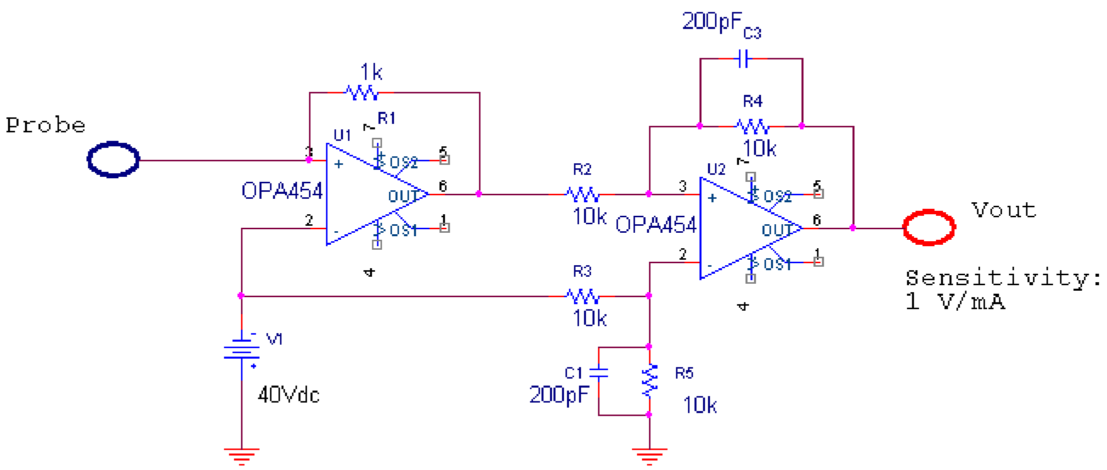

Figure 2.7: The I-V converter circuit used for the measurement of ion saturation current. The sensitivity of the I-V converter is 1 V/mA.

The circuit is made in two op-amp stages; first stage op-amp provides negative bias to the probe, and give an output voltage which is sum of bias voltage and voltage proportional to the probe current. The differential amplifier at the second stage subtracts the bias voltage from the first stage output and gives a voltage signal proportional to the probe current only. The time series of I_{is} thus obtained has a mean and fluctuations which are characteristic of the plasma. Since I_{is} is a measure of density, assuming negligible fluctuations in T_e, fluctuations in I_{is} are measure of density fluctuations. The measurable range of density using SLP with the I-V converter is determined from the measurable output voltage range and probe collection area. The typical measurable density range is between $5 \times 10^{15}\, m^{-3}$ and $1.5 \times 10^{18}\, m^{-3}$.

The floating potential ϕ_f, is indicated by the voltage at which the I-V curve intercepts with the voltage axis; hence $I_p = I_{is} + I_e \simeq 0$, where I_e is given by Eq.(2.4). Ideally ϕ_f can be obtained by simply inserting the probe in the plasma and measuring the voltage acquired by it with a high impedance measuring device. Neglecting the fluctuations in T_e, the fluctuations in ϕ_f indicate fluctuations in ϕ_p. To retain a good frequency response in the measurements of ϕ_f, a voltage follower made of a high common-mode voltage op-amp (PA85) is used as a buffer. The buffer circuit is kept close to the probe connectors on the shafts mounted with probes, followed by cables of sufficient length at the output of the buffer. The circuit diagram of the buffer circuit is shown in Fig. 2.8. The measurable voltage

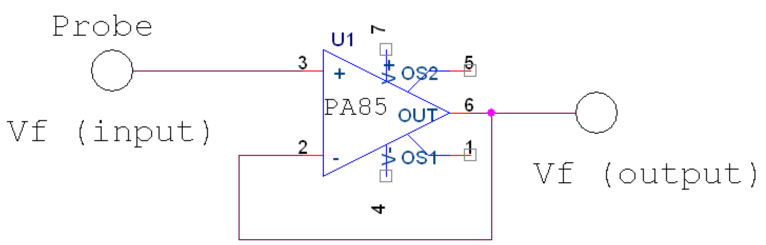

Figure 2.8: Circuit diagram of the voltage follower used for the measurement of floating potential.

range for floating potential is $\phi_f \sim 0$ to $-100\,V$, which is attenuated by a factor of 20, before acquired by the data acquisition system.

The probe current in the transition region in I-V characteristics shown in Fig.2.5, is primarily determined by T_e and n_∞. The electron temperature T_e is given by $kT_e/e = (I_p - I_{is})/(dI_p/dV)$, which can also be directly obtained from an exponential fit to the probe current in the transition region

$$I_p = I_{is}(1 - exp((V - \phi_f)/(kT_e/e))). \tag{2.7}$$

A good estimate for plasma potential ϕ_p can be obtained from the projection on voltage axis from the intersection point of the exponentially fitted curve described in Eq.(2.7), and a straight line fitted to I_p in the electron saturation region. In the present experimental work, however, an emissive probe is used to measure ϕ_p directly. The method of determining ϕ_p from the intersection of curves fitted is described in Chapter 3 and Chapter 4, to corroborate emissive probe measurements.

2.3.2 Triple Langmuir probe

Probe construction

It has been discussed in Sec.2.3.1 that in a magnetized plasma, use of full I-V characteristics of SLP in the transition region can lead to overestimation of T_e [73]. Reliable estimate for T_e can be made only if a part of the I-V characteristics with the probe bias $V < \phi_f$ is used such that electron current drawn is relatively small. A triple Langmuir probe (TLP) operates close to this region of I-V characteristics, with one of the probes exceeding ϕ_f by only a small voltage which is a measure of T_e and drawing a maximum electron current of $2|I_{is}|$ [76, 77]. Hence TLP is useful in simultaneous measurement of T_e and n_∞ without sweeping a voltage across the probe. The TLP used for the measurements on BETA is made up of three tungsten wires of $1\,mm$ diameter and $3\,mm \pm 0.5\,mm$ length, mounted at the corners of a triangle on a ceramic block. A photograph of the TLP is shown in Fig. 2.9. The typical relative error in the calculation of area and estimation of density is $\approx \pm 17\%$. The probe separation between any pair of tips is typically $4\,mm$. The probe tips are mounted such that the cylindrical axes are parallel to the major radius, therefore, perpendicular to the toroidal magnetic field. The probe-ceramic block assembly is mounted through a SS metal shaft radially movable through the radial port.

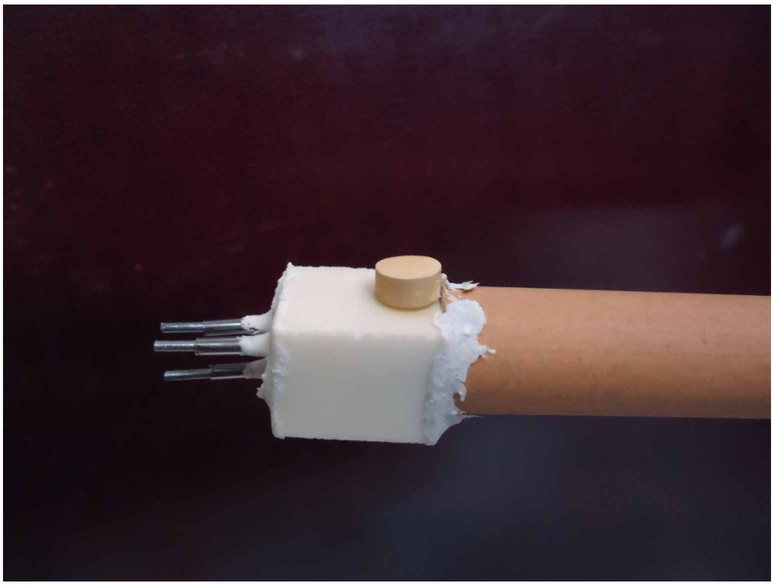

Figure 2.9: A photograph of triple Langmuir probe. Thin capillary tubes are used to enclose the tungsten tips up to certain length from the ceramic block, exposing only 3 mm length of probes.

Signal electronics for TLP measurements

The measurement scheme adopted for TLP is such that one of the three probes is floating, and other two probes are biased with respect to each other. All the probes are, however, floating with respect to the vessel ground or measurement ground both of which are same, and the biasing of the probes is with respect to each other only. Since the probes have a direct reference through plasma only, the biasing circuit has a different 'ground' or reference voltage. The measurements are, therefore, obtained using isolation. The electrical schematic of the measurement method is illustrated in Fig. 2.10. The measurement scheme used here involves the measurement of current flowing between the biased probes which is equal to I_{is} and the floating probe voltage with respect to the positive probe of the two biased probes. The probes are labelled with numbers as follows: 1 - floating, 2 and 3 - biased (2 biased relatively positive). The diagram of the circuit used for TLP measurements is shown in Fig. 2.11. The bias between the probes 2 and 3 (V_{23}) has to be enough ($V_{23} > 3kT_e/e$) so that probe - 3 draws only ion saturation current. A fixed bias of 12 to 24 V between the two probes is provided by a battery. The ion saturation current I_{is} is obtained by measuring voltage drop V_R across

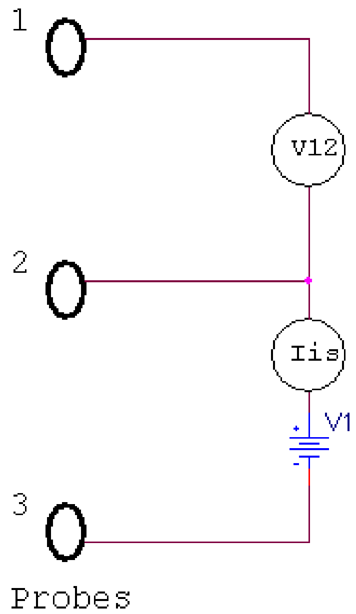

Figure 2.10: Schematic method employed for TLP measurements. ‘1’, ‘2’ and ‘3’ are the numbers labelled for three probes.

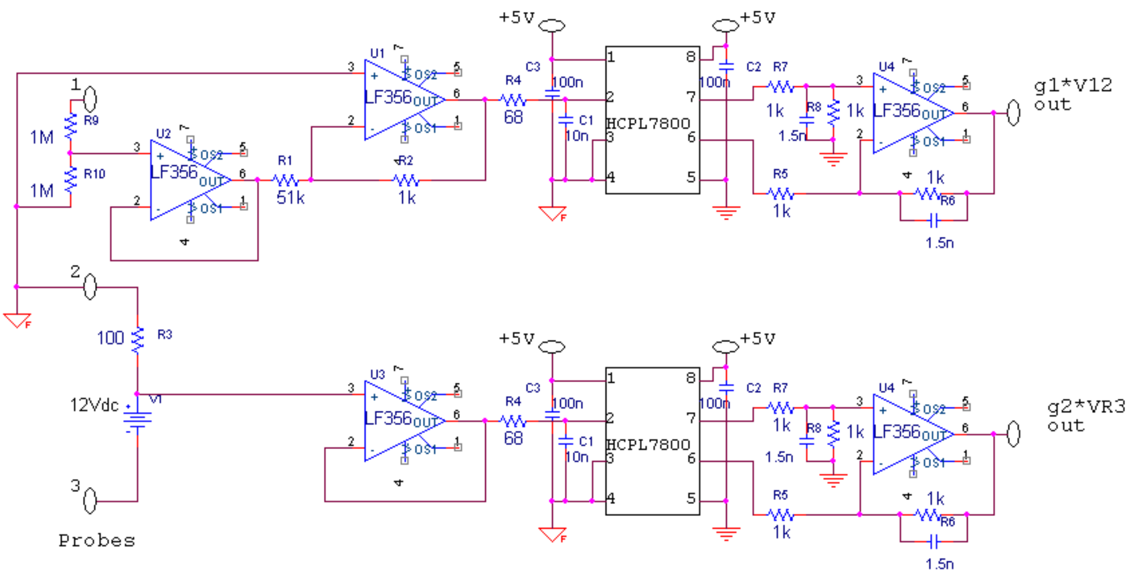

Figure 2.11: Diagram of the circuit used for the operation of TLP. It can be observed that the grounds (or commons) on both sides of the isolation amplifiers are indicated by different symbols.

a small resistance (100 Ω), using high impedance voltage follower. The floating probe-1 voltage with respect to probe-2 (V_{12}) is measured using an op-amp. Both the quantities (V_{12} and V_R) are obtained using analog isolation amplifiers.

In this method of operation for TLP, probe-3 draws a current of I_{is} and probe-2 draws a net current equal to $I_{is} + I_e$ where $I_e \cong -2I_{is}$. Assuming there is only one species of Maxwellian velocity distribution of electrons with temperature T_e, V_{12} is directly proportional to T_e and given by $V_{12} = 0.69kT_e/e$. Hence, T_e is estimated from measured V_{12}. The working range for T_e using the above circuit is between $0.2\,eV$ and $30\,eV$. The maximum range of measurable density from I_{is} obtained using TLP circuit is limited by $5 \times 10^{15}\,m^{-3}$ and $1 \times 10^{18}\,m^{-3}$.

2.3.3 Radial array of Langmuir probes

A linear array of 4 single Langmuir probes is used for simultaneous measurement of density (n) and floating potential (ϕ_f) as a function of time. The probe array is aligned along the major radius in the horizontal mid-plane of the torus and hence referred as a radial array. The successive probe tips are separated by $5\,mm$ whose cylindrical axes are aligned vertically. The entire probe array sitting on a ceramic block which is mounted through a radially movable shaft. A schematic view of the radial array of LPs is shown in Fig. 2.12. A photograph of this probe array is shown in Fig. 2.13. The length of each probe tip is $4\,mm \pm 0.5\,mm$, therefore, the

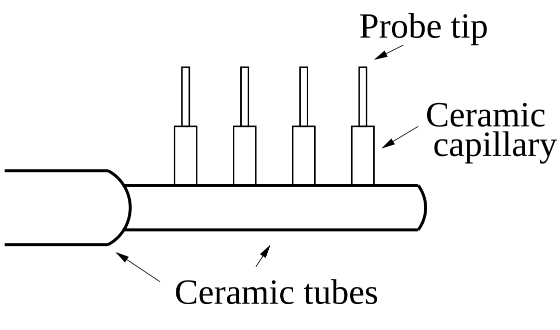

Figure 2.12: A schematic view of the radial array of Langmuir probes. From the ceramic capillaries, 4 mm long probe tips are exposed to the plasma.

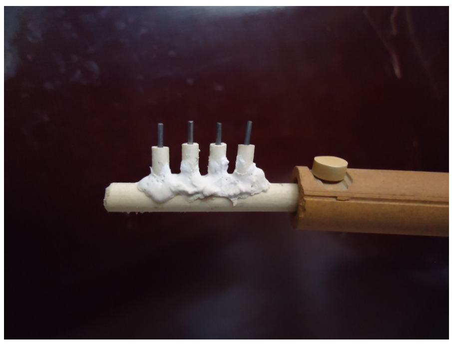

Figure 2.13: A photograph of the radial array of Langmuir probes.

typical relative error in the estimation of area and hence the estimation of density is $\approx \pm 13\%$. Operation of the probes and interpretation of the results are same as described in Sec.2.3.1. An important application of this probe is the estimation of fluctuation induced poloidal particle flux which will be discussed in Chapter 3.

2.3.4 Mach probe

Direct measurement of plasma flow velocity can be obtained using another type of collecting probe, referred as Mach probe. The measurement principle of the Mach probe is based on the asymmetry in the particle flux in upstream and downstream directions when the flow exists. Well understood theoretical models exist for estimation of flow velocity parallel to the magnetic field, from Mach probe measurements [78, 79, 80]. These models which are used for calculation of flow velocity parallel to magnetic field are based on either fluid theory [80, 53, 81] or kinetic theory [82]. Few works relevant to measurement of flow velocities perpendicular to magnetic field have been reported so far, however, either limited in measurement range or applicability [83, 84, 85, 52].

The Mach probe used for estimation of net (or total) poloidal flow velocity on BETA, consists of two circular discs for the collection of charge, mounted on the end surfaces of a cylindrical ceramic block which is $10\,mm$ long and $10\,mm$ in diameter. The circular discs are positioned at $2\,mm$ depth from the end surfaces, with $4\,mm$ aperture open to the incident flux. The schematic view of the Mach probe is shown in Fig. 2.14. The probe is mounted on a radially movable shaft through a radial port. A photograph of the Mach probe with the movable shaft is shown in Fig. 2.15. A model, used for the estimation of flow velocity in any arbitrary direction (θ) with respect to the magnetic field, is based on symmetry arguments to eliminate the magnetic field effect [52]. The cylindrical axis of Mach probe is usually aligned along the direction assumed for the flow and I_{is} at the two end discs is measured. The plasma flow velocity, assumed to be same as ion flow velocity, is estimated from I_{is} measured in the upstream and downstream directions to the flow. From the I_{is} drawn at the two ends of the probe, the net flow velocity in an arbitrary direction θ with respect to the magnetic field can be

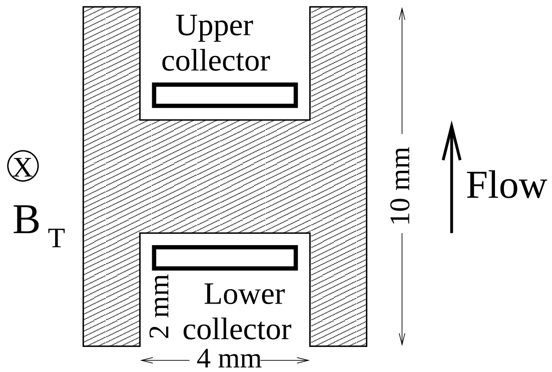

Figure 2.14: A schematic view of the cross-section of the Mach probe, showing the upstream and downstream electrodes for charge collection and the insulating boundaries.

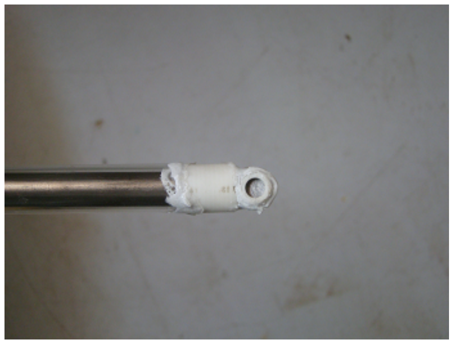

Figure 2.15: A photograph showing the side view of the Mach probe.

calculated using the following equation [52],

$$\frac{v}{c_s} = \frac{1}{\alpha}\frac{I_{is}(\theta+\pi) - I_{is}(\theta)}{I_{is}(\theta+\pi) + I_{is}(\theta)}, \tag{2.8}$$

where c_s is the local ion sound velocity which can be obtained from T_e measurement, α is a constant whose values is 0.5 from Stangeby's result for parallel flow [53]. However, the accuracy of calculation of the flow velocity using Eq.(2.8) is subject to proper calibration of α. This calibration can be done by measuring known flow in the plasma. The calibration for the flow measurements using Mach probe will be discussed in Chapter 3. The resolution of measurements is limited by the inherent asymmetry in the charge collection areas of the disc, whose maximum is found to be less than 10%. The resolution of the measurements is, therefore, given by $v/c_s \sim 0.1$.

Though the derivation of flow velocity perpendicular to the magnetic field using above model is based on elimination of the magnetic field effect, the limit of applicability for this model is $r_{Li}/r_P > 1$ where r_{Li} is the ion larmor radius and r_P is the probe radius [52]. Hence the Mach probe can be used at low magnetic fields only, with the above condition satisfied. For measurement at high magnetic field a probe which is further small in size is necessary. The design and operation of such probe is discussed in the following.

2.3.5 Directional Langmuir probe

The poloidal flow velocity measurement for $B_T \geq 440\,G$ is carried out by a directional Langmuir probe (DLP) similar to the one described in Ref.[52], since $r_{Li} \sim r_P$ for $B_T \geq 440\,G$, for Mach probe. The DLP is made up of a single electrode to keep the probe size minimum. It consists of a $1\,mm$ diameter tungsten wire inserted in a hole of similar inner diameter in a ceramic tube of $3\,mm$ outer diameter. The tungsten wire is made open to the incident charge flux through an aperture of $1\,mm$ diameter on the curved surface of the ceramic tube. The ceramic tube is aligned along the major radius and closed at one end. The open end through which the tungsten wire is inserted, is fixed on a ceramic block which is mounted on a radially movable shaft. The schematic of the DLP is shown in Fig. 2.16. A photograph of DLP is shown in Fig. 2.17. Since DLP is made up of

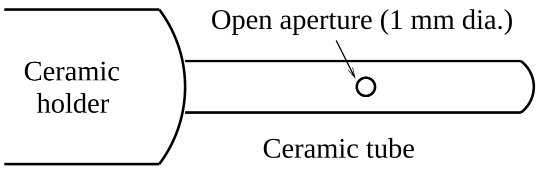

Figure 2.16: A schematic view of directional Langmuir probe.

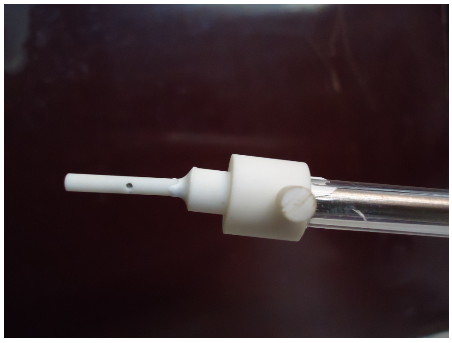

Figure 2.17: A photograph of the directional Langmuir probe. The tungsten wire is exposed through the small aperture on thin long ceramic tube.

a single electrode, poloidal flow measurements are carried out by measuring the upstream and downstream currents on shot to shot basis. The probe is aligned upstream to obtain I_{is}, then rotated by 180^0 to measure downstream I_{is}. The DLP has a small probe area with a single preferable direction, therefore, the charge flux and hence the current drawn by the probe is small. To measure such a low current, a high sensitivity I-V converter is used. The circuit diagram is shown in Fig. 2.18.

Measuring I_{is} upstream and downstream from shot to shot, the flow velocity can

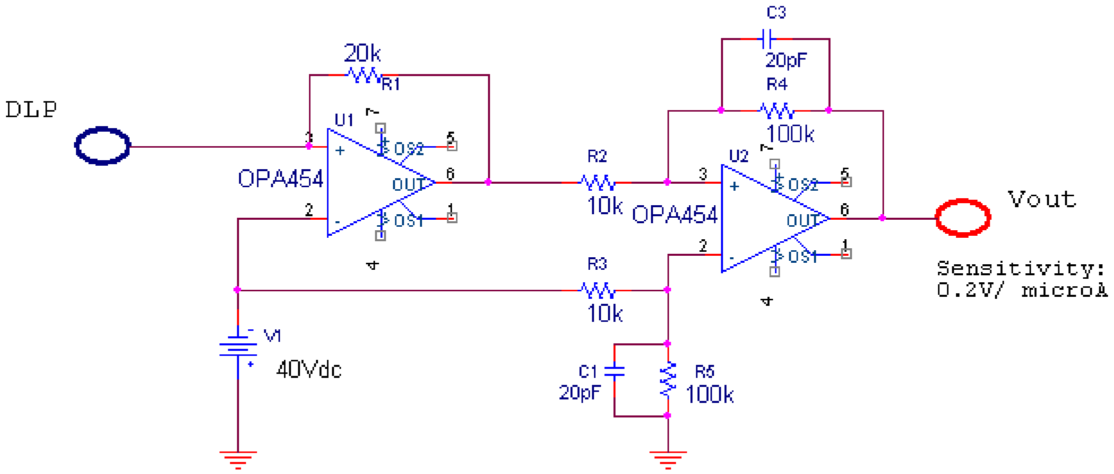

Figure 2.18: The circuit used for measuring low currents collected by DLP.

be calculated using the model described in Sec.2.3.4.

2.3.6 Emissive probe

A direct measurement of ϕ_p can be obtained using an emissive probe, a hot particle flux probe, which also emit electrons due to thermionic emission. The operating principle of the emissive probe is that, if a collecting probe is made to emit electrons and swept for I-V characteristics, the characteristics tend to deviate from the typical characteristics shown for cold probe in Fig. 2.5 in one region and remain unchanged in the other region. The point of deviation in characteristics at which separation of these two regions occurs on voltage axis is the plasma potential. Several methods exist for the operation of emissive probe to determine the above mentioned characteristic point [88]. Two most familiar methods are the inflection point method [86], and floating point method [87, 88]. The inflection point method is based on obtaining the full I-V characteristics of emissive probe with finite emission. In the floating point method, a floating hot probe on sufficient emission tend to attain plasma potential ϕ_p. In the present work, floating point method is used. In the following, the construction and operation of the emissive probe are described.

The emissive probe is made of a tungsten wire of 0.125 mm diameter drawn from a twin bore ceramic tube to form a small loop with 6 mm long wire exposed to the plasma at one end of the tube. The tungsten wire ends drawn from other end of the ceramic tube are pressed against the copper wires of sufficient thickness to fit in tightly in the bores of the tube, to make electrical contact. This method of electrical contact, by physically tightening the wires by pressing against each other, has resulted in reliable electrical contact, observed to be long lasting, even when the tungsten is heated to high temperatures. The twin bore ceramic tube with 3 mm outer diameter, is fixed on a ceramic block which is mounted on a radially movable shaft. A schematic view of the emissive probe is shown in Fig. 2.19. The

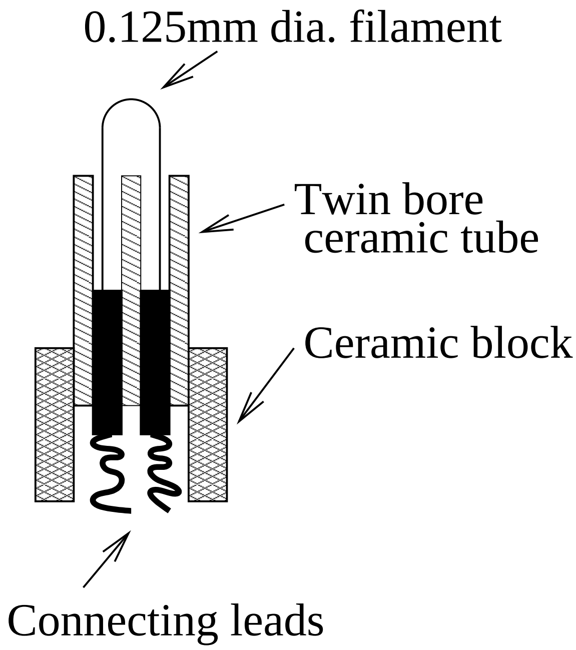

Figure 2.19: Schematic view of the cross-section of emissive probe.

emissive probe loop is heated by passing 2.5 A of DC current across its terminals with an isolated DC power supply. Typically $3 - 6\,V$ drop is observed at the heating DC power supply terminals, depending upon the total length of emissive probe filament. Since the ϕ_p measurements are carried out with continuous heating of the emissive probe filament, a maximum offset of half the voltage drop at the heating power supply can occur in ϕ_p measurements. The voltage on the hot emissive probe is measured using a buffer circuit shown in Fig. 2.8, which is also used for the floating potential measurement.

2.3.7 Signal conditioning and data acquisition

There are two important constraints in recording the analog voltage signals from probe circuits by the standard digitizer modules. First, the analog signal obtained from probes through electrical circuits, in general vary over a wide range of voltage, whereas the digitizers used here have an input voltage range of $\pm 10\,V$ with a 14-bit resolution. For this, an amplifier or an attenuator is used depending on the signal output from the probe circuits. Second, the characteristic fluctuations in the plasma which are reflected in the measured parameters do vary in a wide frequency range; depending upon the sampling frequency of the digitizers, there is an upper cut-off in frequency in analog signal, above which all the frequencies must be attenuated. The analog bandwidth for the signal is determined according to Nyquist criteria to avoid aliasing effect. Both these tasks have been achieved by suitably designed analog circuits labelled as signal conditioning cards.

Two types of signal conditioning cards have been utilized here, for the purpose mentioned above. Both the cards have a pre-amplification or attenuation stages followed by low pass filter. One type of card, labelled as type-1, has a low pass filter of 35 kHz bandwidth. Other type of card, labelled as type-2, has a low pass filter of 100 kHz bandwidth. Since the dominant fluctuations in plasma are typically of low-frequency kind, and significantly lower than 35 kHz, no significant differences are seen on using either of the signal conditioning cards. Multiple number of signal conditioning cards are fixed in an aluminium chassis which is mounted on the diagnostic rack placed in the neighborhood of the experimental vessel. Suitable isolation is provided for inputs from the chassis ground, to avoid possible ground loops from various probe circuits. The output shields from the signal conditioning cards are connected to chassis which is at the ground potential of the vessel. The analog voltage signals from the signal conditioning cards are digitized by a PXI based data acquisition system; the digitizers have a simultaneous sampling with a maximum sampling rate of 2.5 MS/s, a maximum voltage range of $\pm 10\,V$, and a deep on board memory of 16 MS. The trigger for the Data acquisition, which can be chosen with rising or trailing edge of a TTL pulse, has been given with a typical delay of $100\,ms$ with respect to the discharge voltage pulse.

In summary, in this chapter, the details of the experimental apparatus including the vacuum vessel and the subsystems are described in detail. Method of plasma production, various diagnostic techniques and their applicability are discussed. In the next chapter, we proceed to obtain discharge under chosen operating conditions, and characterize them through measurements.

3

Role of fluctuations and intrinsic flows in sustaining mean plasma profiles

3.1 Introduction

As described in Sec.1.2, "rotational transform" does not exist in a simple toroidal plasma and hence there is no equilibrium. The major hindrance in achieving the equilibrium is the vertical charge separation leading to enhanced $\mathbf{E_z} \times \mathbf{B}$ radial losses. Restoration of equilibrium was suggested by two models: one using a conducting limiter which can short-circuit the potential difference due to vertical charge separation, and other by a fast poloidal plasma rotation, leading to the charge neutralization. In the literature survey in Sec.1.3, it has been seen that large fluctuations are always found to be associated with radially well spread mean plasma profiles and improved confinement in a simple toroidal plasma; consequently, plasma confinement time increases by an order of magnitude. Above the background turbulent fluctuations, short-lived coherent structures are believed to be essentially associated with cross-field particle transport. One of the theoretical models, describing the enhanced cross-field transport in the presence of fluctuations is a 'flow-fluctuation cycle'.

The flow-fluctuation cycle described in Sec.1.4, suggests that initially the limiter provides the "seed" equilibrium; the fluctuations generated due to gradients enhance the poloidal flow attained in the initial equilibrium. The enhanced flow back reacts on the fluctuations, thereby limiting the fluctuation amplitude. This flow-fluctuation cycle can be the cause of improved confinement in a simple toroidal plasma.

The experimental investigations presented in this chapter are motivated by identification of two separate regimes of operation where large fluctuations either exist or do not exist in a simple toroidal plasma, produced in BETA. Since the fluctuations are believed to be associated with transport and mean profile modifications, nature of profiles of plasma parameters for both the operation regimes is investigated and the associated fluctuation profiles are obtained. Measurements of the poloidal flow in the plasma for both the operation regimes are made. Through appropriate measurements of typical parameters, direct contribution to the flow by the fluctuations are obtained. The comparisons of various flow measurements reveal that, indeed the fluctuations have significant role in generating intrinsic poloidal flow and an "effective rotational transform".

The experimental investigations begin with demonstrating similar discharge characteristics, for both possible directions of the toroidal magnetic field. This demonstration is followed by a discussion on few practical issues in using Langmuir probes.

3.2 Discharge characteristics - issues

3.2.1 Discharge characteristics with B_T direction

Electrical breakdown of the filled neutral gas is initiated with a hot biased filament in the presence of toroidal magnetic field, as described in Sec.2.2. On achieving the base vacuum, the vessel is filled with argon gas to a neutral pressure of 1×10^{-4} $torr$ and the toroidal field at the minor axis is set at 220 G. The hot filament is biased with a negative pulse for 1 s duration. The voltage across the electrodes when the discharge is sustained, referred as discharge voltage, is denoted by V_d; the discharge current denoted by I_d is measured through a shunt resistance of 0.25 Ω. The discharge pulse is applied during the flat top of the toroidal magnetic field. The discharge characteristics are obtained by varying the magnitude of the negative pulse by a DC power supply with a maximum range of 150 V. To observe possible uncertainty or variations in the discharge current, discharge is obtained 4 times for each applied voltage. Breakdown is found to occur above $40\,V$; the discharge current saturates at $I_d \sim 6\,A$, in the neighborhood of $V_d \sim 60\,V$.

Changing the direction of the current flow in the toroidal field coils, the toroidal magnetic field direction is reversed. This would not change the magnetic field topology; therefore it is expected that the discharge characteristics would remain unchanged. The discharge characteristics, for both directions of toroidal magnetic field, are shown in Fig. 3.1. Small deviations, especially at the breakdown voltage

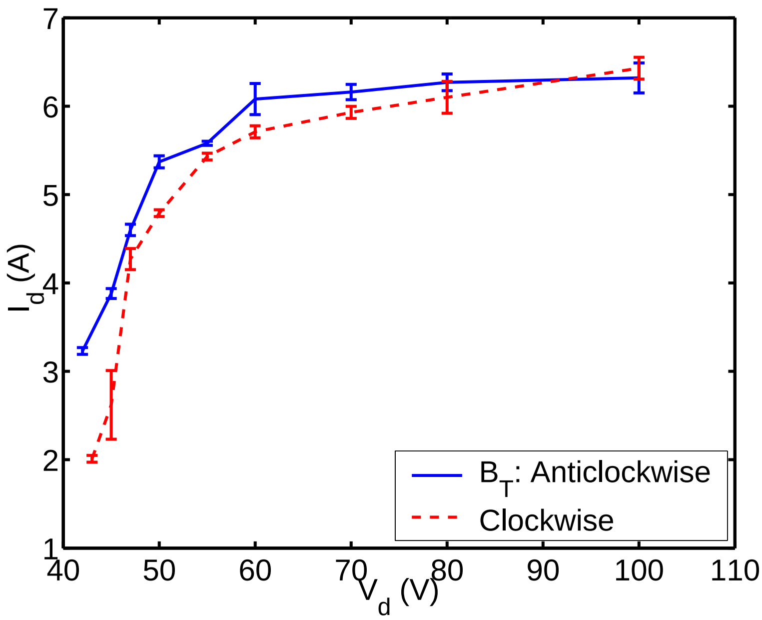

Figure 3.1: Discharge characteristics obtained for two directions of toroidal magnetic field.

may be attributed to the presence of small geometrical asymmetry in placing the filament. All the measurements shown further in the thesis are performed with the toroidal magnetic field in anti-clockwise direction, as viewed from top, unless specified otherwise and the filament current direction is vertically upwards.

3.2.2 Discharge sensitivity to filament heating current

The filament is heated by passing a current $I_f \sim 145\,A$ to initiate and sustain the discharge. Due to the large heating current, a finite magnetic field is produced at the filament surface. The emitted electrons, therefore, execute a complicated trajectories due to the complex magnetic field pattern and the electric field. The emitted electrons have a finite probability of getting trapped again at the filament surface. Simulation results have shown that the escaping of the electrons strongly depends up on the their location of emission and initial velocity [89]. In addition, the fluctuation trend, as visible from the typical measurable parameters is, however, found to be sensitive to the filament heating current I_f for a given mean discharge current. With all the other parameters remaining constant for a mean discharge current of 5 A, the fluctuation trend in discharge current and ion saturation current is found to alter significantly even for a small change in the filament current, i.e. $\Delta I_f \sim 2\ A$. This is illustrated through time series obtained for I_d and I_{is} with $I_f = 142\ A$, 144 A and 148 A, as shown in Fig. 3.2. A blow up of these plots corresponding to a time window of the first 1 ms is shown in Fig. 3.3. The fluctuation trend in I_d and I_{is} is relatively more systematic and steady at $I_f = 142\ A$. The filament current is, therefore set at 142 A for all further measurements.

3.3 Use of Langmuir probes and issues

3.3.1 Langmuir probes - hysteresis effects

Langmuir probes are used for measuring typical plasma parameters such as density (n), electron temperature (T_e) and plasma potential (ϕ_p), as described in Sec.2.3; the measurement of floating potential (ϕ_f) of a Langmuir probe is also described in the same section. The interpretation of the above parameters is based on the particle flux incident on the probe surface, with either a fixed bias or a sweep voltage. The conducting surface of the Langmuir probe is assumed to have negligible emission of secondary electrons or other species due to impurities. Presence of impurities on the surface can either modify the effective probe surface area or introduce other impurity ions in the plasma, thereby modifying the particle flux collected by the probe, both leading to erroneous interpretation of the results. It has been shown that when impurities are present on the surface of the probe, the I-V characteristics of the Langmuir probe are modified [90, 91]. The presence of impurities on the probe surface, therefore, can be detected with a sweep of a symmetric triangular voltage pulse on the probe, which is found to result in a

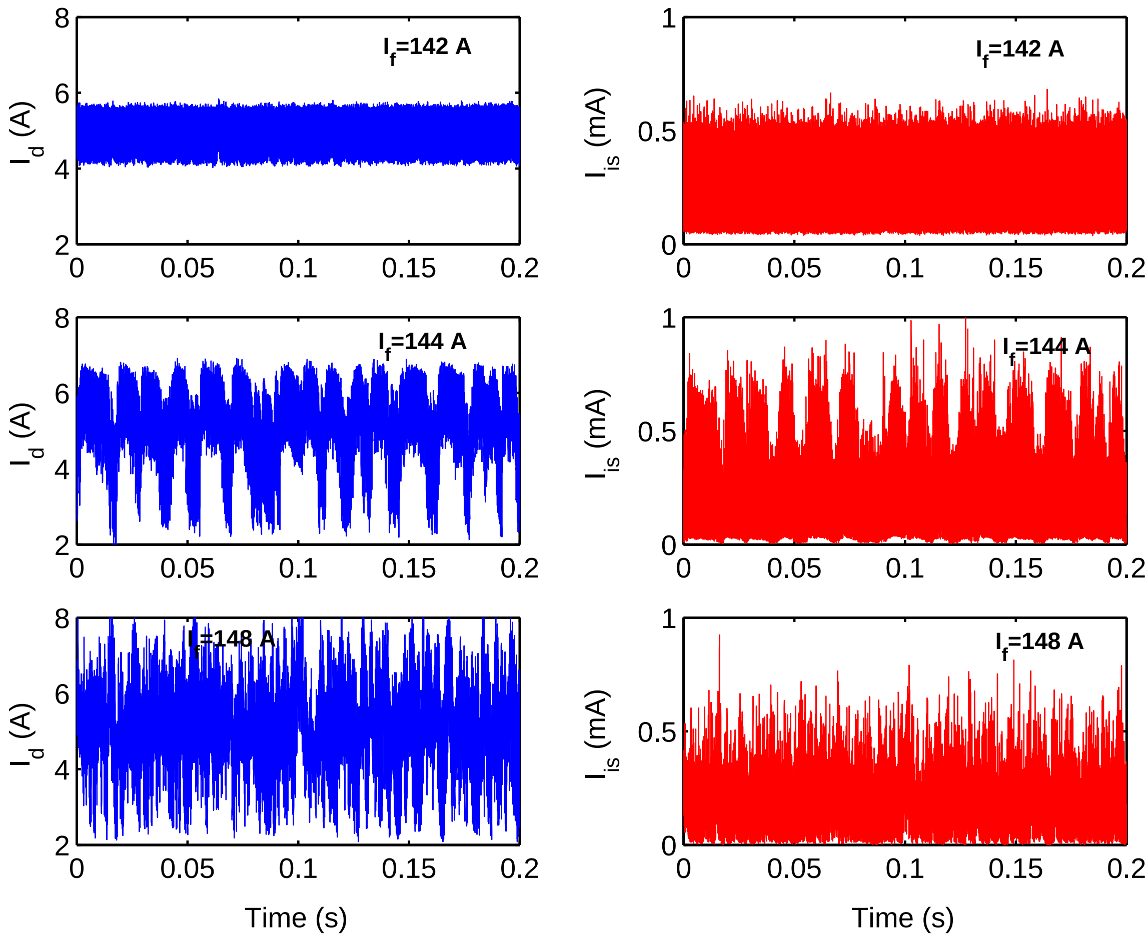

Figure 3.2: The sensitivity of I_d and I_{is} to the discharge with change in I_f. The mean discharge current is set at 5 A in three cases.

asymmetric waveform of probe current. Such observations have been illustrated with newly fabricated probes. Plotting the I-V characteristics of a new probe on current and voltage axes, from the rise time voltage sweep and fall time sweep over each other, hysteresis is observed. It has been found that, after the above Langmuir probes are bombarded with ions by drawing ion saturation current for few tens of minutes, negligible hysteresis is observed in the I-V characteristics. Hence, the probe surface is believed to be contamination free. All the flux probes used for measurements are, therefore, cleaned at regular intervals, using the above mentioned method. The asymmetric I-V characteristics for probes with contaminated surface, is illustrated in Fig. 3.4. For comparison, I-V characteristics of a

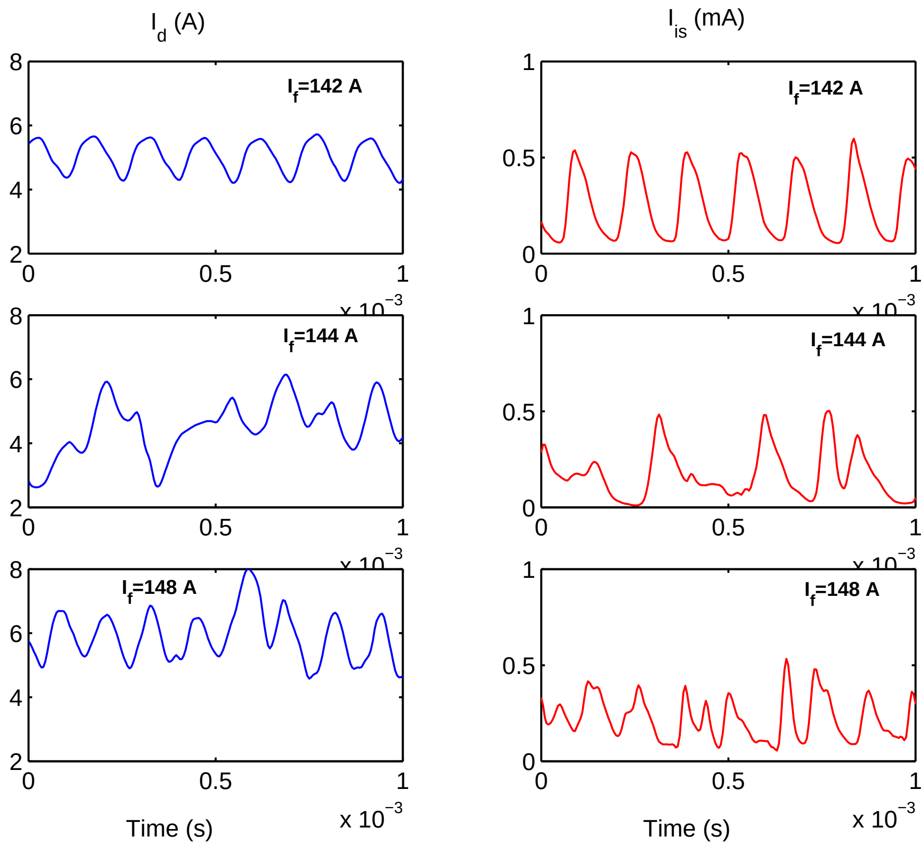

Figure 3.3: A blow up of the time series plots shown in Fig. 3.2, corresponding to the first 1 ms.

clean probe are shown in Fig. 3.5.

3.3.2 Determination of ϕ_{p0} using a cold Langmuir probe

The I-V characteristics obtained with a cold Langmuir probe on sweeping voltage indicate three different regions as described in Sec.2.3.1. When the probe bias changes from a little negative to a little positive voltage with respect to ϕ_{p0}, '0' in the subscript indicating the mean value, the probe current varies from the transition region to electron saturation region. Therefore a "knee" occurs around ϕ_{p0} in between the above mentioned two regions, in the I-V characteristics of the probe. Sawtooth voltage is swept for 40 cycles, from which averaged full I-V characteristics are obtained. An estimation of ϕ_{p0} from I-V characteristics can be made from the intersection point of an exponential function fitted on the

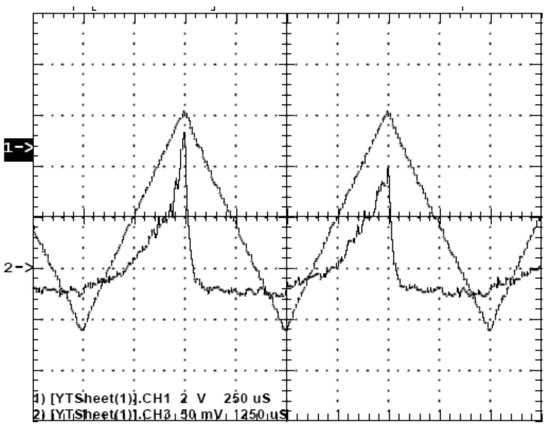

Figure 3.4: Asymmetric I-V characteristics of Langmuir probe, on sweeping a symmetric triangular form of voltage, before the Langmuir probe is cleaned. The probe voltage and current are shown in arbitrary voltage units.

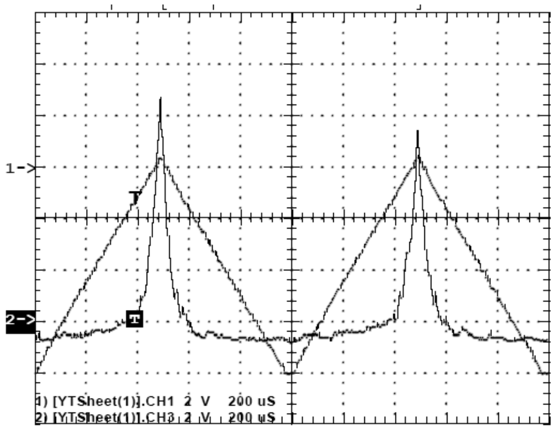

Figure 3.5: The I-V characteristics of Langmuir probe show symmetry after cleaning by ion collection. The probe voltage and current are shown in arbitrary voltage units.

negative side and a linear function fitted on the positive side with respect to the approximate “knee”. The projection of this intersection point on the voltage axis, directly indicates the plasma potential. The time series plots of probe voltage and probe current for 10 cycles are shown in Fig. 3.6. It can be seen from the probe current signal that, as the probe current increases with increasing voltage, the amplitude of the fluctuations on probe current increase significantly. It is clear, therefore, that a single cycle of voltage sweep will not lead to a reasonably good curve fitting to estimate either kT_{e0}/e or ϕ_{p0}. The estimation of ϕ_{p0} using the full I-V characteristics averaged over 40 cycles is illustrated in the Fig. 3.7. The experimental data corresponds to the probe position (R=50 cm, θ = 180^0, z=0 cm) in cylindrical coordinates, where the filament location is chosen as reference for azimuthal direction. With respect to the minor axis, the position is referred as $r = +5\,cm$. In magnetized plasmas, knowing ϕ_{p0}, ϕ_{f0} and kT_{e0}/e for given gas, the value of μ in Eq.(2.5) can be determined [75].

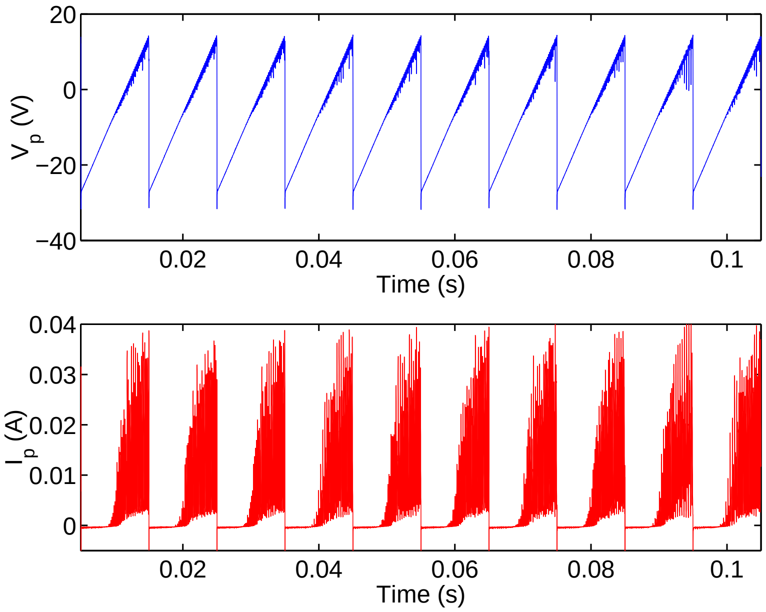

Figure 3.6: Time series of sawtooth ramp voltage (V_p) applied to a SLP, and the probe current (I_p). The voltage ramp-up time period is 10 ms.

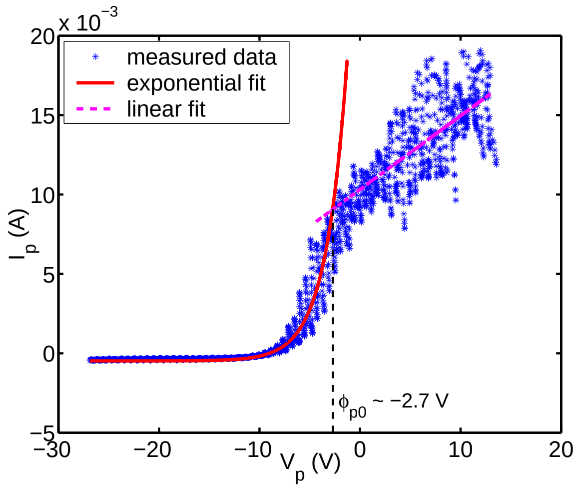

Figure 3.7: Determination of plasma potential from full I-V characteristics of Langmuir probe. The measurements corresponds to discharge with $I_d \sim 5\,A$. From the exponential fit, $kT_{e0}/e \sim 2.1\,eV$. The values of kT_{e0}/e and ϕ_{p0} obtained can be compared with TLP and emissive probe measurements respectively, as described in the later parts of this chapter.

3.4 Measurement methods

Langmuir probe (LP) arrays are used to measure mean density (n_0), mean electron temperature (T_{e0}) and mean floating potential (ϕ_{f0}). A '0' in the subscript indicates the mean value. Density is estimated from the ion saturation current (I_{is}) measured using a triple Langmuir probe (TLP) described in Sec.2.3.2, with 24 V bias between two of its tips and the other tip floating, which also gives simultaneous measurement of kT_e/e [77]. A radial array of Langmuir probes described in Sec.2.3.3, is used for the measurement of I_{is}, with the probe tip biased to $-40\,V$ with respect to the vessel, operating as a single Langmuir probe and ϕ_f measured with high input impedance voltage follower. These measurements using radial probe array are used in fluctuation driven poloidal flux calculations. The three tip Langmuir probe which is used as TLP, is also used to obtain spectral characteristics of fluctuations in poloidal direction. An emissive probe, described in Sec.2.3.6, is used for the direct measurement of mean plasma potential (ϕ_{p0}) [87, 88]. The thin tungsten wire of the emissive probe is heated by 2.6 A of DC current, with a voltage drop of 3 V approximately across the heating power supply. The net voltage drop includes the drop across the length of the probe filament, the voltage drop along the length of the power supply cables and contact resistances between the cables and the filament. Hence, the measured plasma potential can has a maximum offset of half the voltage drop across the heating power supply. The maximum offset in ϕ_{p0} in the present case is $\sim -1.5\,V$. A Mach probe, described in Sec.2.3.4 has been used for the direct measurement of net poloidal flow or total poloidal flow [52]. All the probes are mounted in the horizontal midplane and close to the plane of the limiter, from the radial ports on the outer wall of the torus through shafts which can be moved radially as shown in Fig. 2.2. Multiple measurements at any location are made to obtain average values and error bars in the measurements. The time series of these parameters, suitably filtered using low pass filter of 35 kHz, are acquired at a rate of 200 kS/s, using a computer controlled PXI based data acquisition system. The measurements repeated with low pass filters of 100 kHz bandwidth are described in Chapter 5, where it will be shown that the dominant fluctuations are at low frequencies, and hence the choice of 35 kHz will not eliminate any frequency of interest. The typical physical parameters, relevant to the present experimental investigations are provided in Tab.3.1. A comparison of electron and/or ion cyclotron frequencies with corresponding charge-neutral collision frequencies, as shown in this table, indicates that the plasma is either collisionless or only weakly collisional as described in page 29 of Ref.[100]. In the following sections, the experimental measurements for mean, fluctuation and flow profiles are presented in detail.

Parameter	Value
Ion mass	39.95 amu
Toroidal magnetic field (B_T)	0.022 T
Electron thermal velocity ($v_{th,e}$)	$7.26 \times 10^5\ m/s$
Ion thermal velocity ($v_{th,i}$)	$490.0\ m/s$
Ion acoustic speed (c_s)	$2.68 \times 10^3\ m/s$
Electron plasma frequency ($\omega_{pe}/2\pi$)	$2.84 \times 10^9\ s^{-1}$
Ion plasma frequency ($\omega_{pi}/2\pi$)	$1.05 \times 10^7\ s^{-1}$
Electron cyclotron frequency ($\omega_{ce}/2\pi$)	$6.16 \times 10^8\ s^{-1}$
Ion cyclotron frequency ($\omega_{ci}/2\pi$)	$8.39 \times 10^3\ s^{-1}$
Electron-neutral collision frequency (ν_{en})	$1.28 \times 10^6\ s^{-1}$
Ion-neutral collision frequency (ν_{in})	$865.0\ s^{-1}$
Electron-electron collision frequency (ν_{ee})	$6.71 \times 10^5\ s^{-1}$
Electron-ion collision frequency (ν_{ei})	$4.61 \times 10^5\ s^{-1}$
Ion-ion collision frequency (ν_{ii})	$1.57 \times 10^5\ s^{-1}$
Debye length (λ_D)	$4.0 \times 10^{-5}\ m$
Electron gyro radius (r_{Le})	$1.88 \times 10^{-4}\ m$
Ion gyro radius (r_{Li})	$9.3 \times 10^{-3}\ m$

Table 3.1: The typical physical parameters for argon plasma at $220\,G$ of toroidal magnetic field. For calculations above, it is considered that $kT_e/e \sim 3.0\,eV$, $kT_i/e \sim 0.1\,eV$ and $n_e \simeq n_i \sim 1 \times 10^{17}\ m^{-3}$.

3.5 Discharge conditions - Plasma parameters

3.5.1 Choice of discharge conditions

As described in Sec.3.2.2, the fluctuations in I_d and I_{is} are found to be sensitive to I_f, which appear to be systematic and steady for $I_f = 142\,A$. The filament current is, therefore, chosen to be $142\,A$. The electrical breakdown of the filled gas is found to occur above $40\,V$ as seen from the discharge characteristics in Fig. 3.1, with operating conditions as described in Sec.3.2.1. It is also seen that the discharge current saturates around $60\,V$ with $I_d \sim 6\,A$. Interestingly, the relative fluctuations in I_d and other parameters such as I_{is} and ϕ_f are found to decrease with increase in the discharge voltage. The change in the relative fluctuations in I_d with increase in discharge voltage is shown in Fig. 3.8. The relative

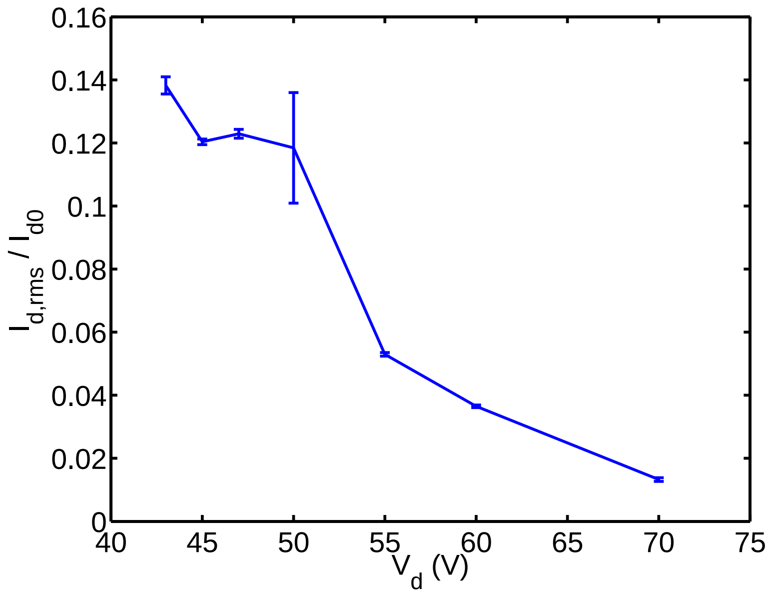

Figure 3.8: Relative fluctuations in I_d with discharge voltage. The time series of I_d are obtained without limiting current on the discharge power supply. $I_{d,rms}$ and I_{d0} indicate fluctuation rms and mean values of I_d time series respectively.

fluctuations in I_d, shown in this figure, are given by the ratio of fluctuation root mean square (rms) to the mean of I_d. The fluctuations in I_d can influence the ionization and hence the density, which will be reflected in the I_{is} measurements. The systematic change in I_{is} with discharge voltage is therefore obtained. The time series plots of I_{is} at $\pm 5\ cm$ with varying discharge voltage are illustrated in Fig. 3.9; however, the traces of I_{is} shown at $-5\ cm$ and $+5\ cm$, for each discharge voltage, are not the simultaneous measurements. It is observed that, at $-5\ cm$

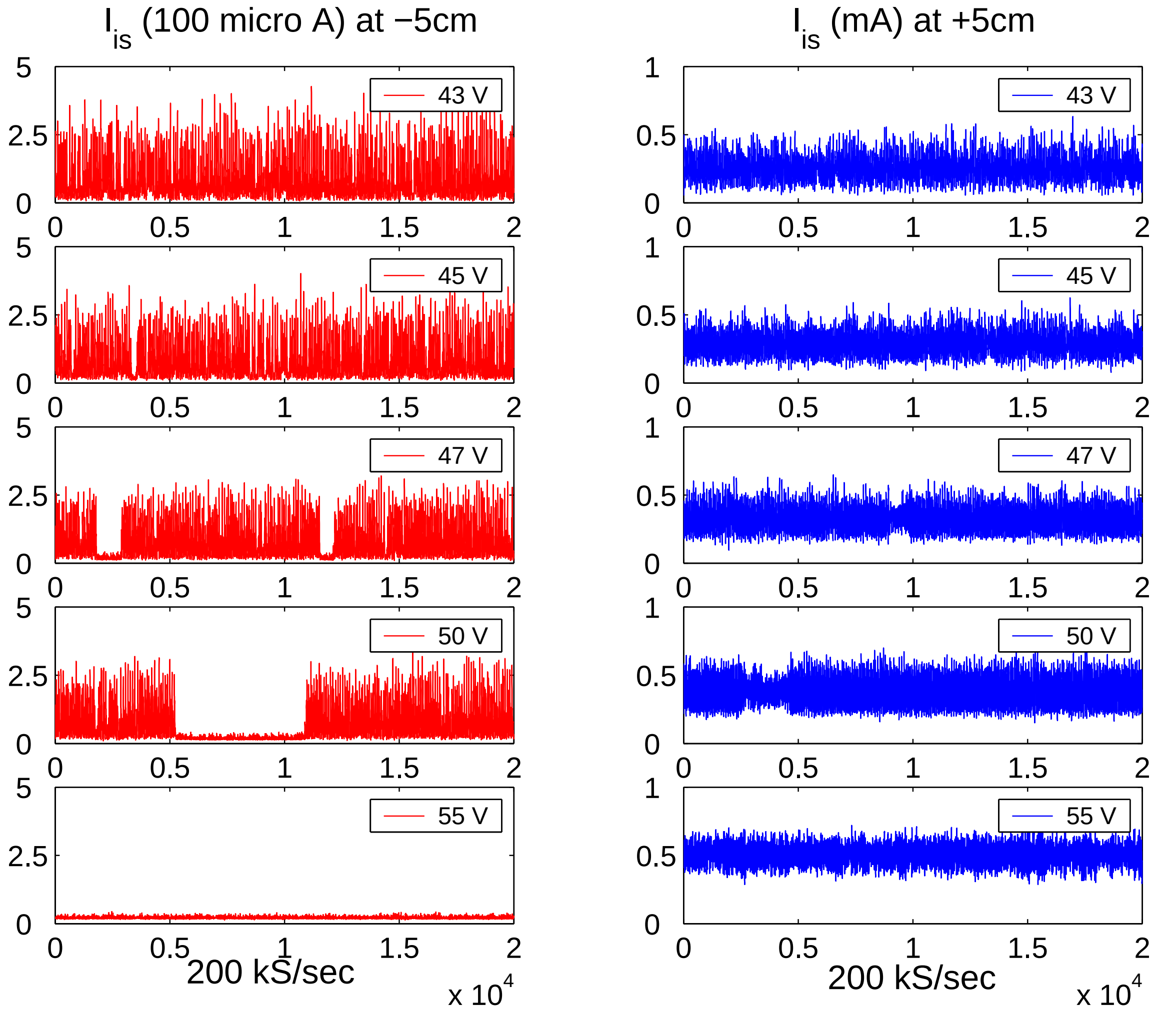

Figure 3.9: Time series plots of I_{is} at $\pm 5\ cm$ with increasing discharge voltages. First column indicates I_{is} at $-5\ cm$ in units of $100\ \mu A$, the second column indicates I_{is} at $+5\ cm$ in units of mA. The corresponding V_d is shown in the legend. The measurement shown in this figure, at $-5\ cm$ and $+5\ cm$ are not the simultaneous measurements.

the mean and fluctuations in I_{is} decreases with increase in discharge voltage. In the case of minimal fluctuations in I_{is} at $-5\ cm$ seen for $55\ V$ of discharge voltage, the corresponding mean value is also found to be too small. At $+5\ cm$, the fluctuations in I_{is} decrease, however, the mean value increases with increase in discharge voltage. For the discharge voltage around 50 V, the fluctuation levels in I_d are seen to change intermittently in time at $-5\ cm$ and $+5\ cm$ both. The above mentioned observations imply a possible connection between the fluctuations and abruptly changing mean values, predominantly at $-5\ cm$. In order to understand the connection between the fluctuations and mean values, which behave distinctly at $-5\ cm$ and $+5\ cm$, time series of I_{is} is obtained simultaneously at the above mentioned locations with 50 V of discharge voltage. The simultaneous measurement repeated four times, is illustrated in Fig. 3.10. Both the probes are, however,

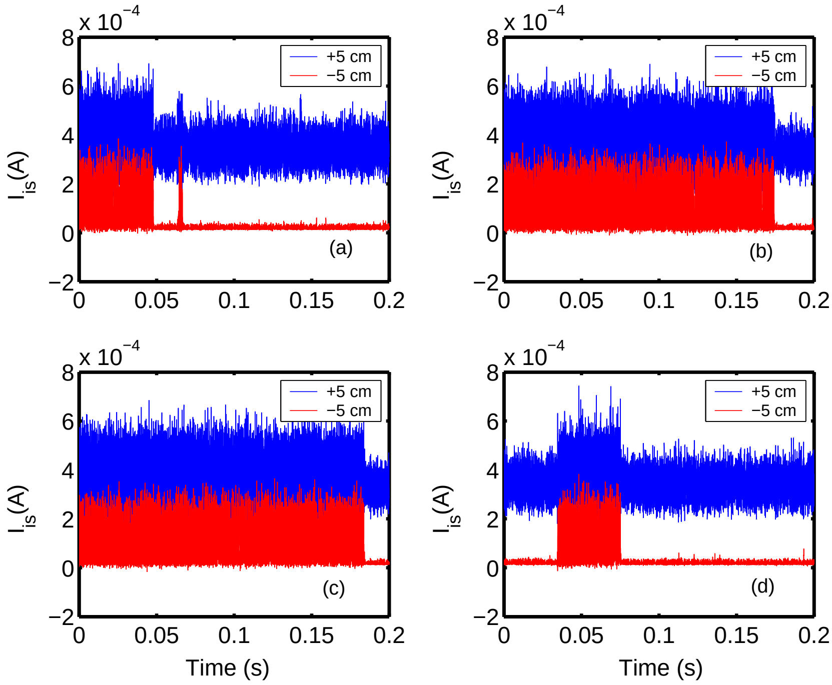

Figure 3.10: Ion saturation current measured simultaneously on both sides of the hot filament, located on the minor axis, with 50 V of discharge voltage, at which large fluctuations occur intermittently. Four plots correspond to four different discharges with the same discharge voltage, indicating intermittent nature of the fluctuations.

not in the same poloidal plane but separated by 22^0 toroidally. From the Fig. 3.10, the intermittent change in the fluctuations in I_{is} at $-5\ cm$ and $+5\ cm$, appear to occur almost simultaneously on the scale shown. As the fluctuations are reduced, the mean value at $+5\ cm$ does not change significantly, whereas the mean value is reduced to negligible values at $-5\ cm$. A blow up of the plot for the instant at which the large fluctuations are excited, is shown in Fig. 3.11; a small delay, approximately 200 μs, is observed between the excitation of fluctuations at $+5\ cm$ and increase in the mean of I_{is} at $-5\ cm$. Hence, it is believed that the excitation of fluctuations is accompanied by filling with plasma at $-5\ cm$.

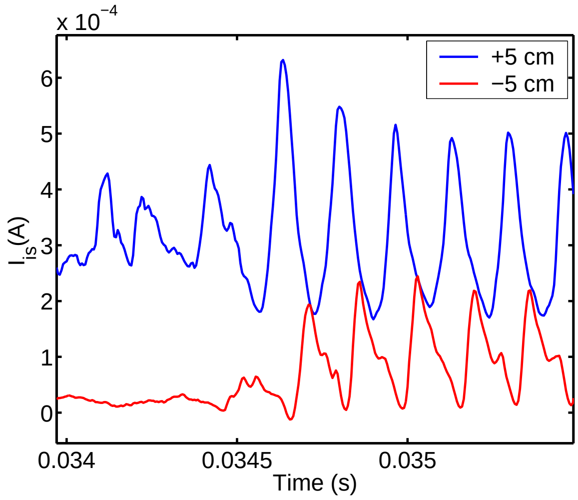

Figure 3.11: A blow up of Fig. 3.10(d). It can be seen that the rise in I_{is} at $-5\ cm$ is lagging with respect to sudden excitation of large fluctuations in I_{is} at $+5\ cm$.

From the above observations, discharge voltage is found to be a crucial parameter with which the fluctuations and filling of the plasma on the high field side (HFS), vary significantly. For a systematic study of the effect of discharge parameters on the plasma profiles, two different discharge conditions with comparable discharge currents but different fluctuation levels, are chosen. At first, with 60 V on discharge power supply initially, discharge current is limited to 5 A, where the discharge voltage across the plasma is 45 V. This case is referred here as the constant current (CC) discharge. Measurement of radial profiles of mean and fluctuating parameters is conducted; poloidal flow velocities are estimated. This is the operating condition where large fluctuations are observed. For second set of measurements, current limit is removed for which the discharge voltage across the plasma is 55 V, i.e., close to the applied voltage and actual discharge current of $6-7\ A$. This case is referred here as the constant voltage (CV) discharge. The fluctuation levels in this case are significantly lower than the first case. Measurement of radial profiles is obtained in this case too. In the results that follows, it will be shown that the plasma profiles obtained in both the cases, differ significantly.

3.5.2 Radial mean profiles

Typical radial profiles of mean ion saturation current and mean floating potential are shown in Fig. 3.12 and Fig. 3.13 respectively, for two discharge conditions. The measurements are carried out with in the limiter inner boundaries, i.e. $r = \pm 9\ cm$. Beyond this region, the mean ion saturation current falls sharply; however, the measurement in the limiter region are not reported in the present thesis work. From the ion saturation current profile for CC discharges, plasma is observed to

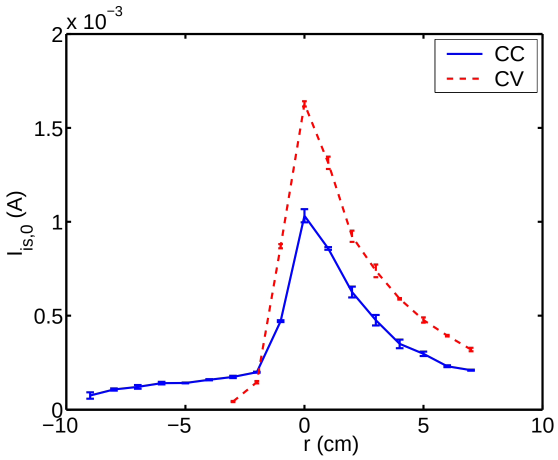

Figure 3.12: Radial profile of ion saturation current with constant current (CC), i.e $I_d \sim 5\ A$; and with constant voltage (CV), i.e. no current limit.

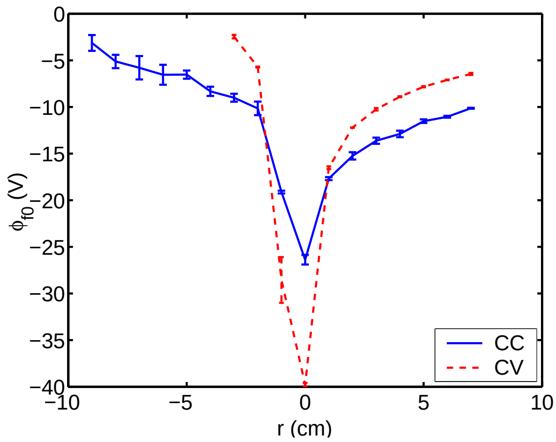

Figure 3.13: Radial profile of floating potential with constant current (CC), i.e $I_d \sim 5\ A$; and with constant voltage (CV), i.e. no current limit.

fill entire radial domain. Corresponding peak density is $\approx 10^{17}\ m^{-3}$. The order of magnitude of $I_{is,0}$ on HFS is similar to that of LFS. For CV discharges, the magnitude of $I_{is,0}$ relatively higher in a region close to minor axis towards LFS, whereas, it is significantly lower on HFS, reaching below the measurement resolution of the probe. This indicates that plasma position is shifted towards LFS on changing from CC to CV discharge. The floating potential profile also indicates a significant change from CC to CV discharges. For CV discharges, the floating potential exhibits a large gradient on HFS, as compared to CC discharges. It seems, therefore, that the plasma profiles which are well spread on both sides with respect to the filament for CC discharge, become one sided for CV discharge. Electron temperature profile for CC case, obtained using TLP, is shown in Fig. 3.14. The same electron temperature profile is shown in Fig. 3.15, with an increased resolution on vertical scale, to indicate the spatial variations. The radial profile of

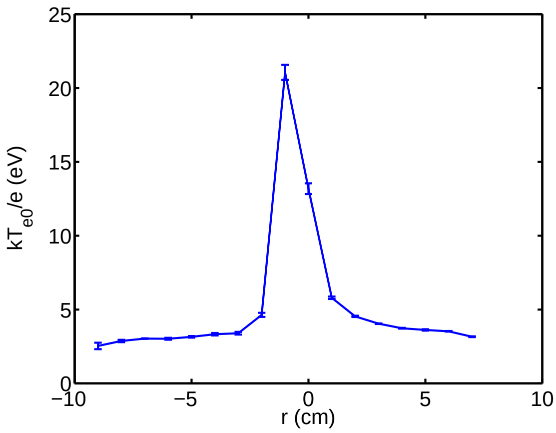

Figure 3.14: Radial profile of electron temperature for constant current discharge, obtained using TLP with a bias of 24 V.

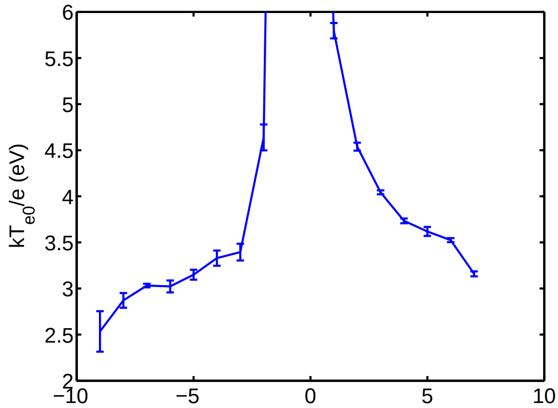

Figure 3.15: A blow up of radial profile of electron temperature for constant current discharge, shown in Fig. 3.14.

kT_{e0}/e exhibit a large peak close to the minor axis and show small variation far from the minor axis. Typical value of kT_{e0}/e at $+5\,cm$ is $\sim 3.5\,eV$ and at $-5\,cm$ is $\sim 3\,eV$. The large values of kT_e/e, close to minor axis may be attributed to the presence of residual primary electrons which are localized close to minor axis [92]. The determination of radial spread of residual primary electrons is described in the Appendix A. It is known that the accuracy of the measurement using TLP is subject to Maxwellian approximation of electron distribution. The plasma potential profiles for both the discharge conditions is shown in Fig. 3.16. As described in Sec.3.4, since the emissive probe is heated continuously with a total voltage drop of $3\,V$, a maximum offset of half this voltage drop, i.e. $-1.5\,V$, can occur. The offset will be uniform through out the radial profile, therefore, no change in the slope of ϕ_{p0} and hence mean radial electric field would occur. For both the discharge conditions, a potential dip close to the minor axis is observed. In the case of CC discharge, a broad potential well is observed; the slope indicates a finite radial electric field, which is significant up to the limiter edge on LFS as well as HFS. In the case of CV discharge, the plasma potential is relatively higher through out the radial profile with shallow profile, indicating reduced electric field in the bulk plasma. It is understood, therefore, that the mean radial electric field in the bulk of the

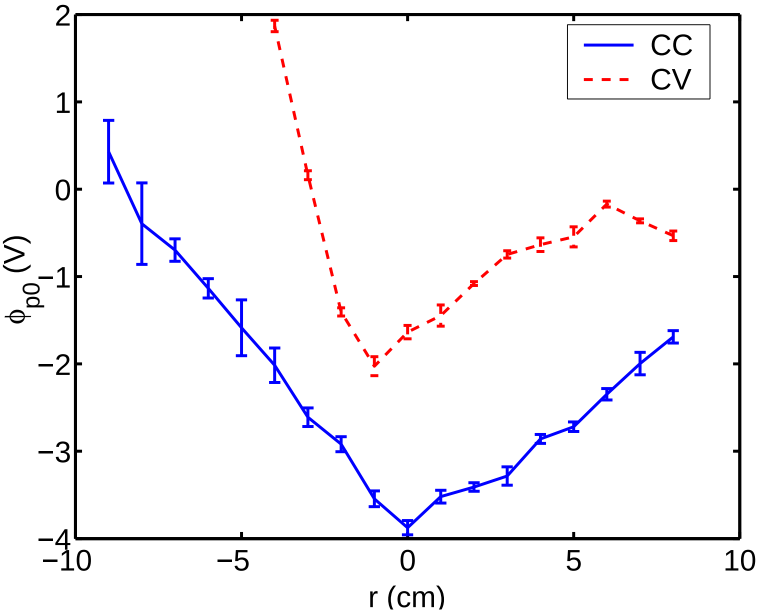

Figure 3.16: Plasma potential profile for constant current (CC) discharge and constant voltage (CV) discharge, obtained using the emissive probe.

plasma, the region away from the filament to the limiter edge, is reduced from CC to CV discharges. Another important observation during the above measurements is that fluctuations in density and floating potential are reduced significantly in the case of CV discharge. The results are described below.

3.5.3 Radial fluctuation profiles

Typical relative fluctuation profiles of ion saturation current and floating potential, for both discharge conditions, are shown in Fig. 3.17 and Fig. 3.18 respectively. The relative fluctuations shown here correspond to the *rms* of the fluctuations normalized to mean values for I_{is}, therefore, equal to $I_{is,rms}/I_{is,0}$; and to kT_{e0}/e for floating potential fluctuations, therefore, equal to $e\phi_{f,rms}/kT_{e0}$. In normalizing the floating potential fluctuations for CV discharge, kT_{e0}/e values of the CC discharge are used, since the kT_{e0}/e values observed are not much different for both the cases as compared to the large difference in absolute fluctuation levels. Assuming negligible fluctuations in kT_e/e, the fluctuations in I_{is} are similar to the density fluctuations, and fluctuations in ϕ_f are similar to the plasma potential fluctuations. For CC discharge, the relative fluctuations in I_{is} are minimum close to the minor

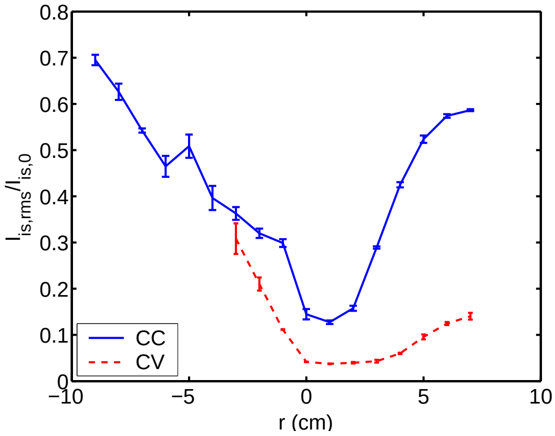

Figure 3.17: Radial profile of relative fluctuations in ion saturation current. 'CC' corresponds to constant current and 'CV' corresponds to constant voltage.

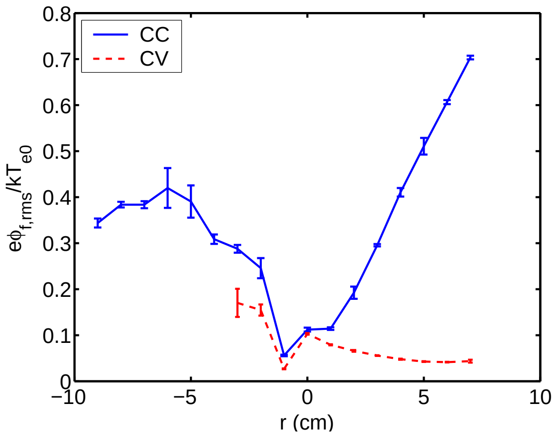

Figure 3.18: Radial profile of floating potential fluctuations relative to kT_e/e. 'CC' corresponds to constant current and 'CV' corresponds to constant voltage.

axis and maximum at the edges; the relative fluctuations in I_{is} reach 0.6 on LFS, and 0.7 on HFS. For CV discharge, the maximum of the relative fluctuations in I_{is} reach 0.15 at the edge on LFS. The relative fluctuations in floating potential for CC discharge, have minimum close to the minor axis and maximum far away from the minor axis; the maximum of relative floating potential fluctuations on LFS reach 0.7, and 0.4 on HFS. The relative potential fluctuations for CV discharge on LFS edge are as low as 0.05. The relative fluctuations, therefore, decrease from CC to CV discharges, significantly in the case of floating potential. As suggested in Sec.3.5.1, since the change in the fluctuation levels is associated with the plasma filling on the HFS, experimental investigation of poloidal transport is carried out. The mean electric field driven poloidal flow is obtained from the mean ϕ_{p0} profile. An average fluctuation driven flow is calculated from the estimated fluctuation induced poloidal flux. A direct measurement of the net or total poloidal flow is obtained using the Mach probe. The results are described in the following section.

3.6 Poloidal transport

3.6.1 Mean electric field driven flow

The electric field in plasma can be obtained from the spatial gradient of plasma potential which is directly measured using an emissive probe, described in Sec.2.3.6. The plasma potential profile measured using emissive probe is shown in Fig. 3.16, for both the discharge conditions. The observed plasma potential values are negative except close to the inner wall. To corroborate emissive probe measurements, plasma potential measurement is also obtained from averaged I-V characteristics of cold LP as described in Sec.3.3.2. This measurement is repeated at several radial locations and plasma potential values obtained in this way are observed to agree within $2\,V$ of the values obtained with emissive probe. Typical I-V characteristics and estimation of ϕ_{p0} at $+5\,cm$ is shown in Fig. 3.7. From the plasma potential profile shown, it is clear that there is a finite mean radial electric field ($\mathbf{E_0}$) from the limiter's edges pointing towards the minor axis, where filament is located. In the case of CC discharge electric field is typically $0.4\,V/cm$ in the outboard region, far from the filament. In the case of CV discharge, its value in this region is $\approx 0.1\,V/cm$ which is comparable to measurement resolution of emissive probe. It may be expected that, close to the minor axis, the presence of fast electrons might have weakly modified the measured ϕ_{p0}. This electric field which is perpendicular to the toroidal magnetic field, can give rise to a finite rotation to the plasma. The radial profile of mean electric field driven flow velocity ($v_{E_0 \times B}$), with $\mathbf{E_0}$ calculated from measured plasma potential profile for CC discharge, is shown in Fig. 3.19. The estimated mean electric field driven velocity values are significantly larger than the net flow velocity measurements which will be discussed in Sec.3.6.3. In order to explain the observed deviation, an attempt is made to find additional flow mechanisms, of which the important one is the fluctuation driven flow. Using appropriately designed Langmuir probes, quantitative estimates pertaining to this phenomenon are made.

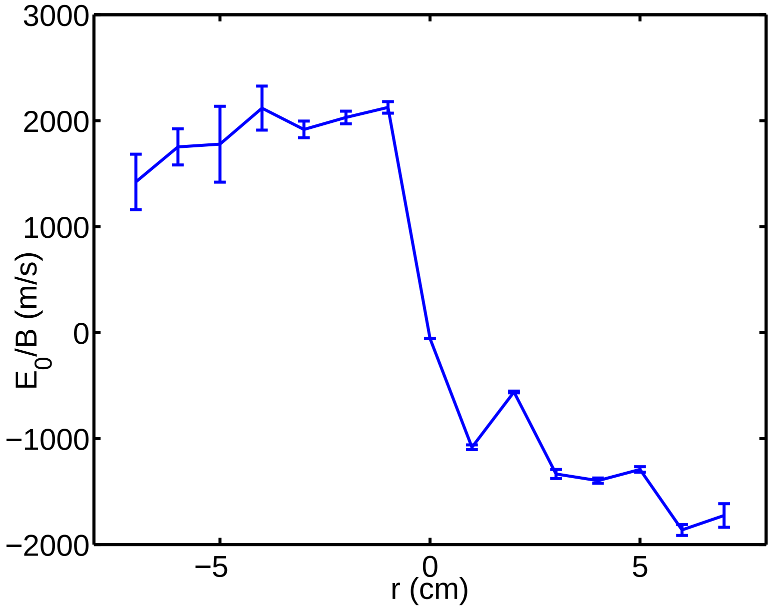

Figure 3.19: Mean electric field driven poloidal flow ($v_{E_0\times B} = E_0/B$) profiles derived from mean plasma potential profiles, directly measured using an emissive probe. The mean electric field (E_0) is calculated using finite difference method and B indicates the local toroidal magnetic field.

3.6.2 Fluctuation driven transport

Large fluctuations are observed in typical plasma parameters in the case of CC discharge, as shown in Fig. 3.17 and Fig. 3.18. These fluctuations and filling with plasma in the entire radial domain bounded by the limiter, are always found to be associated with each other as shown in Fig. 3.10. The mean radial electric field leads to a mean electric field driven poloidal flow due to $\mathbf{E_0} \times \mathbf{B}$ drift, as described in Sec.3.6.1 and hence a mean electric field driven poloidal flux. Similarly, the fluctuating radial electric field also can lead to a finite fluctuation induced poloidal flux depending on the relative phase between the electric field and density fluctuations. Fluctuation driven poloidal flux is estimated from measurements using a radial array of LPs described in Sec.2.3.3, and using methodology for analysis described below. The potential fluctuations on two radially separated probes and density fluctuations on third probe are obtained simultaneously. The fluctuation induced particle flux can be estimated as [12, 54, 55, 56],

$$\Gamma_{fluct} = \frac{1}{B}\langle \tilde{n}\tilde{E} \rangle = \frac{1}{B} C_{nE}(0), \tag{3.1}$$

where $\tilde{n}$ and $\tilde{E}$ indicate fluctuating density and electric field perpendicular to B respectively and C_{nE} indicates the cross covariance of density and potential fluctuations. In general, turbulent fluctuation driven transport estimates are made using spectral analysis technique, where the differential fluctuation driven flux spectrum can be obtained from the further derivation of Eq.(3.1) as [54],

$$\frac{d\Gamma_{fluct}}{d\omega} = \frac{2}{B} k(\omega)|P_{n\phi}| sin[\alpha_{n\phi}(\omega)]d\omega. \tag{3.2}$$

Here $k(\omega)$ is the wave propagation vector for potential fluctuations, perpendicular to the magnetic field and $P_{n\phi}$ and $\alpha_{n\phi}$ are the cross-power and cross-phase respectively, of density and potential fluctuations. Using this method the observed differential flux spectra show sharp peaks with negligible contribution from the frequencies in the background turbulence. A typical differential flux spectrum of fluctuation induced poloidal particle flux at $+5\,cm$ along with $k_r(\omega)$, $P_{n\phi}(\omega)$ and $\theta_{n\phi}(\omega)$ is illustrated in Fig. 3.20. The typical width of the coherent peaks observed in the cross-power spectrum shown in Fig. 3.20(b), and consequently the differential flux spectrum in Fig. 3.20(d) are found to be comparable to frequency resolution used in the spectral analysis. This is illustrated in Fig. 3.21, for the differential spectrum. Hence it is believed that the integration over the differential flux for total flux can be erroneous. In order to verify the possibility of above mentioned error, differential flux spectra is estimated by changing the frequency resolution as illustrated in Fig. 3.22. The total fluctuation induced poloidal flux estimated by integrating over the differential flux spectrum is shown in the legend of Fig. 3.22, against each frequency-resolution used. The peaks in the differential flux spectrum and the total flux obtained are found to vary with frequency resolution, therefore, a good estimate for the total flux can not be made using this method. Using this method, however, the frequencies contributing to finite Γ_{fluct} can be identified. Alternatively the total flux can be estimated from Eq.(3.1) using the definition of cross covariance of time series of density and electric field fluctuations

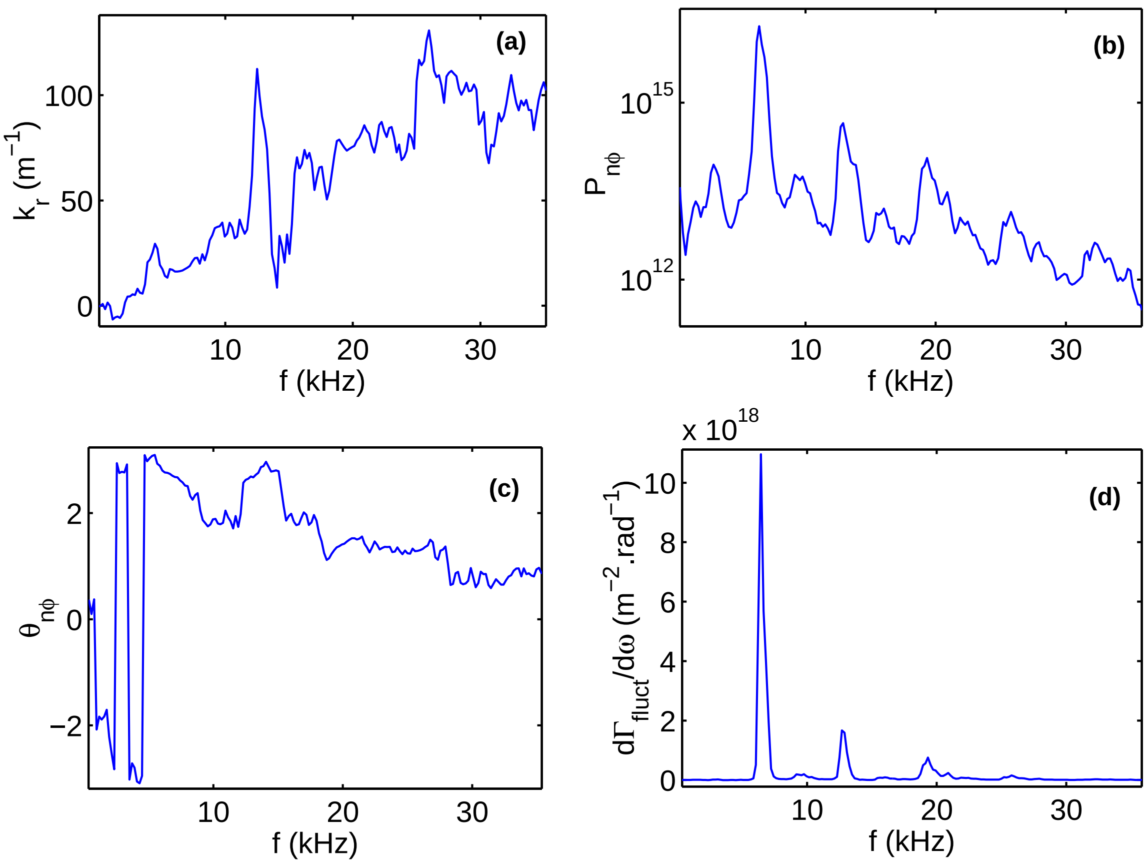

Figure 3.20: An illustration of fluctuation induced poloidal flux estimation using the spectral method of calculation given by Eq.(3.2).

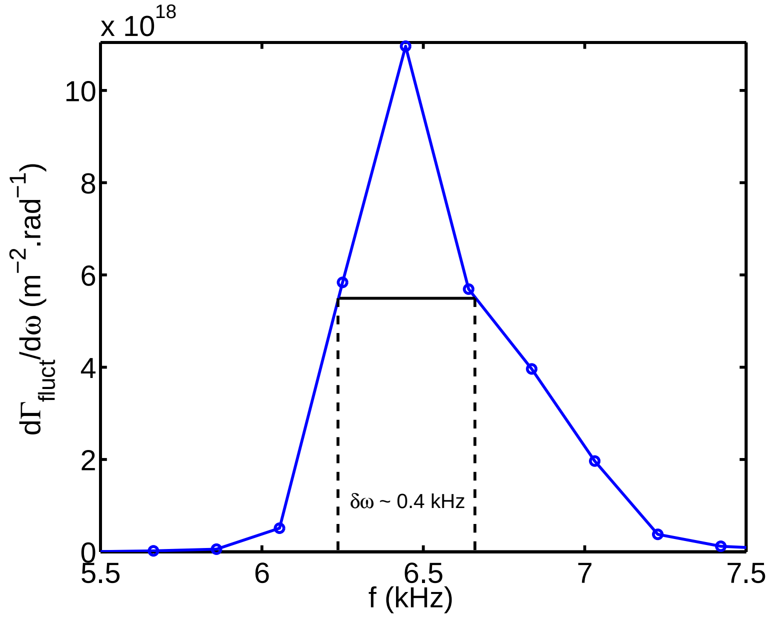

Figure 3.21: A blow up of the Fig. 3.20(d) to observe the typical width of the peak at half of its amplitude. The observed width $\delta\omega \sim 0.4$ kHz, which is just twice the frequency resolution used for the analysis.

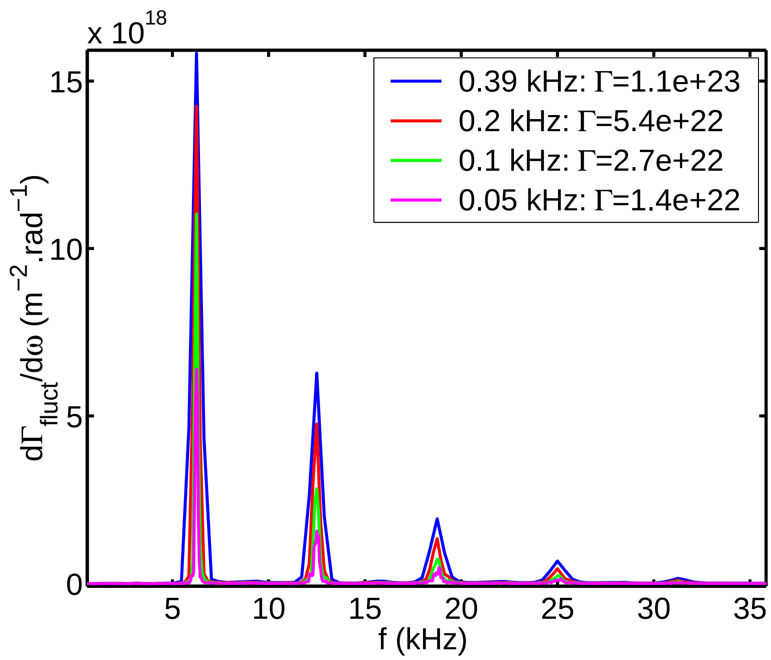

Figure 3.22: The differential spectrum of fluctuation induced flux estimated using Eq.(3.2), with changing the frequency-resolution used for analysis. In the legend, against each frequency-resolution used, Γ_{fluct} obtained on integration is also shown.

given by,

$$C_{nE}(0) = \frac{1}{T}\sum \tilde{n}\tilde{E}\Delta t, \tag{3.3}$$

where Δt is the sampling interval and T is the total sampling time of the data. Fluctuating electric field is estimated from the floating potential measurement on two spatially separated probes and fluctuating density is obtained from the ion saturation current. In other words, the parameters measured would not change for both the methods; only the method of calculation changes. From the fluctuation induced flux estimated using Eq.(3.1) and Eq.(3.3), an equivalent time average flow velocity is defined as

$$v_{fluct} = \frac{\Gamma_{fluct}}{\langle n \rangle}. \tag{3.4}$$

The potential fluctuations can propagate perpendicular to the magnetic field, in either poloidal or radial directions. These correspond to electric field fluctuations in poloidal and radial directions respectively. The poloidal propagation can lead to fluctuation induced radial flux and radial propagation can lead to fluctuation induced poloidal flux. These phenomena are illustrated schematically in Fig. 3.23 and 3.24. Measurement of both these quantities and their radial profiles are described in the following.

Fluctuation induced radial transport

The fluctuation induced radial flux is estimated using the probe structure designed for TLP, described in Sec.2.3.2. The flux is calculated from simultaneously obtained fluctuations in poloidal electric field and density, using Eq.(3.1) and Eq.(3.3). The poloidal fluctuations in electric field are obtained from the floating potential measurement on two vertically aligned probes separated by $4\,mm$. The density fluctuations are obtained from the ion saturation current fluctuations on third probe. With vertically upward electric field and anti-clockwise magnetic field from top-view as positive directions, positive flux is opposite to major radius in the mid-plane. The radial profile of the fluctuation induced radial flux is shown in Fig. 3.25. The fluctuation induced radial flux is found to be outward along the major radius in most of the radial domain; the flux is inwards in a narrow region $-1\,cm < r < 2\,cm$. Therefore, the poloidal electric field fluctuations do not contribute significantly to the inward radial particle transport.

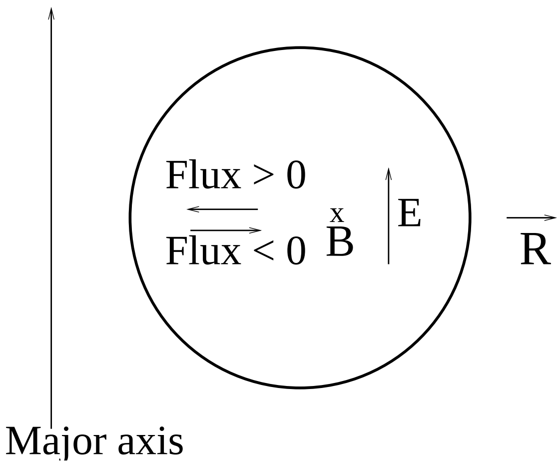

Figure 3.23: A schematic figure showing the poloidal electric field fluctuations $\tilde{\mathbf{E}}$ perpendicular to the toroidal magnetic field B leading to $\Gamma_{fluct,rad}$. Considering vertically upward $\mathbf{E}$ and anticlockwise B from top view as positive directions, '+ve' flux is radially inward.

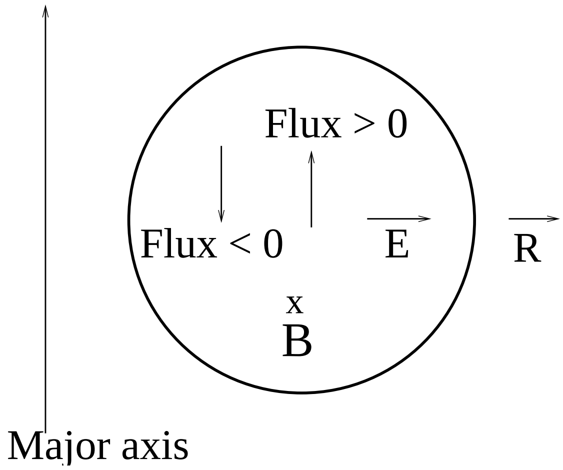

Figure 3.24: A schematic figure showing the radial electric field fluctuations $\tilde{\mathbf{E}}$ perpendicular to B leading to $\Gamma_{fluct,pol}$. Considering radially outward $\mathbf{E}$ and anticlockwise B from top view as positive directions, '+ve' flux is vertically upward.

Fluctuation induced poloidal transport

The fluctuation induced poloidal flux is obtained from radial array of probes described in Sec.2.3.3. The flux is calculated from simultaneously obtained fluctuations in radial electric field and density, using Eq.(3.1) and Eq.(3.3). Floating potential is measured on two probes separated radially by $5\,mm$ and ion saturation current measured on the third probe. The profile of fluctuation induced poloidal flux is shown in Fig. 3.26. With electric field along major radius and anticlockwise magnetic field as positive directions, positive flux is directed upwards. Fluctuation measurements and accordingly the flux values close to the minor axis as shown in Fig. 3.26, show sharp variations spatially, whereas the spatial resolution of the probe is $1\,cm$. Subsequent check for radial wavenumber have shown that the wavelengths are comparable to the probe separation. Strictly speaking, the approximation of measuring $\tilde{n}$ and $\tilde{E}$ at single point is, therefore, not valid. The calculation of v_{fluct} in this region is, therefore, not carried out. Far from this region, fluctuation behavior and calculated flux values change slowly in space and hence the probe resolution is sufficient for flux measurements. A plot, omitting the

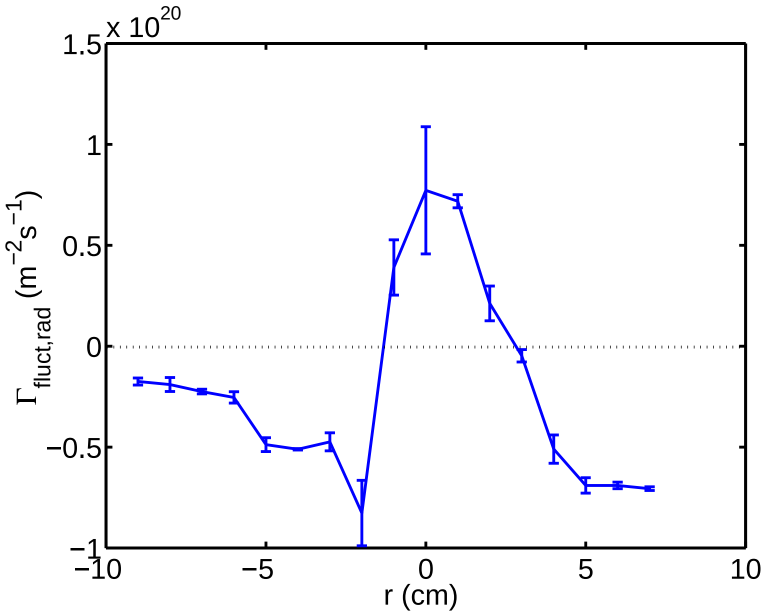

Figure 3.25: Radial profile of fluctuation induced radial flux of particles. This flux is due to the poloidal electric field fluctuations. Positive value indicates that flux is inwards, i.e. opposite to major radius.

data of the poloidal flux close to the minor axis, is shown in Fig. 3.27. From the radial profile of fluctuation driven poloidal flux measurements, v_{fluct} is estimated using Eq.(3.4) and shown in Fig. 3.29. The fluctuation driven flow velocities are significant on the low field side but small on the high field side. Combining the mean field driven flow and fluctuation driven flow, comparisons are made with net flow measurement described in the next section.

3.6.3 Net poloidal flow

Measurement of net poloidal flow of plasma is obtained using a Mach probe described in Sec.2.3.4. For measuring net poloidal flow, Mach probe is aligned vertically. From the ion saturation current drawn on electrodes at the upstream and downstream ends of the probe, the flow velocity can be calculated using Eq.(3.5) which is derived from Eq.(2.8) as

$$\frac{v_{net}}{c_s} = \frac{1}{\alpha} \frac{I_{is,0}(upstream) - I_{is,0}(downstream)}{I_{is,0}(upstream) + I_{is,0}(downstream)}, \tag{3.5}$$

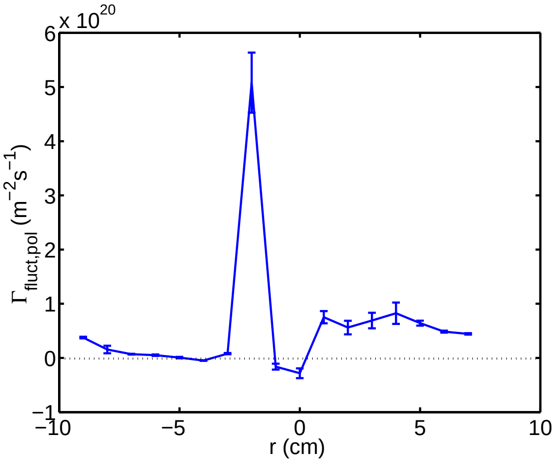

Figure 3.26: Radial profile of $\Gamma_{fluct,pol}$ of particles for CC discharges. This flux is driven by the radial electric field fluctuations. Positive value indicates that flux is upwards.

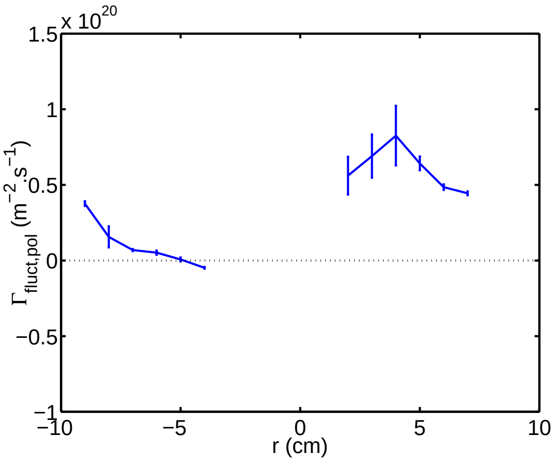

Figure 3.27: The plot of $\Gamma_{fluct,pol}$ shown in Fig. 3.26, omitting the data close to the minor axis. The large variations close to the minor axis were found to be due to the short wavelength nature of the fluctuations.

where c_s is the local ion sound velocity which can be obtained from kT_e/e measurement, α is a constant whose values is 0.5 from Stangeby's result for parallel flow [53]; a '0' in the subscript indicates the mean value for I_{is}. The accuracy of calculation of the flow velocity perpendicular to the magnetic field is, however, subject to proper calibration of α. Conventionally, this calibration can be done by measuring known flow in the plasma. For example, in the measurements for flow on Hyper-I device, using a directional Langmuir probe, the calibration results give $\alpha = 0.45$ [52]. In an attempt for similar calibration, measurements described in Sec.3.6.1 and Sec.3.6.2 could be used. For example, in the region where poloidal fluctuation driven flow is negligible, say at $-5\ cm$, assuming no other contributions to the poloidal flow by other mechanisms, the net flow velocity should be same as mean electric field driven flow velocity. The measured electric field at this location is typically $0.5\ V/cm$ whereas the error in the plasma potential measurements is up to $0.1\ V$, implying a maximum of 20% error in the calculation of electric field and hence the mean electric field driven flow velocity. Using this mean electric field driven flow velocity for the calibration will introduce a maximum uncertainty of 20% in the value of α. In the present measurements $\alpha = 0.5$ is used and it is observed that the net flow velocity and mean electric field driven velocity differ typically by 20% at $-5\,cm$, which is comparable to the maximum uncertainty in mean electric field driven flow measurements. Flow velocity is then calculated for the entire radial profile as shown in Fig. 3.28 for both the operating discharge conditions: CC and CV discharges. The velocities obtained are in units of local ion acoustic velocity. For CC discharge, the magnitude of the maximum net flow on

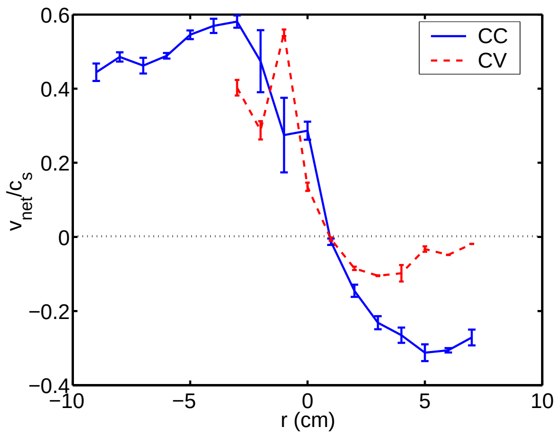

Figure 3.28: Radial profile of net flow velocity measured by Mach probe at $z = 0$. The net flow velocities obtained are in units of local c_s.

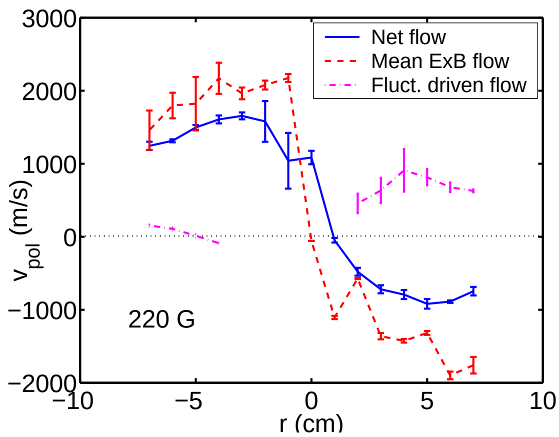

Figure 3.29: Comparison of various poloidal flow velocities: v_{net}, $v_{E_0\times B}$ and v_{fluct}. All the quantities correspond to CC discharges.

LFS is $v_{net} \sim 0.35c_s$; on HFS it is $\sim 0.6c_s$. Using the kT_{e0}/e values from Fig. 3.14, the absolute net flow velocities are calculated in the case of constant current discharge and shown in Fig. 3.29. For the net flow calculations at $-1\,cm$ and $0\,cm$, $kT_{e0}/e = 6.0\,eV$ is used. A comparison of poloidal flow quantities, such as v_{net}, $v_{E_0\times B}$ and v_{fluct} is shown in Fig. 3.29. The net flow velocity, differs from mean electric field driven flow velocity throughout the radial profile, typically from 20% on high field side and up to 50% on the low field side. For $\alpha = 0.5$, assuming that the errors in mean electric field measurements are much below 20%, a flow equal to the difference of net flow and mean electric field driven flow exists, which is unaccounted by the fluctuation driven flow also. It is also equally possible that the observed flow difference on HFS could be a result of the limit in measurement resolution using emissive probe, due to which the accurate calibration of α is not possible. As can be expected, there is a change in the direction of net poloidal flow velocity close to minor axis and the flow velocities are less than local ion acoustic velocity everywhere. Net flow velocities peak far from the filament location, with relatively comparable values up to the limiter's edges. This observation is in contrast to the general belief, from large dip seen in the floating potential profile, that a narrow region with large electric field close to the filament location leads to $\mathbf{E_0} \times \mathbf{B}$ drift and hence a significant flow only close to minor axis. For CV discharge, the magnitude of the maximum net flow on LFS is $\sim 0.1c_s$, which is equal to the measurement resolution of Mach probe, as estimated in Sec.2.3.4. The net flow velocity on LFS for CV discharge is, therefore, significantly lower compared to that of CC discharge. Consequently, similar comparison for poloidal flow velocities is not done for CV discharges.

3.7 Summary

In a filament produced simple toroidal plasma, varying the discharge conditions, two different fluctuation regimes are identified: a large fluctuation regime with $45\,V$ across the plasma referred as CC discharge, corresponding to a current limited discharge and a small fluctuation regime at a higher voltage of $55\,V$ across the plasma, without a current limit, referred as CV discharge. Filament located on the minor axis vertically, injects fast electrons close to the minor axis; hence this region acts as a source region. From the measured plasma parameter profiles, the density peak and potential minimum are observed close to the minor axis, for both the discharge conditions. Interestingly, in the large fluctuation regime, the relative density and potential fluctuations have a minimum in the source region and peak in the edge plasma. The fluctuation levels reach 50% at the edge of the limiter. In the large fluctuation regime, the entire radial domain within the limiter's aperture is filled with the plasma, whereas in the low fluctuation regime, plasma almost disappears from high field side. For the intermediate voltage of $50\,V$ across the plasma, intermittency in the fluctuation levels is observed. Further, in the intermittent fluctuation regime, simultaneous measurement of plasma parameters on the low field side and high field side with respect to the minor axis have been conducted. These simultaneous observations indicate that the existence of fluctuations and filling of plasma in the entire radial domain are associated with each other. Accordingly, measurements for net poloidal flow, mean electric field driven poloidal flow and fluctuation driven poloidal flow were conducted and compared. These poloidal flows were found to be intrinsically generated for CC discharges.

As can be seen in Fig. 3.29, the net poloidal flow velocities measured using Mach probe differ considerably from the mean electric field driven $\mathbf{E_0} \times \mathbf{B}$ drift velocities, typically by 20% on high field side and up to 50% on low field side, subject to the accuracy of Mach probe calibration with $\alpha = 0.5$. The differences in net flow and mean electric field driven flow, on low field side are nearly twice as compared to that on high field side. The measured fluctuation driven flow which is opposite in direction to the mean electric field driven flow, is seen to partially account for the observed differences in mean electric field driven flow and net flow on low field side. Further comparison on low field side close to the limiter, however, shows that the spatial location of maximum fluctuation driven flow does not coincide with the region where the maximum of difference of net flow and mean field driven flow occurs. This discrepancy observed on low field side indicates the possibility of additional mechanisms, contributing to the net flow apart from fluctuation driven flow. Similarly, on the high field side, the observed differences between mean electric field driven flow and net flow indicates a possibility of existence of additional flow mechanisms. At higher discharge voltage, with much reduced fluctuations, measured flow velocity values are less than or comparable to measurement resolutions. At least in the parameter regime chosen here, the present experimental findings suggest that fluctuation driven poloidal flow can play a role in an "effective rotational transform" and thus help in understanding the observed mean profiles.

In the present experimental conditions, whether or not the observed poloidal rotation satisfies the Eq.(1.8), is verified as follows. For the constant current discharge for which the poloidal flows are significant, the right hand side of the above mentioned equation is calculated as follows. From Figures 3.12 and 3.14, $\Lambda \sim 0.04$, in the neighborhood of $r = +5\,cm$. For electrons, the drift $v_D \sim 270\,m/s$. Consequently, $(r/\Lambda)v_D \sim 350 m/s$. The net poloidal flow velocity from Fig. 3.29, in this region is $v_{theta} \sim 10^3\,m/s$. The net poloidal flow is neither much larger to satisfy Eq.(1.8), nor too small to be neglected. It appears, therefore, that the vertical charge separation could be partially neutralized due to poloidal rotation, thereby improving the confinement.

A fluctuation-flow cycle as mechanism for generation of "effective rotational transform" was proposed by Singh et al [29, 47]. This model theoretically describes the generation of flow from fluctuations. This flow is shown to back react on the fluctuations and hence limit the amplitude levels. The fluctuations are assumed to arise out of unstable flute type instability. Though in this chapter, generation of flow from fluctuations is determined experimentally, we have not investigated the role of nature of fluctuations, which will be the subject of the Chapter 4. Furthermore, one may expect that the measured fluctuations must have been moderated by the flow; again we have not attempted to delineate this moderation experimentally. Thus the back reaction of the flow on to the fluctuations is still to be understood experimentally. Hence, the present experimental work can be regarded as a partial support to the fluctuation-flow model. As discussed earlier, lack of perfect matching of the difference of net flow and mean electric field driven flow with the fluctuation driven flow indicates the possibility of additional mechanisms contributing to the net poloidal flow, which requires to be investigated. The major experimental findings in this chapter have been published in **(T. S. Goud et al) Phys. Plasmas 18, 042310 (2011)**.

Demonstrating the role of fluctuations in generating intrinsic flows which further help in sustaining the mean profiles in argon plasma at a given magnetic field, it is understood that change in the nature of fluctuations could affect the nature of flow generations. In this direction, with toroidal magnetic field as a control parameter, nature of fluctuations, associated flows and mean plasma profiles is investigated. The results are presented in the next chapter.

4

Role of toroidal magnetic field in fluctuations and intrinsic poloidal flows

4.1 Introduction

As discussed in earlier chapters, the fluctuation induced flux plays a crucial role in the formation of an "effective rotational transform" in a simple toroidal plasma. It has been also observed that the cross-power and cross-phase of density and potential fluctuations are important parameters in generating the finite fluctuation induced flux. The above said parameters depend up on the nature of instabilities leading to the observed fluctuations [20, 56, 60]. In BLAAMANN experiments, with increase in magnetic field, transition is found to occur from flute mode to drift like modes along with an increase in the turbulence [34, 60]. A similar transition in fluctuations with magnetic field is observed in THORELLO, where highly coherent drift modes at low magnetic field become turbulent with increasing field [20]. However, there have been very few experiments in simple toroidal devices, reporting on transition from coherent to turbulent fluctuating regime accompanied by variations in the flow. For example in BLAAMANN experiments, mean electric field driven flow derived from plasma potential is observed to increase with increasing magnetic field accompanied by improved densities on high field side [60]. A similar phenomena, such as enhanced rotation velocities with increasing magnetic field, with thermal Mach number ranging from 1 to 2, has been observed in the experiments on a cylindrical mirror machine MCX [94].

In this Chapter, a study on the nature of fluctuations, its transitions with magnetic field as a control parameter, consequent changes in poloidal flows and mean profiles in the simple toroidal device BETA, is reported. In particular, a transition in the nature of turbulence with increasing toroidal magnetic field strength and corresponding increase in plasma flow accompanied by improved confinement are reported.

4.2 Operating conditions

1. Filament current $I_f \sim 142\ A$
2. Filling gas: Argon
3. Base pressure $\sim 3 \times 10^{-6}\ torr$
4. Fill pressure $\sim 1 \times 10^{-4}\ torr$
5. $V_d \sim 80\ V$ (initially)
6. $I_d \sim 5\ A$ (unless specified otherwise)
7. B_T (variable) $\sim 220\ G$, $440\ G$, $660\ G$

4.3 Measurement methods

The measurement methods are similar to those described in Sec.3.4, except for the net or total flow measurements. Langmuir probe (LP) arrays are used to measure mean density (n_0), mean electron temperature (T_{e0}) and mean floating potential (ϕ_{f0}). Density is estimated from the ion saturation current (I_{is}) measured using a triple Langmuir probe (TLP) described in Sec.2.3.2, with $12 - 24\ V$ bias between two of its tips and the third tip floating, which also gives simultaneous measurement of T_e [77]. A radial array of Langmuir probes described in Sec.2.3.3, is used for the measurement of I_{is} and ϕ_f in SLP method of operation; for measuring I_{is} the probe tip is biased to $-50\ V$ with respect to the vessel and ϕ_f measured with high input impedance voltage follower. These measurements using radial probe array are used in fluctuation driven poloidal flux calculations. The three tip Langmuir probe which is used as TLP is also used to obtain spectral characteristics of fluctuations in poloidal direction. The emissive probe, described in Sec.2.3.6, is used for the direct measurement of mean plasma potential (ϕ_{p0}) [87, 88]. The thin tungsten wire of emissive probe is heated by 2.6 A of DC current, with an approximate voltage drop of 6 V at the heating power supply. Hence, the measured plasma potential can have a maximum offset of half the voltage drop across the emissive probe filament. The Mach probe, described in Sec.2.3.4, has been used for the direct measurement of net poloidal flow or total poloidal flow of the plasma at 220 G. At high magnetic field the ion Larmor radius becomes comparable to the dimensions of the Mach probe and hence the measurement technique for the net flow is not applicable [52]. Consequently for the poloidal flow measurements at high magnetic field, the directional Langmuir probe, described in Sec.2.3.5, with a small aperture of 1 mm diameter open to the incident charge flux is used. Ion saturation current is measured with DLP aligned upwards as well as downwards and poloidal flow calculations are carried out using a suitable model [52]. Since DLP consists of a single electrode, the upstream and downstream measurements are obtained on shot to shot basis. All the probes are mounted in the horizontal midplane and close to the plane of the limiter, from the radial ports on the outer wall of the torus through stainless steel shafts, which can be moved radially as shown in Fig. 2.2. Multiple measurements at any location are made to obtain average values and error bars in the measurements. The time series of these parameters, suitably filtered using low pass filter of 35 kHz, are acquired at a rate of 200 kS/s, using a computer controlled PXI based data acquisition system. In the following sections, the experimental measurements for mean plasma parameters, relative fluctuations and flow profiles are presented in detail followed by analysis and discussion on identification of instabilities responsible for the observed fluctuations. The typical physical parameters, relevant to the present experimental investigations are provided in Tab.4.1.

Parameter	220 G	440 G	660 G
Ion mass	39.95 amu	39.95 amu	39.95 amu
B_T	0.022 T	0.044 T	0.066 T
$\omega_{ce}/2\pi$	$6.16 \times 10^8\ s^{-1}$	$1.23 \times 10^9\ s^{-1}$	$1.85 \times 10^9\ s^{-1}$
$\omega_{ci}/2\pi$	$8.39 \times 10^3\ s^{-1}$	$1.68 \times 10^4\ s^{-1}$	$2.52 \times 10^4\ s^{-1}$
r_{Le}	$1.88 \times 10^{-4}\ m$	$9.39 \times 10^{-5}\ m$	$6.26 \times 10^{-5}\ m$
r_{Li}	$9.3 \times 10^{-3}\ m$	$4.6 \times 10^{-3}\ m$	$3.1 \times 10^{-3}\ m$

Table 4.1: The typical physical parameters for argon plasma at three values of B_T. For calculations above, it is considered that $kT_e/e \sim 3.0\,eV$, $kT_i/e \sim 0.1\,eV$ and $n_e \simeq n_i \sim 1 \times 10^{17}\ m^{-3}$. The symbols in the first column have same meanings as in Tab.3.1.

4.4 Discharge conditions - plasma profiles

A significant change in the mean plasma parameter-profiles with choice of operating conditions is described in Chapter 3. On increasing the discharge voltage, a systematic change in I_{is} is demonstrated in Sec.3.5.1. It was found that the mean ion saturation current increases at $+5\ cm$ and decreases at $-5\ cm$ with increase in discharge voltage, as shown in Fig. 3.9. At an appropriate intermediate discharge voltage, simultaneous measurement of I_{is} at $\pm 5\ cm$ has indicated a connection between existence of fluctuations and enhanced plasma filling at $-5\ cm$, as shown in Fig. 3.10. Here, simultaneous measurement of I_{is} at $\pm 5\ cm$, varying the discharge voltage, for higher B_T values also, is performed. The upper current limit on the discharge power supply is set at $10\ A$ to prevent arcing, however, the actual I_d is less than $10\ A$. Increasing V_d starting from breakdown voltage for each B_T, time series of I_{is} is obtained simultaneously at $+5\ cm$ and $-5\ cm$. The results described in this section, therefore, correspond to constant voltage discharges. The time series plot of these measurements is shown in Fig. 4.1. A blow up of these plots over a small time window are shown in Fig. 4.2. From this figure, the mean I_{is} reduces at $-5\ cm$, whereas it increases at $+5\ cm$ with increase in V_d, for all values of B_T. The breakdown voltage is found to be higher with increase in B_T. At $220\,G$, a significant decrease is seen in mean of I_{is} at $-5\ cm$ for relatively smaller increase in V_d. These measurements suggest that even at higher values of B_T, the nature

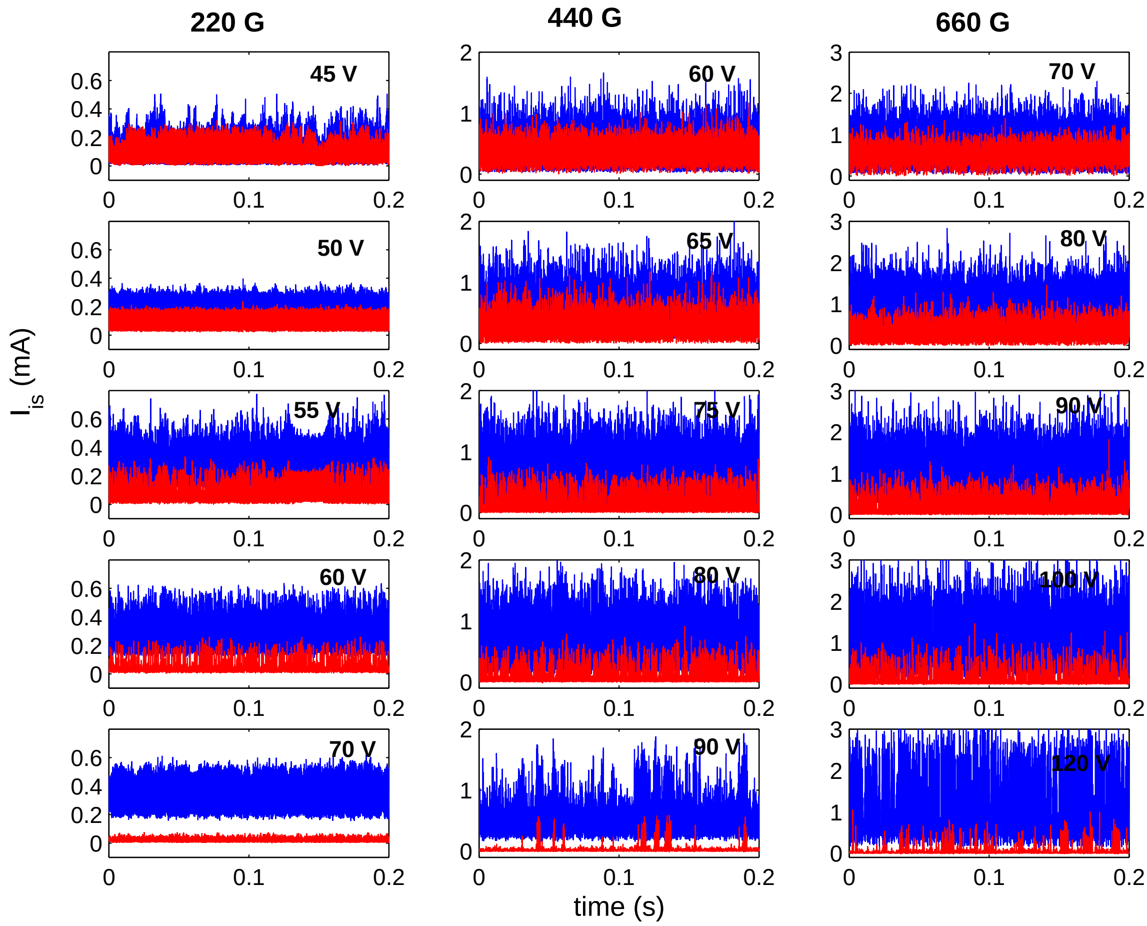

Figure 4.1: Simultaneous measurement of I_{is} at $+5\,cm$ (blue), and $-5\,cm$ (red). Each column corresponds to one particular B_T value, labelled on the top. In each plot, the horizontal axis corresponds to time (s) and the vertical axis correspond to I_{is} (mA). The range of vertical axis is fixed in each column (i.e. each B_T). In each plot, V_d is indicated in the legend.

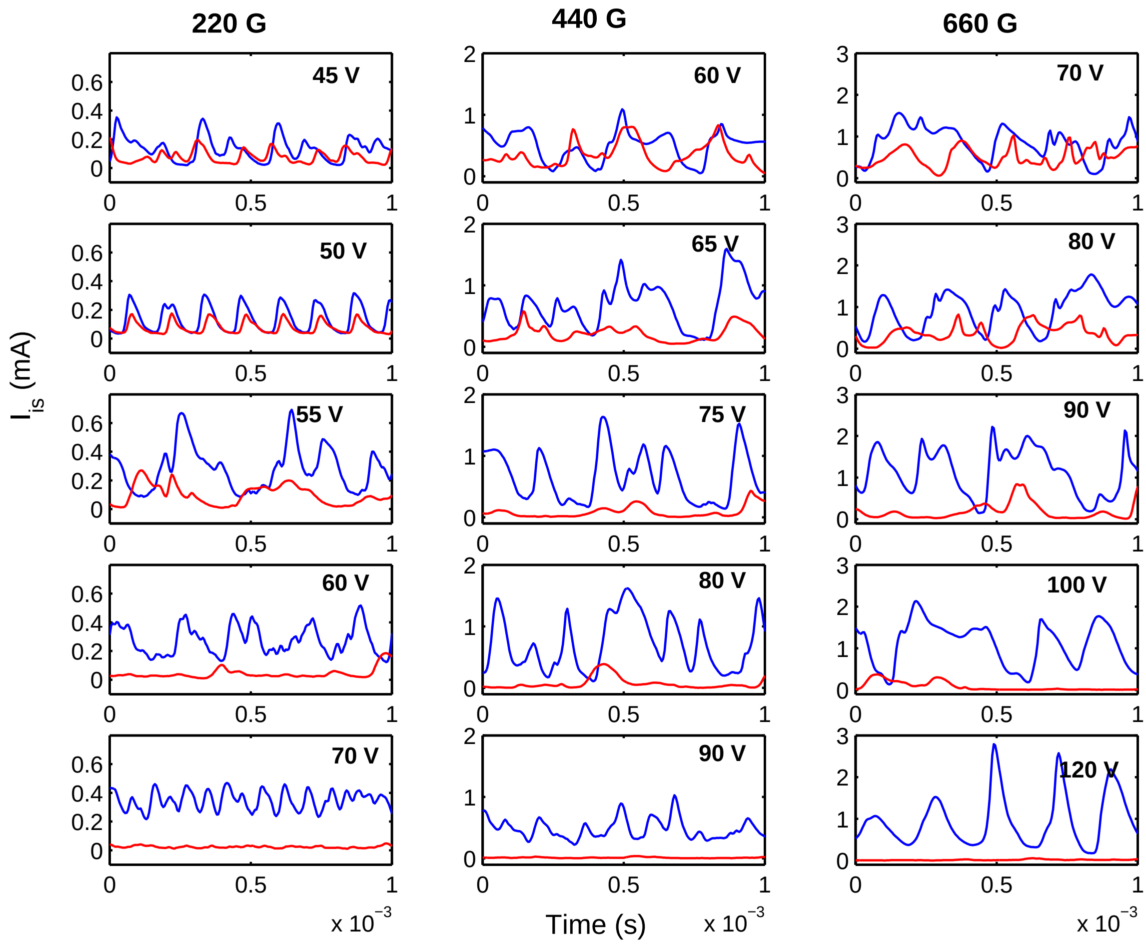

Figure 4.2: A blow up of the time series plots shown in Fig. 4.1, corresponding to the first 1 ms.

of fluctuations and enhanced plasma filling on HFS are associated with the choice of discharge conditions. In the rest of this Chapter, the systematic change in the nature of fluctuations, poloidal flows and consequent mean profiles is investigated as a function of B_T, with $I_d \sim 5\ A$, i.e. constant current (CC) discharges.

4.5 Plasma parameters, radial profiles and transport

The existence of fluctuations, concomitant poloidal flow and plasma spread in the entire radial domain of BETA has been already demonstrated at low magnetic field

($B_T = 220\,G$) in Chapter 3. Since the nature of turbulence can vary with B_T, the poloidal flow mechanism can be modified resulting in interesting flow dynamics. In the present experiments, the toroidal magnetic field (B_T) on the minor axis is set at three different values, viz., $220\,G$, $440\,G$, and $660\,G$ and the discharge is produced. For a given toroidal geometry, the length of toroidal field line is invariant with the magnetic field strength; therefore, the discharge mechanism may not change considerably. This is evident from the observation of similar voltage across the plasma for all the magnetic field values with a constant discharge current. The radial profiles of plasma parameters are obtained for all magnetic field values. The mean and fluctuation profiles of density and potential are obtained and shown in Sec.4.5.1. Sweeping the ramp voltage across the Langmuir probe repeatedly, resulting average I-V characteristics are used for the interpretation of typical plasma parameters to corroborate with the TLP and emissive probe measurements, as described in Sec.4.5.2. Flow measurements, viz., mean electric field driven flow, fluctuation driven flow, and net flow are obtained and shown in Sec.4.5.3.

4.5.1 Radial profiles

Radial profiles of n_0, kT_{e0}/e, and ϕ_{p0} are obtained for three magnetic field values as shown in Fig. 4.3. The radial profile of ϕ_{f0} are shown in Fig. 4.4. Peak in density profile occurs close to the minor axis for all three values of B_T, coinciding with the source region. The peak density values do not seem to change significantly with increase in B_T, whereas systematic increase in density is observed away from the minor axis, significantly on HFS. At $660\,G$, a second broad peak occurs in density around $-6\,cm$. Interestingly, a dip in n_0 is observed at $-2\,cm$ for B_T=$440\,G$ and $660\,G$, which deepens with increasing magnetic field. The shadowing effect in the formation of the above dip in the density is ruled out since there are no other probes in the neighborhood of TLP used for obtaining I_{is}. A possible reason for this dip is the way the plasma is filled on HFS. In Chapter 3, enhanced filling of plasma on HFS is found when the large fluctuations exist, generating the poloidal flows and sustaining mean profiles. In the present case, at higher values of B_T, the variations in the particle flux arriving at a point can vary for different radial locations; hence resulting in a dip. Investigation of transport phenomena is reported in Sec.4.5.3.

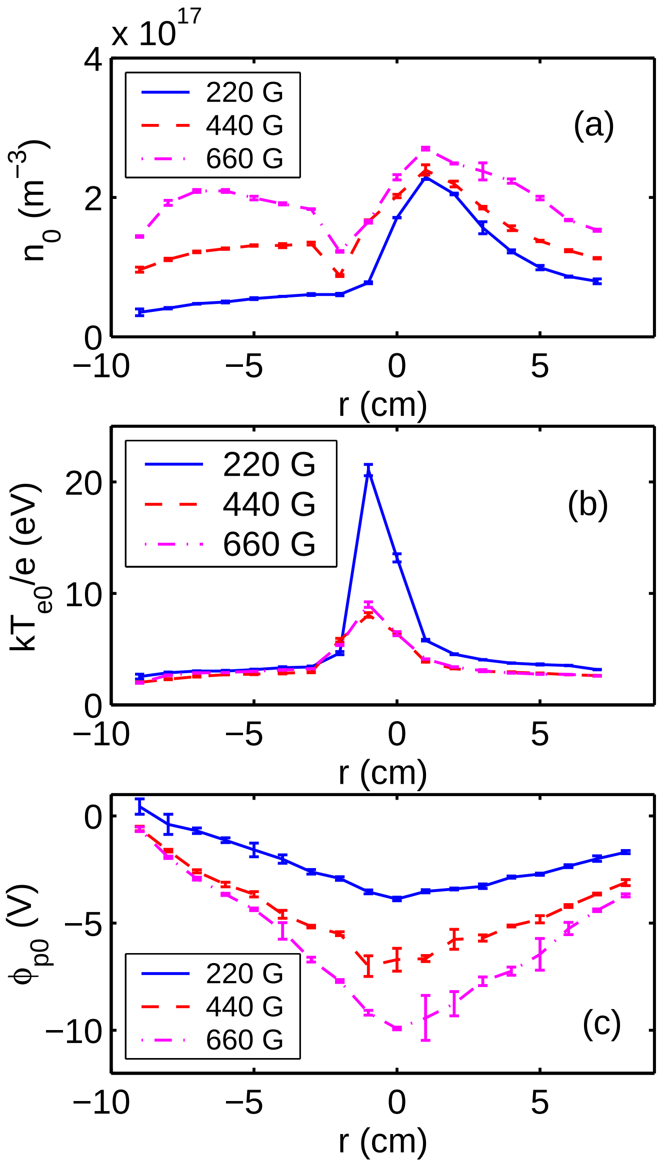

Figure 4.3: Mean radial profiles of (a) density, (b) electron temperature and (c) plasma potential for three values of B_T. The error bars obtained from the multiple measurements at each location, for n_0 and kT_{e0}/e are found to be small.

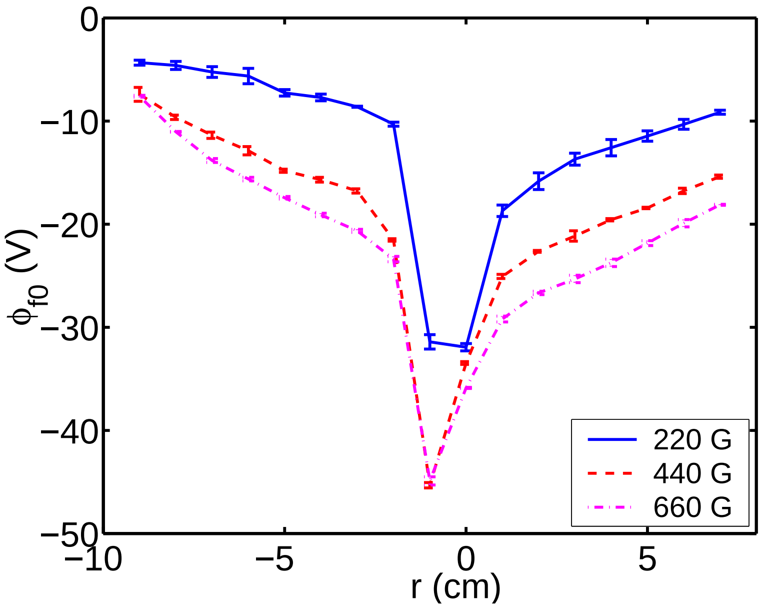

Figure 4.4: Mean radial profiles of floating potential for three values of B_T. The error bars obtained from the multiple measurements at each location are found to be small.

Away from the filament, electron temperature is comparable for all values of B_T on HFS; on LFS, kT_{e0}/e for $220\,G$ is slightly higher than that of higher B_T. At $220\,G$, close to the minor axis, kT_{e0}/e is found to be more sensitive with discharge conditions. A large peak in kT_{e0}/e close to the minor axis for all values of B_T is speculated to be due to the presence of residual fast electron population [92]. From the profile of ϕ_{p0}, it can be seen that the depth of the measured potential well increases with increase in B_T. The potential dip coincides with the filament location indicating that in a steady state condition the electrons injected by the filament result in effective negative charge which is maximum close to the minor axis. The existence of potential dip is also reflected in the ϕ_{f0} profiles shown in Fig. 4.4. The gradient in ϕ_{p0}, which is found to be consistent with the gradient in ϕ_{f0}, indicates the presence of finite mean radial electric field upto the edge of the limiter. The gradient in the mean plasma profiles acts as a free energy source, giving rise to the instabilities and consequent coherent or turbulent fluctuations. The radial profiles of relative fluctuations in I_{is} and ϕ_f, obtained in a poloidal plane are shown in Fig. 4.5. In an attempt to measure electron temperature fluctuations using TLP, fluctuations comparable to noise level are observed and hence it is

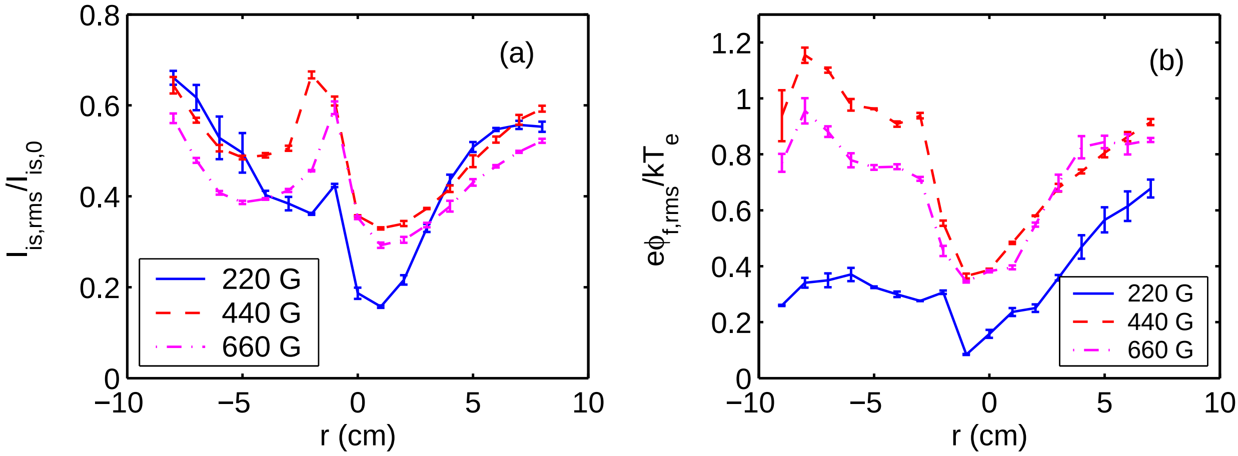

Figure 4.5: Relative *rms* fluctuation profiles of (a) ion saturation current ($I_{is,rms}/I_{is,0}$) which are equivalent of relative density fluctuations (n_{rms}/n_0) when fluctuations in T_e are small; (b) floating potential ($e\phi_{f,rms}/kT_{e0}$) for all three values of B_T are shown.

believed that fluctuations in T_e are small. With relative fluctuations in T_e being small, relative fluctuations in I_{is} are equivalent to the relative density fluctuations. Density and potential fluctuations, both have their minima at the minor axis and peak at the edges. The density fluctuations increase close to the minor axis and remain comparable or exhibit a small decrease at the edges with increase in B_T, with an extra peak appearing around $-2\,cm$ for 440 G and 660 G. The floating potential fluctuations, under low electron temperature fluctuations, represent the fluctuations in plasma potential, i.e. $\phi_{f,rms} \sim \phi_{p,rms}$. The potential fluctuations increase with increase in B_T from 220 G to 440 G throughout the radius and significantly on HFS; the potential fluctuations, on further increase in B_T to 660 G, remain comparable on LFS and decrease on HFS. Since the density and potential (or electric field) fluctuations are found to be associated with poloidal flow which further help in sustaining the mean profiles [29, 47, 93], a systematic study with varying the nature of fluctuations and consequent poloidal flows with toroidal field strength is desirable. Such a study is reported in Sec.4.5.3, Sec.4.6 and Sec.4.7.

4.5.2 Langmuir probe: I-V characteristics

The current-voltage characteristics of Langmuir probes are useful in determining typical plasma parameters, as described in Sec.2.3.1, and Sec.3.3.2. Using full I-V characteristics of a SLP, n_0 is calculated from ion saturation region and kT_{e0}/e is calculated from the transition region. Also, ϕ_{p0} is estimated from the intersection point of the exponential fit in transition region and linear fit in the electron saturation region, as demonstrated in Sec.3.3.2. This exercise is carried out for higher values of B_T, to corroborate the measurements of kT_{e0}/e, measured using TLP, and ϕ_{p0} measured using an emissive probe. The SLP is swept with a voltage range of -40 to +20 V to obtain full I-V characteristics; the voltage sweep is repeated for typically 40 number of cycles with similar rise time, to obtain smooth-averaged characteristics. The time series plots of probe voltage and current for 10 cycles are shown in Fig. 4.6 for 440 G and in Fig. 4.7 for 660 G. The full I-V charac-

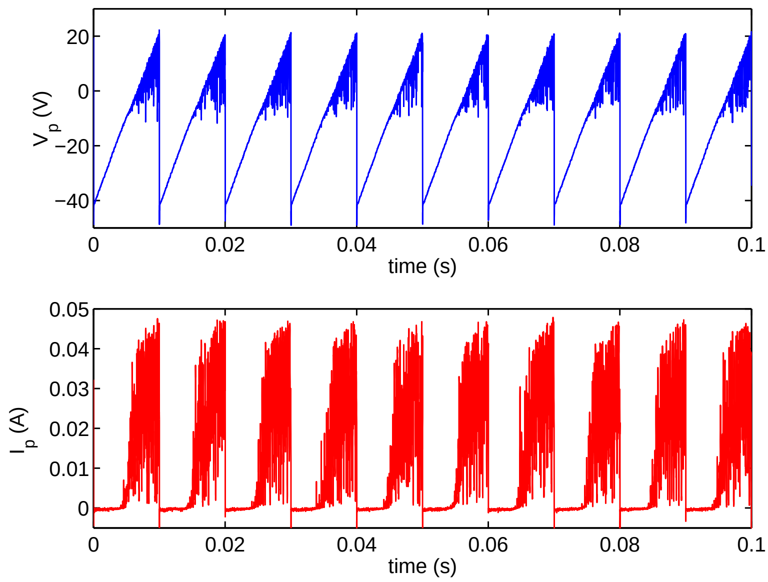

Figure 4.6: Time series of sawtooth ramp voltage (V_p) applied to a SLP, and the probe current (I_p) at 440 G. The voltage ramp-up time period is 10 ms.

teristics obtained on averaging over 40 cycles are suitably fitted with exponential function on negative side and a straight line on positive side, with respect to the knee. From the coefficient in the exponential argument, kT_{e0}/e is derived; from the intersection point, on projecting to voltage axis ϕ_{p0} is determined. The curve

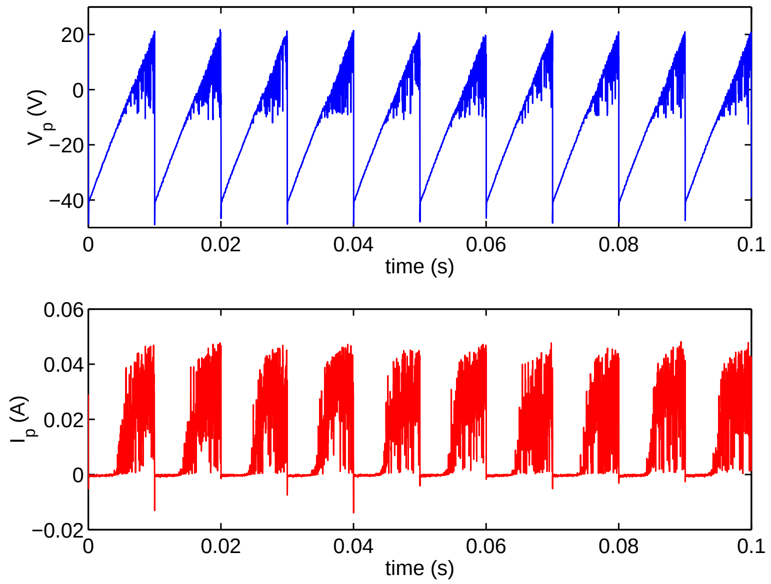

Figure 4.7: Time series of sawtooth ramp voltage (V_p) applied to a SLP, and the probe current (I_p) at 660 G. The voltage ramp-up time period is 10 ms.

fitting is illustrated in Fig. 4.8 for 440 G and in Fig. 4.9 for 660 G.

4.5.3 Poloidal flows

Mean electric field driven flow

From the radial profiles of plasma potential, directly measured using an emissive probe, mean radial electric field $\mathbf{E_0}$ is calculated in the horizontal mid-plane of the torus. The mean radial electric field is observed pointing to the minor axis which provides a $\mathbf{E_0} \times \mathbf{B}$ rotation to the plasma, referred as the mean electric field driven poloidal flow ($v_{E_0 \times B}$). The mean electric field driven flow velocity profile calculated from ϕ_{p0} profile, is shown in Fig. 4.10, for three B_T values. With increase in B_T, the mean field driven flow is observed to remain comparable on LFS; on HFS, though the mean field driven flow decreases on changing B_T from 220 G to 440 G, it remains comparable on further increase of B_T from 440 G to 660 G.

Fluctuation driven flow

The mean radial electric field leads to a mean electric field driven poloidal flow due to $\mathbf{E_0} \times \mathbf{B}$ drift, as described above, and hence a mean electric field driven

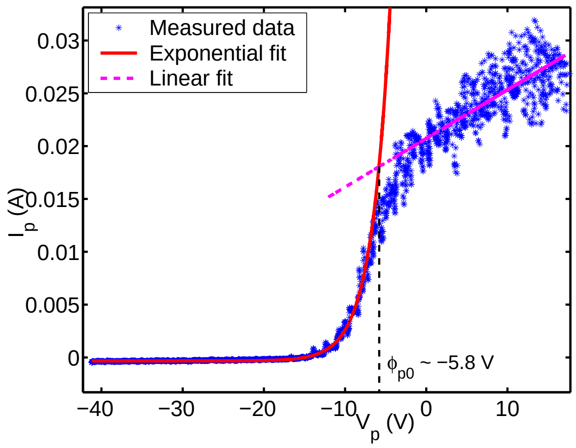

Figure 4.8: Determination of kT_{e0}/e and ϕ_{p0} from full I-V characteristics of a SLP for 440 G. Experimental data corresponds for probe at $+5\,cm$. Observing a knee around $-5\,V$, an exponential fit is done towards negative voltage side which includes ion saturation region and linear fit is done for positive voltage side. From the exponential fit $kT_{e0}/e \sim 2.3\,eV$.

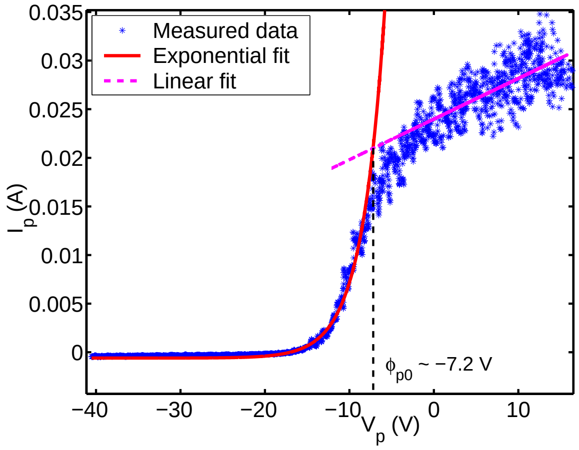

Figure 4.9: Determination of kT_{e0}/e and ϕ_{p0} from full I-V characteristics of a SLP for 660 G. Experimental data corresponds for probe at $+5\,cm$. Observing a knee around $-5\,V$, an exponential fit is done towards negative voltage side which includes ion saturation region and linear fit is done for positive voltage side. From the exponential fit $kT_{e0}/e \sim 2.7\,eV$.

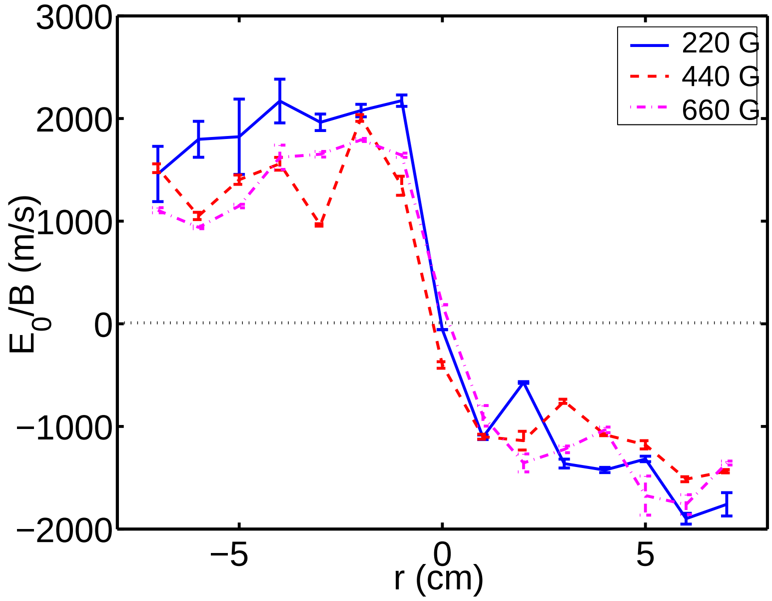

Figure 4.10: Mean electric field driven poloidal flow ($v_{E_0 \times B} = E_0/B$) profiles derived from mean plasma potential profiles, directly measured using an emissive probe. The mean electric field (E_0) is calculated using finite difference method and B indicates the local toroidal magnetic field.

poloidal flux. Similarly, the fluctuating radial electric field also can lead to a finite fluctuation induced poloidal flux depending on the relative phase between the electric field and density fluctuations. This fluctuation driven poloidal flux is found to play a vital role in the generation of self consistent flow and an "effective rotational transform", as described in Chapter 3. Fluctuation driven poloidal flux is estimated from simultaneous measurement of fluctuations in radial electric field and density using a radial array of LPs described in Sec.2.3.3, and the methodology for analysis described in Sec.3.6.2. Here onwards, Γ_{fluct} refers to $\Gamma_{fluct,pol}$, unless specified otherwise. From Γ_{fluct}, estimated using Eq.(3.1) and Eq.(3.3), an equivalent average flow velocity due to fluctuation induced flux can be defined as in Eq.(3.4). Radial profile of Γ_{fluct} is shown in Fig. 4.11 for three B_T values. Close to the minor axis Γ_{fluct} estimates are found to change by an order of magnitude, with a large peak or dip for all values of B_T; subsequent check for typical radial wavelengths shows that the wavelength become comparable to the probe separation. The approximation of measuring $\tilde{n}$ and $\tilde{E}$ at single point is, therefore, not valid. Hence Γ_{fluct} close to the minor axis are not reported. In the rest of the region, the radial

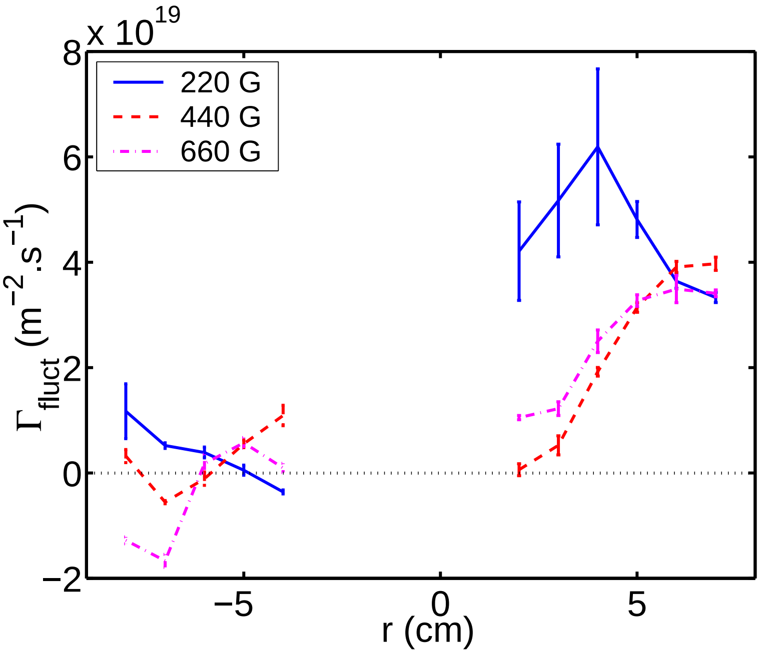

Figure 4.11: The fluctuation driven poloidal flux (Γ_{fluct}) is shown for three values of magnetic field. Here onwards, Γ_{fluct} refers to $\Gamma_{fluct,pol}$, unless specified otherwise. The HFS values are relatively smaller. Due to short wavelength nature of the fluctuations, measurements close to the minor axis are not reliable and hence not shown here.

wavelength is much larger than the probe separation, hence Γ_{fluct} estimation is valid. For all magnetic field values Γ_{fluct} is found to be small on the HFS whereas significant only on LFS. Maximum in Γ_{fluct} occurs in a region close to $+4\,cm$ for $220\,G$. As B_T is increased Γ_{fluct} is found to be reduced and the maxima occur beyond $+5\,cm$ towards the outer wall. Though the fluctuation behavior changes significantly on HFS with increase in B_T, Γ_{fluct} remains comparable. On LFS, the maximum values of Γ_{fluct} remain in the same order of magnitude with increase in B_T. From these Γ_{fluct} profiles, average fluctuation driven flow velocities estimated using Eq.(3.4) are shown in Fig. 4.13.

Net flow

Net poloidal flow or total poloidal flow velocity (v_{net}) measurements are performed either using a two electrode-Mach probe or a single electrode-DLP, as described in Sec.4.3. Mach probe is used for simultaneous measurement of $I_{is,0}$ at upstream and downstream discs. Reduced Larmor radius with increasing B_T, however, prevents one from using Mach probe at higher magnetic field, for reliable measurements. With the single tip DLP, measurements are obtained separately for upstream and downstream current on shot to shot basis. From the measured $I_{is,0}$, net flow velocity is calculated using the Eq.(3.5). For poloidal flow calculation, the calibration of α for Mach probe is discussed in detail in Sec.3.6.3, and $\alpha = 0.5$ is justified with a maximum uncertainty of 20% in the net flow measurements. At high magnetic field the net poloidal flow measurements are performed using DLP with same calibration factor $\alpha = 0.5$. The net poloidal flow velocity obtained from the I_{is} measurements, is in units of local c_s, as shown in Fig. 4.12 for three B_T values. Net poloidal flow is comparable at all B_T on LFS, but increases significantly on HFS reaching sonic speed with increase in B_T, which indicates that the system is highly compressible. Using the measured mean electron temperature profiles shown in Fig. 4.3(b), the absolute net flow velocities are calculated.

Comparative plots of mean electric field driven flow, fluctuating electric field driven flow and net flow in poloidal direction are shown in Fig. 4.13, for each B_T. A general notation v_{pol} is used for the poloidal flow on the vertical axis, on which v_{net}, $v_{E_0 \times B}$ and v_{fluct} are plotted. On LFS, the measured fluctuation driven flow,

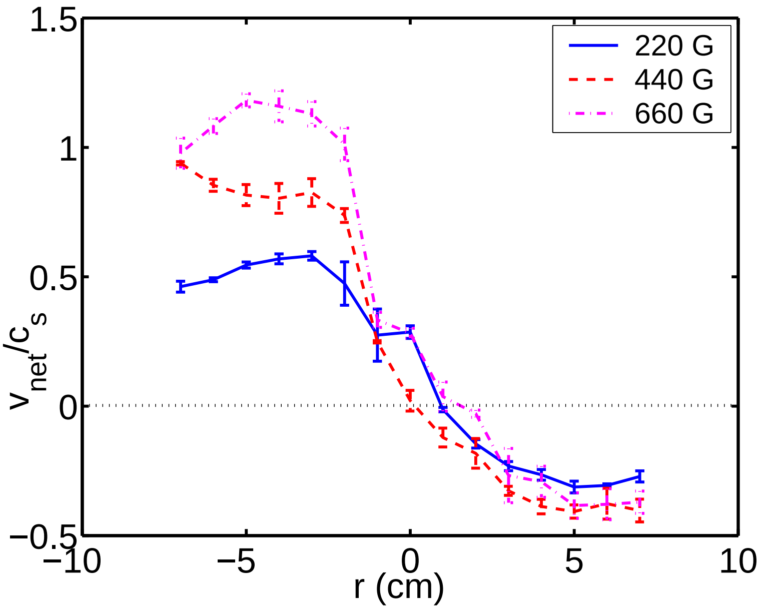

Figure 4.12: The net poloidal flow profiles using measured I_{is} at the upstream and downstream of the poloidal flow. The measurements shown for 220 G are obtained using Mach probe; for 440 G and 660 G measurements are obtained using DLP.

which decreases with increasing B_T, approximately accounts for the differences in the net flow and mean electric field driven flow, for all B_T. Further deviation close to the minor axis is due to the possible modification in the plasma potential due to presence of fast electrons. On HFS, however, the difference between net flow and mean electric field driven flow is observed to increase with increase in B_T which could not be accounted by fluctuation driven flow. Hence, another mechanism of driving a poloidal flow could exist, in addition to the mean and fluctuating electric field driven poloidal flows.

4.5.4 Fluctuation induced radial flux

In Sec.4.5.1, it has been seen that the density on HFS increases four times from 220 G to 660 G. In Sec.4.5.3, it was also seen that there is no significant increase in net poloidal flow on LFS, which could have led to the density build-up on HFS. Since the present measurements are performed in a limited radial domain, that is with in the inner diameter of the limiter, a comparison of net flux to balance for the upward and downward flux is not possible. Other possible mechanisms which

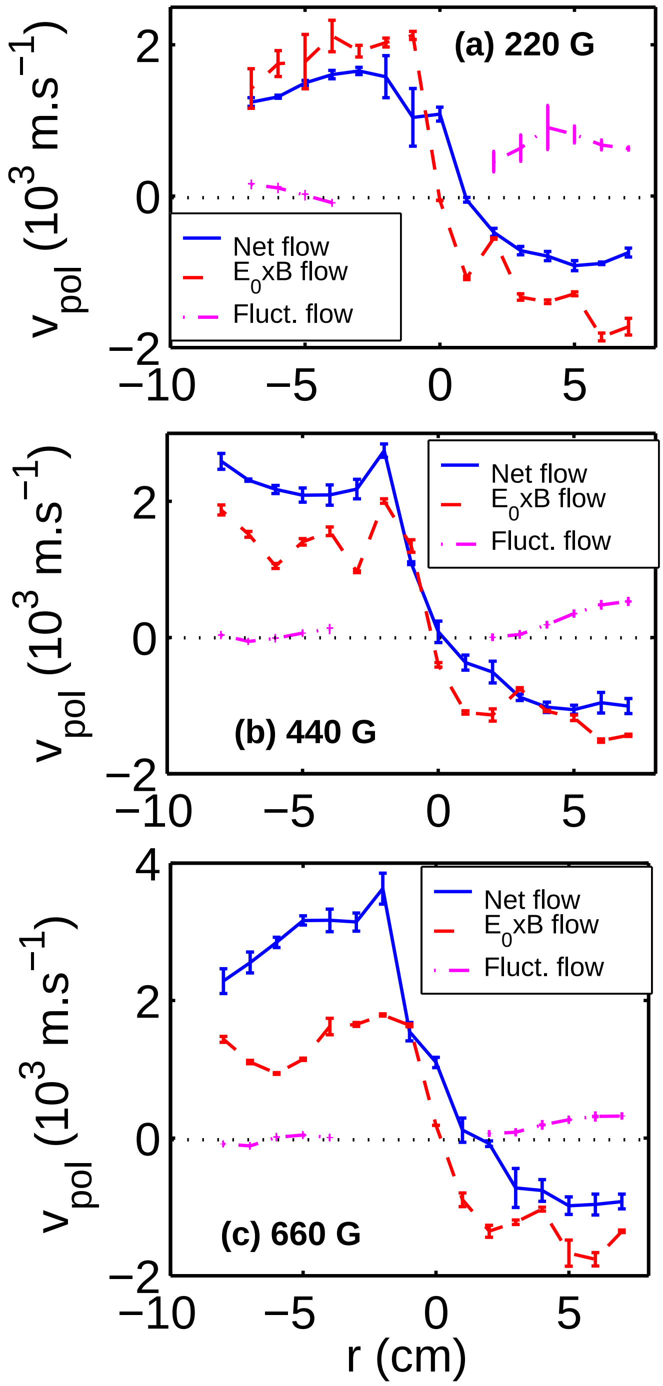

Figure 4.13: Comparative poloidal flow velocities (v_{pol}) for all three values of B_T; (a) 220 G, (b) 440 G and (c) 660 G. For each B_T value net flow is compared with mean electric field driven flow and fluctuation driven flow.

may contribute to the increase in density on HFS can be the fluctuation induced radial flux, increased ionization by primaries on HFS region or reduced loss rate of the plasma on HFS. In order to check if the fluctuation induced radial flux has a contribution in increased densities on HFS for higher values of B_T, measurements are carried out. The measurement method is similar to that described in Sec.3.6.2. The $\Gamma_{fluct,rad}$ is estimated at few radial locations, as shown in Fig. 4.14. The

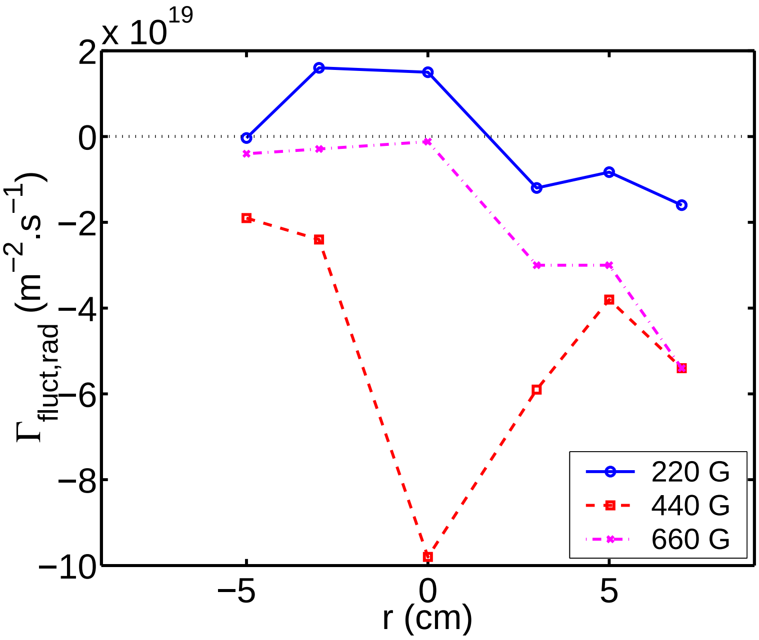

Figure 4.14: Radial profile of fluctuation induced radial flux of particles. This flux is due to the poloidal electric field fluctuations. The positive flux indicates, flux radially inwards.

positive sign of $\Gamma_{fluct,rad}$ indicates flux is radially inwards, i.e. opposite to the major radius. From Fig. 4.14, it can be seen that, only in the case of $220\,G$, the $\Gamma_{fluct,rad}$ is inwards for $-5 < r < 3\,cm$. For higher values of B_T, $\Gamma_{fluct,rad}$ is radially outward all the locations. The increase in density with B_T, therefore, cannot be explained by $\Gamma_{fluct,rad}$. Through the experimental results discussed so far in this chapter, it is established that large fluctuation and intrinsic poloidal flows are always associated with each other, at three magnetic field values used. The fluctuation-flow connection, therefore, essentially helps in sustaining mean profiles in each case. In the following, the nature of fluctuations in density and potential, associated with each magnetic field value is investigated.

4.6 Spectral characteristics

4.6.1 Linear spectral analysis

Nature of fluctuations and turbulence is characterized using spectral analysis techniques. Let x_1 and x_2 denote the time series data of density or potential, with zero mean values; $X_1(\omega)$ and $X_2(\omega)$ denote the discrete Fourier coefficients of x_1 and x_2 respectively, corresponding to the frequency ω. The auto power spectrum is defined as

$$P_{ii}(\omega) = X_i(\omega){X^*}_i(\omega), \tag{4.1}$$

where i =1 or 2 and ${X^*}_i$ indicates complex conjugate of X_i. The labels 1 and 2 correspond to time series of two different quantities, at a given location or the time series of a same physical quantity at two different locations. Then, the cross-power spectrum is defined as

$$P_{12}(\omega) = X_1(\omega){X^*}_2(\omega). \tag{4.2}$$

The coherence between fluctuations represented by time series x_1 and x_2 is given by

$$\gamma_{12}(\omega) = \frac{|P_{12}(\omega)|}{(P_{11}(\omega))^{1/2}(P_{22}(\omega))^{1/2}}, \tag{4.3}$$

and the cross-phase $\theta_{12}(\omega)$ is given by the complex argument of $P_{12}(\omega)$. For a better estimation of the auto-power or cross power coefficients, the coefficients are calculated from large number of bins in to which the time series are divided, and averaged over all bins. Each time series is divided typically in to 78 bins, each with 512 number of samples. From the Nyquist criteria, the upper cut-off in the frequency is half the sampling rate, therefore, 100 kHz. The bandwidth of the analogue filter is 35 kHz, which is well below the Nyquist frequency. Typical auto power spectra of density and potential fluctuations on HFS and LFS are shown in Fig. 4.15. At 220 G, strong coherent peaks in density fluctuations occur with a fundamental frequency of 6.5±0.4 kHz along with several harmonics, dominant compared to the background fluctuations. The fluctuation power reduces systematically for subsequent harmonics. This happens on both sides of the minor axis, i.e. HFS and LFS. Similar coherent peaks are observed in potential spectra with the same fundamental frequency. The systematic reduction in power for successive

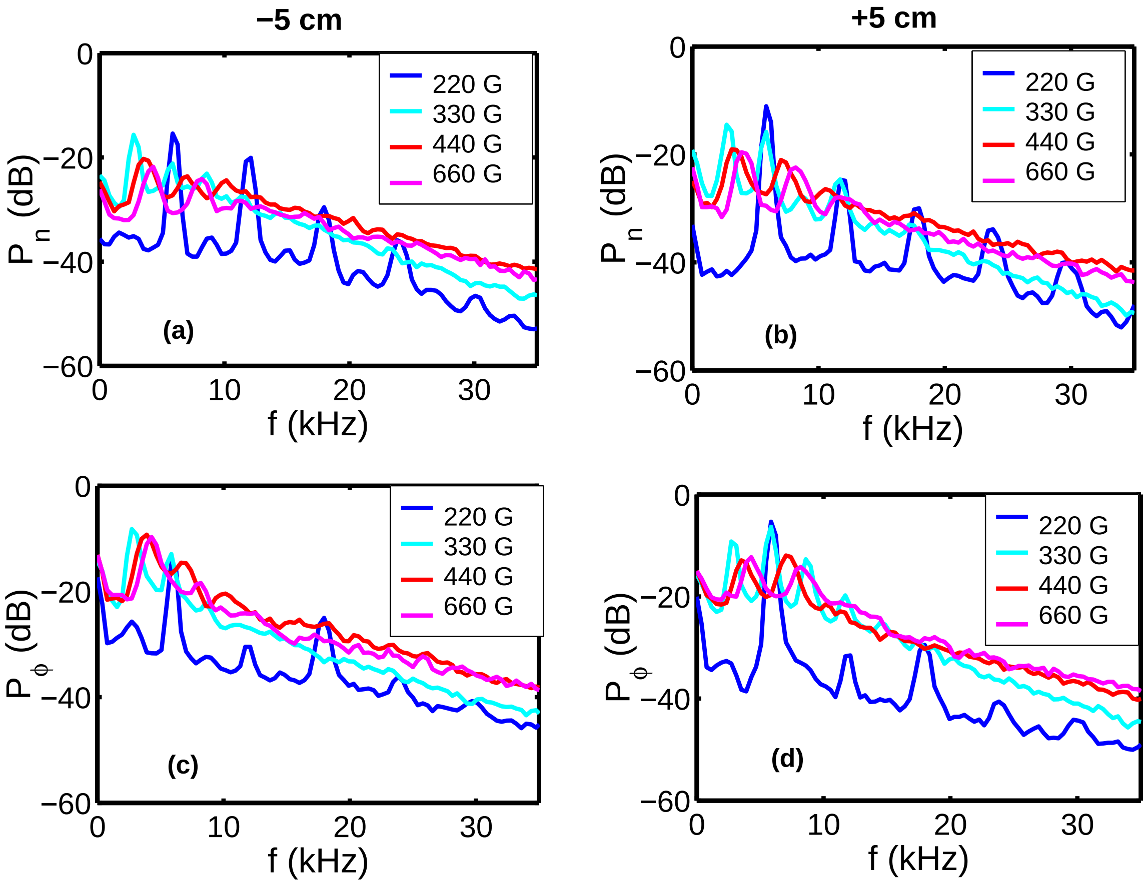

Figure 4.15: Typical density and potential auto power spectra on HFS and LFS for all the values of B_T. Frequency is indicated by f and power is indicated by P_n and P_ϕ for density and potential respectively. Figures (a) and (c) are power spectra of $\tilde{n}$ and $\tilde{\phi}$ respectively at $-5\,cm$. Similarly, (b) and (d) are for $+5\,cm$.

harmonics is, however, not observed. For example, the second harmonic in the potential spectra has similar or lower power than the third harmonic as observed at ± 5 cm. At 440 G and 660 G the background turbulence increases significantly and the peaks are broadened; third and higher harmonics disappear. Since a significant change in the nature of power spectra is observed on changing the magnetic field from 220 G to 440 G, power spectra is also obtained for 330 G as shown in Fig. 4.15, to see if there is a smooth transition. The observed power spectra for 330 G retain third and fourth harmonics at $+5\,cm$. The observed fundamental frequency at 330 G is not an intermediate value of the fundamental frequencies at 220 G and 440 G; however the dominant peak in potential fluctuations at $+5\,cm$ for 330 G coincide with the corresponding peak for 220 G as can be seen in Fig. 4.15(d). Therefore, transition from coherent to turbulent fluctuations above 220 G is rapid with increase in the magnetic field. The nature of power spectra at 330 G is, however, close to the power spectra at 440 G, for example the fundamental frequency for 330 G is 2.8 kHz. The fundamental frequency changes monotonically from 2.8 kHz at 330 G to 3.5 kHz at 440 G and 4.3 kHz at 660 G, the frequency resolution being 0.4 kHz. Interestingly, the above said gradual change in fundamental frequency is not observed to begin from 220 G. A small peak at 2.8 kHz is, however, observed at $-5\,cm$ in both density and potential spectra. The dominant frequency (6.5 kHz) at 220 G is though less than the ion cyclotron frequency (f_{ci}) in most of the bulk region, it becomes comparable to the calculated f_{ci} in the limiter's shadow. Since the measurements in the shadow region of the limiter are not performed, the relevance of this distinct frequency with plasma parameters in this region and ion cyclotron frequency, is not understood. The nature of fluctuations can be understood further by estimating the wave number and hence the dispersion characteristics.

The local wave number and frequency spectrum $S(k,\omega)$ of potential fluctuations and dispersion characteristics are estimated using the measurements obtained from two spatially separated probes and the analysis method described in Ref.[57]. The use of this analysis method is briefly described as follows. The two probes are separated by $\delta x = 4\,mm$ and aligned vertically to acquire two time series of floating potential. The time series x_1 and x_2 obtained from the probes is divided into a number of records M = 312 in total, of 512 samples each. From the argument

$(\theta^j(\omega))$ of complex cross power coefficients corresponding to j^{th} record of each time series x_1 and x_2 as defined in Eq.(4.2) and the probe separation δx, sample local wave number at a frequency ω is defined as $k^j(\omega) = \theta^j(\omega)/\delta x$. The wave numbers estimated in this way are bound to the interval $[-\pi/\delta x, \pi/\delta x]$. This wave number range is divided into N_c (even number) partitions each with a width given by $\Delta k = 2\pi/\delta x N_c$. The local wavenumber and frequency spectrum $S(k,\omega)$ is then defined as

$$S(k,\omega) = \frac{1}{M}\sum_{j=1}^{M} I_{[0,\Delta k)}[k - k^j(\omega)] \times \frac{1}{2}[P_{11}^j(\omega) + P_{22}^j(\omega)], \tag{4.4}$$

where

$$I_{[0,\Delta k)}[k - k^j(\omega)] = \begin{cases} 1 & \text{if } k \leq k^j(\omega) < k + \Delta k, \\ 0 & \text{otherwise,} \end{cases} \tag{4.5}$$

$P_{11}^j(\omega)$ and $P_{22}^j(\omega)$ indicate auto-power for frequency ω for j^{th} record at corresponding probes as defined in Eq.(4.1). The conditional spectrum is defined as

$$s(k|\omega) = \frac{S(k,\omega)}{\frac{1}{2}[P_{11}(\omega) + P_{22}(\omega)]}, \tag{4.6}$$

where $P_{11}(\omega)$ and $P_{22}(\omega)$ are frequency spectral densities or auto power spectra for two time series as defined in Eq.(4.1). The first moment of conditional spectrum is calculated as [57]

$$\bar{k}(\omega) = \sum_{m=-N_c/2+1}^{N_c/2} k_m s(k_m|\omega), \tag{4.7}$$

where $k_m = m\Delta k$; $\bar{k}(\omega)$ is the average wave number. The range of wave number that can be estimated for a given $\delta x = 4\,mm$ is $-7.8\,cm^{-1} < k_m < +7.8\,cm^{-1}$; choosing $N_c = 100$, $\Delta k \sim 0.16\,cm^{-1}$. The wave number and frequency spectral density $S(k,\omega)$ is estimated using Eq.(4.4); the conditional spectrum is estimated using Eq.(4.6). The average poloidal wave number $\bar{k}_\theta$ is estimated using Eq.(4.7) for the spectra at ± 5 cm and shown in Fig. 4.16. The poloidal wave propagation is observed to be clockwise in the plane of the limiter shown in Fig. 2.2, i.e. propagation is upwards on HFS and downwards on LFS. The fundamental frequencies

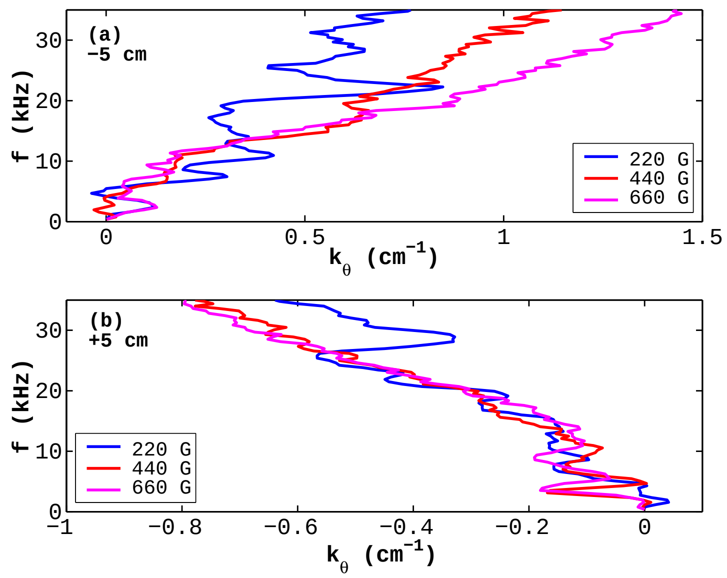

Figure 4.16: Average poloidal wave number for potential fluctuations on HFS and LFS for all values of B_T; (a) at $-5\,cm$ and (b) $+5\,cm$. The convention for the direction is such that positive k_θ indicates wave propagation upwards. The k_θ measurements at $-5\,cm$ and $+5\,cm$ indicate wave propagation in clockwise direction in the poloidal plane of limiter shown in Fig. 2.2.

and corresponding average poloidal wave numbers estimated above, will be used in the identification of instabilities in Sec.4.7.

4.6.2 Power spectra for lower B_T

In Sec.4.6.1, it has been seen that the coherent modes occurring for $220\,G$, rapidly transform into turbulent fluctuations at higher values of B_T. It is understood, therefore, that the toroidal magnetic field has a significant influence on the nature of fluctuations. It is expected for $B_T < 220\,G$ also, a significant change can occur in the power spectrum. The power spectra are, therefore, obtained for $B_T \sim 165$ G, 110 G and 55 G; the density power spectra are shown in Fig. 4.17 and potential power spectra are shown in Fig. 4.18. At $55\,G$, fluctuation are small and have no dominant modes above the turbulence. For $110\,G$, a significant peak appears with 4 kHz frequency. The fluctuations grow with coherent peaks possessing large power at $165\,G$. At $220\,G$, the power slightly reduces as compared to $165\,G$. It

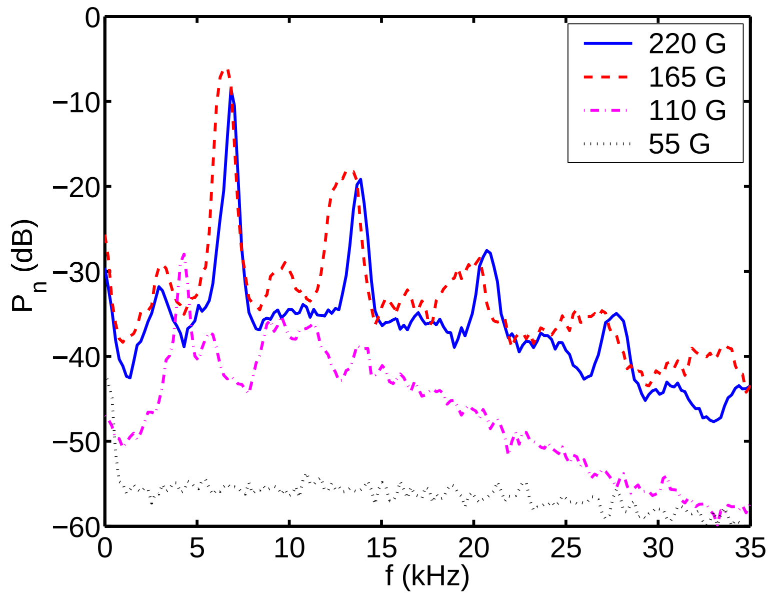

Figure 4.17: Density auto power spectra at $+5\,cm$ for lower values of B_T. Frequency is indicated by 'f'and power is indicated by P_n for density.

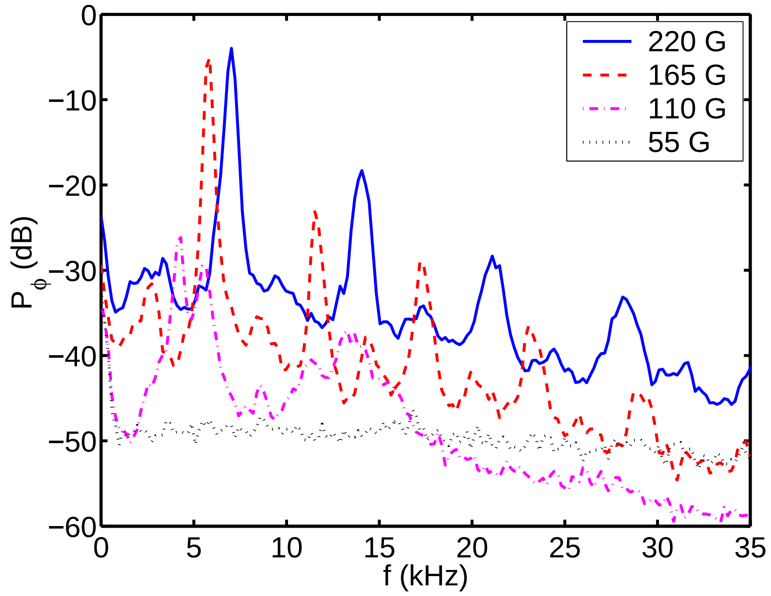

Figure 4.18: Potential auto power spectra at $+5\,cm$ for lower values of B_T. Frequency is indicated by 'f'and power is indicated by P_ϕ for potential.

appears, therefore, that a threshold occurs in B_T around $110\,G$ for the on-set of instability.

4.6.3 Bispectral analysis

The linear spectral analysis described above to obtain typical power spectra is under the assumption that fluctuation amplitude is small. In the bulk region of the plasma large fluctuations are observed, hence the underlying process can be expected to be nonlinear. The nonlinear interaction of the modes at various frequencies can generate a broad band spectrum and result in a turbulence. The nonlinear coupling of waves can be estimated from the bispectral analysis, which is a well known third order spectral technique [58]. This technique can be useful to discriminate between nonlinearly coupled waves and the spontaneously excited independent waves in a self-excited fluctuation spectrum. The squared bicoherence $b^2(\omega_1, \omega_2)$ of two frequencies ω_1 and ω_2 which measures the fraction of power in a given spectral band due to the quadratic coupling, is defined as

$$b^2(\omega_1, \omega_2) = \frac{|\frac{1}{M}\sum_{i=1}^{M} X_1^i(\omega_1)X_1^i(\omega_2)X_1^{i*}(\omega_1+\omega_2)|^2}{(\frac{1}{M}\sum_{i=1}^{M}|X_1^i(\omega_1)X_1^i(\omega_2)|^2)(\frac{1}{M}\sum_{i=1}^{M}|X_1^i(\omega_1+\omega_2)|^2)}, \tag{4.8}$$

where M is the total number of records. The statistical significance level for $b^2(\omega_1, \omega_2)$ is given by 1/M [59]. If $b^2(\omega_1, \omega_2) = 1$, then it implies that the entire power at frequency $\omega_1 + \omega_2$ is due to the nonlinear interaction of modes at ω_1 and ω_2. A value less than 1 indicates that the power at $\omega_1 + \omega_2$ is only partly due to the interaction of modes at ω_1 and ω_2. The calculation of squared bicoherence b^2 over the entire power spectrum is performed for all the values of B_T. The plots of bicoherence for fluctuations in I_{is} at $-5\,cm$ are shown in Fig. 4.19, where $f_i = \omega_i/2\pi$. Maximum values for b^2 are observed in the case of $220\,G$, with $b^2_{max} \approx 0.93$ for second harmonic; the fundamental frequency being 6.5 kHz. For the third harmonic, the squared bicoherence is found to be $b^2 \approx 0.86$. For higher magnetic fields, b^2 reduces sharply and $b^2_{max} \approx 0.2$. This value is still much above the statistical significance level in $b^2(\omega_1, \omega_2)$ which is 0.003 for our value of $\mathrm{M} = 312$. Hence, at higher magnetic fields there is a relatively weak but nontrivial coupling; though the bicoherence for harmonics is reduced, it relatively increases for other frequencies in the background turbulence. Bicoherence plots for the fluctuations in

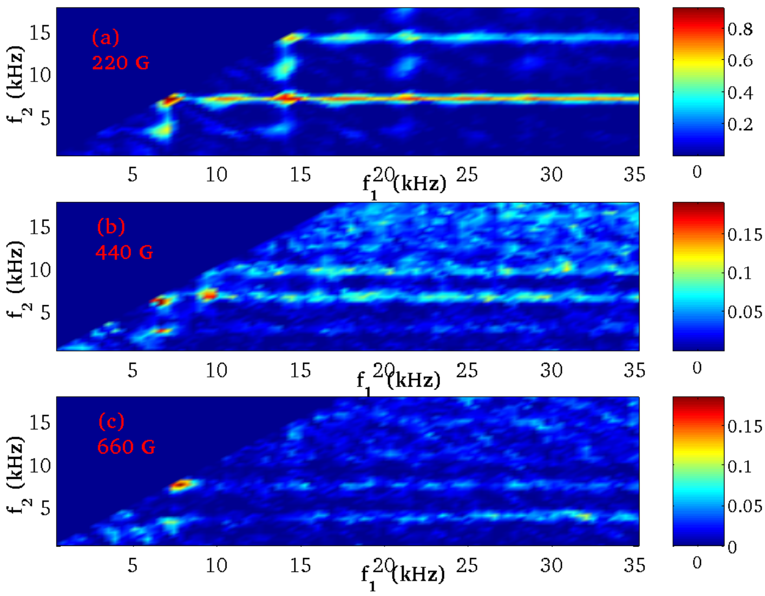

Figure 4.19: Squared bicoherence for fluctuations in I_{is} at all values of B_T; (a) 220 G, (b) 440 G and (c) 660 G. Since the analog bandwidth is 35 kHz, the frequencies beyond this are not shown though the Nyquist frequency is 100 kHz. The statistical significance level for $b^2(\omega_1, \omega_2)$ is defined by $1/\mathrm{M} \approx 0.003$.

ϕ_f at $-5\,cm$ are shown in Fig. 4.20. Similar to the fluctuations in I_{is}, maximum of bicoherence is found in the case of 220 G, which sharply decreases with increasing magnetic field. The increased bicoherence for the small amplitude fluctuations at 440 G and 660 G in the background turbulence, indicates an increased nonlinear coupling between them and hence the generation of turbulence. In the following we attempt to find the underlying source of instabilities responsible for the observed fluctuations.

4.7 Identification of instabilities

In order to identify the instabilities responsible for the observed fluctuations in plasma parameters, the calculation of real frequencies, dispersion relation and comparison with theoretical model is a useful technique. Experimental determination of the parallel wave number ($k_{\parallel}$) is a reliable method to identify the type of instability since this will clearly distinguish between drift or flute kind of instabilities.

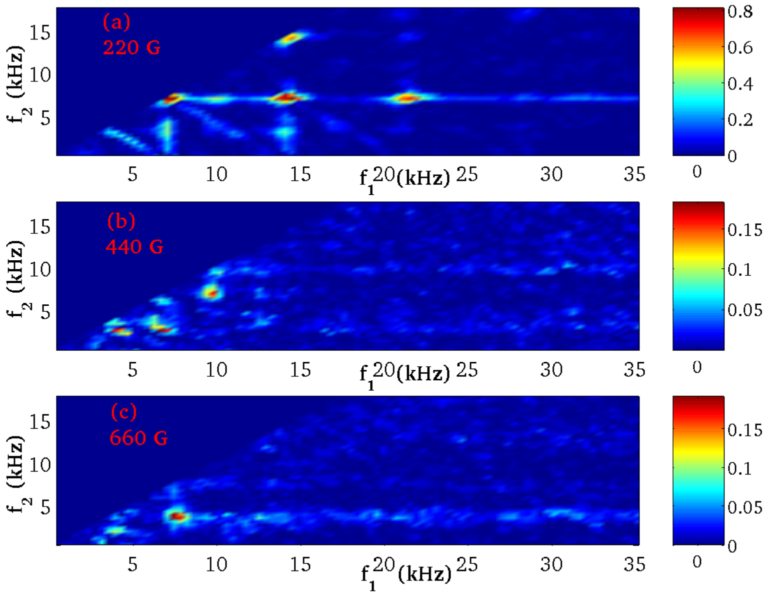

Figure 4.20: Squared bicoherence for fluctuations in ϕ_f at all values of B_T; (a) 220 G, (b) 440 G and (c) 660 G. Since the analog bandwidth is 35 kHz, the frequencies beyond this are not shown though the Nyquist frequency is 100 kHz. The statistical significance level for $b^2(\omega_1, \omega_2)$ is defined by 1/M $\approx$ 0.003.

In toroidal geometry, however, accurate alignment of two probes on a single magnetic field line is a difficult task; misalignment of the probes to estimate $k_{\parallel}$ will result in measurement of projection of $k_{\perp}$. Such carefully performed measurements have been reported in the past in TORPEX experiments [56, 95], with use of sophisticated alignment for the probes. At present vertical arrays of probes, which can be placed with a reasonably good precision in two poloidal planes far apart, are not available in our experimental apparatus. In the following we use an alternate method to identify the instabilities. The cross-phase and coherence between density and potential fluctuations estimated from experimental measurements are compared with the theoretically predicted values [20, 60, 56]. From the analytical expression, instability growth rate is estimated using the experimentally derived profiles of plasma parameters. In the following, it will be shown that the coherence and cross-phase vary significantly on changing the magnetic field from 220 G to 440 G; further increase in magnetic field from 440 G to 660 G do not show a significant variation. The fluctuations at 220 G are in coherent regime; at 440 G

and 660 G, the fluctuations are in turbulent regime.

4.7.1 Fluctuations at 220 G - Coherent regime

The cross-phase and coherence of dominant peaks in Fig. 4.15 in density and potential fluctuation spectra are calculated using simultaneously obtained density and floating potential measurements by Langmuir probes separated by 5 mm. The radial profiles of the cross-phase and coherence are shown in Fig. 4.21. At 220 G,

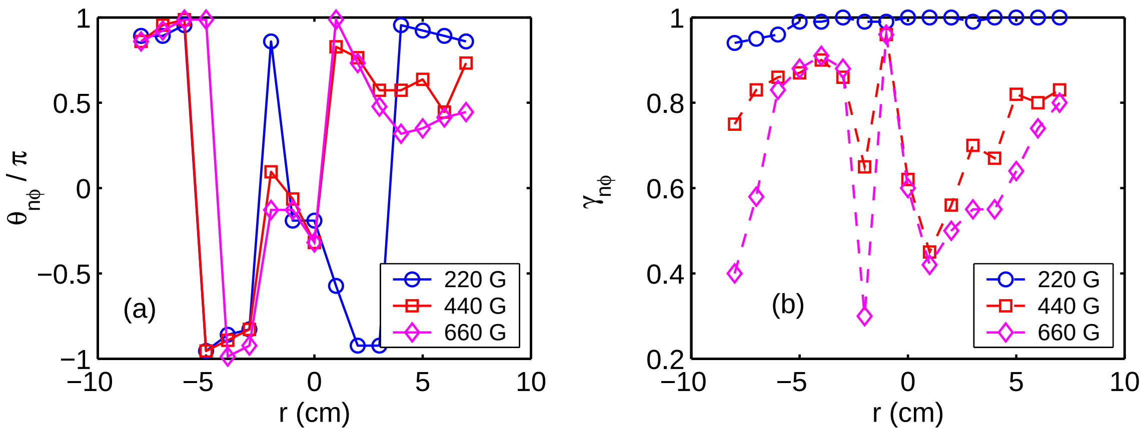

Figure 4.21: Profiles of (a) cross-phase ($\theta_{n\phi}$) and (b) coherence ($\gamma_{n\phi}$) of density and potential fluctuations for all values of B_T. The values shown correspond to the dominant peaks in the corresponding frequency spectra.

the cross-phase $\theta_{n\phi} \approx \pm 0.9\pi$ throughout the radial profile except close to the minor axis. The abrupt jump in $\theta_{n\phi}$ from positive to negative or vice versa when $|\theta_{n\phi}| \approx \pi$, do not indicate any significant change in the nature of the fluctuations. It rather indicates a well known convention namely a small lag or lead in the fluctuations from being exactly out of phase. A large deviation in $\theta_{n\phi}$ from $\pm\pi$ for measurements close to the minor axis can be either due to (i) the wavelength (not shown here) being comparable to the probe separation or (ii) change in the nature of fluctuations itself. We believe that the above indicated deviation is due to wavelengths becoming comparable to the probe separation at locations close to the minor axis. The fluctuations at 220 G have coherence $\gamma_{n\phi} \approx 1$, over the entire radial profile. Though the fluctuations are highly coherent with large amplitude, the fluctuation induced poloidal particle flux corresponding to 220 G as shown in

Fig. 4.11 is found to be small due to $\theta_{n\phi} \approx \pm 0.9\pi$ [54].

The observed cross-phase and coherence indicates that the fluctuations are of flute kind. The density gradient and effective gravity which is the centrifugal force, are anti-parallel to each other as can be seen from Fig. 4.3(a); hence favorable for the growth of R-T driven instability on LFS which is a flute mode. In the past, using low-frequency fluid equations, and comparison with a Q-machine plasma column, properties of various instabilities have been studied by Jassby [96]. From the above work by Jassby, it has been found that the electron continuity and momentum equations give the density fluctuations in terms of potential fluctuations. The ratio $(e\tilde{\phi}/kT_e)/(\tilde{n}/n_0)$ is found to be characteristic of the instabilities; for Kelvin-Helmholtz instability $(e\tilde{\phi}/kT_e)/(\tilde{n}/n_0) \gg 1$, for Centrifugal instability $(e\tilde{\phi}/kT_e)/(\tilde{n}/n_0) \geq 1$ and for resistive drift instability $(e\tilde{\phi}/kT_e)/(\tilde{n}/n_0) \leq 1$. For fluctuations which are due to R-T instability, in general $e\tilde{\phi}/kT_e \geq \tilde{n}/n_0$ [20, 46]. From the measurement of relative fluctuations shown in Fig. 4.5, the ratio of potential and density fluctuations is obtained and shown in Fig. 4.22. On LFS it is

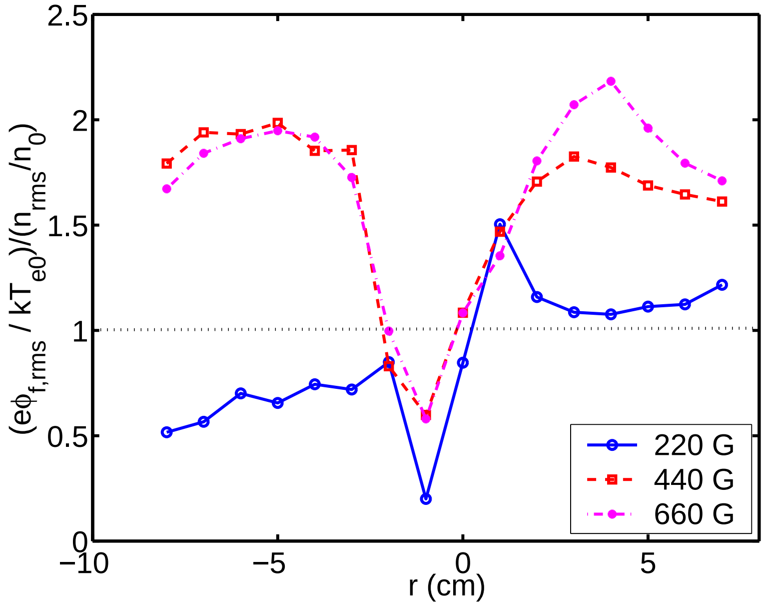

Figure 4.22: Ratio of relative potential and density fluctuations. The potential fluctuations are those obtained from the floating potential fluctuations. The *rms* indicate the root mean square of fluctuations.

observed that $(e\tilde{\phi}/kT_e)/(\tilde{n}/n_0) \geq 1$. From the power spectrum shown in Fig. 4.15, observed fundamental frequency f is 6.5 kHz, which is same for the entire radial domain. The Doppler shifted frequency ω_1 $(= \omega - \bar{k}_\theta v_{E_0\times B})$ can be calculated from the frequency in lab frame (ω), poloidal wave number ($\bar{k}_\theta$) and the $\mathbf{E_0} \times \mathbf{B}$ velocity ($v_{E_0\times B}$) of the plasma. From the experimentally estimated $\bar{k}_\theta \sim 16m^{-1}$ and $v_{E_0\times B} \sim 1700ms^{-1}$ at $+5\,cm$, $\bar{k}_\theta v_{E_0\times B}/2\pi \sim 4.3kHz$, whereas the observed lab frequency is 6.5 ± 0.4 kHz. The Doppler shifted frequency is small compared to the lab frequency. Hence, the observed lab frequency is believed to be the Doppler shift itself. Similar observations are reported from other simple toroidal devices [64]. Hence the fluctuations observed on LFS, which are of flute kind as seen from the measured cross-phase and relative fluctuations, are driven by R-T instability.

On HFS observed fluctuations are of same frequencies as on LFS as can be seen from Fig. 4.15, with high coherence and approximately out of phase density and potential fluctuations, that is $\theta_{n\phi} \approx \pm 0.9\pi$ as shown in Fig. 4.21. Hence the fluctuations on HFS seems to be of flute kind, however the ratio of potential and density fluctuations goes below 1. The density gradient is parallel to the effective gravity in this region as can be seen from Fig. 4.3(a), which is not favorable for the growth of R-T mode. A possible source of flute mode on HFS is velocity shear driven Kelvin-Helmholtz (K-H) instability. Analytical estimates of growth rates with velocity shear is, however, possible only for special forms of the density and velocity profiles. For example in Ref.[10], to find a simple solution, it is assumed that density and angular flow velocity are constant in two regions but make a discontinuous jump at an interface r $= r_s$, the radial distance from center of rotation. The two regions on either side of the step profile are labelled as 1,2 with corresponding densities N_1 and N_2; corresponding velocities v_1 and v_2 such that $N_1 > N_2$ and $v_1 < v_2$. Defining $\alpha_{1,2} = N_{1,2}/(N_1 + N_2)$, $\omega_{1,2} = v_{1,2}/r_s$, $\gamma_{KH} = (1/2r_s^2)(kT_i/eB)$ with ion temperature T_i, the imaginary part of the frequency or growth rate for a mode number m, is given by [10, 61]

$$[Im(\omega)]^2 = -[(m-1)\alpha_1\omega_1 + (m+1)\alpha_2\omega_2 + \gamma_{KH}(m^2-1)(\alpha_2-\alpha_1)]^2 + m(m-1)\alpha_1\omega_1^2 + m(m+1)\alpha_2\omega_2^2 + \gamma_{KH}m(m^2-1)(\omega_1+\omega_2)(\alpha_2-\alpha_1). \quad (4.9)$$

With the observed large gradients in density and net flow velocity in the region $-3\,cm < r < 0\,cm$, approximate step profiles exist, similar to the profiles described above. K-H instability is, therefore expected to grow close to the shear layer in the above said region where the magnetic field can be considered to be uniform. Observing $r = -2\,cm$ as the point of discontinuity, region towards LFS is labelled as region 1 and region towards HFS is labelled as region 2. The step nature of the density and net poloidal flow velocity are illustrated in Fig. 4.23 and Fig. 4.24 respectively. The corresponding densities for region 1 and 2 from Fig. 4.3(a) are

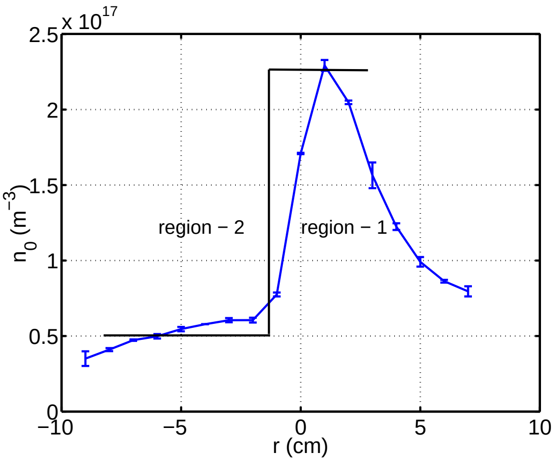

Figure 4.23: In the theoretical calculations a step kind of profile as illustrated from the radial profile of measured density profile, for 220 G is used.

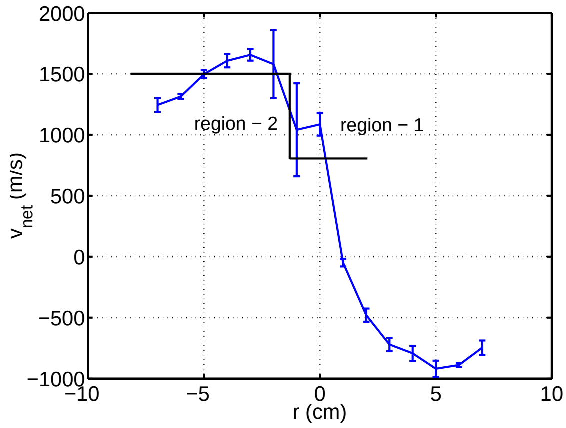

Figure 4.24: In the theoretical calculations a step kind of profile as illustrated from the radial profile of measured net flow velocity, for 220 G is used

$2.3 \times 10^{17} m^{-3}$, $0.5 \times 10^{17} m^{-3}$ respectively; corresponding absolute velocities calculated from net poloidal flow in Fig. 4.12 and Fig. 4.3(b) are $800 ms^{-1}$, $1500 ms^{-1}$ for region 1 and 2 respectively. The center of rotation of plasma is at $r = +1\,cm$ as shown in Fig. 4.12. Using $m = 1$, the estimated growth rate for K-H instability is $4 \times 10^{3} s^{-1}$. The observed flute mode, however is seen to be in the entire radial domain extending upto the limiter's edge on HFS. Hence this argument alone is not sufficient to explain the entire fluctuation behavior. Another possible source of observed fluctuations on HFS is that the fluctuations which are generated on LFS, get convected to HFS due to poloidal flow in the plasma.

4.7.2 Fluctuations at $440\,G$ and $660\,G$ - Turbulent regime

At higher values of B_T that is $440\,G$ and $660\,G$, on LFS the cross-phase $\theta_{n\phi}$ for the dominant peak above the turbulence background, significantly deviates from $\pm\pi$ as shown in Fig. 4.21(a). The coherence $\gamma_{n\phi}$ is reduced throughout the radius; on LFS, the maximum coherence $\gamma_{n\phi,max} \sim 0.85$ at the limiter's edge as shown in Fig. 4.21(b), for both $440\,G$ and $660\,G$. This behavior on LFS with increasing magnetic field indicates a progressive deviation from flute nature of the coherent fluctuations observed at $220\,G$. From the measured plasma parameters at $440\,G$ and $660\,G$, suitable conditions for other possible instabilities that are likely to exist on LFS are examined. These instabilities include Simon Hoh (SH), Modified Simon Hoh (MSH), drift resistive instability and resistive Rayleigh Taylor modes. An essential condition for the growth of SH and MSH is $\mathbf{E}.\nabla n > 0$ which is satisfied in LFS region. Simon Hoh instability which exists in a collisional, magnetized plasma due to unequal drift velocities of ions and electrons in poloidal direction, can lead to the growth of poloidal perturbations [97, 98]. Simon Hoh instability is less likely to occur since the ion-neutral collision frequency ($\approx 10^3 s^{-1}$) is an order less than the ion gyro-frequency ($\approx 10^4 s^{-1}$) and hence the observed plasma is a collision less plasma. Modified Simon Hoh instability can occur in collision less plasma due to substantial difference in the Larmor radii of ions and electrons, with a real frequency intermediate to the electron and ion cyclotron frequencies [99]. However, observed frequencies are much smaller than ion and electron cyclotron frequencies. The theoretical growth rate calculations for SH and MSH instabilities [100], indicate that the growth rate decreases with increase in B_T and there is no threshold on B_T for the excitation of these modes. Our experimental observations, however, indicate that these fluctuations which are observed at high values of B_T are found to have a threshold value of B_T for their excitation. Hence SH and MSH are less likely to be the source of fluctuations at high magnetic field.

Another possible source of the observed fluctuations on LFS with cross-phase comparable to that of experimentally measured, is drift resistive instability. The essential condition for the growth of this instability is finite fluctuations in T_e [100]; as discussed in Sec.4.5.1, fluctuations in T_e are comparable to noise level and hence believed to be small. Also theoretical calculations [100] show that the potential fluctuations scale with B_T, that is they would increase with B_T. However in our experiments we find that as B_T is increased from 440 G to 660 G, the potential fluctuations decrease as shown in Fig. 4.5(b). Hence the drift resistive is also less likely the source of fluctuations. The observed cross-phase values are close to the theoretically predicted values for resistive R-T instabilities [100]. Hence on LFS, the fluctuations which are R-T unstable and are flute like at 220 G, deviate from flute nature; possibly the fluctuations become resistive R-T type with increase in magnetic field. For 440 G, the dominant frequency observed is 3.5±0.4 kHz; Doppler shift at +5 cm corresponding to 440 G, with $\bar{k}_\theta \sim 17m^{-1}$ and $v_{E_0\times B} \sim 1600ms^{-1}$, is $\bar{k}_\theta v_{E_0\times B}/2\pi = 4.3$ kHz. At +5 cm for 660 G, $\bar{k}_\theta \sim 18m^{-1}$ and $v_{E_0\times B} \sim 1700ms^{-1}$, the Doppler shift is $\bar{k}_\theta v_{E_0\times B}/2\pi = 4.8$ kHz. These frequencies are in agreement with the observed lab frequencies with in the uncertainty in $\bar{k}_\theta$ estimation.

On HFS on the other hand, for high values of B_T, the cross-phase $\theta_{n\phi}$ for the dominant peak remains close to π as shown in Fig. 4.21(a); the maximum of $\gamma_{n\phi}$ is 0.9 at r = -4 cm, which is relatively larger than the $\gamma_{n\phi}$ on LFS as shown in Fig. 4.21(b). These observations indicate that flute mode persist on HFS, even for 440 G and 660 G though the fluctuations on LFS are not of flute kind. These flute modes may have originated on the HFS since the observed coherence is maximum in this region. In order to find the origin of flute like fluctuations on HFS, possible conditions are discussed as follows. In the case of 440 G, the density gradient which is parallel to effective gravity on HFS is not favorable for the growth of R-T instability. However, the flute modes are observed for both 440 G and 660 G with comparable frequencies, extending in the same spatial region. Since a velocity shear is observed in this region with varying density profile for both magnetic field values, these flute modes can be attributed to the K-H instability. The relative potential fluctuations shown in Fig. 4.5(b) are larger at 440 G and 660 G compared to those at 220 G; as can be seen from Fig. 4.22, the ratio of potential and density fluctuations $(e\tilde{\phi}/kT_e)/(\tilde{n}/n_0) \approx 2$. This trend observed on HFS is in favor of existence of velocity shear driven K-H instability. Calculations similar to the 220 G case, using the measured densities and flow velocities in the two regions separated by $r = -2\,cm$, show growth rates of $5 \times 10^3 s^{-1}$ and $6 \times 10^3 s^{-1}$ for 440 G and 660 G respectively for the K-H instability. Though the velocity shear is strong at $r = -2\,cm$, turbulence is seen through out the HFS region. A summary of the dominant mechanism of the instabilities is tabulated as shown in Tab.4.2.

B_T	HFS	LFS
220 G	K-H/Convection from LFS	R-T
440 G	K-H	resistive R-T
660 G	K-H	resistive R-T

Table 4.2: A tabular summary of the dominant instabilities on HFS and LFS for each value of B_T.

4.8 Summary

In a simple toroidal plasma, varying the toroidal magnetic field, study of transition in fluctuations from highly coherent regime to a turbulent regime is performed and corresponding poloidal flows are estimated. Measured mean density profiles have indicated a significant density build-up on HFS with increasing magnetic field; the mean density on HFS goes up by 3-4 times with increase from 220 G to 660 G. The increased density on HFS is accompanied by the enhanced net poloidal flow in this region. On LFS, negligible changes are observed in the absolute net poloidal flow with increase in magnetic field. The density on LFS, however, goes up by 2 times on increasing the magnetic field from 220 G to 660 G, thus increasing the particle flux poloidally from the LFS region. The observed significant increase in density on HFS can be due to the increased poloidal flux from the LFS region. Whether or not this increased poloidal flux is sufficient to explain the increased density on HFS, is not addressed quantitatively in the present work. The poloidal flows are found to be self-consistently generated. Though there is a transition from coherent to turbulent regime with increasing magnetic field, the fluctuation driven poloidal flux remains comparable on the LFS. On the HFS, the observed difference between the measured net flow and the mean flow derived from measured plasma potential profile could not be accounted for by the measured fluctuation driven flow. The differences may, therefore, be attributed to the presence of another flow mechanism which is not addressed here. From the density mean profiles, the density gradient remains comparable on the LFS whereas interesting features such as change in the direction of the density gradient occur locally on the HFS with increasing magnetic field. The change in the ratio of relative potential and density fluctuations with increasing magnetic field give a signature of a possible change in the nature of fluctuations and hence the turbulence.

Radial profiles of cross-phase $\theta_{n\phi}$ indicate the existence of flute like fluctuations on HFS at all the three magnetic field values, that is B_T=220 G, 440 G and 660 G. At 220 G, the out of phase fluctuations in n and ϕ through out the radial profile, except close to the minor axis, are due to a highly coherent flute mode. The observed flute mode is due to R-T instability on LFS; the same flute mode may be convected to the HFS with poloidal plasma flow. Generation of flute like fluctuations at 220 G on HFS, due to velocity shear driven K-H instability, however, can not be ruled out. At 440 G and 660 G, the fluctuations appear more turbulent, which is evident from the typical power spectra on both LFS and HFS. The cross-phase of density and potential fluctuations becomes comparable or less than $\pi/2$ on LFS with reduced coherence, which may be attributed due to resistive R-T mode. Hence the LFS fluctuations which are flute type due to R-T mode at 220 G deviate from flute nature with increasing magnetic field and possibly become resistive R-T mode fluctuations. Though the fluctuations on HFS at 220 G can be attributed due to convection of the flute mode from LFS, at 440 G and 660 G the flute like fluctuations do not exist on LFS which could have been convected to HFS similarly. The fluctuation on HFS, therefore, are due to K-H instability. Hence it is understood that at 440 G and 660 G, with a strong background turbulence throughout the radius, there exist a mode which is K-H unstable on the HFS and possibly resistive R-T kind on the LFS.

In summary, with increase in magnetic field in a simple toroidal plasma, a transition from coherent to turbulent regime in plasma parameters is observed. This transition is found to be accompanied by the enhanced poloidal flow in the plasma and improved densities. Characterization of the fluctuations under various conditions is performed by digital spectral analysis. Using linear spectral analysis, fluctuation spectra and poloidal wave numbers are estimated. From the cross spectral analysis and growth rate calculations, the most possible mechanisms of instabilities are discussed. Hence in a simple toroidal compressible plasma, the study of nature of fluctuations, transition to turbulence and associated poloidal flows with a toroidal magnetic field as a control parameter is carried out. The increased densities by several factors reported in this work demonstrates that an intimate relationship exists between the fluctuations, self consistently generated poloidal flows and enhanced confinement. The major findings presented in this chapter have been published in **(T. S. Goud et al) Phys. Plasmas 19, 032307 (2012)**.

Varying B_T as a control parameter to change the nature of fluctuations, and investigate consequent poloidal flows and mean profiles, it has been elucidated that fluctuation induced flow plays the role of "effective rotational transform" under varying turbulent conditions. The role of ion mass as another important parameter in the fluctuation induced "effective rotational transform", is investigated, and the results are presented in the next chapter.

5

Role of ion mass in fluctuations and intrinsic poloidal flows

5.1 Introduction

Generation of significant poloidal flows in a simple toroidal plasma, which exist only when the fluctuations induced poloidal flux is finite, has been the most important conclusion of the experimental results in Chapter 3. In addition to this, observation of enhanced poloidal flows and improved confinement with transition from coherent to turbulence on increasing toroidal magnetic field, has been the successive conclusion from the experimental results in Chapter 4. Another important parameter, which can possibly influence the fluctuations and poloidal transport in a simple toroidal plasma is the ion mass. In general, in simulations for investigating transport properties of ion temperature gradient instabilities in tokamak, using the isotopes of Hydrogen, ion thermal diffusivity is found to decrease with mass [101]. In the above work it was also found that a lighter isotope involves more unstable modes with a higher level of fluctuations than that of a heavier one. It is understood from the theoretical arguments, that in a tokamak, the confinement degrades with increase in ion mass [63]. The experimental observations on DIII-D tokamak, however, have shown that the confinement increases with increase in ion mass. No robust theory exist for the isotope scaling of tokamak experiments. In the present work, study of change in the nature of turbulence and transport with a wide range of ion mass, has been carried out in a simple toroidal device. Though the tokamak plasmas are limited to lighter atomic masses, the present study of mass scaling may throw light in understanding the interplay of isotope effect and flow dynamics.

In TORPEX experiments, blobs are seen to be generated from radially elongated interchange modes, which are responsible for the intermittent cross-field transport [35, 36]. By varying the ion mass, the blob size was observed to change which in turn changes the cross-field propagation velocity of the blob [39, 102]. In another set of experimental observations in TORPEX plasma, blobs were also observed in drift-interchange dominated regime [37]. The transition from ideal interchange mode to drift-interchange mode is achieved by reducing the helical pitch of the toroidal magnetic field lines [40]. The above transition is found to occur at the same helical pitch for hydrogen, helium and argon plasmas, though the dominant frequencies were different. The change in the dominant frequency is attributed to change in $\mathbf{E} \times \mathbf{B}$ rotation velocity, induced by the potential well. The depth of the potential well is found to depend on ion mass as seen from the Pedersen conductivity [33]. Changing the ion mass, the poloidal drift velocity of the plasma can therefore change. In a recently built simple toroidal device LATE, the current flowing to the upper and lower parts of the limiter and device panels due to particle drifts are explicitly measured in hydrogen plasma [22]. In subsequent experiments on LATE, plasma profiles for different species such as helium, neon, argon have been obtained and compared to investigate the role of ion [62].

In the present work we report the experimental observations of mean profiles of plasma parameters, fluctuations and associated poloidal flows in a simple toroidal plasma, produced using various inert gases under similar discharge conditions. A change in the nature of fluctuations, accompanied by variations in poloidal flows and mean profiles with increase in ion mass is investigated. An attempt is made to identify the instability mechanisms responsible for the observed fluctuations in each case.

5.2 Operating conditions

1. Filament current $I_f \sim 142\ A$

2. Base pressure $\sim 3 \times 10^{-6}\, torr$

3. Fill pressure $\sim 1 \times 10^{-4}\, torr$

4. $V_d \sim 70\, V$ (initially)

5. $I_d \sim 5\, A$

6. $B_T \sim 220\, G$

7. Filling gas: argon, krypton or xenon

5.3 Measurement methods

The mean and fluctuating plasma parameters have been measured using charge collecting and emitting probes. These probes include a triple Langmuir probe (TLP), a radial array of Langmuir probes (LPs), a Mach probe and an emissive probe. All the probes are mounted through the radial ports located on the outer wall of the torus, close to the poloidal plane where limiter is located; the probes can be moved in and out radially in the horizontal mid-plane. The probe construction and measurement methods have been described in Chapter 2. The ion saturation current (I_{is}), hence the density (n) and electron temperature (T_e) are simultaneously obtained using TLP [77]. Simultaneous measurements of I_{is} and floating potential (ϕ_f) are obtained using radial array of LPs. Density fluctuations are obtained from I_{is} measured using I to V converter; the electric field fluctuations are obtained from the floating potential measured on two probes using voltage followers with high common mode voltage. Mean plasma potential (ϕ_{p0}) is obtained using an emissive probe in floating point method [87, 88]. A Mach probe is used for the measurement of net poloidal flow velocity in the plasma, by collecting ion saturation current in the upstream and downstream to the flow simultaneously. Multiple measurements are performed for each parameter at each radial location by producing multiple discharges, from which error bars are estimated. The analog signals are passed through low pass filters of 100 kHz bandwidth, for which the signal conducting cards of type-2 described in Sec.2.3.7 are employed, and then acquired by digitizers at a sampling rate of 400 kS/s. In the sections that follow, obtaining discharges with each gas, the experimental results and analysis are described. The typical physical parameters, relevant to the present experimental investigations are provided in Tab.5.1.

Parameter	argon	krypton	xenon
Ion mass	39.95 amu	83.8 amu	131.29 amu
B_T	$0.022\,T$	$0.022\,T$	$0.022\,T$
$v_{th,e}$	$7.26 \times 10^5\, m/s$	$7.26 \times 10^5\, m/s$	$7.26 \times 10^5\, m/s$
$v_{th,i}$	$490.0\, m/s$	$338.0\, m/s$	$270.0\, m/s$
c_s	$2.68 \times 10^3\, m/s$	$1.85 \times 10^3\, m/s$	$1.48 \times 10^3\, m/s$
$\omega_{pe}/2\pi$	$2.84 \times 10^9\, s^{-1}$	$2.84 \times 10^9\, s^{-1}$	$2.84 \times 10^9\, s^{-1}$
$\omega_{pi}/2\pi$	$1.05 \times 10^7\, s^{-1}$	$7.24 \times 10^6\, s^{-1}$	$5.78 \times 10^6\, s^{-1}$
$\omega_{ce}/2\pi$	$6.16 \times 10^8\, s^{-1}$	$6.16 \times 10^8\, s^{-1}$	$6.16 \times 10^8\, s^{-1}$
$\omega_{ci}/2\pi$	$8.39 \times 10^3\, s^{-1}$	$4.0 \times 10^3\, s^{-1}$	$2.55 \times 10^3\, s^{-1}$
ν_{en}	$1.28 \times 10^6\, s^{-1}$	$1.28 \times 10^6\, s^{-1}$	$1.28 \times 10^6\, s^{-1}$
ν_{in}	$865.0\, s^{-1}$	$598.0\, s^{-1}$	$477.0\, s^{-1}$
ν_{ee}	$6.71 \times 10^5\, s^{-1}$	$6.71 \times 10^5\, s^{-1}$	$6.71 \times 10^5\, s^{-1}$
ν_{ei}	$4.61 \times 10^5\, s^{-1}$	$4.61 \times 10^5\, s^{-1}$	$4.61 \times 10^5\, s^{-1}$
ν_{ii}	$1.57 \times 10^5\, s^{-1}$	$1.08 \times 10^5\, s^{-1}$	$8.66 \times 10^4\, s^{-1}$
r_{Le}	$1.88 \times 10^{-4}\, m$	$1.88 \times 10^{-4}\, m$	$1.88 \times 10^{-4}\, m$
r_{Li}	$9.3 \times 10^{-3}\, m$	$1.34 \times 10^{-2}\, m$	$1.68 \times 10^{-2}\, m$

Table 5.1: The typical physical parameters for three gases, with $B_T \sim 220\,G$. For calculations above, it is considered that $kT_e/e \sim 3.0\,eV$, $kT_i/e \sim 0.1\,eV$ and $n_e \simeq n_i \sim 1 \times 10^{17}\, m^{-3}$. The symbols in the first column have same meanings as in Tab.3.1.

5.4 Plasma parameters, radial profiles and transport

The plasma is produced using one of the three gases, namely argon, krypton and xenon. To minimize the possible impurity ions in the subsequent discharges with different gases, two steps are taken: the vacuum vessel is pumped for a long time before injecting the new gas followed by cleaning of the vessel wall with low density continuous discharge for tens of minutes. For all the gases, the breakdown is found to occur for a discharge voltage in the range of $40 - 45\,V$. All the measurements reported here are done with discharge current limited to $5\,A$, therefore, corresponding to CC discharges. The radial profiles of plasma parameters are obtained with operating conditions and the measurement techniques described in Sec.5.2 and Sec.5.3 respectively. The mean and fluctuation profiles are shown in Sec.5.4.1. The estimated poloidal flows, associated with the above mean profiles are described in Sec.5.4.2. In Sec.5.5, the spectral characteristics of the measured fluctuations are presented and an attempt is made to identify the underlying mechanism of instabilities responsible for the observed fluctuations.

5.4.1 Radial profiles

The measured radial profiles of $I_{is,0}$, kT_{e0}/e and n_0 are shown in Fig. 5.1. The ion saturation current decreases with increase in ion mass; on LFS the decrease is small and on HFS the decrease is significant. The radial profiles of kT_{e0}/e for different gases, however, differ significantly from each other. Though kT_{e0}/e decreases monotonically with increase in ion mass, the radial profiles of kT_{e0}/e for argon and krypton are relatively closer on LFS. A peak in kT_{e0}/e, indicating a possible presence of fast electrons [92], occurs at $-1\,cm$ coinciding for argon and krypton; for xenon, the peak in kT_{e0}/e occurs at $-2\,cm$. The radial shift in peak is, however, comparable to the spatial resolution of measurements, which is $1\,cm$. Though the density n_0 calculated from $I_{is,0}$ and kT_{e0}/e profiles shows small changes in the region $-9\,cm < r < -4\,cm$, it increases monotonically in the the region $r > -4\,cm$ with increase in ion mass. The density is found to increase systematically upto a factor of 2 at the limiter edge on LFS with increase in ion mass, that is from argon to xenon, though the discharge current is similar in each case. In the following, an attempt is made to understand the increase in density with ion mass, with possible change in the electron drift velocity.

In a conducting medium with charge carriers of charge q, number density n_q and drift velocity v_d, the current through an area A is given by $I = qn_qAv_d$. The drift velocity is given by $v_d = \mu_d E$, where μ_d is the mobility of charge carriers. The

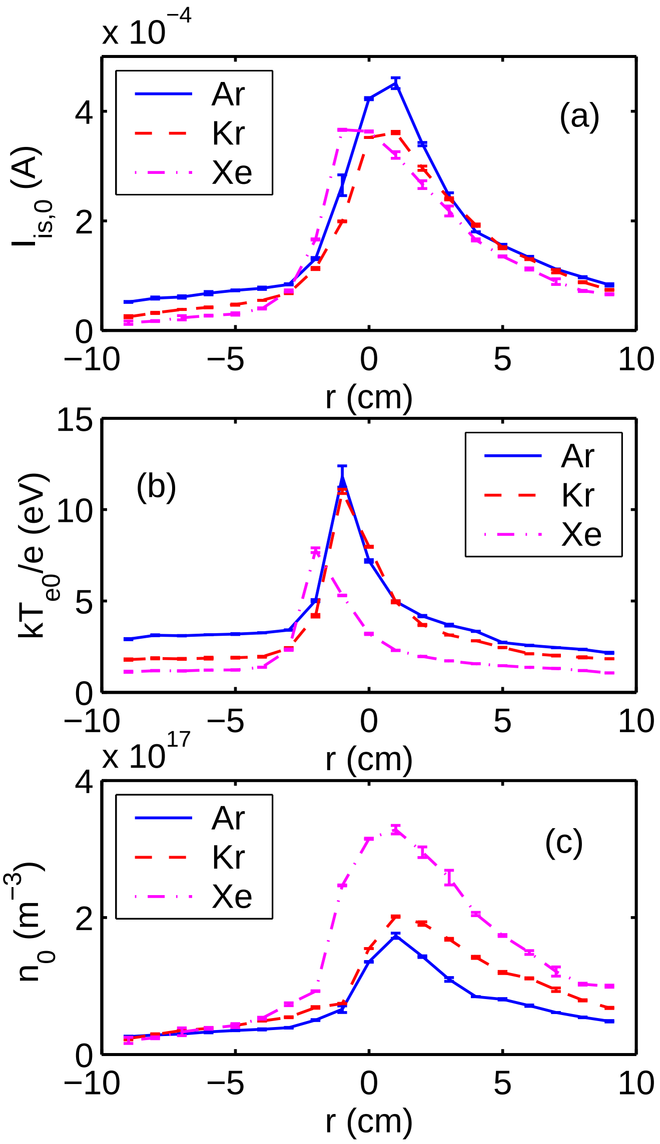

Figure 5.1: Mean radial profiles of (a) Ion saturation, (b) electron temperature and (c) plasma density for three gases. For the estimation of density, corresponding kT_{e0}/e values are used. The error bars obtained from the multiple measurements at each location are found to be small.

mobility is determined by relaxation time (τ) and charge carrier mass (m_q), as $\mu_d = q\tau/m_q$. The quantity τ is inversely proportional to the inelastic electron-neutral momentum-transfer cross section (S). For $I = I_d$, assuming the discharge current is entirely due to electron drift, τ represents the average relaxation time between electron inelastic collisions with the neutral atoms. Since I_d is constant and the arbitrary area A is similar for all the gases, the quantity n/S should remain constant irrespective of the gas, where n is the electron density. The inelastic electron-neutral momentum-transfer cross section $S \sim 3\times10^{-16}\ cm^2$, $2\times10^{-16}\ cm^2$, $4\times10^{-16}\ cm^2$ for argon, krypton, xenon respectively for corresponding kT_e/e measured at the limiter edge on LFS [104]. From argon to xenon, S increases by 30%. The corresponding increase in density, from argon to xenon is however 100%. The increase in density from argon to xenon, therefore, can only be partially explained by the decrease in electron drift velocity.

The density gradient is found to increase with increase in ion mass, on both sides of the minor axis. The inverse density gradient scale lengths (L_n^{-1}) on LFS, estimated from observed mean density profiles, are 12 m^{-1}, 14 m^{-1}, 17 m^{-1} for argon, krypton and xenon respectively. The profiles of ϕ_{f0} and ϕ_{p0} are shown in Fig. 5.2, both of which exhibit a dip close to the minor axis. At the bottom of the dip in floating potential profile shown in Fig. 5.2(a), $\phi_{f0} \sim -43V$ for argon, $\sim -36\,V$ for krypton and xenon both. A broad potential well extending in the region $-1\,cm < r < 3\,cm$ is, however, seen from the ϕ_{p0} profile for all the gases. The depth of the potential well reduces with increase in ion mass as does the gradient, indicating reduced mean radial electric field ($\mathbf{E_0}$). The mean radial electric field on LFS is maximum in the case of argon with $\mathbf{E_0} \sim 0.7\,V/cm$. The decrease in the gradient of ϕ_{p0} with increase in ion mass is systematic on LFS; on HFS the change in the gradient occurs non-monotonically.

The profiles of relative fluctuations in I_{is} and ϕ_f are shown in Fig. 5.3(a) and (b) respectively. In an attempt to measure electron temperature fluctuations using TLP, fluctuations comparable to noise level are observed and hence it is believed that fluctuations in T_e are small. In a similar device BLAAMANN, it has been observed that, electron temperature fluctuations become important for high neutral pressures [105]. Assuming electron temperature fluctuations are negligible, the rel-

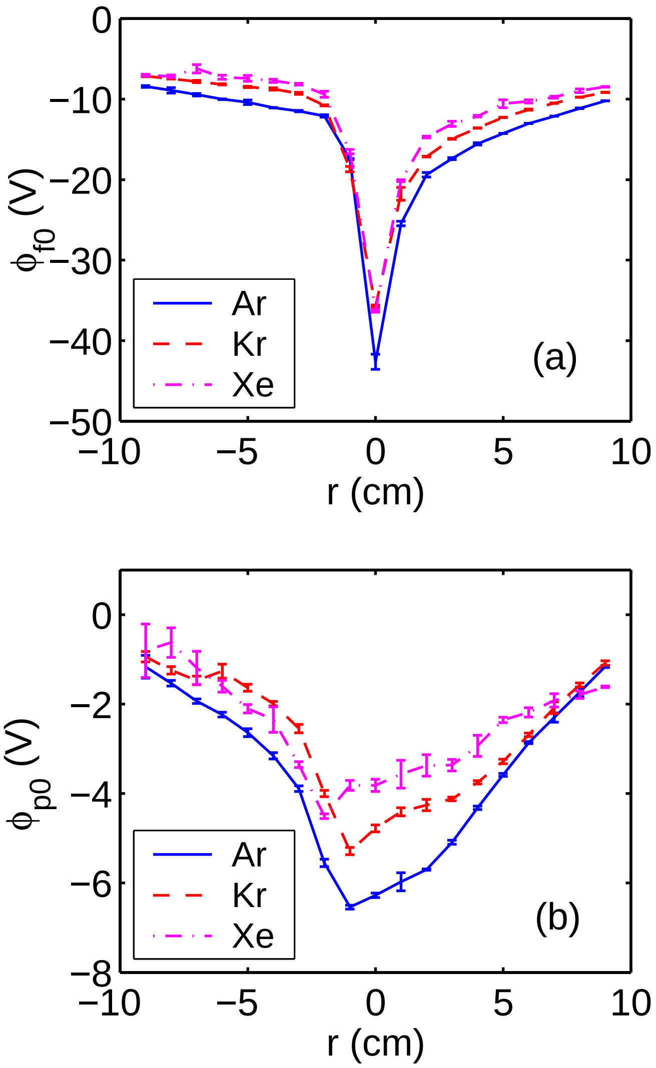

Figure 5.2: Mean radial profiles of (a) floating potential and (b) plasma potential. It can be noted that the range of vertical scale of the two plots are not same. The entire ϕ_{p0} profile may be shifted further negative by $-3\,V$ maximum, accounting for the half the voltage drop across the emissive probe filament.

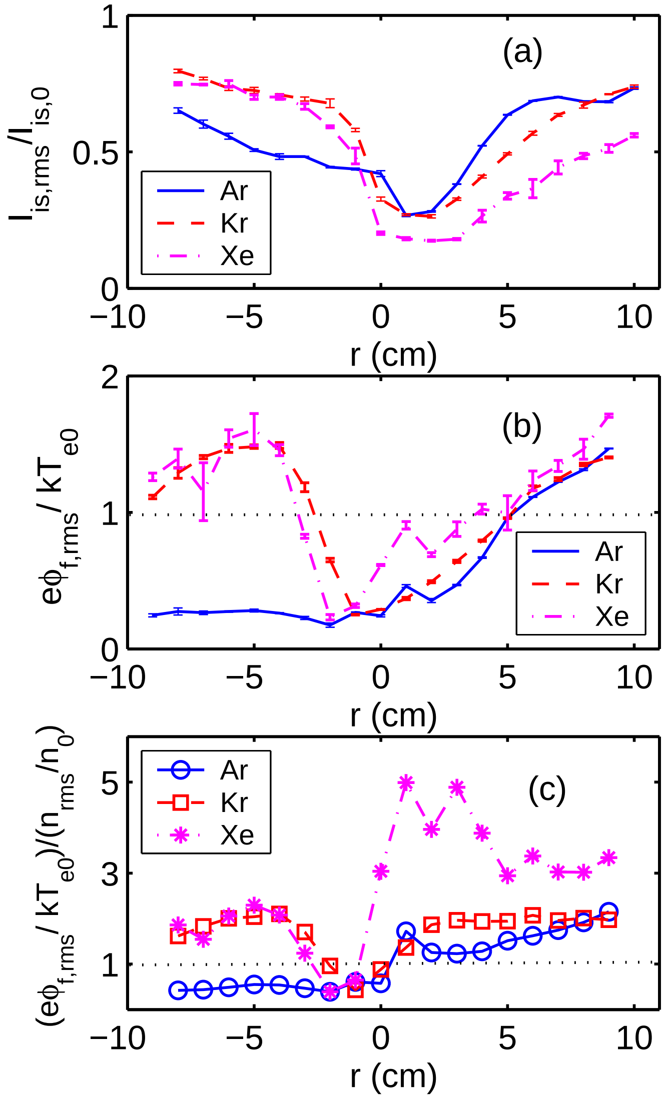

Figure 5.3: Relative *rms* fluctuation profiles of (a) ion saturation current ($I_{is,rms} = \tilde{I_{is}}$) and (b) floating potential ($\phi_{f,rms} = \tilde{\phi_f}$) are shown for all three gases. With fluctuations in T_e being small $(\tilde{I_{is}}/I_{is,0}) \sim (\tilde{n}/n_0)$ and $\tilde{\phi_f} \sim \tilde{\phi_p}$. In (c), the ratio of potential to density fluctuations are shown. The potential fluctuations are normalized to mean electron temperature.

ative fluctuations in ion saturation current represent relative density fluctuations ($I_{is,rms}/I_{is,0} \simeq n_{rms}/n_0$). The relative density fluctuations are minimum at the minor axis and maximum at the edges of the limiter. The relative density fluctuations decrease on LFS with increase in ion mass; at $r = +9\,cm$, $n_{rms}/n_0 \sim 0.7$ for argon and 0.5 for xenon. On HFS, the relative density fluctuations though increase from argon to krypton, a small decrease is seen from krypton to xenon at $r = -9\,cm$. The fluctuations in floating potential normalized to kT_{e0}/e represent the relative plasma potential fluctuations for negligible temperature fluctuations. The relative potential fluctuations are minimum at the minor axis and maximum far from the minor axis. At $r = +9\,cm$, $e\phi_{f,rms}/kT_{e0} \sim 1.5$ for argon, krypton and reach 1.7 for xenon. The relative potential fluctuation profile for argon, however, remains flat in the region extending from minor axis towards HFS with $e\phi_{f,rms}/kT_{e0} \sim 0.25$. An abrupt jump in $e\phi_{f,rms}/kT_{e0}$ on HFS is observed with increase in ion mass from argon to krypton. From krypton to xenon, only a small change is seen in the relative potential fluctuations on HFS; the maximum of $e\phi_{f,rms}/kT_{e0} \sim 1.6$ in the case of xenon on HFS. The ratio of relative fluctuations in potential to density is shown in Fig. 5.3(c); this ratio ~ 2 at $r = +9\,cm$ for argon and krypton. For xenon, this ratio changes non-monotonically on LFS, and reaches 3 on the LFS edge. On HFS, the maximum of the ratio of relative fluctuations in potential to density is 0.5 for argon, which is ~ 2 for krypton and xenon. Though the relative fluctuations in potential and density show a systematic change with increase in ion mass, the change in the relative potential fluctuations from argon to krypton, on HFS is significantly large. In the following it will be shown that the mean and fluctuating quantities lead to cross-field particle transport. A detailed investigation of mechanisms of poloidal transport is presented.

5.4.2 Poloidal flows

Mean electric field driven flow

The mean potential well leads to the poloidal rotation of the plasma, referred as mean electric field driven flow. The mean electric field driven flow calculated from $\mathbf{E_0} \times \mathbf{B}$ drift, is given by $v_{E_0 \times B} = E_0/B$. Here $\mathbf{E_0}$ is the mean radial electric field derived from ϕ_{p0} profile and $\mathbf{B}$ is the toroidal magnetic field. At each location,

E_0 is calculated from mean plasma potential on the neighboring points using the central difference formula; the error bars are constructed from $\delta E_0/E_0 \sim \delta\phi_{p0}/\phi_{p0}$. On LFS, $v_{E_0\times B}$ is found to decreases monotonically with increase in ion mass. A peak in $v_{E_0\times B}$ occurs close to the minor axis. On HFS, $v_{E_0\times B}$ profiles do not exhibit a systematic change with increase in ion mass. The profiles of $v_{E_0\times B}$ are compared with other measurements of poloidal flow in Fig. 5.6.

Fluctuating electric field driven flow

The fluctuating radial electric field can lead to a finite fluctuation induced poloidal flux depending on the relative phase between the electric field and density fluctuations. This fluctuation driven poloidal flux is found to play a vital role in the generation of self consistent flow and an effective rotational transform as described in previous chapters. Fluctuation driven poloidal flux is estimated from measurements using a radial array of LPs described in Sec.2.3.3 and using methodology for analysis described in Sec.3.6.2. The fluctuation induced flux (Γ_{fluct}) in poloidal direction, is calculated using Eq.(3.1) and Eq.(3.3), from the electric field and density fluctuations obtained simultaneously. Radial profile of Γ_{fluct} is shown in Fig. 5.4 for three gases. The Γ_{fluct} is found to be small on HFS and significant only on

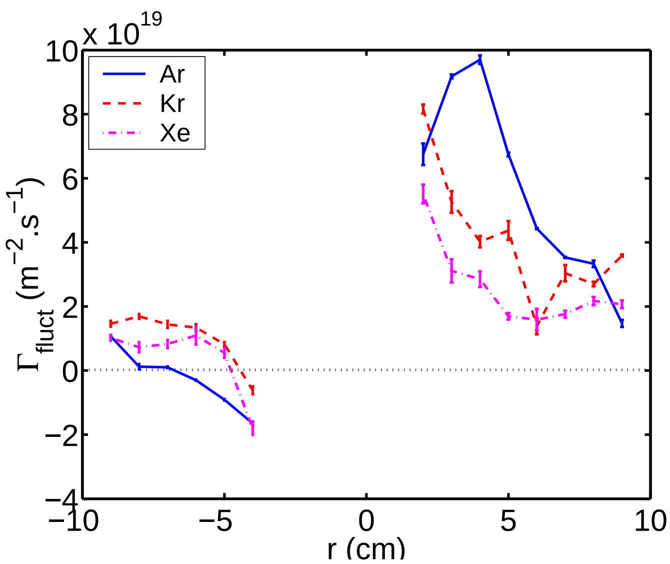

Figure 5.4: The fluctuation driven poloidal flux is shown for three gases. Due to short wavelength nature of the fluctuations, the Γ_{fluct} estimation close to the minor axis are not reliable and hence not shown here.

LFS, for all the gases. The Γ_{fluct} is maximum for argon, decreases monotonically on LFS with increase in ion mass, and becomes minimum for xenon. On LFS edge, Γ_{fluct} values are comparable to the values on HFS. From Γ_{fluct}, estimated using Eq.(3.1) and Eq.(3.3), an equivalent average flow velocity v_{fluct} due to fluctuation induced flux is estimated from Eq.(3.4). The profiles of v_{fluct} are compared with other measurements of poloidal flow in Fig. 5.6.

Net flow

Direct estimation of net poloidal flow or total poloidal flow velocity is performed using a Mach probe, with two electrodes for simultaneous measurement of I_{is} at the upstream and downstream to the flow. The cylindrical axis of the probe is aligned vertically in the horizontal mid-plane, to measure the net poloidal flow. From the measured $I_{is,0}$, net flow velocity is calculated using the Eq.(3.5). For poloidal flow calculation, the calibration of α for Mach probe is discussed in detail in Sec.3.6.3, and $\alpha = 0.5$ is used, with a maximum uncertainty of 20% in the net flow measurements. Use of Eq.(3.5) for the calculation of flow velocity perpendicular to the magnetic field is valid in the limit $r_{Li}/r_p > 1$ where r_{Li} is the ion Larmor radius and r_p is the probe radius. For argon ion, $r_{Li} \sim 10\,mm$ which is greater than the Mach probe disc radius $r_p \sim 2\,mm$. With increase in ion mass r_{Li} increases further, therefore $r_{Li} \gg r_p$ holds. The net poloidal flow velocities calculated using Eq.(3.5) are obtained in units of local c_s. Using the kT_{e0}/e profiles shown in Fig. 5.1(b), the absolute net flow velocities are calculated. In Fig. 5.5 net flow velocity profiles are shown in normalized and absolute velocity units both. The normalize velocity profiles overlap in LFS region with a maximum $v_{net}/c_s \sim 0.4$ for all the gases. On moving towards the HFS, small deviations occur at the minor axis. On the HFS, the net flow velocity exceeds c_s for all gases, with maximum $v_{net}/c_s \sim 1.3$, indicating plasma is highly compressible. The absolute net flow velocity (v_{net}) decreases monotonically over the entire radius with increase in ion mass. The magnitude of v_{net} is, however, much larger on HFS, for all the gases.

The net flow estimated from Eq.(3.5) is based on the asymmetry in the net ion saturation flux to the electrodes, upstream and downstream to the flow. The flow obtained using Mach probe is, therefore, the total flow and hence referred as net

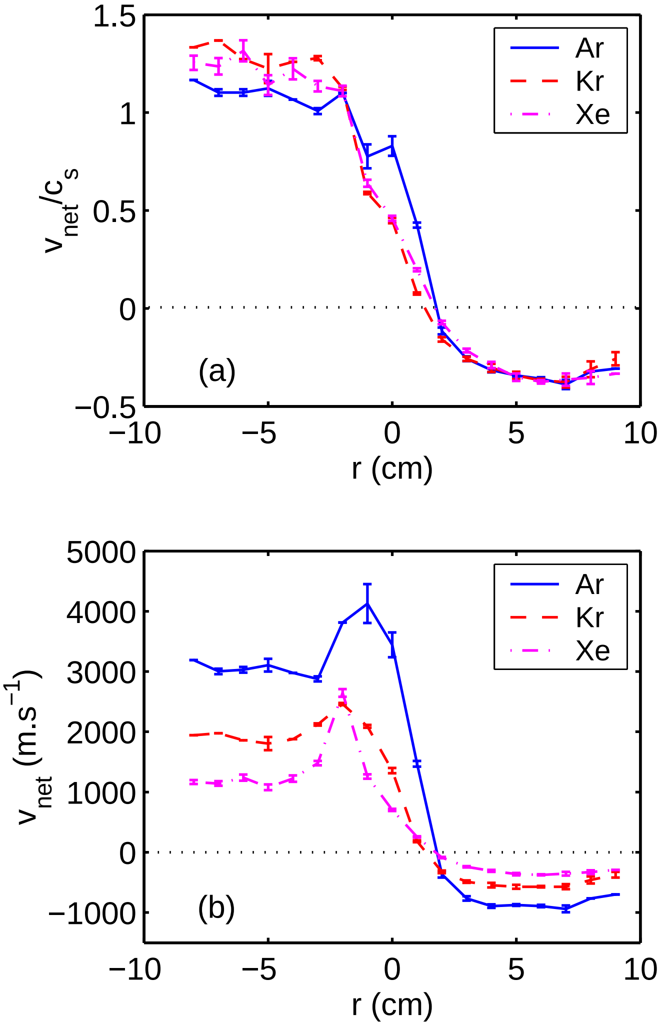

Figure 5.5: The net poloidal flow velocity profiles from measured I_{is} at the upstream and downstream using Mach probe, (a) in units of local c_s and (b) in absolute magnitude. The large values of v_{net} in (b) in the region $-2\,cm < r < 0\,cm$, can be due to large values of kT_{e0}/e.

flow. The mean and fluctuating electric fields are found to drive a significant poloidal flow as seen above. A comparison of the poloidal flows due to above two mechanisms with the net flow is, therefore, made in Fig. 5.6, for each gas. A

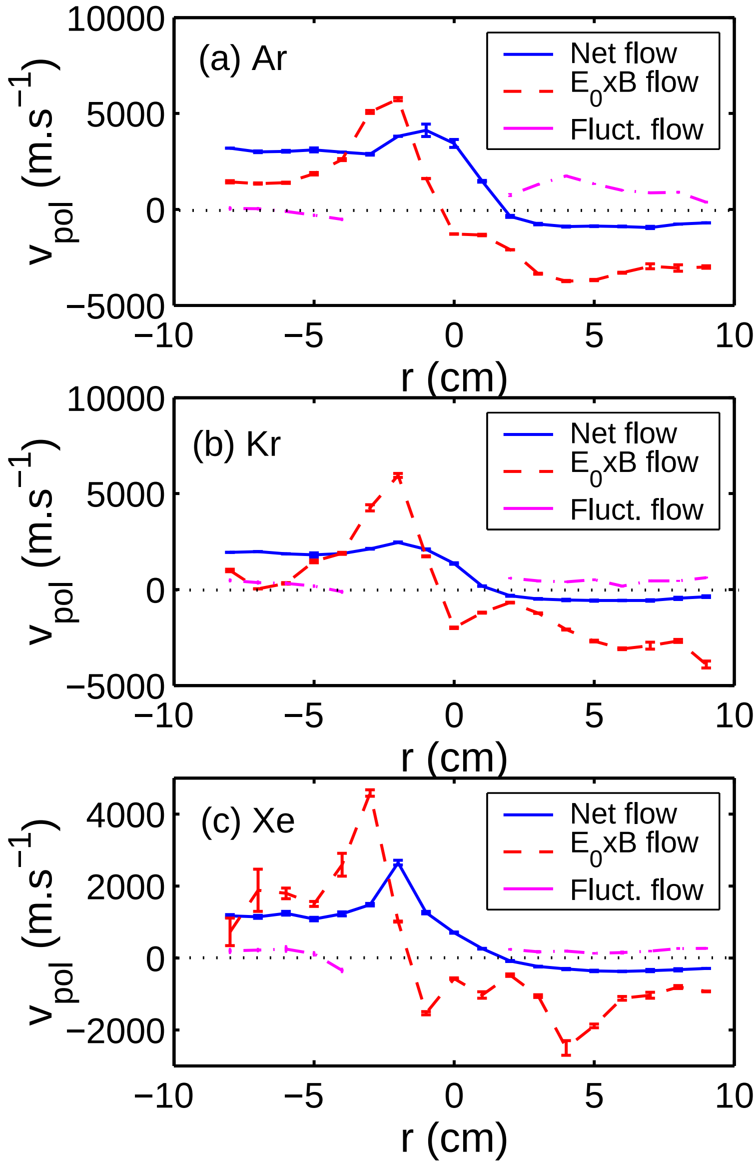

Figure 5.6: Comparative plot of poloidal flow for all three gases: (a) argon, (b) krypton and (c) xenon. In each case the net flow is compared with mean field driven flow and fluctuation driven flow.

general notation v_{pol} is used for the poloidal flow on the vertical axis, on which v_{net}, $v_{E_0\times B}$ and v_{fluct} are plotted. Though $v_{E_0\times B}$ and v_{fluct} are significant in the case of argon, the sum of these could not account exactly for the net flow profile v_{net}. Other mechanisms of poloidal flow can exist in addition to the mean and fluctuating electric field driven flow, to account for the net poloidal flow. One important conclusion from the comparative plot of poloidal flows for argon is that, v_{fluct} is opposite in direction to the $v_{E_0 \times B}$ and consistently $v_{net} < v_{E_0 \times B}$. In the case of krypton and xenon, v_{fluct} is found to be small on the scale shown for v_{pol}. Hence, the fluctuations may play a crucial role in the cross-field particle transport, which systematically change with the ion mass. The change in the nature of fluctuations with increase in ion mass can be understood using spectral analysis.

The mean electric field driven flow velocity can be determined analytically from the Pedersen conductivity as $v_{theo} = I_d B / 2\pi r M_i \nu_i n$ [33]; here I_d-discharge current, B-toroidal field, r-radial distance from the center of rotation, M_i-ion mass, ν_i-ion neutral collision frequency, n-electron density. In the present experimental observations, M_i and $n \equiv n_0$ vary with the gas whereas all other parameters being constant. From argon to xenon, $M_{Xe}/M_{Ar} \sim 3.3$ and $n_{Xe}/n_{Ar} \sim 2$; therefore v_{theo} is expected to decrease by a factor ~ 6.6. The mean field driven flow estimated from measured plasma potential profile is found to decrease by a factor ~ 2.3 from argon to xenon. The absolute net flow observed is also found to decrease by a factor ~ 2.5 from argon to xenon.

Observing systematic variations in the mean plasma profiles in Sec.5.4.1 and poloidal flows in Sec.5.4.2, we proceed to understand the nature of the fluctuations associated with these profiles.

5.5 Spectral characteristics - Instability mechanism

5.5.1 Linear spectral analysis

The relative fluctuations in density and potential are found to be significantly large. The relative density fluctuations change gradually over the entire radius whereas relative potential fluctuations show an abrupt jump on HFS, with increase in ion mass as shown in Fig. 5.3. The nature of fluctuations and the underlying mechanism responsible for the fluctuations can be understood using spectral analysis techniques [57]. The analysis method used for the estimation of auto-power and cross-power spectra is described in Sec.4.6.

The estimated auto-power spectra for density and potential fluctuations at ±5 cm are shown in Fig. 5.7, for all the gases. In each case, similar first harmonic fre-

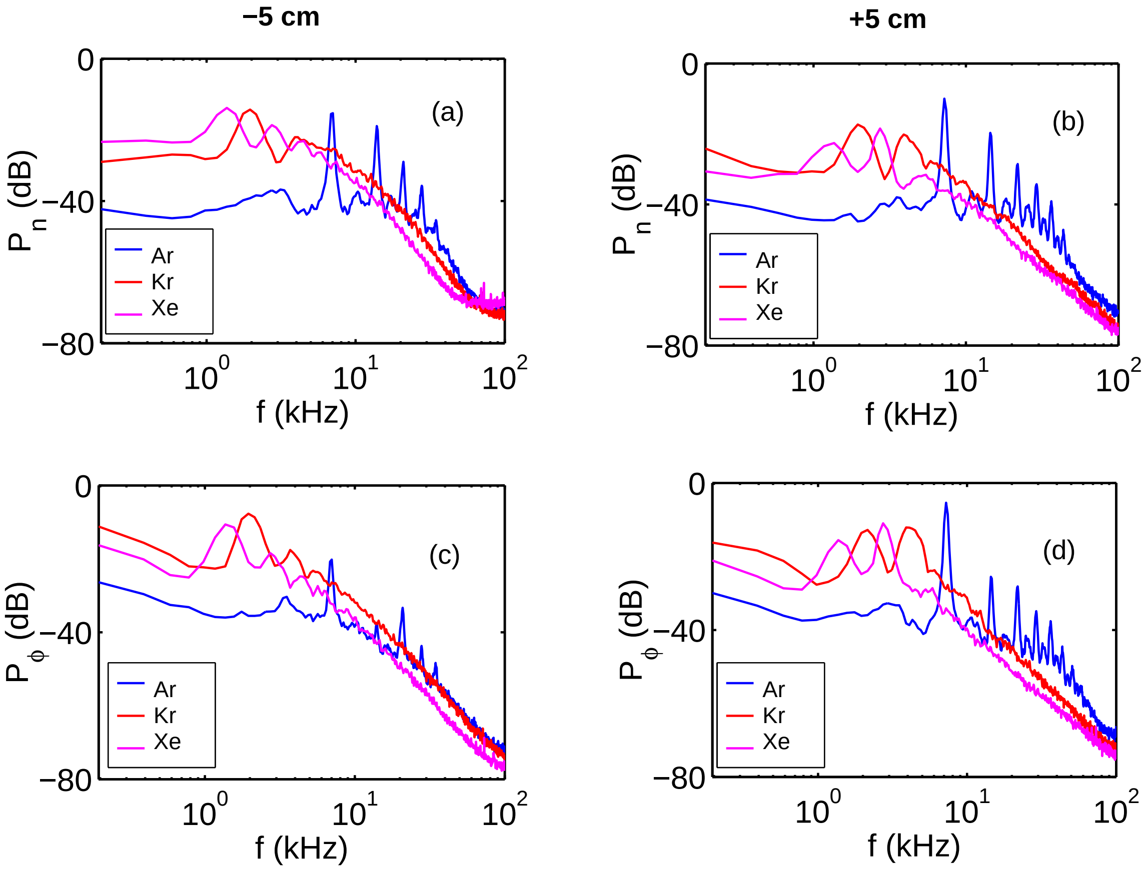

Figure 5.7: Typical density and potential auto power spectra on HFS and LFS for all the three gases. Frequency is indicated by f and power is indicated by P_n and P_ϕ for density and potential respectively. Figures (a) and (c) are power spectra of $\tilde{n}$ and $\tilde{\phi}$ respectively at -5 cm. Similarly, (b) and (d) are at +5 cm.

quencies are observed in auto-power spectra for both the regions LFS and HFS, represented by +5 cm and −5 cm respectively. For argon, the fluctuations in both the density and potential exhibit relatively strong peaks compared to the background turbulence, with a fundamental (first harmonic) frequency of 7 ± 0.2 kHz, accompanied by several harmonics. A small broad peak at 3 kHz is also observed in all the auto-power spectra for argon. With increase in ion mass, the fundamental frequency shifts to lower side and the background turbulence increases; third and higher harmonics are found to diminish in the powerspectra. For argon, the fundamental frequency is found to be the dominant frequency over the entire radial domain. The fundamental frequency for krypton is 2 ± 0.2 kHz which is the only dominant mode above the background turbulence on HFS. The second harmonic for krypton has relatively similar power as the fundamental frequency on LFS, which can be observed from Fig. 5.7(b) and (d). In the case of xenon, the fundamental frequency is 1.3 ± 0.2 kHz which is the dominant mode on HFS. Interestingly, in both the density and potential fluctuations for xenon on LFS, the second harmonic is found to be the dominant peak. The dominant nature of the second harmonic for xenon is apparent from the power spectra at $+5\,cm$ as shown in Fig. 5.7(b) and (d). In the case of argon, the estimated average poloidal wave number $\bar{k}_\theta \sim 16\,m^{-1}$ as shown in Fig. 4.16 which corresponds to mode number $m = 1$; the fundamental frequency is found to be dominated by the plasma rotation frequency at all magnetic field values [103]. In the present case with various ion masses, considering 3 kHz as the fundamental frequency for argon, the fundamental frequency scale with the net poloidal flow velocity. The dominant frequency for argon is, however, comparable to the ion cyclotron frequency at the limiter edge on LFS ($f_{ci} \sim 7$ kHz). The relevance of this dominant mode with f_{ci} needs to be investigated further. In the case of krypton and xenon, the observed fundamental frequency is less than f_{ci}. The estimated power spectra will be used in the identification of instability mechanism responsible for the fluctuations.

5.5.2 Identification of instabilities

Identification of the instabilities responsible for the fluctuations is possible with the experimental estimation of real frequencies, dispersion relation and comparison with theoretical models. Though the parallel wave number ($k_\parallel$) can clearly distinguish between the drift and flute kind of modes, the experimental determination of which is a difficult task, as described in Sec.4.7. The possible instabilities are, therefore, identified using the estimated cross-phase ($\theta_{n\phi}$), coherence ($\gamma_{n\phi}$) of density and potential fluctuations. The growth rates have been calculated. The profiles of $\theta_{n\phi}$ and $\gamma_{n\phi}$ for the fundamental frequency and the second harmonic, are shown in Fig. 5.8. Measurements close to the minor axis ($-3\,cm < r < +1\,cm$)

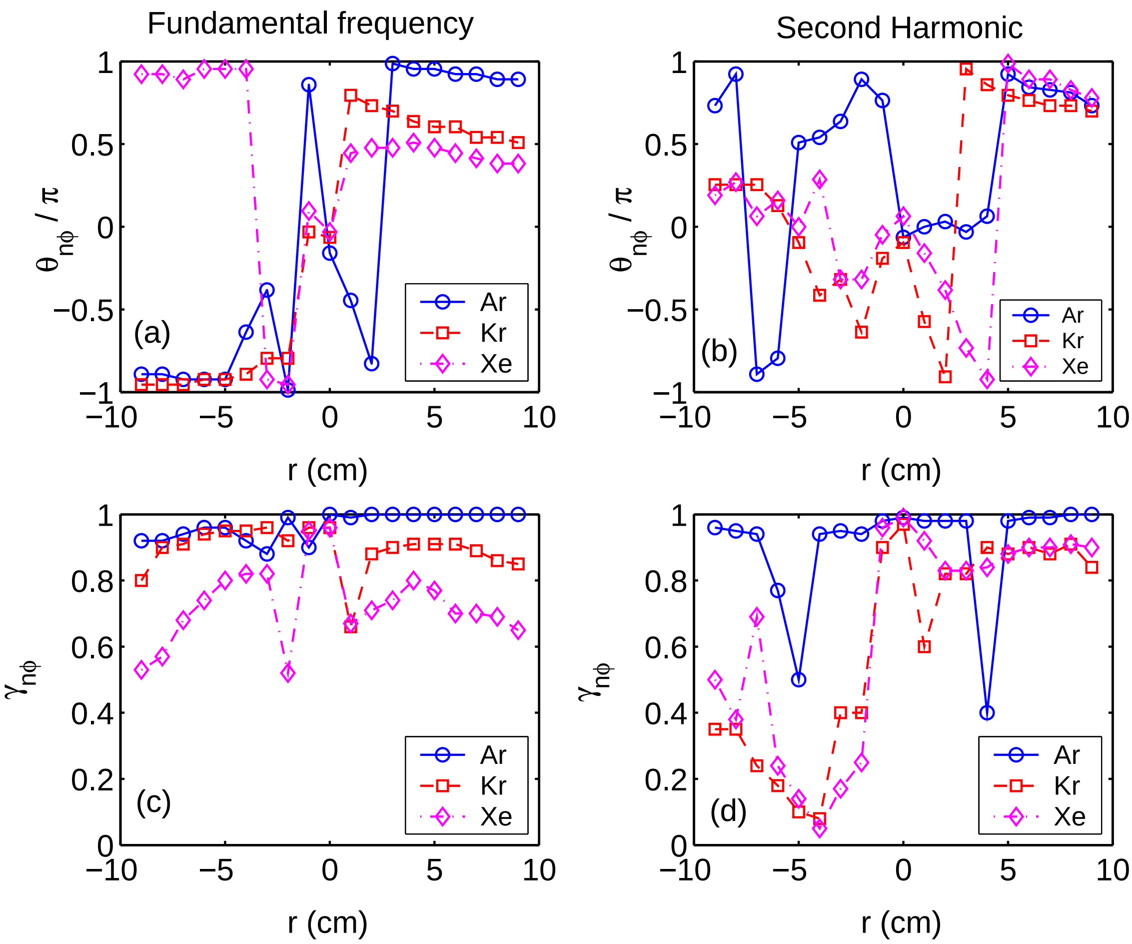

Figure 5.8: Profiles of cross phase ($\theta_{n\phi}$) for (a) fundamental frequency and (b) second harmonic; coherence ($\gamma_{n\phi}$) for (c) fundamental frequency and (d) second harmonic of density and potential fluctuations for all gases. For Ar, fundamental frequency is the dominant mode over the entire radial domain. On LFS for Kr and Xe, second harmonic becomes comparable or dominant than the fundamental frequency. Change in the sign when $|\theta_{n\phi}| \approx \pi$ indicate either a small lead or lag in the propagation of potential to density fluctuations.

can be erroneous due to the observed short wavelength nature of the fluctuations for all the gases. In the following it will be shown that coherent fluctuations occur for argon, which turn out to be turbulent in the case of krypton and xenon, with all the external parameters for the discharge remaining the same.

Coherent fluctuations

In the case of argon, the fundamental mode (7 kHz) and its harmonics are found to be highly coherent which are described in Sec.4.6. For the fundamental frequency in the case of argon on LFS, the cross-phase $|\theta_{n\phi}| \approx 0.9\pi$; and the coherence $\gamma_{n\phi} \approx 1$. From Fig. 5.3(c), the ratio of relative fluctuations in potential to density $(e\phi_{f,rms}/kT_e)/(n_{rms}/n_0) > 1$. Therefore these fluctuations are of flute type, generated due to density gradient driven Rayleigh-Taylor (R-T) instability, as discussed in detail in Sec.4.7.

On HFS, the density and potential fluctuations are out of phase for the fundamental frequency; that is $|\theta_{n\phi}| \approx 0.9\pi$ with reduced coherence, however, $\gamma_{n\phi} \geq 0.9$. The observed fluctuations, therefore, appear to be of flute type. The ratio $(e\phi_{f,rms}/kT_e)/(n_{rms}/n_0)$ is, however, less than 1. The fluctuations on HFS can be due to the convection of fluctuations from LFS due to the plasma flow. This argument is supported by the estimated coherence which is maximum on LFS and reduced on HFS. Step nature of density and velocity profiles are seen from Fig. 5.1(c) and Fig. 5.5, which can favor the growth of velocity shear driven Kelvin-Helmholtz (K-H) instability, as described in Sec.4.7.1. The origin of fluctuations on HFS due to K-H instability, therefore, cannot be ruled out.

For the second harmonic in the case of argon, $\theta_{n\phi}$ and $\gamma_{n\phi}$ has comparable values as the fundamental mode, in the regions $r < -6\ cm$ and $r > +5\ cm$; therefore, the second harmonic is of flute type in this region. In the region $-6\ cm < r < +5\ cm$, $\theta_{n\phi}$ and $\gamma_{n\phi}$ deviate significantly from that of fundamental mode.

Turbulent fluctuations

The turbulent fluctuations in the case of argon, have significantly low power than the highly coherent fundamental frequency and its harmonics. For krypton and xenon, from Fig. 5.8, $\gamma_{n\phi}$ for the fundamental frequency is significantly less than 1 on LFS, indicating reduced coherence in the fluctuations. The increased background turbulence can be seen from the auto-power spectra shown in Fig. 5.7. For krypton, $\theta_{n\phi}$ and $\gamma_{n\phi}$ are relatively lower in the region from minor axis to the LFS edge; $\theta_{n\phi} \sim 0.5\pi$ and $\gamma_{n\phi} \sim 0.85$ at the edge of the limiter on LFS. Similarly for xenon, $\theta_{n\phi}$ and $\gamma_{n\phi}$ for the fundamental frequency, are further lower from minor axis to the LFS edge; $\theta_{n\phi} \sim 0.4\pi$ and $\gamma_{n\phi} \sim 0.65$, both minimum at the edge of the limiter on LFS. The decrease in coherence on LFS occurs monotonically with increase in ion mass, from argon to xenon. Similarly, the increase in deviation of $\theta_{n\phi}$ from π is seen to occur monotonically on LFS with increase in ion mass. The fundamental or first harmonic frequency fluctuations on LFS are, therefore, found to deviate progressively from coherent flute modes to turbulent fluctuations with increase in ion mass and possibly become resistive R-T mode as observed from cross-phase values.

Besides the fundamental mode on LFS for krypton and xenon, the second harmonic is also found to be relatively significant in amplitude. In the case of krypton, the second harmonic has similar power compared to the fundamental mode on LFS. For krypton, the $\gamma_{n\phi}$ for second harmonic is comparable to that of the fundamental mode on LFS; the $\theta_{n\phi}$ for the second harmonic is relatively closer to π compared to the fundamental frequency. In the case of xenon, the second harmonic has higher power than the fundamental mode on LFS. Interestingly, for xenon the second harmonic has relatively higher $\gamma_{n\phi}$ than the fundamental frequency on LFS. The cross-phase is relatively closer to π compared to the fundamental frequency, with $\theta_{n\phi} > 0.8\pi$. Hence for krypton and xenon, though the fundamental frequency is non-flute like on LFS, the second harmonic becomes relatively a dominant mode which is flute-like.

For the fundamental frequency on HFS, the coherence $\gamma_{n\phi}$ for krypton is comparable to that of argon, however, decreases significantly for xenon as can be seen from Fig. 5.8(c). The cross-phase $|\theta_{n\phi}| \approx 0.9\pi$, on HFS for krypton and xenon both. The fluctuations on HFS for krypton and xenon appears to be flute like. The ratio of the relative fluctuations in potential to density $(e\phi_{f,rms}/kT_e)/(n_{rms}/n_0) > 1$ as shown in Fig. 5.3(c), which is true for flute like fluctuations. In the case of krypton and xenon, since the fundamental frequency is non-flute like on LFS, the possibility of convection of fundamental-flute modes to HFS can be ruled out. A possible source of flute mode on HFS is velocity shear driven K-H instability. With a step kind of velocity and density profiles on HFS at $r = -2\ cm$, the growth rate is calculated from the analytical expression using the experimentally determined density and velocity profiles [10, 61]. Two regions on either side of the discontinuous point are labelled as 1 and 2, with corresponding densities N_1, N_2, velocities v_1, v_2 such that $N_1 > N_2$ and $v_1 < v_2$. The center of poloidal rotation of the plasma as seen from Fig. 5.5, is $r = +1\,cm$. The growth rate of K-H instability is estimated using the Eq.(4.9). For argon the corresponding densities are $18\times10^{16}\,m^{-3}$, $4\times10^{16}\,m^{-3}$, corresponding velocities are $800\,ms^{-1}$ and $3000\,ms^{-1}$; the growth rate for K-H instability is $7\times10^{3}\,s^{-1}$. For krypton, the corresponding densities are $20\times10^{16}\,m^{-3}$, $5\times10^{16}\,m^{-3}$, corresponding velocities are $500\,ms^{-1}$ and $1900\,ms^{-1}$; the estimated growth rate for K-H instability is $5\times10^{3}\,s^{-1}$. For xenon, the corresponding densities are $30\times10^{16}\,m^{-3}$, $7\times10^{16}\,m^{-3}$, corresponding velocities are $500\,ms^{-1}$ and $1200\,ms^{-1}$; the estimated growth rate for K-H instability is $3\times10^{3}\,s^{-1}$. In the case of krypton and xenon, estimated coherence for the fundamental mode is maximum in this region of HFS, hence this region is believed to be the source region of the observed flute mode on HFS.

The second harmonic on HFS for krypton and xenon, is relatively small in amplitude. Moreover, the corresponding $\gamma_{n\phi}$ is too low such that $0 < \gamma_{n\phi} < 0.3$ in the region $-6\,cm < r < -2\,cm$. The corresponding cross-phase is such that $0 < |\theta_{n\phi}| < 0.4\pi$. This region is where a velocity shear exists and hence favorable for the growth of K-H instability. The second harmonic which is highly coherent on LFS, becomes poorly coherent on HFS for krypton and xenon both. It is, therefore, believed that the fundamental mode which is a velocity shear driven K-H mode is favorable, and the second harmonic is suppressed on HFS. The second harmonic is found to have maximum growth on LFS, for krypton and xenon. A summary of the dominant mechanism of the instabilities is tabulated as shown in Tab.5.2.

5.6 Summary

A current less toroidal plasma produced by a hot cathode discharge with argon, krypton and xenon gases at $220\,G$ of toroidal magnetic field, is studied for its fluctuation-flow behavior with varying ion mass. In each case, mean and fluctuation profiles of plasma parameters are obtained. The observed plasma profiles are always found to be associated with the existence of large fluctuations and the

Gas	HFS	LFS
Ar	K-H/Convection from LFS (I)	R-T (I)
Kr	K-H (I)	mixed ($P_I \sim P_{II}$)
Xe	K-H (I)	R-T (II)

Table 5.2: A tabular summary of the dominant fluctuations and respective harmonics, shown in brackets, on HFS and LFS for all the gases. The 'mixed' case indicates that flute (II: R-T) type and non-flute (I: resistive R-T) like modes have comparable powers, i.e $P_I \sim P_{II}$. I and II indicate first and second harmonic respectively.

plasma is spread in the entire radial domain. Further the mean profiles are found to change systematically with increase in ion mass; electron temperature is seen to decrease and the plasma density increases with increase in ion mass. The relative fluctuations are also observed to change systematically with increase in ion mass.

Significant poloidal flows are found to co-exist with the observed radial profiles of mean plasma parameters, for all the gases. The radial profiles of net poloidal flow in units of local ion acoustic velocity are seen to be comparable for all the gases except for small variations on HFS. The net flow velocity exceeds the ion acoustic velocity on HFS and is significantly smaller than ion acoustic velocity on LFS. On an absolute scale the net poloidal flow, though different in magnitude on LFS and HFS, exhibit similar scaling in both the regions with increase in ion mass. On LFS, the net poloidal flow, mean electric field driven poloidal flow and fluctuation induced poloidal flow are all found to decrease with increasing ion mass. Though the fluctuation driven flow is significant, it accounts only partially for the difference between the net flow and mean electric field driven flow. In the case of argon, the measurements under similar conditions were reported earlier, in Chapter 3. Due to a possible small variation in discharge conditions, the actual profiles are different from earlier measurements for argon. It can be noted, however, that this does not change the sense of fluctuation driven poloidal flow, mean electric field driven poloidal flow and net poloidal flow.

The cross-phase and coherence profiles indicate the existence of flute-like modes for argon plasma. The reduced coherence with increase in ion mass indicates transition to turbulence. The transition from coherent to turbulence is associated with reduced net poloidal flow. In our previous work with increasing magnetic field for argon plasma, transition to turbulence in the entire radial domain is found to be associated with enhanced flow and improved densities on HFS [103]. Though a similar transition to turbulence in the entire radial domain occurs with increase in ion mass in the present set of experiments, the density remains comparable on HFS.

In the case of argon plasma, the fundamental frequency is the dominant mode which is flute-like over the entire radial domain. Though the background turbulence is found to increase for krypton and xenon, the fundamental modes on HFS indicate flute like behavior. The coherence for the fundamental mode is found to be relatively higher on HFS than LFS for krypton and xenon. Since flute like fluctuations do not exist on LFS in the case of krypton and xenon, a possibility is that the observed flute like fluctuations are generated on HFS itself. With a strong velocity shear observed on HFS, growth rates for K-H instability are estimated from experimentally estimated density and velocity profiles. It is found that the estimated growth rates are significant, hence it is believed that the flute like fluctuations on HFS are K-H unstable. Interestingly, the second harmonic becomes relatively important in the case of krypton and xenon on LFS, which is flute-like. For krypton, the second harmonic is similar in amplitude as the fundamental mode; for xenon, the second harmonic even becomes the dominant mode. The frequency of the second harmonic in the case of krypton and xenon becomes comparable to the ion-cyclotron frequency at the edge of the limiter on LFS. The relevance of the second harmonic with ion-cyclotron frequency needs to be investigated further. The flute-like fluctuations, therefore dominate on LFS even for krypton and xenon. Though similar frequencies are observed in the entire radial domain, the dominant modes are different in LFS and HFS in a given discharge, atleast in the case of xenon. The major findings presented in this chapter have been published in **(T. S. Goud et al)** **Phys. Plasmas 19, 072306 (2012)**.

From the experimental investigations presented in this chapter, it has been observed that, the existence of fluctuations and associated poloidal flows help in sustaining mean profiles, in a simple toroidal plasm with different ion mass. It is understood, therefore, that the intrinsic poloidal flow plays a role of "effective rotational transform" in a simple toroidal plasma under varying magnetization and a wide range of ion masses. The statistical properties of the fluctuation induced flux showing characteristic behavior, under varying conditions of the discharge are described in the next chapter.

6

Statistical properties of the fluctuation induced flux

6.1 Introduction

In previous chapters, the role of fluctuation induced flux in formation of an "effective rotational transform" has been studied. On changing the control parameters such as toroidal magnetic field and ion mass, the fluctuations are seen to change from coherent to turbulent type. In this chapter, we report the statistical properties [65] of the fluctuation induced poloidal and radial flux. The statistical properties are interpreted from the probability distribution of the all the flux events in a given time series of the fluctuation induced flux. Further interpretation of the statistical properties is carried out by calculating associated quantities of the probability distribution. Observing the nature of the probability distribution, the Gaussian or non-Gaussian nature of fluctuation induced flux can be evident. The non-Gaussian nature of the fluctuation induced flux may be associated with either non-Gaussian nature of density and potential fluctuations [66] or Gaussian fluctuations in above stated quantities which are weakly coupled with each other [65].

This chapter is organized as follows. Typical statistical quantities are defined in Sec.6.2, in which the calculations are carried out for various time series of fluctuation induced poloidal flux. Similar analysis has been carried for the fluctuation induced radial flux in Sec.6.3. Brief conclusions of this analysis and comparisons are presented in Sec.6.4.

6.2 Fluctuation induced poloidal flux - Statistical analysis

A variety of operating conditions for the discharges and various measurements are described in the previous chapters. Typical mean plasma parameters, fluctuations and possible instabilities have been also discussed. The fluctuation induced poloidal flux has been found to play a key role in sustaining poloidal flows and radially well spread mean density profiles. In the following, estimation of time series and the statistical properties of the fluctuation induced poloidal flux have been carried out.

6.2.1 Estimation of time series of flux

The radial electric field fluctuations can lead to $\mathbf{\tilde{E}_r} \times \mathbf{B}$ poloidal flux where $\mathbf{\tilde{E}_r}$ is the fluctuating radial electric field. Depending on the cross-phase relation between electric field and density fluctuations, the fluctuation induced poloidal flux can be finite [54, 55]. The fluctuation driven flux is estimated from time series obtained using a radial array of LPs described in Sec.3.6.2. The time series of radial electric field fluctuations are estimated from the potential fluctuations obtained on two spatially separated probes and density fluctuations are estimated from the fluctuations in I_{is} on a third probe, all obtained simultaneously. The time series of the flux is then estimated as

$$\Gamma_T = \frac{1}{B}\tilde{n}\tilde{E}_r, \tag{6.1}$$

where $\tilde{n}$ and $\tilde{E}_r$ are the fluctuation time series corresponding to density and radial electric field, possessing zero mean values. The average of Γ_T, indicated by $\langle\Gamma_T\rangle$, can be non-zero depending upon the relative phase between $\tilde{n}$ and $\tilde{E}_r$. The time series of $\tilde{n}$, $\tilde{E}_r/B$ and Γ_T are shown in Fig. 6.1. The finiteness of the average fluctuation induced poloidal flux is observable from Fig. 6.1(c). A blow up of the plots in Fig. 6.1 over a time window of $5\,ms$, is shown in Fig. 6.2. In the following, estimation of statistical properties of Γ_T is described.

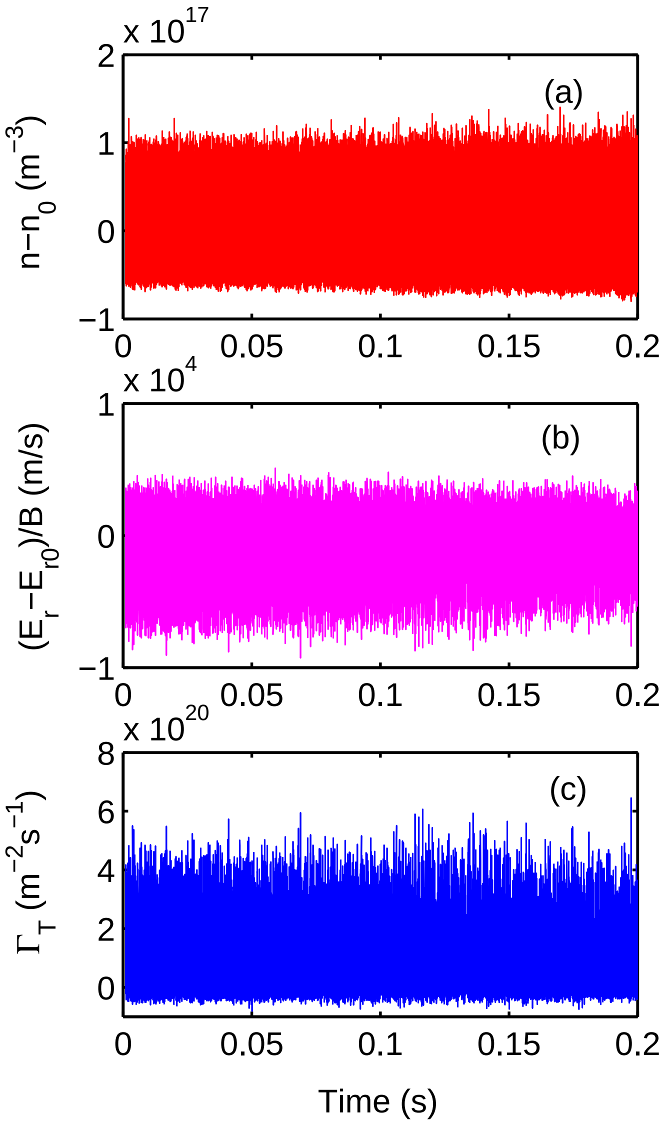

Figure 6.1: A time series plot of (a) $\tilde{n}$, (b) $\tilde{E}_r/B$ and (c) $\Gamma_T(pol)$ from the measurements at $+4\,cm$, where $\langle\Gamma_T(pol)\rangle$ is maximum.

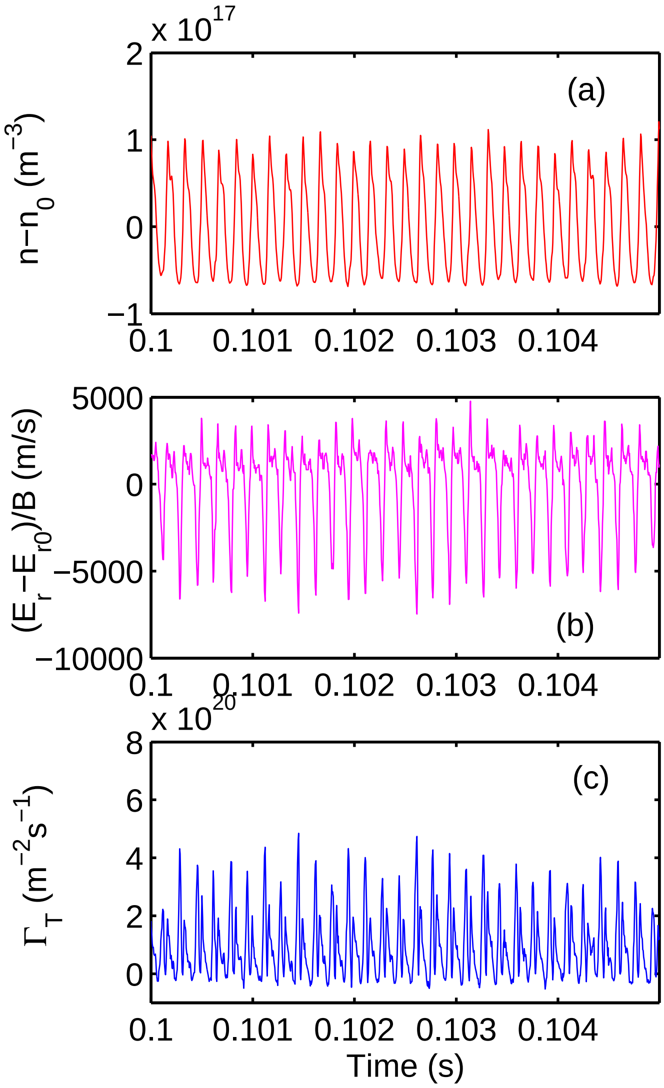

Figure 6.2: A blow up of plots in Fig. 6.1, over a window of 5 ms

6.2.2 Statistical properties

The statistical properties of Γ_T are estimated using the analysis similar to that described in Ref.[65]. It has been found that, $\langle\Gamma_T\rangle$ can vary by an order of magnitude at different radial locations, though the amplitude of Γ_T is of the same order of magnitude. The normalized time series Γ_T is, therefore, obtained by dividing with fluctuating *rms* value as $\Gamma_n \equiv \Gamma_T/\Gamma_{T,rms}$. A plot of Γ_n corresponding to Γ_T in Fig. 6.1(c), is shown in Fig. 6.3. The probability distribution function (PDF) of

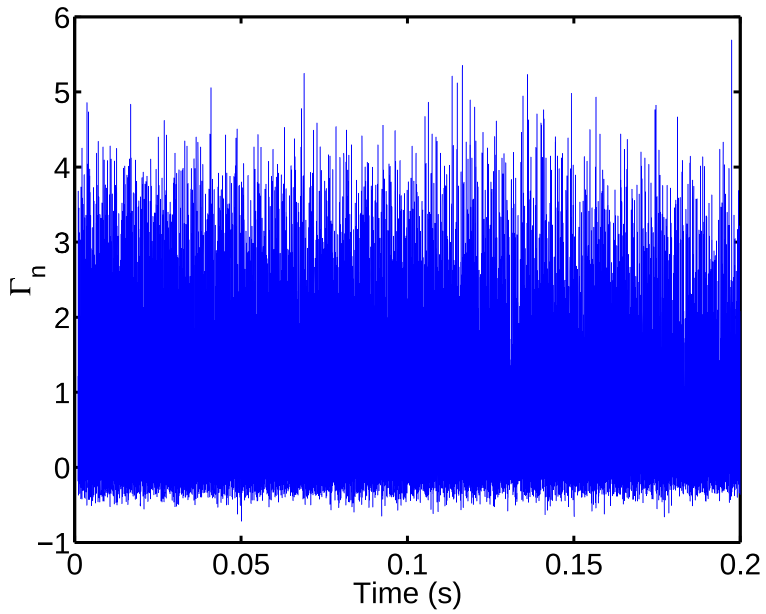

Figure 6.3: A time series plot of Γ_n estimated from Γ_T shown in Fig. 6.1(c)

Γ_n is constructed from the histogram as

$$p(\Gamma_n) = \frac{N_{\Gamma_n}}{N}, \tag{6.2}$$

where N is the total number of data samples in Γ_n, and N_{Γ_n} is the number of samples within $\Gamma_n \pm w/2$, w being the common width of the intervals into which the entire range of Γ_n is divided. In the present case, a range in Γ_n with a width of 20 is divided into 80 intervals, resulting in $w = 0.25$. The function $p(\Gamma_n)$, therefore, indicates the fraction of total events with normalized flux value lying in a small window w around Γ_n. A plot of PDFs at few radial locations on LFS, is shown in Fig.6.4; these PDFs corresponds to argon discharges at $B_T \sim 220\,G$. Clearly, the

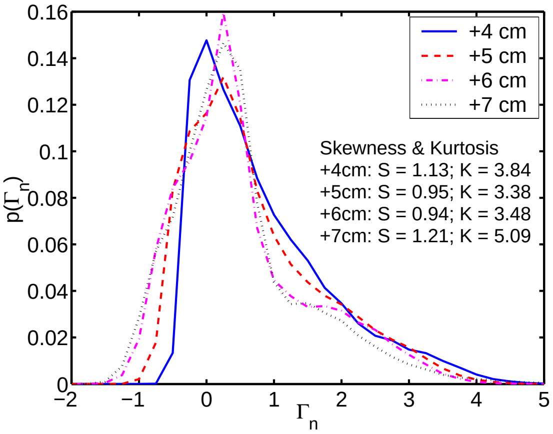

Figure 6.4: PDF of fluctuation induced poloidal flux for argon with 220 G, at different radial locations on LFS.

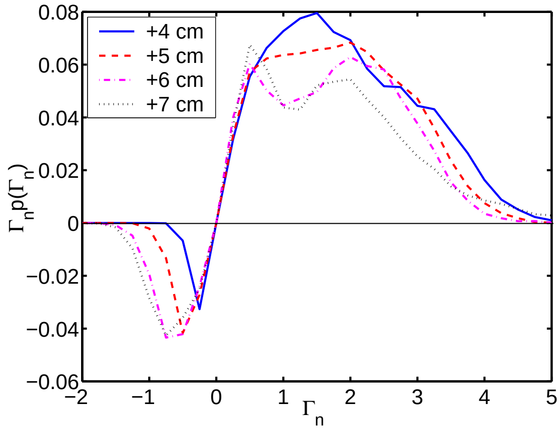

Figure 6.5: Flux fraction function of fluctuation induced poloidal flux for argon with 220 G, at different radial locations on LFS.

PDFs of Γ_n are non-Gaussian in nature. The deviations from Gaussian nature can be quantified by skewness (S) and kurtosis (K), defined as

$$S = \langle(\Gamma_n(t) - \langle\Gamma_n\rangle)^3\rangle/\sigma^3, \tag{6.3}$$

and

$$K = \langle(\Gamma_n(t) - \langle\Gamma_n\rangle)^4\rangle/\sigma^4, \tag{6.4}$$

where σ is the standard deviation of Γ_n. The skewness is a measure of the symmetry and kurtosis is a measure of sharpness of the peak of the PDF; for a normal distribution $S = 0$, indicating a perfect symmetry, and the value of the kurtosis $K = 3$. A positive S indicates a shift towards right, a negative S indicates shift towards left, whereas $K > 3$ indicates sharper PDF than a normal distribution. From Fig. 6.4, it is observed that for all the radial locations, the PDFs have a rightward shift; consequently the length of the curves are relatively longer on positive side. For $+4\,cm$, on negative side of Γ_n, there are significant number of events but with smaller magnitude of Γ_n. On moving towards $+7\,cm$, the number of events with higher magnitude of Γ_n on negative side increases. No monotonic changes in S and K are seen with change in radial position.

A flux fraction function is defined as the product $\Gamma_n \times p(\Gamma_n)$, as a function of Γ_n. A plot of flux fraction function corresponding to the PDFs in Fig.6.4, is shown in Fig.6.5. The flux fraction function indicates the fractional contribution to the flux due to all the events in a small interval in the neighborhood of Γ_n. A summation of the flux fraction function over the entire range of Γ_n results in $\langle\Gamma_n\rangle$, the average flux in normalized units. Since $p(\Gamma_n) > 0$ is true always, $\Gamma_n p(\Gamma_n)$ will be according to the sign of Γ_n. A significant variation in the profiles of the peaks on both sides of $\Gamma_n = 0$ would mean that $\langle\Gamma_n\rangle$ can be considerable in magnitude; from Fig. 6.5 the average flux is positive, which is directed upward.

High field side

Similar plots of PDFs of Γ_n and flux fraction on HFS, for argon plasma at $B_T \sim 220\, G$ are shown in Fig. 6.6 and Fig. 6.7 respectively. The PDFs indicate that the

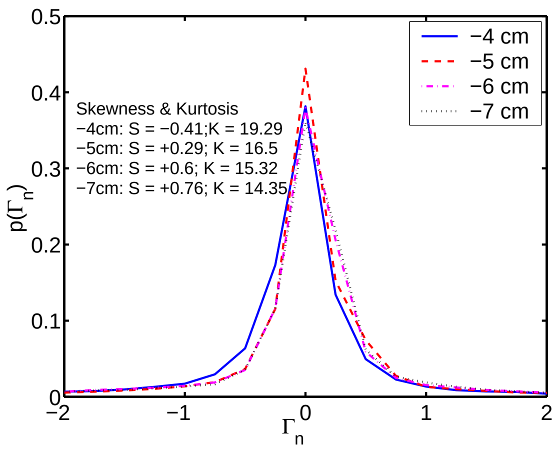

Figure 6.6: PDF of fluctuation induced poloidal flux for argon with 220 G at different radial locations on HFS.

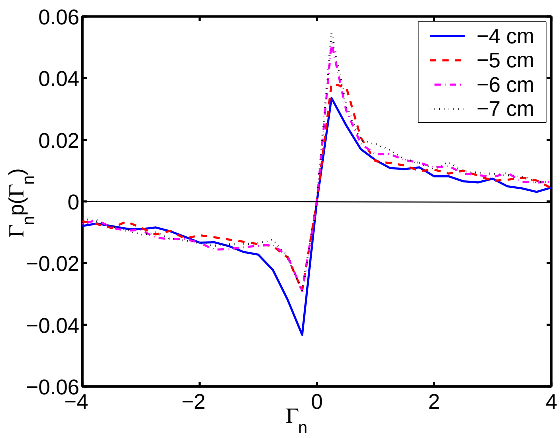

Figure 6.7: Flux fraction function of fluctuation induced poloidal flux for argon with 220 G, at different radial locations on HFS.

flux events are relatively more evenly distributed around $\Gamma_n = 0$. On moving from -4 to $-7\, cm$, however, a shift in PDF towards positive side of Γ_n is observed. The shift can also be seen from S changing from -0.41 at $-4\, cm$ to $+0.76$ at $-7\, cm$. The change in sharpness of the distribution is also systematic, as indicated by K, for above radial variation. From the flux fraction function, it is more obvious that nearly equivalent contributions occur from negative and positive Γ_n events.

Accordingly, the average flux turns out to be small. Physically, it can be interpreted as the fluctuation induced flux due to oscillating electric field is comparable in both the directions, therefore, on the net flux tends to be small.

Contribution from large flux events

From the time series of Γ_n, shown in Fig. 6.2(c), it can be seen that the flux events occur with a periodic behavior. This figure corresponds to coherent fluctuations in argon plasma at $B_T \sim 220\,G$. The time series, however, show sharp variations with flux shooting up to large amplitudes during each cycle over a small time window indicating bursty nature, a characteristic of the non-Gaussian distribution. It means that, the time series of the fluctuation induced flux indicate the large amplitude flux events occurring periodically. The contribution from bursty events to the average fluctuation induced flux can be described quantitatively by a comparison of cumulative flux fraction and cumulative probability of the flux events. The cumulative probability for $\Gamma_n' > \Gamma_n$ from the upper limit is given by

$$p_{>\Gamma_n} = \sum_{\Gamma_n}^{\infty} p(\Gamma_n'). \tag{6.5}$$

Similarly, cumulative flux fraction is given by

$$F_{>\Gamma_n} = \sum_{\Gamma_n}^{\infty} p(\Gamma_n')\Gamma_n'. \tag{6.6}$$

A plot of cumulative probability versus cumulative flux fraction for argon plasma with $B_T \sim 220\,G$, at $\pm 7\,cm$ is shown in Fig. 6.8. These plots can be interpreted as follows. The point on flux fraction at which the cumulative probability becomes 1, indicates the average flux in normalized units. Drawing a line parallel to the vertical axis from this point, intersects the curve at another point. For example, the curve corresponding to $+7\,cm$ has intercept at ≈ 0.3. This means that, beginning from ∞ (or $\Gamma_{n,max}$), only 30% of the events account for the actual average flux. The remaining 70% of the flux events, which are distributed on positive and negative sides of Γ_n add up approximately to zero.

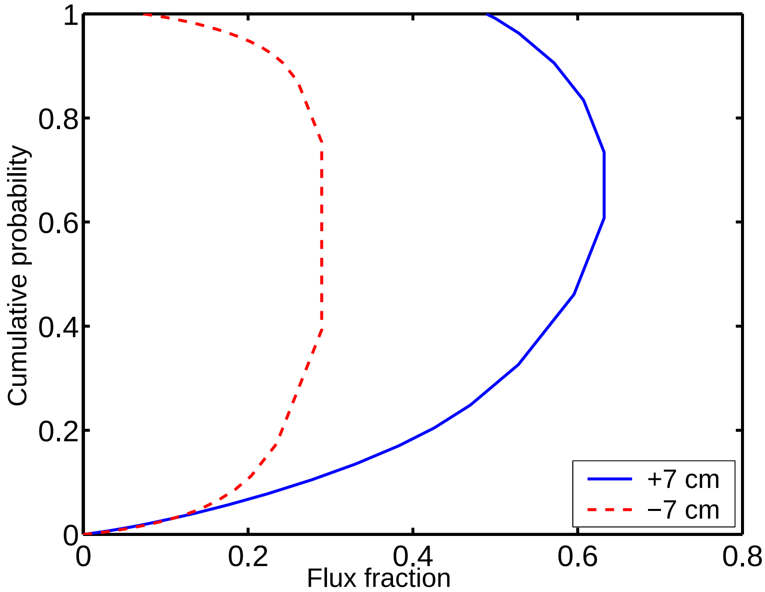

Figure 6.8: A plot of cumulative probability versus cumulative flux fraction for argon plasma with $B_T \sim 220\,G$ at $\pm 7\ cm$.

Quantile-quantile plots

A comparison between the PDFs can be made using quantile-quantile plots. Let p_1 and p_2 are two PDFs to be compared with corresponding cumulative PDFs F_1 and F_2, from the lower limit, defined as

$$F_i(\Gamma_n) = \sum_{-\infty}^{\Gamma'_n} p_i(\Gamma'_n), \tag{6.7}$$

where $i = 1, 2$. A plot of $\Delta F \equiv F_1 - F_2$ vs F_1, describes how equivalent are the two PDFs. If one of the PDFs above, is the theoretical representation of the other which is estimated from the experiments and if the plot of ΔF vs F_1 show scattered points, around $\Delta F = 0$, then it indicates that ΔF is due to the statistical noise. If the above plot shows a continuous function, then the theoretical PDF is not a good representation of the experimentally obtained PDF. On the other hand, if the comparison of two experimentally obtained PDFs corresponding to two different radial locations gives a continuous function in the plot of ΔF vs F_1, it would mean that the two PDFs are not equivalent or cannot be represented by a single analytical expression. The deviation of PDF from Gaussianity is attributed to a coupling between the density and electric field fluctuations, which is a measure of cross-phase between them [65]. Quantile-quantile plots corresponding to PDFs at various radial locations on LFS, with respect to the PDF at $+7\,cm$ for argon plasma at $B_T \sim 220\,G$ are shown in Fig. 6.9. None of the ΔF plots in the above

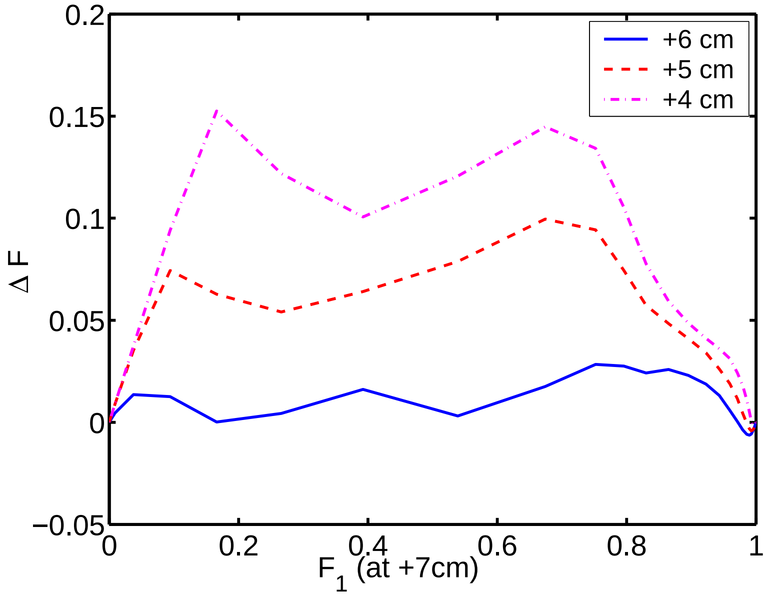

Figure 6.9: A quantile-quantile plot of PDFs at few radial locations for argon plasma at $B_T \sim 220\,G$ with respect to the PDF at $+7\,cm$. ΔF is calculated with F_2 corresponding to the location shown in the legend.

figure show random variations about $\Delta F = 0$. Moving far from $+7\,cm$, however, the variations in ΔF plots increase systematically. It can be believed, therefore, that an analytical expression for PDF at $+7\,cm$ progressively deviates on moving towards $+4\,cm$. The variations in PDF can be attributed to changes in the cross-phase between density and electric field fluctuations.

6.2.3 Effect of magnetic field

The effect of toroidal magnetic field on the radial profile of fluctuation induced poloidal flux is described in Chapter 4. The comparative plot of $\langle \Gamma_T \rangle \sim \Gamma_{fluct}$, the fluctuation induced poloidal flux, with B_T is shown in Fig. 4.11. It can be observed from this figure that, though $\langle \Gamma_T \rangle$ for $220\,G$ is significant in the entire range of $+2\,cm < r < +7\,cm$, for higher B_T, it becomes significant in the region

$r \geq +4\,cm$ only. From the above mentioned work, it has been also seen that the nature of fluctuations changes from coherent to turbulence with change in B_T from 220 G to 440 G. But the magnitude of $\langle \Gamma_T \rangle$ at the limiter's edge on LFS remains in the same order of magnitude for all values of B_T. Consequently, the time series of $Gamma_T$ indicate intermittent flux events, at higher B_T values, hence increased bursty nature. The flux behavior at high B_T is, therefore, highly non-periodic in nature unlike the 220 G case. A comparison of PDFs for three values of B_T is shown in Fig. 6.10; the corresponding flux fraction function are shown in Fig. 6.11. Changing B_T from 220 G to 440 G, significant variation is

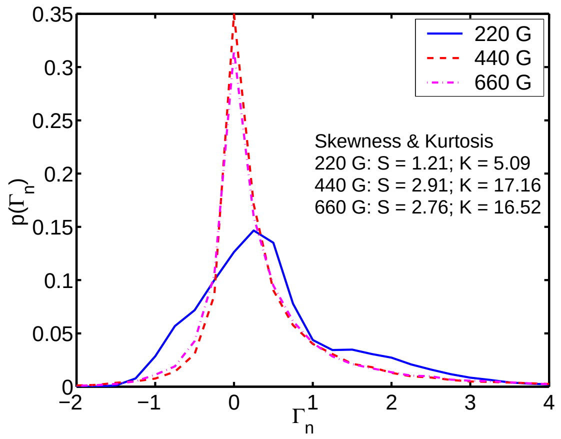

Figure 6.10: PDF of fluctuation induced poloidal flux for argon at $+7\,cm$ for different values of B_T.

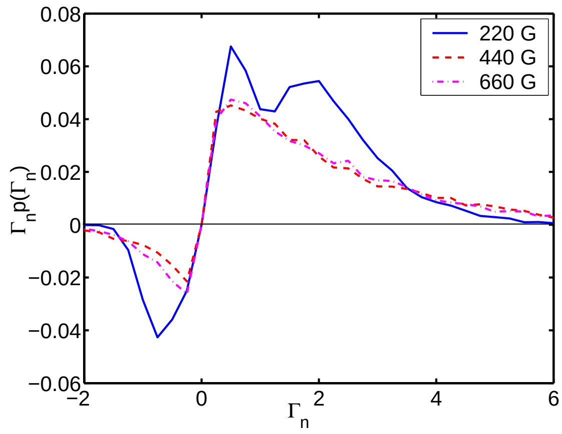

Figure 6.11: Flux fraction function of fluctuation induced poloidal flux for argon at $+7\,cm$ for different values of B_T.

seen in the PDF and the flux fraction, from these figures; however, no significant variation is seen on further change in B_T to 660 G. The occurrence of only minor variations in statistical properties of the fluctuation induced poloidal flux, is in accordance with the minor variations observed in the power spectra and nature of fluctuations from the instability analysis in Sec.4.7.

6.2.4 Effect of ion mass

Discharges have been produced with different gases such as argon, krypton and xenon at a given $B_T \sim 220\,G$, to study the role of ion mass in fluctuations, consequent poloidal flows and mean profiles as described in Chapter 5. The comparative plot of $\langle \Gamma_T \rangle \sim \Gamma_{fluct}$ for all different gases is shown in Fig. 5.4. The average fluctuation induced flux $\langle \Gamma_T \rangle$ is significant for all the ion mass, however, decreases with increase in ion mass; $\langle \Gamma_T \rangle$ decreases radially outward in the region $+4\,cm < r < +9\,cm$ for all gases. The fluctuation spectra changes from coherent at argon to turbulent for krypton and xenon. Consequently, the time series plot of the fluctuation induced flux indicate intermittent flux events and hence the bursty nature. The periodicity of the flux events is, therefore, not seen for krypton and xenon discharges. Comparative plots of PDFs at $+4\,cm$ and corresponding flux fractions are shown in Fig. 6.12 and Fig. 6.13 respectively. In the PDF plots, the

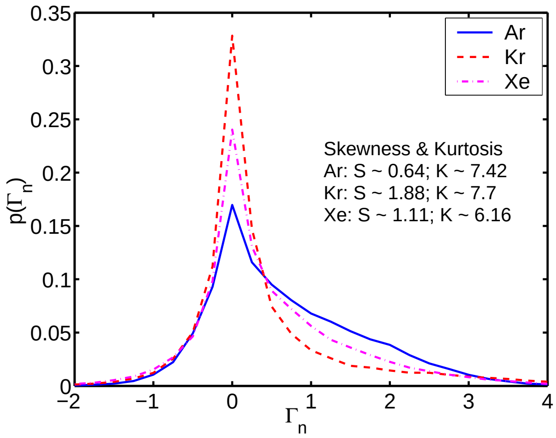

Figure 6.12: PDF of fluctuation induced poloidal flux with $B_T \sim 220\,G$ at $+4\,cm$, for different gases.

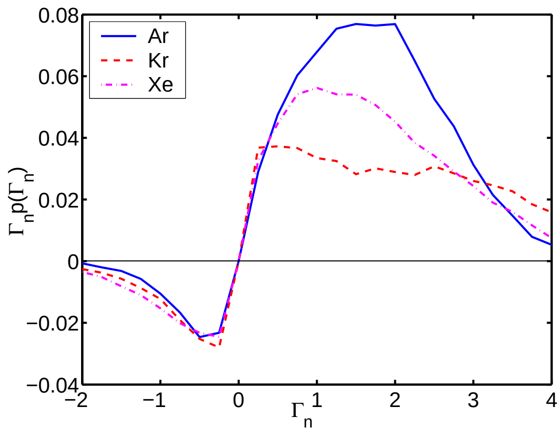

Figure 6.13: Flux fraction function of fluctuation induced poloidal flux with $B_T \sim 220\,G$ at $+4\,cm$, for different gases.

tail on the negative side of Γ_n has negligible variations with ion mass; however, a non-monotonic change is seen with increase in ion mass. Consequently, the flux fraction on the negative side has negligible variation with change in ion mass, whereas non-monotonic variations are reflected on the positive side from argon to xenon.

6.3 Fluctuation induced radial flux - Statistical analysis

In fusion devices such as tokamaks, fluctuation induced radial flux of charge particles is one of the mechanisms degrading the plasma confinement. Regardless of the shape of the plasma and typical plasma parameters, strong similarities are found in statistical properties of the fluctuation induced radial flux in different fusion devices [65]. The poloidal electric field fluctuations lead to $\tilde{\mathbf{E}}_\theta \times \mathbf{B}$ radial flux, where $\tilde{\mathbf{E}}_\theta$ indicates fluctuating poloidal electric field. The estimation of Γ_T and Γ_n is similar to that described in Sec.6.2, with E_r replaced by E_θ. The statistical properties of the fluctuation induced radial flux are obtained and the significant features are discussed.

The fluctuation induced radial flux on LFS is found to be along the major radius, similar to that observed in fusion devices. A plot of PDFs of fluctuation induced radial flux at few radial locations is shown in Fig. 6.14. The corresponding flux fraction function is shown in Fig. 6.15. The PDFs show minor variations on nega-

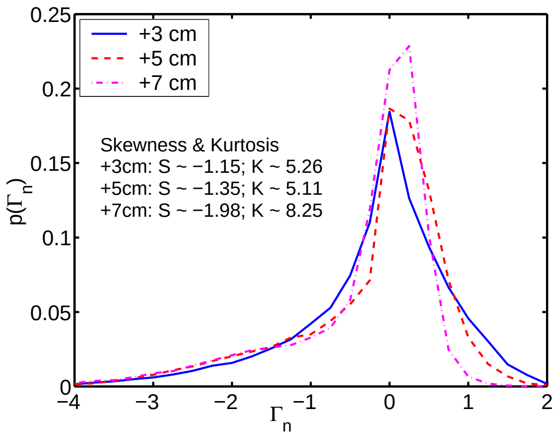

Figure 6.14: PDF of fluctuation induced radial flux for argon with 220 G, at different radial locations on LFS.

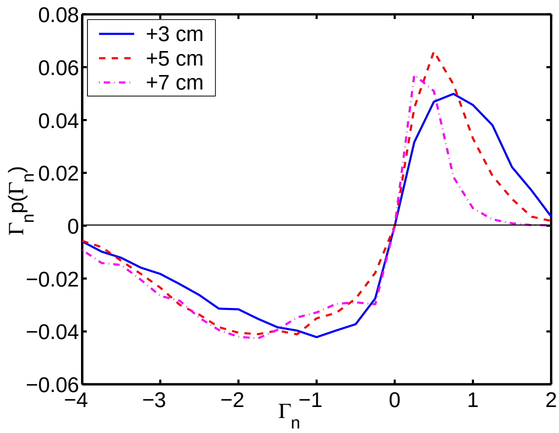

Figure 6.15: Flux fraction function of fluctuation induced radial flux for argon with 220 G at different radial locations on LFS.

tive side of Γ_n, whereas significant variations on positive side moving far from the minor axis. The PDFs, therefore, appear to be skewed to the left. Similar variations are seen in flux fraction. The flux fraction function also indicates that, as one moves radially away from the minor axis, the inward flux events are reduced, and the contribution from the large flux events, to the average flux is significant.

The variations in PDFs and the flux fraction function at $+7\,cm$ with change in B_T are shown in Fig. 6.16 and Fig. 6.17 respectively. Significant variation occurs

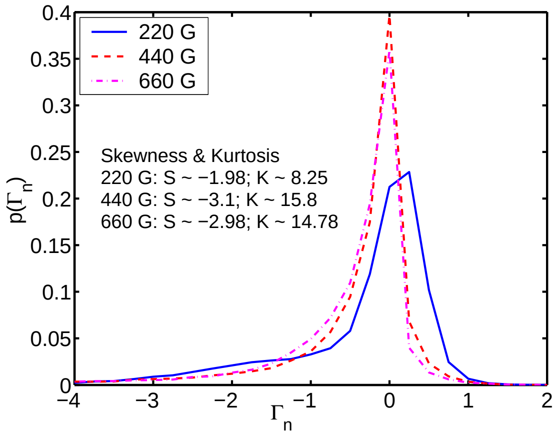

Figure 6.16: PDF of fluctuation induced radial flux for argon at three values of B_T.

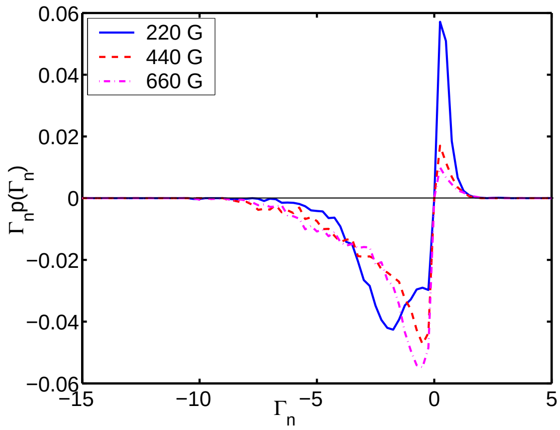

Figure 6.17: Flux fraction function of fluctuation induced radial flux for argon at three values of B_T.

in PDFs on positive side of Γ_n changing B_T from 220 G to 440 G; the PDFs are skewed to the left, which is also indicated by the parameter S. On further change in B_T to 660 G, only minor variations occur in PDF. The variations in PDFs are reflected in flux fraction functions for positive Γ_n.

The variations in PDFs and the flux fraction function for different gases, at +4 cm are shown in Fig. 6.18 and Fig. 6.19 respectively. Non-monotonic variations in

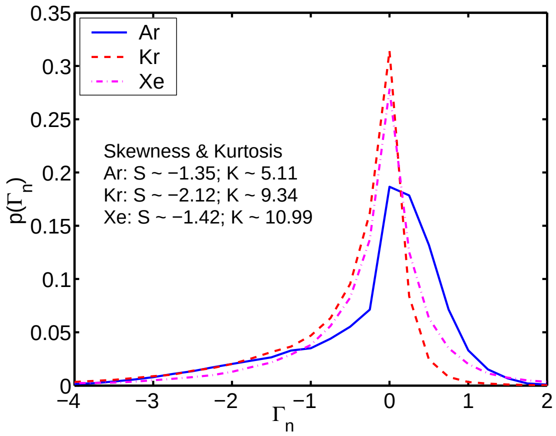

Figure 6.18: PDF of fluctuation induced radial flux at 220 G for three gases.

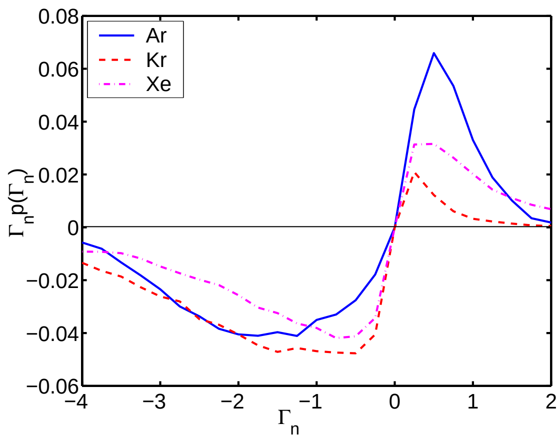

Figure 6.19: Flux fraction function of fluctuation induced radial flux at 220 G for three gases.

PDFs of fluctuation induced radial flux with increase in ion mass are observed, which also reflect in the flux fraction function.

6.4 Summary

In a simple toroidal plasma, electric field fluctuations accompanied by fluctuations in density, lead to finite fluctuation induced flux. The radial electric field fluctuations lead to poloidal flux, and the poloidal electric field fluctuations lead to radial flux. The time series of fluctuation induced flux normalized to the fluctuation rms of the flux, is in general found to have an uneven distribution around the zero axis. The PDF of the fluctuation induced flux events gives a quantitative representation of the above stated uneven distribution in terms of symmetry and flatness of the profiles, quantified by skewness and kurtosis respectively. The flux fraction function indicates the direction of the resultant average flux.

On LFS, for argon plasma at $B_T \sim 220\,G$, the PDFs at different radial locations are dissimilar in nature. This signifies that the nature of fluctuation induced flux can vary locally. A comparison from quantile-quantile plots shows that, on moving radially away from one location, the PDF of the fluctuation induced flux changes systematically. A single analytic expression, therefore, cannot exist to account for the PDFs at different radial locations. On HFS, the PDFs are relatively more symmetric as compared to LFS, resulting in lower magnitudes of average fluctuation induced flux. Another important feature of the fluctuation induced flux observed is its bursty nature. Consequently, the flux events have intermittent and non-Gaussian behavior. The non-Gaussian or near-Gaussian nature of the flux indicates a finite coupling between the density and electric field fluctuations. The deviation from Gaussianity is a measure of cross-phase between the density and electric field fluctuations which is found to vary as seen in previous chapters. The fluctuation induced flux on LFS is characterized by large flux events, at some radial locations, leading to a double hump in the flux fraction function. The contribution to the average flux from the large flux events can be observed quantitatively from the comparison of cumulative flux fraction and cumulative PDF.

On varying toroidal magnetic field, a transition occurs in the nature of fluctuations highly coherent at low magnetic field to turbulent at a higher magnetic field, as described in Chapter 4; further increase in magnetic field do not show any significant impact on the nature of fluctuations. With varying magnetic field the intermittency of the bursts of flux increases. At low magnetic field 220 G, the flux events are relatively more periodic in nature. In the analysis for statistical properties, a significant change is seen in PDFs accompanying the above transition from coherent to turbulent fluctuations. The PDFs remain comparable on further increase in magnetic field, i.e. from 440 G to 660 G. It appears, therefore, that the nature of fluctuation induced poloidal flux is significantly different in coherence and turbulent conditions. On varying ion mass, though a transition to turbulence occurs from argon to krypton and xenon, a monotonic change in the PDFs is not seen.

The fluctuation induced radial flux is found to be radially outward. This flux is characterized by large flux events in the edge of the limiter, similar to the edge plasma in fusion devices. On varying the the magnetic field, the variations in PDF occur similar to the case of the fluctuation induced poloidal flux; that is significant variation occurs in PDFs accompanied by transition from coherent to turbulence. In the case of varying the ion mass, the change in the PDFs for fluctuation induced radial flux is non-monotonic, as occurs in the case of fluctuation induced poloidal flux.

In summary, the fluctuation induced flux shows non-Gaussian distribution of flux events. Interestingly, the bursty events occur in both the quantities, that is fluctuation induced poloidal flux and radial flux. The periodicity in the flux events reduces with transition to turbulence. The statistical properties of the fluctuation induced flux are similar to the transport properties in tokamaks, under turbulent conditions.

The important conclusions from various experimental investigations, subsequent theoretical and statistical understanding in this thesis are described in the next chapter. From present understanding, the scope for further investigations is presented.

7

Conclusions and future scope

7.1 Conclusions

Generation of plasma flow and its connection to the electric field and magnetic field fluctuations are the phenomena of fundamental interest in astrophysical plasmas as well as the plasmas confined in the laboratory. In toroidal fusion devices such as tokamaks and stellarators, though fluctuations play an important role in a variety of transport of particles and energy, some of these mechanisms are found to severely degrade the confinement. To investigate the role of fluctuations in transport in toroidal configurations, a simple toroidal device has proven to be a good alternate choice.

In a simple toroidal plasma, the curvature and gradient drifts lead to vertical charge separation, hence a vertical electric field $\mathbf{E_z}$. Consequently, $\mathbf{E_z} \times \mathbf{B}$ drift leads to the outward radial transport of particles; therefore, equilibrium does not exist in a simple toroidal plasma. In the experimental observations reported in Chapter 3, presence of large fluctuations and radially well spread mean profiles are seen in current limited discharges. The discharge is produced with argon gas at a toroidal magnetic field of $220\,G$ and a discharge current of $5\,A$. On removing the current limit (i.e. same as constant voltage condition), a significant shift in the mean profiles is seen, outward along the major radius. In the intermediate regime, the fluctuation levels change intermittently. Simultaneous measurement of ion saturation current on LFS and HFS have indicated a possible time correlation between the onset of large fluctuations on LFS and density build-up on HFS region, which otherwise has low densities. These observations reveal a possible connection between the existence of fluctuations and poloidal flows. In order to make quantitative studies, measurement of poloidal flows is carried out. The net (or total) poloidal flow is obtained using a flow probe. The mean electric field driven poloidal flow is derived from plasma potential profiles, directly measured using an emissive probe. From the fluctuation induced poloidal flux, estimated from measurements using a radial array of probes, an average fluctuation driven poloidal flow is calculated. The fluctuation driven flow can be finite depending on the cross-phase of density and potential fluctuations. A significant difference exists between the net flow and mean electric field driven flow. The estimated fluctuation driven flow is found to partially account for the difference between the net flow and mean electric field driven flow. Additional poloidal flow mechanisms can exist, apart from mean and fluctuating electric field driven poloidal flows. Through these studies, the role of fluctuation driven poloidal flow as an "effective rotational transform" has been elucidated.

The coherence and cross-phase between density and potential fluctuations are, in general, characteristic of the instabilities generating the fluctuations. Magnetic field is found to be an important control parameter to obtain transitions in fluctuation regimes in a simple toroidal plasma. Establishing the fluctuation-flow connection associated with mean profiles in argon plasma at $220\,G$ as described in Chapter 3, varying the strength of the magnetic field, changes in the nature of fluctuations, poloidal flow generation and attaining mean profiles are investigated. The results are presented in Chapter 4. A transition occurs in the nature of fluctuations from highly coherent at low magnetic field to turbulent at high magnetic field. The transition to turbulence is found to be accompanied by enhanced poloidal flow on HFS; the net flow velocity is found to exceed ion acoustic velocity for $660\,G$ on HFS; thus the flow is compressible on HFS. The increased flow on HFS is accompanied by increased densities, and hence, enhanced confinement. On LFS, however, no significant change in the poloidal flow is observed with increase in magnetic field strength. The frequency of the dominant mode is found to be of the order of the Doppler shift, i.e. consistent with the estimated dispersion relation and the poloidal flow velocity. On examining the coherence and cross-phase, the dominant fluctuations on HFS appear to be flute-like at all the magnetic field values, which are possibly due to K-H instability; on LFS the R-T fluctuations at low magnetic field tend to become resistive R-T type at high magnetic field values. Through this work, it is demonstrated for the first time that in a toroidal compressible plasma, an intimate relationship exists between the fluctuations, self-consistently generated flows and enhance confinement.

Through the experimental studies reported in Chapter 4, it is understood that change in the nature of fluctuations with increasing magnetic field is associated with enhanced flow and improved confinement. Plasma flow is intrinsically associated with ion mass, thus making it another important parameter through which the mean plasma profiles and transport in a simple toroidal plasma can vary. In general, the experimental investigation of confinement with mass scaling in tokamak have indicated that the confinement increases with increase in ion mass, which is opposite to the theoretical prediction. In the present experimental studies, a change in the nature of fluctuations, consequent flows and mean profiles is investigated for different gases, viz. argon, krypton and xenon. The results are presented in Chapter 5. The net poloidal flow and the fundamental frequency of fluctuations, which is seen to be approximately the rotation frequency of the plasma itself, are found to increase with decrease in ion mass. Highly coherent fluctuations which occur in the case of argon, become turbulent at higher ion mass. The dominant fluctuations are, however, found to be flute-like for all ion masses.

The statistical properties of the time series of fluctuation induced poloidal flux indicates that the flux is characterized by the presence of large sporadic transport bursts. The probability distribution function (PDF) of the fluctuation induced flux is non-Gaussian in nature. Though PDFs of the flux show systematic variation with the control parameters, they remain non-Gaussian at all the conditions. This in turn indicate a finite coupling between the density and potential fluctuations. The non-Gaussian nature is also seen in the case of fluctuation induced radial flux.

In summary, fluctuations and intrinsic poloidal flow generation and their role in sustaining mean profiles in a current less toroidal plasma is investigated for the first time in a simple toroidal device, under various fluctuation regimes. The variation in fluctuation regime is achieved by two control parameters namely magnetic field strength and mass of the species. At first, the nature of fluctuations is found to vary with increase in magnetic field; the consequent mean plasma profiles and poloidal flows are obtained. Enhanced poloidal flows and improved densities are seen with increasing magnetic field. In the second part, the nature of the fluctuations is also found to vary with increase in ion mass, the corresponding mean plasma profiles and poloidal flows are estimated. Reduced poloidal flows are observed with increase in ion mass. The underlying mechanism of the instabilities under various fluctuation regimes is identified. This thesis provides the first clear experimental evidence for generation of intrinsic poloidal flow from fluctuations and hence may be regarded as partial support to the model of flow-fluctuation cycle as a mechanism of producing an “effective rotational transform”, in a simple toroidal device.

7.2 Future scope

From the experimental investigation of poloidal flows described in this thesis, the net poloidal flow could not be accounted by the sum of the mean and fluctuating electric field driven flows. The unaccounted difference was attributed to either limitations in the accurate calibration for Mach probe measurement of flow or the presence of additional poloidal flow mechanisms. An attempt is made to check for the additional flow mechanisms as follows. The net flow velocity calculation is based on ion saturation currents, upstream and downstream to the flow. One possible additional mechanism of poloidal flow is the diamagnetic drift of ions. Since the ion temperature is known to be small, consistently the diamagnetic drift is also found to be small. For example, in the case of argon plasma at $220\,G$, with $kT_i/e \sim 0.1\,eV$, $L_n^{-1} \sim 15\,m^{-1}$, the diamagnetic drift $v_{Di} = (kT_i/eB)(L_n^{-1}) \sim 70\,m/s$, which is small. The diamagnetic drift of ions, therefore, cannot account for the unaccounted difference of the poloidal flow. Experimental and theoretical investigations may be carried further to check for other possible mechanisms.

In the present work, the experimental results are in partial agreement with the ‘flow-fluctuation cycle’ in a simple toroidal plasma, i.e. fluctuation driving a poloidal flow. The role of radial velocity fluctuations in creating effective ponderomotive force is not investigated. The experimental investigation of this mechanism will lead to a complete demonstration of flow-fluctuation cycle experimentally, and hence explains the existence of "effective rotational transform" in a simple toroidal plasma.

The magnetic field topology in a simple toroidal plasma is known to play a crucial role in the nature of the instabilities. At a given toroidal magnetic field strength, varying the vertical magnetic field, the helicity of the magnetic field lines oriented in the vertical direction can be changed. Measurements of this kind have indicated transitions in the fluctuation regimes from ideal interchange to resistive interchange and drift-waves [40]. A study on change in the nature of the poloidal transport on possible transitions in fluctuations with magnetic field helicity is desirable. The vertical magnetic field is, therefore, another control parameter in addition to the toroidal magnetic field and ion mass which have been done in this thesis.

In the present investigations in a simple toroidal plasma, a radial potential well is essentially sustained under large fluctuation regimes, leading to mean electric field driven poloidal flow. The presence of radially varying excess negative charge is believed to be important in sustaining the potential well. It can be desirable to investigate the phenomena of flows and fluctuations with multiple filaments; for example, a second filament in addition to the present single filament. The peaked nature of density profiles produced with multiple filament source can offer an easier control of the gradients in plasma profiles and result in changes in the nature of fluctuations. Obtaining radial profiles of mean and fluctuating plasma parameters, poloidal flow quantities and nature of fluctuations will be the subject of interest, for the plasma produced with more than one filament.

The density profiles produced on striking a discharge using a filament has been seen to lead to a peaked density profiles, as stated above. It is also possible to sustain a discharge using radio frequency (RF) source. In this method, profiles with reduced density gradient may be produced. Study of fluctuations and flows in this regime can be an interesting task and comparison with filament based studies reported here, may throw important insight into the problem.

A

Fast electron spread in filament assisted discharge

A.1 Filament source - Origin of fast electrons

In simple toroidal device with pure toroidal magnetic field, plasma is commonly produced using either a hot filament or electron cyclotron waves. In addition to these two methods, plasma production using lower hybrid waves was also demonstrated in ACT-I [17]. The filament is in general mounted vertically, heated to sufficient high temperatures for thermionic emission and biased negatively with respect to the conducting vessel wall. The emitted electrons, though possibly confined to a narrow vertical region in the neighborhood of the magnetic field lines intercepting the filament, may undergo vertical drift due to gradient and curvature in magnetic field, and consequently $\mathbf{E_z} \times \mathbf{B}$ drift along the major radius.

A.1.1 Thermionic emission

On heating a uniform metal surface to a temperature T, the electron current density emitted from its surface is given by Richardson-Dushman formula [106]

$$J = AT^2 exp(-b/T), \tag{A.1}$$

where the coefficient A was believed to be a constant, b is the work function characteristic of the metal. Later it was found that the coefficients A and b defined in Eq.(A.1) depend on other parameters; typically A is of the form $A = U(1 - r)$

where U is a universal constant given by $120\, A/cm^2K^2$, r is the electron reflection coefficient; b is a function of T [107]. The emission current density given by Eq.(A.1) is referred to as the temperature saturated emission current which largely depends on temperature T for a given metal.

A.1.2 Emission saturation

If a metal surface is heated to a temperature T to emit electrons, the true electron current density that is emitted need not be the same as given by the Eq.(A.1). This is because the electron emission in an accelerating field never becomes completely saturated. Any escaping electron is attracted back towards the metal by a force due to the induced positive charge on the metal surface, which is referred as Schottky effect [108]. Close to the metal surface, there exists a potential barrier at a distance known as critical distance, which depends on the externally applied accelerating electric field and the inter-atomic structure in the metal. This critical distance can be one or two orders higher than the inter-atomic distances or some times of the same order for large external electric fields. If the electron escapes this barrier, then it can be referred as emitted.

Above description refers to a single electron crossing the potential barrier, formed due to the potential modified by the inter-atomic structure of the metal. The current of electrons that flows in high vacuum from a hot cathode to an anode increases at first and then becomes saturated, with space charge distribution in accord with Poisson's equation. This is due to the excess space charge modifying the potential profile in the vacuum which is referred as space charge effect [109]. This can be illustrated best by considering an electron flow between a set of parallel planes; the passage of electrons emitted from a hot cathode plate at zero potential to an anode plate with potential V, at a distance d. When the emission current (I) from the cathode is low, the potential profile is linear; as I increases, the electron-charge modifies the potential profile between the plates. The accelerating electric field at the surface of cathode is maximum (V/d) at low emission, starts reducing with an increase in the emission, eventually reaches zero for sufficiently large I. Assuming that the electrons are emitted with negligible velocities, further increase in cathode temperature will not increase the emission current. This is because the electric field can become negative at cathode surface, therefore the electron is repelled back to cathode. The upper limit on the current density that can flow between the above set of parallel planes is known as space charge limited current, given by Child-Langmuir law [110],

$$I = \frac{2^{1/2}}{9\pi}\left(\frac{e}{m}\right)^{1/2}\frac{V^{3/2}}{d^2}, \tag{A.2}$$

where e and m are charge and mass respectively for electron. Substituting these values, we get

$$I = 2.334 \times 10^{-6} V^{3/2} d^{-2} A.cm^{-2}. \tag{A.3}$$

For a given set of parallel plates with a fixed distance, the maximum current density flowing between the plates is given by Eq.(A.3); therefore the current density is limited by the applied voltage. In the filament produced plasma, assuming the edge of the sheath surrounding the filament as the anode, an approximate sheath thickness can be estimated. Using the Eq.(A.3), for 5 A of discharge current emitted from filament biased to $-60\,V$, the approximate sheath thickness turns out to be 0.5 mm. If the electrons are emitted with finite initial velocities, then the space charge limited current is modified such that, a sufficient negative field has to appear close to cathode to repel the electrons back. In other words, the space charge limited current increases with increase in emission velocity of electrons.

A.1.3 Current carrying filament in toroidal magnetic field

In present experiments, a 2 mm diameter tungsten filament is heated to high temperature by passing 150 A of filament current (I_f) typically. Due to the large current through the filament, a magnetic field of $\sim$ 300 G is generated at the surface of the filament. Since this field is comparable to the externally applied magnetic field, the electron emission from the filament can be affected. The electron executes a complicated trajectory as soon as it is emitted; therefore a finite probability exists for the electron to get trapped by the filament [89]. Therefore the emitted electron population and the breakdown to sustain discharge can be affected.

The hot filament with current (I_f) flowing along a unit vector $\hat{\mathbf{I}}$ perpendicular to the external toroidal magnetic field ($\mathbf{B_T}$), is subject to a force $\mathbf{F_l} = I_f(\hat{\mathbf{l}} \times \mathbf{B_T})$ force. Since the current flows in the vertical direction, the force is either along or opposite to the major radius. The typical force per unit length on the filament is $3\ N/m$. Therefore the hot filament will bend when the toroidal magnetic field is ON which leads to a small shift in the source region during the discharge.

A.2 Spatial spread of residual primary electrons

A.2.1 Residual primary electrons - Theoretical back ground

The electrons emitted from the negatively biased hot filament are accelerated across the sheath surrounding the filament, gaining energy equal to the voltage drop across the sheath. These electrons which are referred to as primary electrons, possess energy typically of the order of the bias to filament. The primary electrons lose their energy due to the inelastic collision with neutral gas atoms, such as atomic excitations and ionization. All the collisions of a primary electron with neutral gas atoms will not lead to ionization, though it possesses energy higher than ionization energy of the gas atom. For instance, in Townsend's original theory of ionization by collisions, it was assumed that ionization of gas atoms or molecule occurs whenever it is struck by an electron whose speed exceeds the minimum ionizing speed. It was found later that the probability of ionization is, however, zero for impact energies up to the ionizing potential, then increases to a maximum which is less than 0.5 at impact energies of about $150\,eV$, followed by a decrease as the energy is further increased up to $1000\,eV$ [111]. For inelastic scattering of primary electrons by argon atoms, the cross section is given by $\sigma \sim 2.5 \times 10^{-16}\ cm^2$ for electron incident with typical energy $\sim 50\ eV$. If the neutral density of argon atoms is n_n, the mean free path for the primary electrons is,

$$\lambda_m = \frac{1}{n_n \sigma}. \tag{A.4}$$

For a neutral pressure of $1 \times 10^{-4}\ torr$, $n_n = 3.5 \times 10^{12}\ cm^{-3}$. Therefore $\lambda_m \sim 1.1 \times 10^3\ cm = 11\ m$. With the major radius $R = 0.45\ m$, the half circumference $\pi R = 1.41\ m$ and $\lambda_m \gg \pi R$. This has following interesting consequences:

- primary electrons execute few circuits toroidally before losing their energy,

- the primary electrons exist toroidally far from the filament.

A.2.2 Experimental determination of the spread

It is important to know the spatial spread of primary electrons in a simple toroidal plasma because,

1. this region is believed to be the source region of the plasma, where maximum ionizing collisions would occur,
2. if this region retains excess of negative charge even after the discharge is sustained, it will result in a potential well leading to the rotation of the plasma.
3. the presence of energetic primary electrons will affect interpretation of measurement by Langmuir probes and other charge flux probes [112].

The primary electrons posses high energy which is typically much larger than the thermal electron temperature (T_e) of the bulk plasma. Therefore detection of these electrons is possible with a suitable application of potential barriers. A retarding field energy analyzer (RFEA) is an instrument using which a beam or a distribution of charged particles can be detected. In the following, the construction of RFEA used in BETA for the detection of residual primary electrons, the method of operation and the measurements are described.

RFEA construction

The retarding field energy analyzer (RFEA) used to probe the radial spread of fast electrons consists of a stack of a slit, two grids and a collector plate. A schematic of RFEA is shown in Fig. A.1. Stainless steel (SS) mesh with dimensions of $0.13 \times 0.13 \times 0.07\, mm^3$, is used for making grids. The geometrical transmission through the grid is approximately 40%. The entrance slit (S) is a circular hole with a diameter of $0.8\, mm$ in a SS plate at the front end of RFEA, in contact with the plasma. Since slit aperture is much larger than Debye length, slit plate does not have a control on the potential of entire aperture. However the slit aperture will be useful in allowing only a thin beam of electrons to be transmitted inside RFEA. The entrance slit is followed by grid-1 (G1), whose purpose is to repel all positive

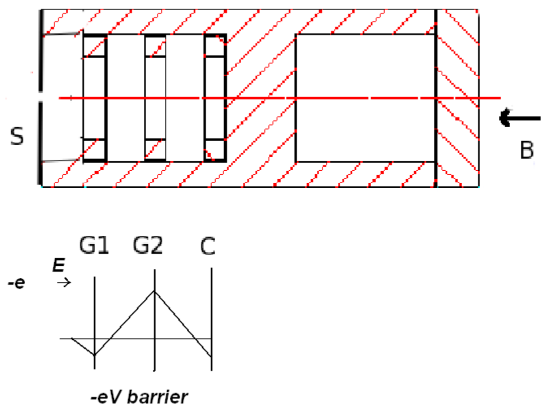

Figure A.1: A schematic view of cross-section of a RFEA. In the bottom, a schematic of the potential barrier for electron is shown; the electron will be transmitted if $E > -eV_{G2}$.

ions. The grid-1 is followed by grid-2 which is the electron repeller, to selectively transmit the electrons by varying the potential barrier over its surface. Since grid-1 and grid-2 are made of mesh with a size less than twice the Debye length, the potential barrier over the grids can be controlled by the grid bias voltage. The grid-2 is followed by collector plate (c), to collect the transmitted electrons from grid-2. Collector is made of a SS plate of diameter $8\,mm$. The successive components are separated by ceramic washers with $10\,mm$ inter-spacing. The entire stack is mounted in a ceramic housing. The axis of the cylindrical stack of RFEA is aligned along the toroidal magnetic field. The entrance grid is grounded. Working with RFEA to find the radial spread of fast electrons, grid-1 is given a sufficient positive bias to repel all the ions. The grid-2 is biased to a negative voltage which is varied from shot to shot during the pulsed operation of plasma discharge. The selectively transmitted electrons are collected at the surface of collector plate and the collector current is measured across a resistance, typically $1-10\,k\Omega$ in the path connecting from collector to the ground.

RFEA operation

The detection of residual primary electrons or fast electrons in the plasma is performed by selectively transmitting the electrons with an energy above a threshold. The schematic electrical connections for RFEA components are shown in Fig. A.2, which illustrates its principle of operation. The entrance slit-plate of the RFEA is

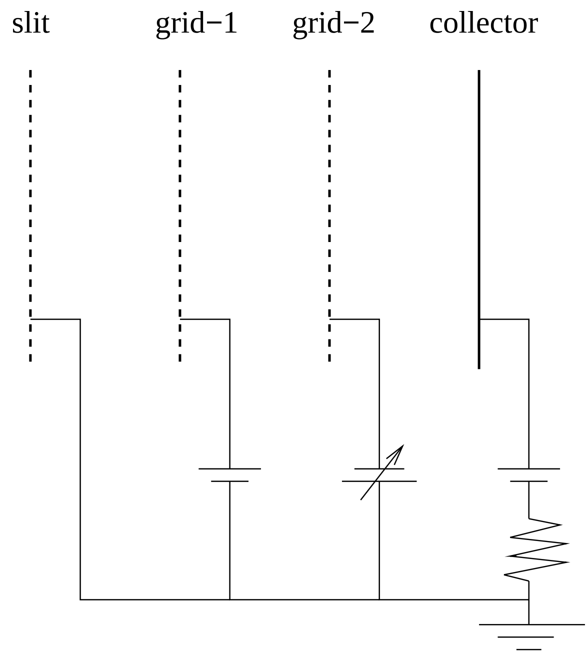

Figure A.2: Schematic electrical connections to the components of RFEA is shown.

grounded. The grid-1 (G1) is positively biased to repel all the ions, that are transmitted through the slit. Since the ion temperature T_i is small and $T_i \ll T_e$, a small positive bias above plasma potential is sufficient to repel all the ions. The typical plasma potential ϕ_p, as shown in the subsequent experimental results described in Sec.3.5.2, lies in a range $-10\,V < \phi_p < +5\,V$. The voltage applied on grid-1 is $+20\,V$ with respect to the ground potential. The grid-2 is negatively biased with respect to ground to selectively transmit the electrons. The selective transmission of the electrons is achieved by the application of a variable discriminating voltage on grid-2. For a perfectly collimated beam of electron current I_{beam} with mono energetic species of energy E, the current transmitted through grid-2 with a negative bias V_{G2}, is a step function which can be described as [48],

$$I = \begin{cases} I_{beam} & \text{for } V_{G2} > |E|/(-e), \\ 0 & \text{for } V_{G2} \leq |E|/(-e), \end{cases} \tag{A.5}$$

Real beams always have a momentum and energy spread due to which the above function is never an exact step function, rather have a decay kind of profile at the cut-off voltage. If the electrons incident on grid-2, however, have a distribution in energy then the electron current transmitted through grid-2 with increase in its negative bias, approaches zero asymptotically. The electrons transmitted through grid-2 are incident on the collector plate. The collector plate is biased with a small positive voltage to avoid the formation of virtual cathode due to space charge limited current [51], as described in Sec.A.1.2. The electron current collected by the collector plate is measured across a small resistance. With varying bias on grid-2, the actual energy spread of residual primary electrons can be understood.

Typical discharge - radial profile of fast electrons

The operating conditions chosen for the discharge while determining the typical radial spread of fast electrons are as follows. The neutral pressure is 5×10^{-5} *torr* of argon; the toroidal magnetic field is 215 G or 860 G; the 2 mm diameter filament is heated by passing 150 A of current; the hot filament is biased to $-80\,V$ with respect to the ground potential. The RFEA is mounted in a horizontal mid-plane through a radial port so that the axis of the stack of grids is parallel to the toroidal field. The RFEA is located close to the limiter so that it is far from the toroidal location where the filament is located. With a given negative bias V_{G2} on grid-2, a radial profile of collector current I_c is obtained. RFEA is subsequently moved radially to generate a radial profile of measurements of I_c. The magnitude of I_c is found to be significant in a narrow region with a peak close to the minor axis. The measurements are performed with V_{G2} = -60 V,-80 V, -100 V, -120 V and -140 V. The radial profiles of I_c corresponding to these measurements are shown in Fig. A.3. The peak in I_c occurs close to the minor axis, however, the magnitude of I_c falls to below the measurement resolution with in a small distance on both sides from the peak. As expected, the peak in I_c reduces with increase in V_{G2}. Though the filament bias is -80 V, finite I_c is measured at collector for $V_{G2} > -80V$.

Fast electron profiles: with $\mathbf{B_T}$ and I_f

The current carrying filament in a toroidal magnetic field is subject to a force which is perpendicular to the the direction of I_f and B_T as described in Sec.A.1.3. Changing the direction of I_f, radial profiles of I_c are obtained using RFEA, to check a possible shift in the radial spread of fast electrons; the results are shown in

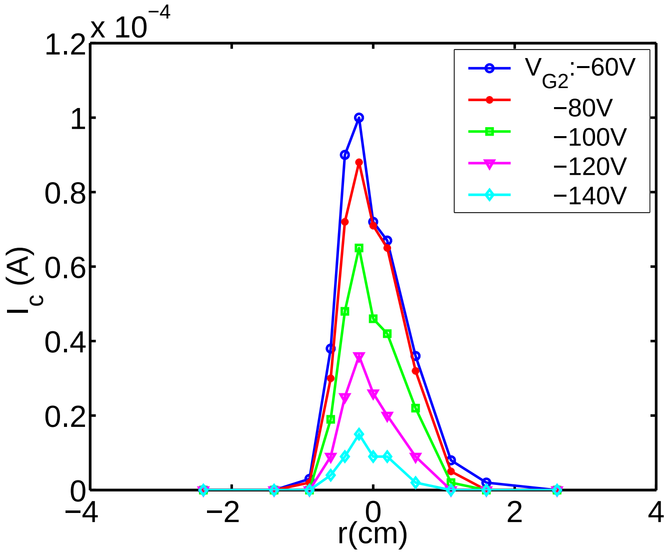

Figure A.3: Radial profile of collector current (I_c), at different repelling voltages on grid-2.

Fig. A.4. In one case I_f is vertically downward and in the other case I_f is upward. With increase in toroidal magnetic field B_T, the larmour radius decreases; hence the vertical drift speed due to $\nabla\mathbf{B}$ and curvature drifts decreases as can be seen from,

$$\bar{v}_{\mathbf{R}+\nabla\mathbf{B}} = \pm\frac{\bar{r}_L}{R_c} v_{th}\hat{z}, \tag{A.6}$$

where r_L is the electron larmor radius, R_c is the radius of curvature of the magnetic field and v_{th} is the thermal velocity of the electron. The reduced vertical drift velocity with increased magnetic field may lead to increased radial spread. The radial profile of I_c are obtained for two magnetic field values, $215\,G$ and $860\,G$ for each direction of the filament current. The Measurements are obtained for a fixed bias of $-70\,V$ on grid-2. The profiles thus obtained are shown in Fig. A.4. The peak of the collector current I_c is found to shift on changing the direction of I_f, which is in accordance with the physical bending of the filament in presence of magnetic field. With all other parameters kept the same, the peak in I_c is found to be lower when the filament bends radially outwards than when the filament bends inward. The observed radial shift in the peak of radial profile of I_c at $215\,G$ is approximately $1.5\,cm$; at $860\,G$, the radial shift is seen to be less than $1\,cm$. With increase in magnetic field, however, increase in the peak of I_c profile is not

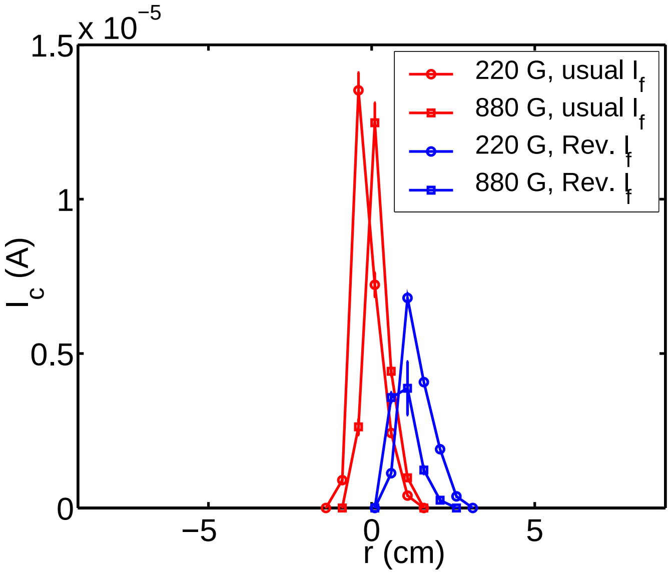

Figure A.4: Radial profile of collector current (I_c) for a fixed bias of V_{G2} =-70 V, two possible directions of filament current, two values of toroidal magnetic field B_T = 215 G and 860 G.

observed.

Measurement issues with RFEA

Though RFEAs are widely used for the detection of electron energy distribution, in most of the cases the application is limited to determine axial energy distribution only [113, 114]. The use of parallel plates produces a uniform axial electric field, due to which only the axial component of the electron velocity is retarded. A parallel beam after passing through an aperture of radius r_0 with collector located at a distance d will have a divergence. The limiting resolution in the energy E of the incident electron is given by

$$\Delta E/E = r_0^2/(16d^2). \tag{A.7}$$

With the mesh open aperture $r_0 = 130\mu m$ and inter plate separation $d = 10\,mm$, $\Delta E/E \sim 1.6 \times 10^{-5}$.

For effective energy dependent retardation of the electrons, the mesh size should be less than twice the sheath thickness in order so that potential over the mesh opening is nearly uniform. The Debye length $\lambda_D \sim 75\mu m$, therefore the above condition is met. As mentioned earlier, the geometrical coefficient calculated from mesh dimensions is 0.4. For such a magnetized plasma, however, there are two more parameters, namely Larmor radius and pitch of the helix executed by the particles, which can influence the actual transmission of charged particles through the mesh [115, 50]. The actual transmission of the electrons is determined by the probability of the escaping of the electrons, without hitting the mesh walls due to gyration. A better estimation for transmission coefficient of incident electrons can be done using Monte Carlo simulations.

Estimation of fast electron density

The collector current I_c of RFEA for a given negative bias on grid-2, is a measure of total electron flux above a cut-off in electron energy. The total electron flux above a cut-off negative voltage, for a given velocity distribution function of electrons, can be obtained by integrating for the area under the curve, above a cut-off velocity. The profiles of I_c obtained with high repelling voltages on grid-2 are believed to be part of the high energetic tail of the distribution function. From the results shown in Fig. A.4 for I_c obtained with a repelling voltage of $V_{G2} = -70\,V$ and toroidal field of $215\,G$, the fast electron density is estimated with following assumptions:

1. the plasma potential ϕ_p is small,
2. all the electrons are incident with an energy $E_f = -70\,V$,
3. the entrance slit with diameter 0.8 mm, weakly alters electron transmission therefore the total transmission coefficient $T = 0.16$, (0.4 for each grid).

The density of fast electrons (n_f) is calculated from

$$I_c = n_f e A v_f \times T, \tag{A.8}$$

where the velocity v_f is calculated from $E_f = (1/2)mv_f^2$, A is the area of slit aperture and e is the magnitude of electron charge. The profile of fast electron density estimated using Eq.(A.8), is shown in Fig. A.5. For comparison, the bulk plasma density is also shown. The bulk plasma density is estimated from ion

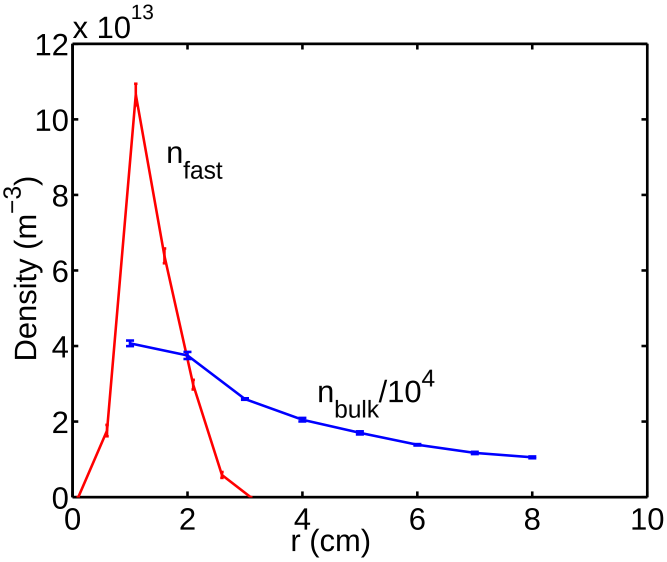

Figure A.5: Fast electron density profile; a comparison with bulk plasma density.

saturation current and the electron temperature obtained from I-V characteristics of a Langmuir probe. It is observed that the fast electron density is very low; typically 3-4 orders lower than the bulk plasma density.

A.3 Summary

The radial spread of fast electrons is determined experimentally in a simple toroidal plasma, using RFEA. On application of appropriate potential barriers, radial profiles of the transmitted electron currents for few discriminating voltages are obtained. The observed radial profiles of electron currents exhibit sharp peak close to the minor axis. Finite electron currents are observed for repelling voltages much larger than the applied negative bias to the filament. The gradients observed in the electron current profiles are significantly larger, that is the electrons with large energies are distributed in a narrow region, close to the minor axis. The typical width of this narrow region is approximately 2 cm. It is believed that the parameters such as electron temperature and floating potential, possibly get modified in this region. The major findings of this work have been published in **(T. S. Goud et al)** **J. of Phys.: Conf. Ser. 208, 012029 (2010)**.

Bibliography

[1] K. Ida, N. Ohyabu, T. Morisaki, Y. Nagayama, S. Inagaki, K. Itoh, Y. Liang, K. Narihara, A. Yu. Kostrioukov, B. J. Peterson, K. Tanaka, T. Tokuzawa, K. Kawahata, H. Suzuki, A. Komori, and LHD Experimental group, Phys. Rev. Lett. 88, 015002 (2001).

[2] T.C. Hender, R. Fitzpatrick, A.W. Morris, P.G. Carolan, R.D. Durst, T. Edlington, J. Ferreira, S.J. Fielding, P.S. Haynes, J. Hugill, I.J. Jenkins, R.J. La Haye, B.J. Parham, D.C. Robinson, T.N. Todd, M. Valovic, and G. Vayakis, Nucl. Fusion 32, 2091 (1992).

[3] C. Forest, R. Kendrick, A. Bayliss, M. Nornberg, E. Spence, American Physical Society, 45th Annual Meeting of the Division of Plasma Physics, Oct 27-31, 2003.

[4] J. E. Rice, A. Ince-Cushman, J. S. deGrassie, L. -G. Eriksson, Y. Sakamoto, A. Scarabosio, A. Bortolon, K. H. Burrell, B. P. Duval, C. Fenzi-Bonizec, M. J. Greenwald, R. J. Groebner, G. T. Hoang, Y. Koide, E. S. Marmar, A. Pochelon and Y. Podpaly, Nucl. Fusion 47, 1618 (2007).

[5] R. J. Bickerton, Phil. Trans. R. Soc. Lond. A 357, 397 (1999).

[6] F. Ryter, F. Imbeaux, F. Leuterer, H.-U. Fahrbach, W. Suttrop, and ASDEX Upgrade Team, Phys. Rev. Lett. 86, 5498 (2001).

[7] F. Ryter, F. Leuterer, G. Pereverzev, H.-U. Fahrbach, J. Stober, W. Suttrop, and ASDEX Upgrade Team, Phys. Rev. Lett. 86, 2325 (2001).

[8] W. Dorland, F. Jenko, M. Kotschenreuther, and B. N. Rogers, Phys. Rev. Lett. 85, 5579 (2000).

[9] S. Niedner, B. D. Scott, and U Stroth, Plasma Phys. Control. Fusion 44, 397 (2002).

[10] Gerald I. Kent, Norman C. Jen, and Francis F. Chen, The Phys. Fluids 12, 2140 (1969).

[11] G. Prasad, D. Bora, and Y. C. Saxena, Phys. Plasmas 1, 1832 (1994).

[12] R. Jha, P. K. Kaw, S. K. Mattoo, C. V. S. Rao, Y. C. Saxena, R. Singh, Aditya Team, Nuclear Fusion 33, 1201 (1993).

[13] R. J. Taylor, M. L. Brown, B. D. Fried, H. Grote, J. R. Liberati, G. J. Morales, and P. Pribyl, Phys. Rev. Lett. 63, 2365 (1989).

[14] S. Yoshikawa, W. L. Harries, and R. M. Sinclair, Phys. Fluids 6, 1506 (1963).

[15] R. V. Nieuwenhove, Plasma Phys. Control. Fusion 34, 873 (1992).

[16] S. H. Muller, A. Fasoli, B. Labit, M. McGrath, M. Podesta, and F. M. Poli, Phys. Rev. Lett. 93, 165003 (2004).

[17] K. L. Wong, M. Ono, and G. A. Wurden, Rev. Sci. Instr. 53, 409 (1982).

[18] D. Bora, Phys. Lett. A 139, 308 (1989).

[19] K. Rypdal, E. Gronvoll, F. Oynes, A Fredriksen, R. J. Armstrong, J. Truslen and H. L. Pecseli, Plasma Phys. Control. Fusion 36, 1099 (1994).

[20] C. Riccardi, D. Xuantong, M. Salierno, L. Gamberale, and M. Fontanesi, Phys. Plasmas 4, 3749 (1997).

[21] C. Theiler, A. Diallo, A. Fasoli, I. Furno, B. Labit, M. Podesta, F. M. Poli, and P. Ricci, Phys. Plasmas 15, 042303 (2008).

[22] S. Nishi, T. Sakabe, M. Uchida, H. Tanaka and T. Maekawa, Plasma Phys. Contol. Fusion 52, 065011 (2010).

[23] G. Prasad, D. Bora, and Y. C. Saxena, Geophysical Research Letters 19, 241 (1992).

[24] G. Prasad, D. Bora, and Y. C. Saxena, Geophysical Research Letters 19, 245 (1992).

[25] A. K. Singh, R. Kaur, S. K. Mattoo, and A. Hirose, Phys. Plasmas 11, 328 (2004).

[26] R. Kaur, A. K. Singh, and S. K. Mattoo, Phys. Plasmas 4, 2955 (1997).

[27] P. K. Sharma, and D. Bora, Plasma Phys. Control. Fusion 37, 1003 (1995).

[28] A. K. Singh, and Y. C. Saxena, Phys. Plasmas 1, 2926 (1994).

[29] R. Singh, S. Mahajan, and K. Avinash, Phys. Rev. Lett. 77, 1504 (1996).

[30] Frank J. Oynes, Hans L. Pecseli, and Kristoffer Rypdal, Phys. Rev. Lett. 75, 81 (1995).

[31] A. Fredriksen, C. Riccardi and L. Cartegni, Rev. Sci. Instrum. 74, 1588 (2003).

[32] Frank J. Oynes, Ole-Morten Olsen, Hans L. Pecseli, Ashild Fredriksen, and Kristoffer Rypdal, Physical Review E 57, 2242 (1998).

[33] K. Rypdal, and S. Ratynskaia, Phys. Plamsas 11, 4623 (2004).

[34] K. Rypdal, O. E. Garcia, and J.-V. Paulsen, Phys. Rev. Lett. 79, 1857 (1997).

[35] I. Furno, B. Labit, M. Podesta, A. Fasoli, S. H. Muller, F. M. Poli, P. Ricci, C. Theiler, S. Brunner, A. Diallo, and J. Graves, Phys. Rev. Lett. 100, 055004 (2008).

[36] I. Furno, B. Labit, A. Fasoli, F. M. Poli, P. Ricci, C. Theiler, S. Brunner, A. Diallo, J. P. Graves, M. Podesta, and S. H. Muller, Phys. Plasmas 15, 055903 (2008).

[37] S. H. Muller, C. Theiler, A. Fasoli, I. Furno, B. Labit, G. R. Tynan, M. Xu, Z. Yan, and J. H. Yu, Plasma Phys. Control. Fusion 51, 055020 (2009).

[38] M. Podesta, A. Fasoli, B. Labit, I. Furno, P. Ricci, F. M. Poli, A. Diallo, S. H. Muller, and C. Theiler, Phys. Rev. Lett. 101, 045001 (2008).

[39] C. Theiler, I. Furno, P. Ricci, A. Fasoli, B. Labit, S. H. Muller, and G. Plyushchev, Phys. Rev. Lett. 103, 065001 (2009).

[40] Paolo Ricci, and B. N. Rogers, Phys. Rev. Lett. 104, 145001 (2010).

[41] P. H. Diamond, and Y. B. Kim, Phys. Fluids B 3, 1626 (1991).

[42] C. Holland, J. H. Yu, A. James, D. Nishijima, M. Shimada, N. Taheri, and G. R. Tynan, Phys. Rev. Lett. 96, 195002 (2006).

[43] G. R. Tynan, M. J. Burin, C. Holland, G. Antar and N. Crocker, Phys. Plasmas 11, 5195 (2004).

[44] G. R. Tynan, C. Holland, J. H. Yu, A. James, D. Nishijima, M. Shimada, and N. Taheri, Plasma Phys. Control. Fusion 48, S51 (2006).

[45] M. J. Burin, G. R. Tynan, G. Y. Antar, N. A. Crocker, and C. Holland, Phys. Plasmas 12, 052320 (2005).

[46] F. Brochard, E. Gravier, and G. Bonhomme, Phys. Plasmas 12, 062104 (2005).

[47] Sangeeta Mahajan, R. Singh, and K. Avinash, Phys. Plasmas 4, 2612 (1997).

[48] J. Arol Simpson, Rev. Sci. Instr. 32, 1283 (1961).

[49] R. A. Pitts and R. Chavan, Rev. Sci. Instr. 74, 4644 (2003).

[50] I.S.Nedzelskiy, C.Silva, H.Figueiredo, H.Fernandes, and C.A.F.Varandas, Rev. Sci. Instr. 77, 10E729 (2006).

[51] A.W.Molvik, Rev. Sci. Instr. 52, 704 (1981).

[52] Kenichi Nagaoka, Atsushi Okamoto, Shinji Yoshimura, and Masayoshi Y. Tanaka, Journal of the Physical Society of Japan 70, 131 (2001).

[53] P. C. Stangeby, Phys. Fluids 27, 2699 (1984).

[54] E. J. Powers, Nuclear Fusion 14, 749 (1974).

[55] R. J. Bickerton, Nuclear Fusion 13, 290 (1973).

[56] A. Fasoli, B. Labit, M. McGrath, S. H. Muller, G. Plyushchev, M. Podesta, and F. M. Poli, Phys. Plasmas 13, 055902 (2006).

[57] J. M. Beall, Y. C. Kim, and E. J. Powers, J. Appl. Phys. 53, 3933 (1982).

[58] Young C. Kim, and Edward J. Powers, IEEE transactions on plasma science PS-7, 120 (1979).

[59] A. E. White, S. J. Zweben, M. J. Burin, T. A. Carter, T. S. Hahm, J. A. Krommes and R. J. Maqueda, Phys. Plasmas 13, 072301 (2006).

[60] Claudia Riccardi, and Ashild Fredriksen, Phys. Plasmas 8, 199 (2001).

[61] H. Sugai, A. Komori, T. Sawafuzi, N. Sato, and Y. Hatta, The Phys. Fluids 20, 90 (1977).

[62] S. Nishi, T. Sakabe, M. Uchida, H. Tanaka and T. Maekawa, Plasma Phys. Control. Fusion 52, 125004 (2010).

[63] K. Lackner, and N.A.O. Gottardi, Nuclear Fusion 30, 767 (1990).

[64] L. Federspiel, B. Labit, P. Ricci, A. Fasoli, I. Furno, and C. Theiler, Phys. Plasmas 16, 092501 (2009).

[65] B. A. Carreras, C. Hidalgo, E. Sanchez, M. A. Pedrosa, R. Balbin, I. Garcia-Cortes, B. van Milligen, D. E. Newman and V. E. Lynch, Phys. Plasmas 3, 2664 (1996).

[66] R. Jha, P. K. Kaw, S. K. Mattoo, C. V. S. Rao, Y. C. Saxena, and ADITYA Team, Phys. Rev. Lett. 69, 1375 (1992).

[67] H. M. Mott-Smith and Irving Langmuir, Phys. Rev. 28, 727 (1926).

[68] V. I. Demidov, S. V. Ratynskaia and K Rypdal, Rev. Sci. Instr. 73, 3409 (2002).

[69] D. Bohm, E. H. S. Durhop and H. S. W. Massey in Characteristics of Electrical Discharges in Magnetic Fields (Edited by A. Guthrie and R. K. Walkerling). McGraw-Hill, New York (1949).

[70] S. A. Cohen, J. Nucl. Mater. 76 & 77, 68 (1978).

[71] P. C. Stangeby, J. Phys. D: Appl. Phys. 15, 1007 (1982).

[72] R. A. Pitts and P. C. Stangeby, Plasma Phys. Contol. Fusion 32, 1237 (1990).

[73] J. A. Tagle, P. C. Stangeby and S. K. Erents, Plasma Phys. Control. Fusion 29, 297 (1987).

[74] P. C. Stangeby, G. M. McCracken, S. K. Erents and G. Matthews, J. Vac. Sci. Technol. A 2, 702 (1984).

[75] M. Podesta, A. Fasoli, B. Labit, M. McGrath, S. H. Muller and F. M. Poli, Plasma Phys. Control. Fusion 47, 1989 (2005).

[76] R. Budny and D. Manos, J. Nucl. Mater. 121, 41 (1984).

[77] D. Diebold, E. Y. Wang, J. Pew, G. Winz, R. Breun, W. Li, H. Y. Che and N. Hershkowitz, Rev. Sci. Instr. 61, 2870 (1990).

[78] G. Proudfoot, P. J. Harbour, J. Allen and A. Lewis, J. Nucl. Mater. 128-129, 180 (1984).

[79] J. Allen and P. J. Harbour, J. Nucl. Mater. 145-147, 264 (1987).

[80] I. H. Hutchinson, Phys. Fluids 30, 3777 (1987).

[81] I. H. Hutchinson, Phys. Rev. A 37, 4358 (1988).

[82] K-S. Chung and I. H. Hutchinson, Phys. Rev. A 38, 4721 (1988).

[83] H. Amemiya, A. Tsushima and G. Fuchs, Contrib. Plasma Phys. 39, 515 (1999).

[84] H. Van Goubergen, R. R. Weynants, S. Jachmich, M. Van Schoor, G. Van Oost and E. Desoppere, Plasma Phys. Control. Fusion 41, L17 (1999)

[85] R. Hatakeyama, N. Hershkowitz, R. Majeski, Y. J. Wen, D. B. Brouchous, P. Proberts, R. A. Breunn, D. Roberts, M. Vukovic and T. Tanaka, Phys. Plasmas 4, 2947 (1997).

[86] J. R. Smith, N. Hershkowitz and P. Coakley, Rev. Sci. Instr. 50, 210 (1979).

[87] Robert F. Kemp and J. M. Sellen, Jr., Rev. Sci. Instr. 37, 455 (1966).

[88] N. Hershkowitz and M. H. Cho, J. Vac. Sci. Technol. A 6, 2054 (1988).

[89] R. Kaur and S. K. Mattoo, Plasma Sources Sci. Technol. 18, 015003 (2009).

[90] W.E.Amatucci, P.W.Schuck, D.N.Walker, P.M.Kintner, S.Powell, B.Holback and D.Leonhardt, Rev. Sci. Instr. 72, 2052 (2001).

[91] P. Spatenka, R. Studeny and H. Suhr, Meas. Sci. Technol. 3, 704 (1992).

[92] T. S. Goud, R. Ganesh, K. Sathyanarayana, D. Raju, K. K. Mohandas, C. Chavda, Aruna M. Thakkar, and N. C. Patel, Journal of Physics: Conference Series 208, 012029 (2010).

[93] T. S. Goud, R. Ganesh, Y. C. Saxena, D. Raju, K. Sathyanarayana, K. K. Mohandas, and C. Chavda, Phys. Plasmas 18, 042310 (2011).

[94] J. Ghosh, R. C. Elton, H. R. Griem, A. Case, R. Ellis, A. B. Hassam, S. Messer, and C. Teodorescu, Phys. Plasmas 11, 3813 (2004).

[95] F. M. Poli, P. Ricci, A. Fasoli, and M. Podesta, Phys. Plasmas 15, 032104 (2008).

[96] D. L. Jassby, Phys. Fluids 15, 1590 (1972)

[97] Albert Simon, Phys. Fluids 6, 382 (1963).

[98] F. C. Hoh, Phys. Fluids 6, 1184 (1963).

[99] Y. Sakawa, C. Joshi, P. K. Kaw, F. F. Chen, and V. K. Jain, Phys. Fluids B 5, 1681 (1993).

[100] Sangeeta Mahajan, Thesis, Institute for Plasma Research, Gandhinagar, 1997.

[101] W. W. Lee, and R. A. Santoro, Phys. Plasmas 4, 169 (1997).

[102] A. Fasoli, A. Burckel, L. Federspiel, I. Furno, K. Gustafson, D. Iraji, B. Labit, J. Loizu, G. Plyushchev, P. Ricci, C. Theiler, A. Diallo, S. H. Mueller, M. Podesta and F. Poli, Plasma Phys. Control. Fusion 52, 124020 (2010).

[103] T. S. Goud, R. Ganesh, Y. C. Saxena, D. Raju, K. Sathyanarayana, K. K. Mohandas, and C. Chavda, Phys. Plasmas 19, 032307 (2012).

[104] Y. Itikawa, Atomic Data and Nuclear Data Tables 14, 1 (1974).

[105] A. Fredriksen, C. Riccardi and G. Longoni, Rev. Sci. Instr. 72, 457 (2001).

[106] Saul Dushman, Rev. Mod. Phys. 2, 381 (1930).

[107] J. A. Becker, Rev. Mod. Phys. 7, 95 (1935).

[108] Karl T. Compton and Irving Langmuir, Rev. Mod. Phys. 2, 123 (1930).

[109] Irving Langmuir and Karl T. Compton, Rev. Mod. Phys. 3, 191 (1931).

[110] I. Langmuir, Phys. Rev. 2, 450 (1913).

[111] K. T. Compton and C. C. Van Voorhis, "Probability of ionization of gas molecules by electron impacts", Palmer Physical Laboratory, Princeton, 436 (1925)

[112] P. C. Stangeby, Plasma Phys. Control. Fusion 37, 1031 (1995)

[113] Lewis B.Leder and J.Arol Simpson, Rev. Sci. Instr. 29, 571 (1958).

[114] Y.Cui, Y.Zou, A.Valfells, M.Reiser, M.Walter, I.Haber, R.A.Kishek, S.Bernal, and P.G.O'Shea, Rev. Sci. Instr. 75, 2736 (2004).

[115] A.S.Wan, T.F. Yang, B.Lipschultz, and B.LaBombard, Rev. Sci. Instr. 57, 1542 (1986)